INSTITUT POLYTECHNIQUE DE PARIS

NNT : 2021IPPAX061

Thèse de doctorat

Vortex-induced vibrations on industrial chimneys

Thèse de doctorat de l'Institut Polytechnique de Paris
préparée à l'École polytechnique

École doctorale n°626 École doctorale de l'Institut Polytechnique de Paris (EDIPP)
Spécialité de doctorat : Mécanique des fluides et des solides, acoustique

Thèse présentée et soutenue à Palaiseau, le 8 octobre 2021, par

ØYVIND MORTVEIT ELLINGSEN

Composition du Jury :

Vincent Denoël Professeur, Université de Liège (ArGEnCo)	Rapporteur
Carlo Cossu Directeur de recherches, CNRS (LHEEA)	Président Rapporteur
Claudio Mannini Research Associate, University of Florence (CRIACIV/DICEA)	Examinateur
Emmanuel de Langre Professeur, IP Paris (LadHyX)	Examinateur
François Coiffet Ingénieur développement, Poujoulat Group (CERIC)	Examinateur
Pascal Hémon Ingénieur de recherche, CNRS (LadHyX)	Directeur de thèse
Xavier Amandolese Maître de conférences, CNAM (LMSSC)	Invité Co-directeur de thèse
Olivier Flamand Ingénieur recherche et expertise, CSTB (CAPE)	Invité

A thank you to Frank, Nikolai, Reidar, Tequila and Rupa for motivating me to start and keeping writing.

Acknowledgment

This written work marks the end of a 3-year journal where half of it was spent displaced from my office at LadHyX. The work done has been challenging, with its ups and downs, but I would like to firstly thank Xavier, Oliver and Pascal for the opportunity to do this PhD. Secondly, I would like to thank Aurélien, François and Julien for their contribution to my work and the project and to thank the CSTB, CNES and Beirens (of the Poujoulat Group) for funding this work. Without their expertise and feedback, this work would not be successful. In addition, their continuous feedback on experimental and quarterly reports simplified the writing process which I'm retrospectively grateful for.

This work could also not have happened without the aid of the technicians and staff at CSTB Nantes. Firstly, I would therefore like to thank Isabel, Tristan and Hélène for helping me with administrative problems such as scheduling my vacation days and delivering my lunch checks. Secondly, I would like to thank the technicians working at CSTB for their help, e.h. Jocelyne, Cyril and Guillaume for helping perform the wind tunnel tests; Yves, Brewal and Yvan and Dominique for their help with the field experiment; and Bruno, Mathieu and Stephane for helping manufacture the models used. Thirdly, I would like to thank Graham and Fabrice for their scientific help and discussions. Lastly, I would like to thank Aurélien, Fabien, François and the rest of the workers at Beirens and the Poujoulat Group for helping me better understand how chimneys are designed and their help in designing the chimney used for the field tests.

Like at CSTB and at the Poujoulat group, there are people at LadHyX who's help and friendship warrants acknowledgment. For instances, Antoine, Akhil, Ernesto, Tullio and Kevin made life at LadHyX much better and really helped me acclimatize to the office; I'm really grateful for their assistance and friendly discussions. I would also like to thank Blaise and Graham for their work in keeping up the lab spirit pre pandemic as well as Toaï and Daniel for helping me set me up for remote work which made working from Norway for large parts of my PhD a possibility.

Finally, I would like to thank my girlfriend Rupa, my parents Harald and Ingebjørg, my siblings Irene (and her boyfriend Håvard) and Jarle, my nephew Nikolai and my friends at home and abroad for motivating me to finish; I'm especially happy for the writing help given by Nikolai. The last acknowledgment goes to three furry creatures who's kept me warm and motivated to work; thank you Frank, Reidar and Tequila.

Contents

Nomenclature

List of symbols

Symbol	Description
X, Y, Z	Dimensional positions in meters
x, y, z	Dimensionless positions
$\mathbf{x}$	Dimensionless vector position
U	Dimensional flow speed
$\mathbf{u}$	Flow velocity vector
u, v, w	Flow velocity components in x, y and z direction
Tu	Turbulence intensity
p	Pressure
ω, f	Frequencies in radians per second and Hertz
ν	Kinematic viscosity
ρ	Density
d	Structural diameter
h	Structural height
ψ	Mode shape
$m(z)$	Mass per unit length
k	Stiffness
ζ, δ	Viscous damping ratio and logarithmic decrements
k_δ	Roughness size
C	Force coefficient
r_i	Dimensionless amplitude of variable i
α	Eigenvalue or energy for bi-orthogonal decomposition
Φ, Ψ	Topos and chronos pair (of bi-orthogonal decomposition)
SD	Standard deviation of (value)
$R(x, y)$	Correlation between variables x and y
$C_{x,y}$	Coherence between variables x and y
MAC	Modal assurance criterion
K_ξ, K_W	Mode shape and correlation length factor
$S(f)$	Power spectra
B	Turbulence bandwidth (spectral models)
A, ϵ	Empirical wake force constants

List of subscripts

Symbol	Description
l	Lift
d	Drag
M	Mass
add	Added (point) mass
σ	Standard deviation
n	Natural (first natural)
s	Vortex shedding
$crit$	At critical vortex-shedding frequency ($f_s = f_n$)

Dimensionless numbers and derived parameters

Symbol	Description	Definition	Unit
λ	Aspect ratio	h/d	[-]
St	Strouhal number	$f_s d/U$	[-]
Re	Reynolds number	Ud/ν	[-]
U_R	Reduced speed	$U/f_n d$	[-]
ω_q	Fluid/structure frequency ratio	$U_r St$	[-]
m_e	Equivalent mass	$\int_0^1 m\psi^2 dz / \int_0^1 \psi^2 dz$	[kg/m]
μ	Mass ratio	$(m_e + \frac{\pi\rho d^2 C_M}{4})/\rho d^2$	[-]
Sc	Scruton number	$2m_e\delta/\rho d^2$	[-]
Rr	Relative roughness	k_δ/d	[-]

Part I

Introduction and state of the art

Chapter

1 Foreword and motivation

> *"Unless you try to do something beyond what you have already mastered, you will never grow."*
>
> Ronald E. Osborn

Flue-gas stacks, or industrial chimneys, and launch vehicles are examples of tall and slender circular structures with large diameters that can be prone to vortex-induced vibrations. These vibrations can be significant when the shedding frequency, which increases linearly with incoming wind speed, is close to the natural frequency of the structure. When these vortex-induced vibrations occur, they create a nonlinear feedback loop that strengthens the vortex-forces and in turn the vibrations. While turbulence-induced vibrations occur at high wind speeds, the vortex-induced vibrations can happen at low speeds.

Industrial chimneys are often used to disperse pollutants in the air so that the concentration is within the legal limits near the ground. Increased regulations have led to the need of better filtration devices and taller chimneys like the concrete chimneys shown in figure 1.1. These tall and massive chimneys aren't necessarily the most economical and you're more likely to see smaller but slenderer steel chimneys like the ones in figure 1.2. Due to economic and safety reasons, it's necessary to build accurately designed chimneys that can withstand the static and dynamic forces applied to it (e.g. static wind load, turbulence and vortex-shedding); this requires good wind tunnel techniques and predictive models that accurately predict the static deformation and dynamic amplitude response. If the amplitude response is large, a well predicted response will also aid in designing effective tuned mass-dampers that can reduce the response.

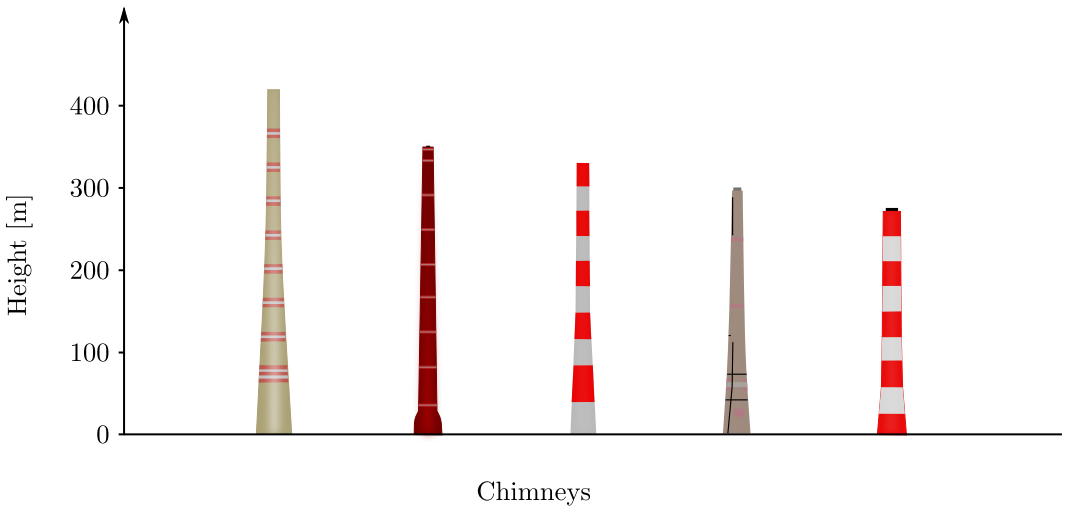

Figure 1.1: *Tall concrete chimney examples found on SkyscraperPage.com [1].*

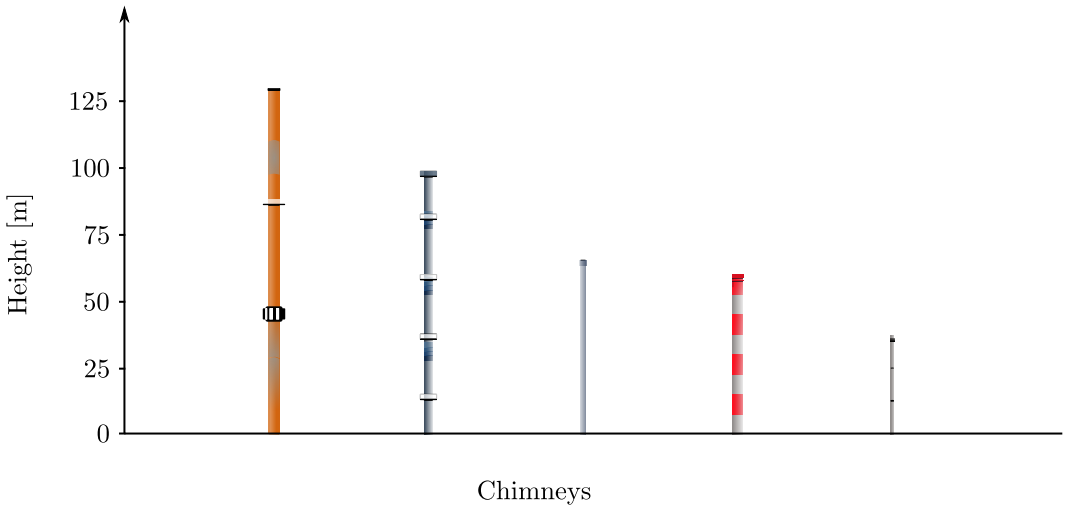

Figure 1.2: *Slender steel chimney examples produced by Beirens and VL Staal (Poujoulat group) [2, 3].*

Getting good response predictions are not trivial and a naive wind tunnel implementation might over predict the wind load due to vortex-shedding by as much as 400% [4]. This is due to the aerodynamic forces on a circular cylinder being Reynolds number dependent and the values seen in the field for large structures can rarely be recreated in wind tunnels. Good wind tunnel techniques are therefore needed to correctly predict vortex-induced vibrations.

Some, like the previously cited researchers, say that predictive models should be used instead of wind tunnel experiments. There are many possible models to use (e.g. the Eurocode standard included two vortex-induced vibration models [5] and there are more in the scientific literature [6, 7]) though not all of them are applicable for the design of industrial chimneys or have an unsatisfactorily performance. In addition, the predictions are contradictory and many open questions remains on how to best include all aerodynamic and structural parameters in the models. For instance, the effect of turbulence or surface imperfections on the predictions remain unclear in the non-design code models as is the effect super-critical Reynolds number flow around circular cylinders ($Re > 10^6$ e.g. large diameter chimneys). The design code models have issues as well and fail to include the effect of tuned mass-dampers and in producing the amplitude response needed to design them. Computational methods (FEM/CFD combinations) could be used to predict vortex-induced vibrations and help design tuned mass-dampers but can be difficult. For instance, the simulations can fail due to mesh deformation, the CFD calculations needs validation at super-critical Reynolds numbers and the computational power needed to test a single speed/configuration makes testing many configurations costly.

The goal of this work is thus threefold. Firstly, it aims at improving the collective understanding of vortex-shedding on large circular structures (like industrial chimneys) by experimentally determining the unsteady pressure distribution for 2D circular cylinders at super-critical Reynolds numbers ($Re > 10^6$). Secondly, it aims to improve or validate the wind tunnel techniques used to determine vortex-induced vibrations of industrial chimneys and similar slender structures with circular cross section at super-critical Reynolds numbers using small-scale models. Lastly, predictive models, like those in the Eurocode, will be compared with a newly defined predictive model and validated using the experimental data to determine the best model for a given situation. All of the above is done using wind tunnel experiments (at large and small scales), a field test using a full-scale chimney-like object and appropriate analytic techniques.

Chapter

2 Vortex-induced vibrations of slender structures with circular cross section

A brief introduction

Flow around a smooth circular cylinder and the vortex-shedding from it can be complex. For instance, the location of minimum pressure and the minimum pressure coefficient changes with the Reynolds number. In addition, the separation point and pressure coefficient in the separated region is highly Reynolds number dependent as is the behavior of the shed vortices in the wake behind the cylinder. Add motion and the flow field becomes even more complex by adding nonlinear coupling between the fluid and structural oscillation. This coupling gives rise to vortex-induced vibrations which are hard to model and not fully understood. When adding 3D dimensional effects, the flow and vortex-induced vibration becomes even more complex with correlation, coherence, end-effects and more complex modes of oscillation. This chapter is an introduction to the parameters and factors that affects the flow around cylinder like structures with circular cross-sections and vortex-induced vibrations. It will also be shown that there are important knowledge gaps later chapters will fill.

2.1 Stationary cylinders in cross flow

2.1.1 The Reynolds number effect

The Reynolds number is one of the most important parameters in classifying and predicting the flow field near a circular cylinder. This dimensionless parameter, given in equation (2.1), relates the inertial and viscous forces experienced by a fluid and helps determine how flows behave. For a circular cylinder, the inertial forces are ρU^2, with ρ and U being the fluid density and speed respectively, and the viscous forces $\mu U/d$, with μ and d being the dynamic viscosity and diameter respectively.

$$Re = \frac{\rho U d}{\mu} = \frac{U d}{\nu}. \tag{2.1}$$

Rather than being separated into two flow categories, e.g. laminar or turbuent as for pipe flow, the flow around a cylinder can be categorized into several distinct regions based on the Reynolds number. This is visualized in figure 2.1 which is based on the wake and flow separation visualization and descriptions of Lienhard [9] and Blevins [6]. The difference is that figure 2.1 uses the naming convention of Szechenyi [10] which is more similar and consistent with the naming of Mach number regimes. In addition to showing how flow around a circular cylinder changes, figure 2.1 shows the changes in the mean drag coefficient with the Reynolds number (cf. the textbook of White [11] or paper of Roshko [8] for the evolution of C_d). The flow changes around a cylinder and the mean drag are intrinsically linked as the mean drag around a cylinder is dependent on the shear and pressure.

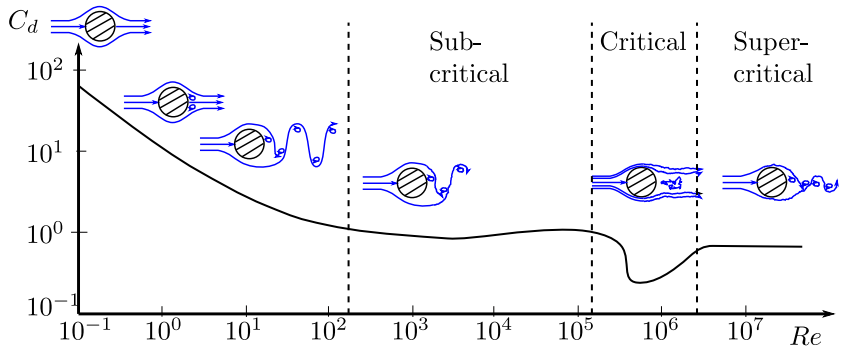

Figure 2.1: *Definition of Reynolds number regions and how mean drag coefficients changes with the Reynolds number. Inspired descriptions by Roshko [8] and Lienhard [9] as cited by Blevins [6].*

At very low Reynolds numbers, $Re \lessapprox 5$, the boundary layer flow around the cylinder and in the wake behind the cylinder is laminar and fully attached. As the Reynolds number is increased, up to $Re \approx 40$, the flow stays laminar but separates from the cylinder as symmetric vortex pairs behind the cylinder. Beyond Reynolds numbers of 40 and up to 150, the shed vortices are alternating instead of symmetrically pairwise and are called von Kármán vortices. These shed vortices are strong and gives rise to alternating lift and drag forces. While the flow separation changes from pairwise to periodically alternating vortices, the flow over and behind the cylinder is still laminar at these Reynolds numbers. For the regions mentioned so far, the drag coefficient decreases from a value of $\mathcal{O}(10^2)$ to $\mathcal{O}(10^0)$ [6, 8].

For industrial chimneys (cf. figures 1.1 and 1.2), launch vehicles and other circular civil engineering structures, the Reynolds number will be greater than what's described so far. Even for a wire with a 1 cm diameter, the Reynolds number will be above 600 when the wind speed is 1 m/s. The first Reynolds number range of interest, is the sub-critical Reynolds number range which is the region between first and second dashed line of figure 2.1 ($Re \in [150, 3 \cdot 10^5]$). In this Reynolds number range, there's a large change in the flow behind the cylinder. While the boundary layer flow over the cylinder stays laminar up to separation point (near $\theta_s \approx \pm 80°$ from the stagnation point[1]), the shed vortices and wake is increasingly turbulent. The width of the vortex street behind the cylinder and strength of the shed vortices are similar to at lower Reynolds number, i.e. the width is relatively large and the shed vortices are strong and periodic [6, 8, 12]. Canonically, the mean drag converges towards a value of $C_d = 1.2$ in this region and lasts until the sub-critical Reynolds region ends at $Re \approx 3 \cdot 10^5$ [6, 10, 12–14].

Beyond Reynolds numbers of $Re \approx 3 \cdot 10^5$, the flow around circular cylinders changes dramatically and enters the critical region. This region comprises of Reynolds numbers between $3 \cdot 10^5$ and 1-3 $\cdot 10^6$ for circular 2D cylinders as shown in figure 2.1 (between the second and third dashed lines). In this range, the boundary layer flow starts transitioning from being fully laminar to being turbulent but can have a double separation process with the final separation being in the rear ($\theta_s \approx \pm 140°$) [10, 13].

At early critical Reynolds numbers, the boundary layer flow can start as laminar, separate from the cylinder before reattach as turbulent boundary layer flow. If asymmetrically formed, these laminar separation bubbles give a mean lift. As the final separation is far in the rear, the wake is relatively narrower and more chaotic with an irregular and weak vortex-shedding signature. In addition to changing the surface flow, the mean drag coefficient has a steep decline at low critical Reynolds numbers before reaching the global minimum drag coefficient and subsequently increase. This drastic change in mean drag coefficient is why the flow change

[1] Point near the front where the fluid speed is zero and static pressure coefficients is greatest.

at critical Reynolds number is often referred to as the "drag crisis" [6, 8, 12, 15].

The final Reynolds number region, and the one that's most relevant for chimneys and launch vehicles, is the super-critical Reynolds number region at $Re >$ 1-3 $\cdot 10^6$ (after the last dashed line in figure 2.1) [6, 10, 12, 13]. Experimental data at super-critical Reynolds numbers are scarcer than the previously described regions [16, 17]. A reason for the lack of data is the need for more complex and specialized wind-tunnels[2] (e.g. highly pressurized wind tunnels [8, 16, 17, 19–22], different flow mediums [23] or high speed wind tunnels giving high Mach numbers [24]) or modified cylinders triggering an earlier boundary layer flow transition [10, 17, 25–28].

The experimental data available at super-critical Reynolds numbers do identify some general trends. Firstly, the boundary layer flow around the cylinder is fully turbulent just like the wake's. Secondly, regular vortex-shedding is re-established at super-critical Reynolds numbers with a shedding point that starts near $\theta_s \approx \pm 140°$ though it's much more chaotic [6, 8, 15, 17, 21, 24, 29] [15]. As the Reynolds number is increased, the shedding point moves towards the front ($\theta_s \approx \pm 110°$) but stays in the rear half. This change in the separation point means that the wake width is narrow at the start of the super-critical region but increases with the Reynolds number [6, 8, 12, 16, 17, 21, 24]. Like the boundary layer flow, the drag coefficient stabilizes at a fairly constant value at super-critical Reynolds numbers and this new value is lower than at sub-critical Reynolds numbers (in the range $C_d \in [0.7, 0.75]$ [8, 21, 22] though other works cite a lower value cf. [13, 30, 31]).

2.1.2 Steady and unsteady aerodynamic forces

Pressure distribution

At Reynolds numbers of interest ($Re > 3 \cdot 10^5$), the distribution of unsteady pressure is the main source of aerodynamic forces on a cylinder; skin friction is at most 3% of the total mean drag [11, 19, 20]. To compare the pressure distributions from different experiments, it's better to use a dimensionless pressure like the pressure coefficient

$$C_{p,\theta_i}(t) = \frac{2(p(\theta_i, t) - p_{\text{inf}})}{\rho U^2}, \tag{2.2}$$

with p and p_{inf} being the static pressure on the cylinder and in the free stream respectively.

From these time series, statistics such as the mean value and standard deviation (SD or subscript σ) or root-mean-square (rms) can be found. Note that the mean, SD and rms values are related through rms $= \sqrt{\text{mean}^2 + \text{SD}^2}$. This means that the "rms of the fluctuating components" sometimes used in the literature is identical to the standard deviation [26, 32–40]. The mean and SD pressure coefficients are shown in figures 2.2 and 2.3 respectively. The mean pressure distributions on a smooth cylinder at several Reynolds number regions are based on the data of Achenbach [19] while standard deviation results at the sub-critical are by West and Apelt [41].

The mean pressure distribution is the major contributor to the mean drag and lift forces. Ideally, the mean pressure distribution will have bilateral/reflection symmetry around the centerline between 0 and 180° (mirror image). This should lead to a zero mean lift force but as seen in figure 2.2, the mean force isn't always symmetric [19, 20]. Due to flow and surface imperfections, there can be a nonzero mean lift force and the lift can be significant with larger flow instabilities like separation bubbles [19–21, 24].

In potential flow theory, the flow is fully attached around the cylinder and the pressure drag zero. Due to flow separation in the rear, the pressure "flats out" (like in 2.2) and there's a

[2]Super-critical Reynolds numbers are theoretically simpler to reach in water as the kinematic viscosity is $\mathcal{O}(10^1)$ smaller. These tunnels come with their own challenges that needs to be overcome (e.g. cavitation, size, required mass-flow rate, high fidelity force measurements and sensor equipment that can handle the fluctuating pressure and the humidity [18]). As an example, the water speed needs to be 10 m/s to reach a Reynolds number of 10^6 if using a cylinder with a diameter of 0.1 m and water at 20°C. If the water tunnel is 1x1 m^2, this corresponds to a mass-flow rate of 10000 kg/s and a kinetic energy of 500 kW.

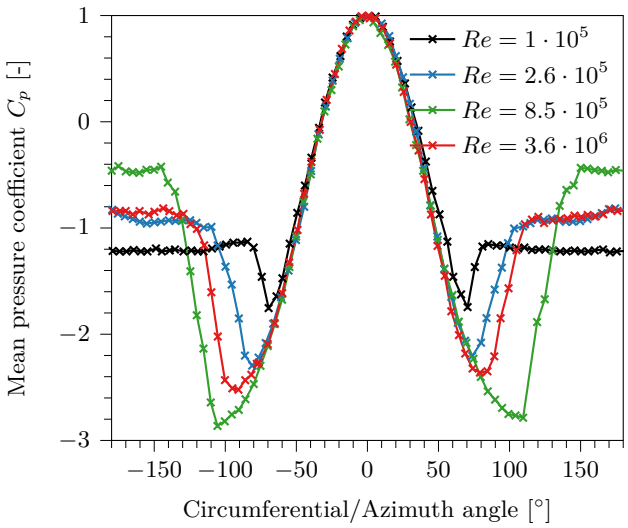

Figure 2.2: *Distribution of mean pressure coefficient for a smooth cylinder tested in a high pressure wind tunnel by Achenbach [19].*

pressure imbalance in the flow direction which leads to a mean drag force. When the separation occurs further in the rear, the flat pressure value in the rear is increased which decreases the drag. This can be seen when comparing figures 2.1 and 2.2 at sub-critical ($Re = 1.0 \cdot 10^5$), critical ($Re = 8.5 \cdot 10^5$) and super-critical Reynolds numbers ($Re = 3.6 \cdot 10^6$). At $Re = 2.6 \cdot 10^5$, there's a transition from sub-critical to critical Reynolds numbers which leads to lower drag and later separation than at lower Reynolds numbers. The base pressure in the wake and separation angle are largest for Reynolds numbers in the critical Region and smallest at sub-critical which corroborates the separation angle/drag coefficient relationship [11, 19, 20, 22, 24, 42].

Data on the distribution of standard deviation of pressure coefficient is rarer than the mean distribution. Basu [13] explains the difference for this as "more sophisticated instrumentation and measurement techniques are required for measuring [$C_{l,\sigma}$ and $C_{d,\sigma}$]". This also explains why data on unsteady drag and lift are rarer than mean drag and Strouhal number [22, 24]. It also explains why figure 2.3, showing the distribution of standard deviation of pressure coefficient for a smooth cylinder, only contains Reynolds numbers up to $1.31 \cdot 10^5$. Still, the standard deviation of pressure shows that the pressure oscillations are higher at the top of the cylinder ($\theta \in [70, 100]$) which should contribute to unsteady lift and a second higher oscillation region in the rear which should contribute to unsteady drag [41, 43, 44].

Calculating aerodynamic forces

As mentioned, the aerodynamic forces on a cylinder can be found using the surface pressure distribution as the effect of skin friction is relatively low at high Reynolds numbers [11, 19, 20, 26]. These forces are found by spatially integrating the pressure distributions projected in the directions of the drag or lift (aligned and perpendicular with the free stream direction respectively). For discretely measured pressure, the integral is replaced by a summation [26, 42] and the two-dimensional drag coefficients is calculated by

$$C_d(t) = \frac{2}{\rho d U^2} \sum_{i \in K} p(t, \theta_i) \cos(\theta_i) r \phi_i, \tag{2.3}$$

where K is the set of measurement locations in a 2D ring and $p(t, \theta_i)$ is the pressure at location i at time t. θ_i is the angle between location i and the reference location (making for force at the reference purely in drag direction), and $r\phi_i$ is the "integration length" (radius times angle

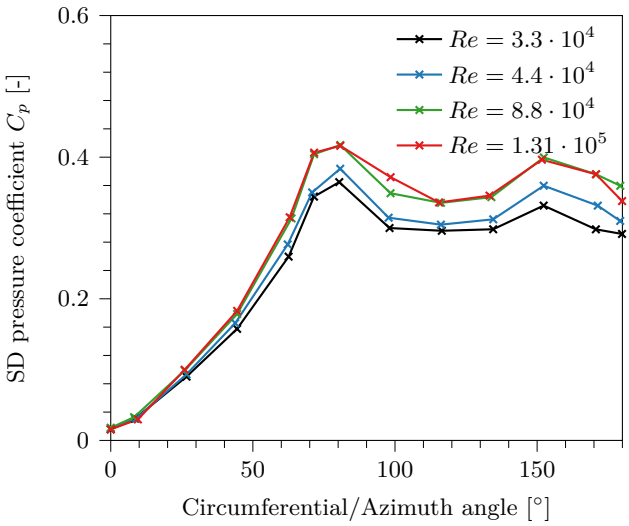

Figure 2.3: *Distribtuion of standard deviation of pressure coefficient for a smooth cylinder tested in a wind tunnel by West and Apelt [41].*

sensor i is working over). Similarly, the discrete lift force is found using

$$C_l(t) = \frac{2}{\rho d U^2} \sum_{i \in K} p(t, \theta_i) \sin(\theta_i) r \phi_i. \tag{2.4}$$

Unsteady forces

Using equations (2.3) and (2.4), the statistics of the force coefficients can be calculated similarly to the pressure's. While the mean drag and lift have been discussed previously, but the fluctuating force components have not. Relative to the total force, the fluctuating drag components are of lesser importance than the lift's. Up to 100% of the total unsteady lift (real rms) is from the SD value whereas the total unsteady drag is dominated by the mean [45, 46].

For sub-critical Reynolds numbers, 0.3 has been reported as a "classical" value for the lift coefficient's oscillation amplitude due to vortex-shedding [6, 14] which is similar to Schewe's results at low Reynolds numbers [16] (see figure 2.4). This value is lower than the results of Cheung and Melbourne [30], Blackburn and Melbourne [47] and the summarized results of Basu [13], Ribeiro [48] and Ruscheweyh [49]; the latter specified the SD lift coefficient as 0.7 at sub-critical Reynolds numbers.

In the review of Demartino and Ricciardelli [31], a large range of SD lift coefficients were found at sub-critical Reynolds numbers ($C_{l,\sigma} \in [0.09, 0.5]$) [8, 16, 36, 50–52]. A possible reason for the scatter in SD lift coefficient, is the method for calculating the forces: If found by integrating over the entire length of the cylinder, e.g. using a force balance, the phase difference between the forces (e.g. from cells of vortex-shedding) can change the total force from the 2D pressure values. Another posibility, is the influence of roughness. While the SD lift coefficient is scattered, the "classical" value reported isn't too far off from the other references. It's possible that the SD lift coefficient is in the range $C_{l,\sigma} \in [0.3, 0.4]$ at sub-critical Reynolds numbers and that it increases towards 0.4 when it's about to transition to critical Reynolds numbers [6, 13, 14, 16, 22].

What's more consistent among experiments, is how the SD lift coefficient changes qualitatively at critical and super-critical Reynolds numbers. As the Reynolds number reaches critical Reynolds numbers, $\approx 10^5$, the SD lift coefficient drops before reaching a minimum value at a Reynolds number of $4 \cdot 10^5$. From this point, the SD lift coefficient slowly increases towards a value in the range $C_{l,\sigma} \in [0.08, 0.15]$; the exact value depends on the experiment in question [13,

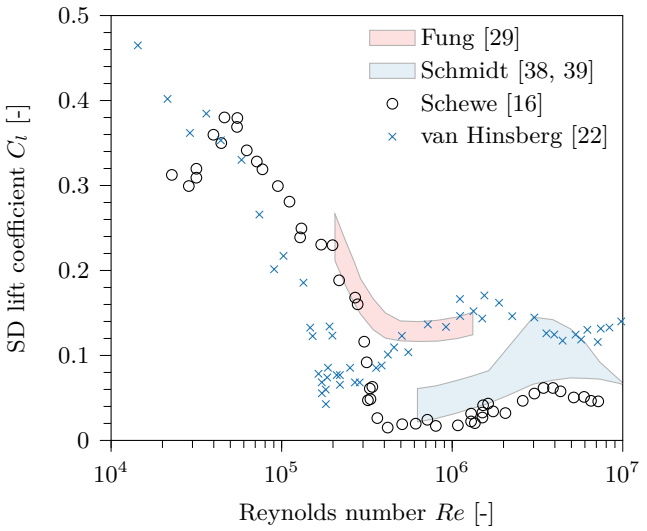

Figure 2.4: *Standard deviation of (SD) lift coefficient for smooth cylinders (Fung [29], Schmidt [38, 39] and Schewe [16]) and one rough cylinder (van Hinsberg [22]) tested in wind tunnels.*

16, 24, 30, 31, 47, 48]. The change in SD lift coefficient is, therefore, similar to how the mean drag coefficient changes with Reynolds number. The biggest difference between the mean drag and SD lift data, is the increased scatter that should be due to the lack of data and difficulty in getting accurate measurements (e.g. force-balance issues and number and precisison of unsteady pressure sensors) [13, 22, 24].

There's even less information on SD drag coefficient than lift but the available data suggests it's lower than the SD lift and behaves similarly to it. The exact value varies and some studies give a high SD drag coefficient (≈ 0.35) at sub-critical Reynolds numbers [30, 53] but the majority gives a low value in the range $C_{d,\sigma} \in [0.03, 0.12]$ [12, 29, 31, 33, 38, 39, 44]. For all studies, the SD drag coefficient behaves like the mean drag and SD lift when increasing the Reynolds number. On a fixed cylinder, the characteristic frequency of the fluctuating drag tends to be twice the oscillation frequency of the fluctuating lift [6].

Characteristic shedding frequency

Like how the forces change with the Reynolds number, so do the characteristic vortex-shedding frequency and forced frequency. To better compare experiments, a characteristic and dimensionless shedding frequency called the Strouhal number is used; this number is defined in equation (2.5). The experimental data on the vortex-shedding frequency is more available than the unsteady forces. This is because the vortex-shedding frequency can be measured both from the applied force (e.g. unsteady pressure [54] or force-balance [22, 24]) and the wake fluctuations which is easier to measure (e.g. using Cobra probes or hot-films and wires to measure the speed fluctuations in the wake) [8, 21, 23, 25].

$$St = \frac{f_s d}{U} = \frac{\omega_s d}{2\pi U}. \tag{2.5}$$

A representative selection of the Strouhal number for a smooth circular cylinder at sub-critical, critical and super-critical Reynolds numbers is shown in figure 2.5. The presented Strouhal number is measured using two different locations and those of Achenbach and Heinecke [21] and Adachi [25] uses the wake whereas Zan's [54] uses pressure and wake measurements. As mentioned, the vortex-shedding is strongly periodic at sub-critical Reynolds numbers and the bandwidth of vortex-shedding is narrow making it easy to identify. For these Reynolds

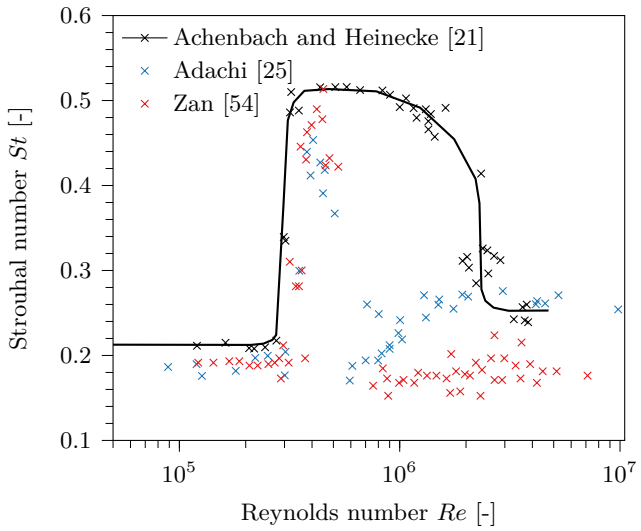

Figure 2.5: *Strouhal number for smooth cylinders tested in wind tunnels.*

numbers, the characteristic shedding frequency is consistent in the literature and is in the range $St \in [0.18, 0.21]$ [5, 6, 8, 9, 12–14, 16, 21, 23–25, 31, 36, 49, 54–56].

At critical Reynolds numbers, the vortex-shedding's bandwidth widens and more chaotic. The Strouhal numbers that are identified are higher and more diverse than at sub-critical Reynolds numbers and can be found in the range $St \in [0.25, 0.55]$ as figure 2.5 shows. At super-critical Reynolds numbers, the vortex-shedding becomes easier to identify and the bandwidth becomes narrower than the critical's. The super-critical Strouhal number has a commonality with sub-critical values in that both converge towards a constant value but the exact super-critical value varies between experiments. As shown in figure 2.5, some experiments give a Strouhal number in the range $St \in [0.25, 0.27]$ [8, 13, 21, 23–25, 36, 56] whereas others give a super-critical Strouhal number close to 0.2 [17, 54]. There is one major difference between the studies giving high and low super-critical Strouhal numbers: The tests giving the higher Strouhal numbers tend to be measured in the wake whereas the lower Strouhal numbers tend to be measured using unsteady pressure measurements.

2.1.3 Modified Reynolds numbers

One of the best practices for determining the loading on large civil engineering structures, like vortex-shedding, is to use boundary layer wind tunnels. As the models need to be scaled down in the wind tunnels, it's difficult to reach super-critical Reynolds numbers and the load will be incorrect [4]. To fix this, the test conditions are normally changed so that super-critical Reynolds numbers flow on smooth cylinders can be simulated. There are several tactics to achieve this and it includes using uniformly distributed roughness elements (e.g. sandpaper or emery paper) [10, 21, 25, 57, 58], discrete roughness elements (e.g. ribs or wires) [28, 37, 48, 59], turbulence intensity and atmospheric boundary layers [40, 60]. While triggered, the resulting super-critical unsteady forces can be different from that on a smooth cylinder.

Effect of Roughness on aerodynamics

As mentioned, added surface roughness can cause the transition to critical and super-critical Reynolds numbers to occur at lower Reynolds numbers (in absolute value) [11, 13, 40]. Most studies on the effect of surface roughness on flow over a cylinder focused on uniform surface roughness and its effect on the mean drag coefficient and the Strouhal number. The sparse data on SD lift with added uniform roughness suggest that the SD lift coefficient is increased

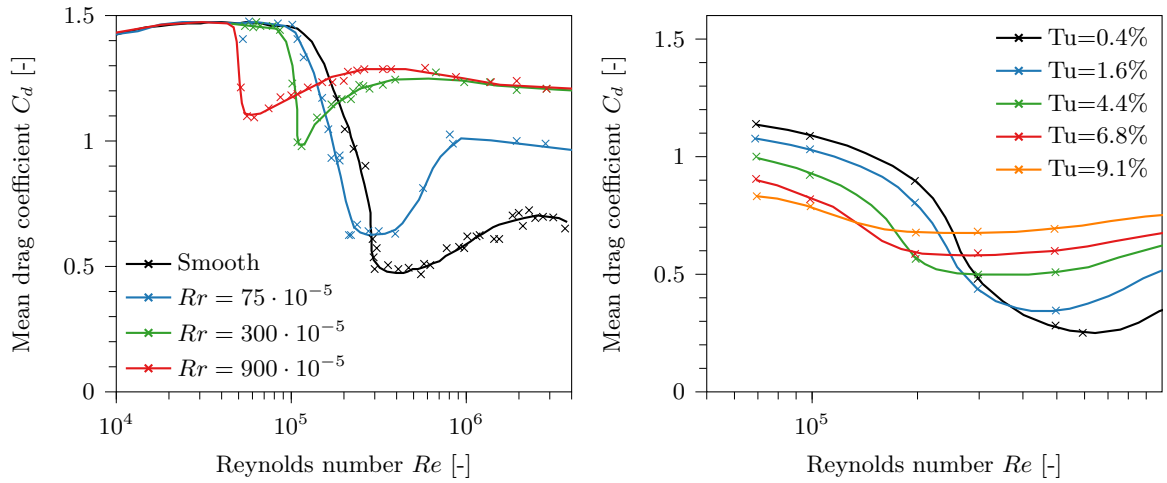

(a) *Uniform flow and rough cylinder using data from Achenbach and Heinecke [21].*

(b) *Turbulent flow results of Blackburn and Melbourne [53] and Cheung and Melbourne [30].*

Figure 2.6: *Mean drag coefficient for smooth and rough cylinders tested in wind tunnels.*

when using a rougher cylinder. This is shown in figure 2.4 using the data of van Hinsberg on a cylinder with uniform roughness of height $Rr \approx 10^{-3}$ [22, 48]. Its postulated that this is due to a stronger and stable vortex-shedding process [25, 61].

Surface roughness affects the mean drag in two ways and both can be seen in figure 2.6a. Firstly, the drag crisis and turbulent boundary layer flow (critical Reynolds numbers) is triggered at lower Reynolds numbers. Secondly, the triggered boundary layer flow has a larger mean drag coefficient at super-critical Reynolds numbers. The increase in drag is related to the thickness of the boundary layer flow: Added roughness gives a thicker boundary layer that separates earlier. This in turn decreases the base pressure (in the rear) and increases the minimum pressure on the cylinder [10, 13, 17, 19–23, 26, 27, 31, 40, 58, 62, 63]. Güven et al. [63] attributed the higher mean drag to a decreased difference between the minimum and rear pressures but a lower rear pressure acting over a larger area will increase the drag alone.

The best description of what roughness does to the Strouhal number, is that it "smooths out" the curve as a function of Reynolds number as shown in figure 2.7a. With added roughness, the higher Strouhal number "hump" at critical Reynolds numbers is reduced as is the Strouhal number at super-critical Reynolds numbers [10, 13, 17, 21, 22, 25, 54, 58, 61, 62, 64]. With the largest uniform roughness, the hump is completely smoothed out and there's only a small increase in the Strouhal number.

In addition to changing the shedding frequency, the added roughness has a second effect: It makes the vortex-shedding more periodic and stronger at super-critical Reynolds numbers and the vortex-shedding's frequency spectrum becomes a narrowband single peak [10, 13, 17, 21, 22, 25, 58, 61, 62, 64]. This effect is also seen at critical Reynolds numbers which could explain the smaller Strouhal number hump. Essentially, the overall effect of uniformly added roughness is to increase the mean drag coefficient, give clearer and stronger vortex-shedding peaks (in frequency domain), move the transition to and from critical Reynolds number to lower Reynolds numbers and to "smooth out" any instabilities caused during the transition [61, 64].

The most promising results at simulating higher Reynolds number flow is by Ribeiro [28, 37]. Ribeiro's lengthwise ribs not only best reproduced the mean forces [28], but also the unsteady force spectrum [37]. Still, the ribs trigged earlier flow separation which lowered the minimum pressure coefficient and increased it in the rear; This increased the mean and fluctuating force coefficients [28, 31, 37, 48]. While it's effective at triggering super-critical Reynolds numbers, the rib height needs to be as small or the flow will be overly distorted when compared to smooth,

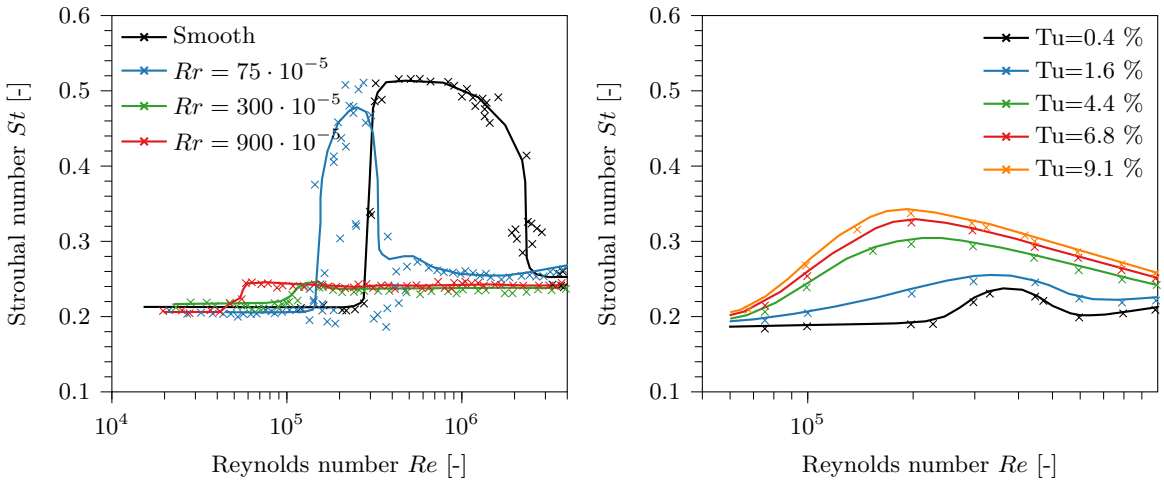

(a) *Uniform flow and rough cylinder using data from Achenback and Heinecke [21].*

(b) *Turbulent flow results of Blackburn and Melbourne [53] and Cheung and Melbourne [30].*

Figure 2.7: *Strouhal number for smooth and rough cylinders tested in wind tunnels.*

super-critical data. For instance, the added ribs quickly cause the point of minimum pressure to move forward when compared to a smooth cylinder. An alternative to ribs, is to use either two strategically placed roughness elements to prematurely trigger super-critical flow or to have a surface similar to that of stranded cables [31].

Nigim and Batill [65] and Perry et al. [66] explained how the attached ribs affect the surface flow. They found that the surface flow depends on the ratio of rib height to spacing. For small ratios, the surface vortices are small and becomes trapped between rib ridges while for large ratios, the surface vortices can interact with and become part of the flow over cylinders [65, 66]. The use of ribs have some limitations: Only one inflow direction can be investigated (the unsteady pressure distribution can easily become asymmetric), they need to be placed at specific intervals and there's no simple formula for determining the required height, width and spacing.

Effect of turbulence on aerodynamics

An earlier transition to and from the critical Reynolds number region is one of the effects of increased turbulence intensity in addition to changing the strength of the forces and vortex-shedding characteristics [30, 40, 47, 53, 67]. As figures 2.6–2.8 show, this is similar to the effect of roughness and needs to be accounted for. The effect of increased turbulence on the Strouhal number is to increase it for all Reynolds numbers. The turbulence intensity has another effect on the Strouhal number: It increases the bandwidth and lowers the peak values [43, 47, 53, 67, 68]. Increased turbulence affects the mean drag in a more complex manner and it decreases the mean drag at sub-critical Reynolds numbers but increases it at critical [30, 53, 54].

Like the mean drag, the SD lift and drag is decreased at sub-critical Reynolds numbers with increased turbulence but it increases the SD values at critical [47, 53]. When combining turbulent flow, 10.5%, with surface roughness (lengthwise ribs) at simulated super-critical Reynolds numbers (post drag-crisis), the SD lift coefficient was found to be closer to smooth cylinder's. The main difference was that power spectra and the peak values had a larger bandwidth with increased turbulence [48].

The turbulent length scale can be as important as the turbulence intensity [69]. When the turbulence length scale is large, the effect of turbulence is small and can be regarded as a slowly changing mean wind speed. Small length scales, on the other hand, can interact with the surface flow and either damp or amplify the vortex-shedding. Its effect depends on the surface and turbulence conditions and is related to how the turbulence penetrates the surface shear

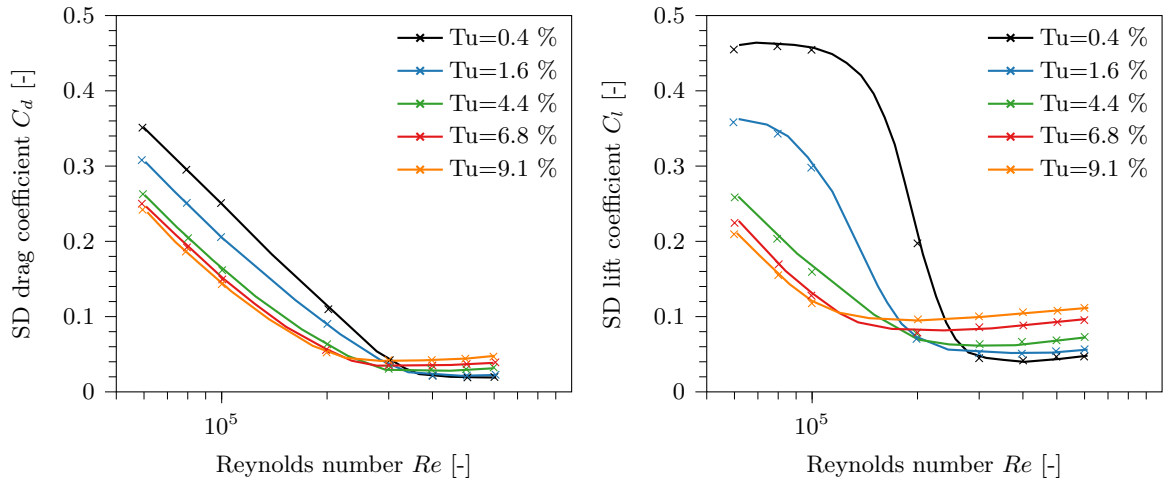

(a) *SD drag coefficient.*

(b) *SD lift coefficient.*

Figure 2.8: *Standard deviation of (SD) lift and drag on smooth cylinder in turbulent flow using data from Blackburn and Melbourne [53] and Cheung and Melbourne [30].*

layers.

Batham [60] found that added roughness was unnecessary when simulating the flow over a large chimney using a small-scale model in a turbulent atmospheric boundary layer wind tunnel. These results need to be taken with a pinch of salt as the full-scale chimney showed no significant vortex-induced vibrations. The unsteady aerodynamic forces were instead due to turbulence and the added turbulent atmospheric boundary layer was enough to mimic the full-scale loading.

Effective Reynolds numbers

A useful tool in wind tunnels would be an equivalent Reynolds number that determins the simulated Reynolds number a priori. Both Nakamura and Tomonari [58] and Szechenyi [10] tried to create such an equivalent Reynolds number based on added uniform roughness height and found that an assumed minimum roughness height was needed for smooth surfaces ($Rr = 3.5 \cdot 10^{-5}$). Similar techniques have been recommended by ESDU (Engineering Sciences Data Unit) [57]. The use of such a number was disputed by Basu [13] and Buresti [62]. While the surface roughness trigger turbulent boundary layer flow at lower Reynolds numbers, they found that it couldn't adequately replicate the pressure distribution, force coefficients and Strouhal number well enough at the same time, as figures 2.6–2.8 shows, and that roughness distribution and type needs to be included. Basu and Buresti also found that the modified Reynolds numbers didn't satisfactorily collapse the data to a single curve. While Basu dismissed the use of a roughness based Reynolds number, roughness height was still found useful in deriving expressions for the transition to super-critical Reynolds number and unsteady force characteristics [13].

Another parameter that makes an equivalent Reynolds number difficult to define, is that turbulence intensity, length scale and gradient plays a role in the boundary layer flow transition [30, 40, 47, 53]. While the equivalent roughness Reynolds number has been debunked, it's possible that correctly tuned added turbulence could negate the change in unsteady forces.

A better modified Reynolds number could be based on wake characteristics. Adachi [25] attempted to define a universal Reynolds number using the wake width, wake spacing and base pressure coefficient that collapsed the available mean drag and Strouhal number data so a single curve. The modification is similar to the modified drag coefficient and Strouhal number of Roshko [8] and Griffin [70]. Adachi and Griffin found that Griffin number (product of wake drag coefficient and wake Strouhal number) was almost constant in all relevant Reynolds number regimes (sub-critical, critical and super-critical when ignoring tests with separation bubbles)

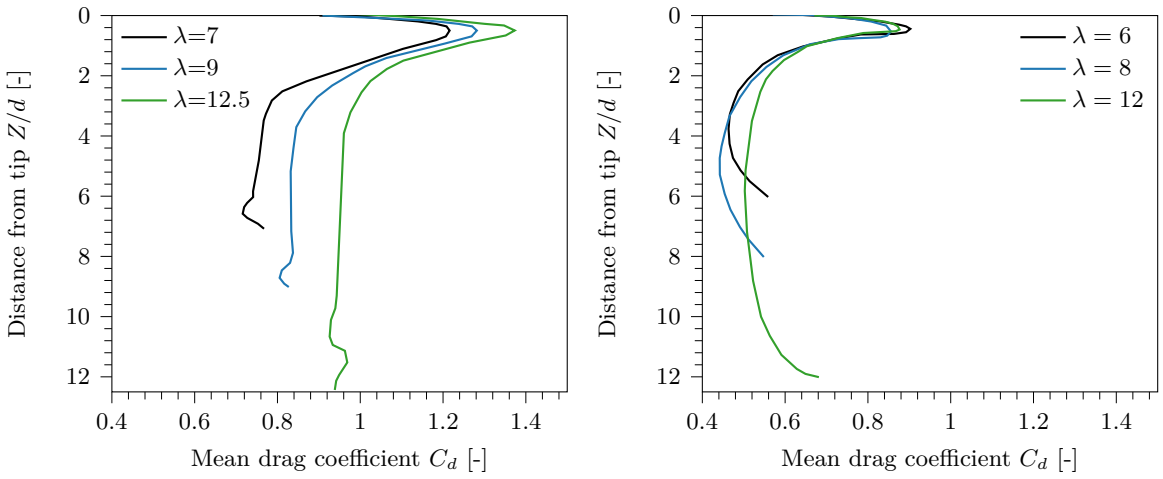

(a) *Sub-critical* $Re = 1.33 \cdot 10^4$ *[71].* **(b)** *Super-critical* $Re = 2.7\text{-}5.4 \cdot 10^6$ *[77].*

Figure 2.9: *Mean drag coefficients for smooth cylinders at different aspect ratios (λ) and Reynolds number regimes using the experimental data of Gould et al. [77] and Okamoto and Yagita [71].*

while Roshko's number does not [8, 25, 70]. Still, using wake length as characteristic length pose issues; it's easier to measure the size of an object than it is to get accurate wake readings for a real and arbitrary 3D structure. Also, the drag coefficient and Strouhal number can be wrong compared to a smooth cylinder even if their product is correct.

2.1.4 Changes in forces with 3D effects

Like the structural parameters, the fluid flow over the 3D cylinder is different from a 2D cylinder. This needs to be accounted for when doing scaled aeroelastic wind tunnel experiments (cf. [60] for chimney models, [26, 35, 71] for general cylindrical structures, [72] for super-tall buildings and [73–76] for launch vehicles). The loading can be greatly under predicted or over predicted[3] if the 3D effects are not accounted for or wrongly accounted for in scaled tests. The cause of these 3D effects are many and include the boundary layer profile, aspect ratio and end effects.

3D forces

Due to end effects, the flow near the tip separates differently than the rest of the cylinder with more regular 2D vortex-shedding only occurring when away from the tip region [35, 42, 69]. This has a large effect on the 3D forces experienced by circular cylinders as shown in figures 2.9 and 2.10. In the tip region, the extra vorticity reduces the base pressure which increases the mean drag coefficient to a maximum value around 0.5 diameters from the tip. As the distance from the tip is increased, the sectional flow characteristics reduces the mean drag to such an extent that the overall drag over the height is reduced [34, 35, 42, 44, 69, 71, 77, 78]. These effects on mean drag are shown in figure 2.9a for sub-critical Reynolds numbers [71, 79] and in figure 2.9b for super-critical [71, 77, 79]. When compared, the evolution with distance from the tip is similar but with a different scaling. Still, Basu [69] argued that tip effects (and the effect of aspect ratio) should be smaller at super-critical Reynolds numbers as the pressure difference between the front and rear of the cylinder should be smaller.

According to the results of Fox and Apelt [44], Fox and West [78] and Fox, Apelt and West [34] on a cylinder with aspect ratio of 30, the SD forces changes differently with height than the mean drag. While the mean drag has its maximum value in a small area near the tip, the SD force coefficients decreased to a minimum value near 5 diameters from the tip. As the distance

[3] Up to 400% according to Vickery and Daly [4] when also in the wrong Reynolds number regime.

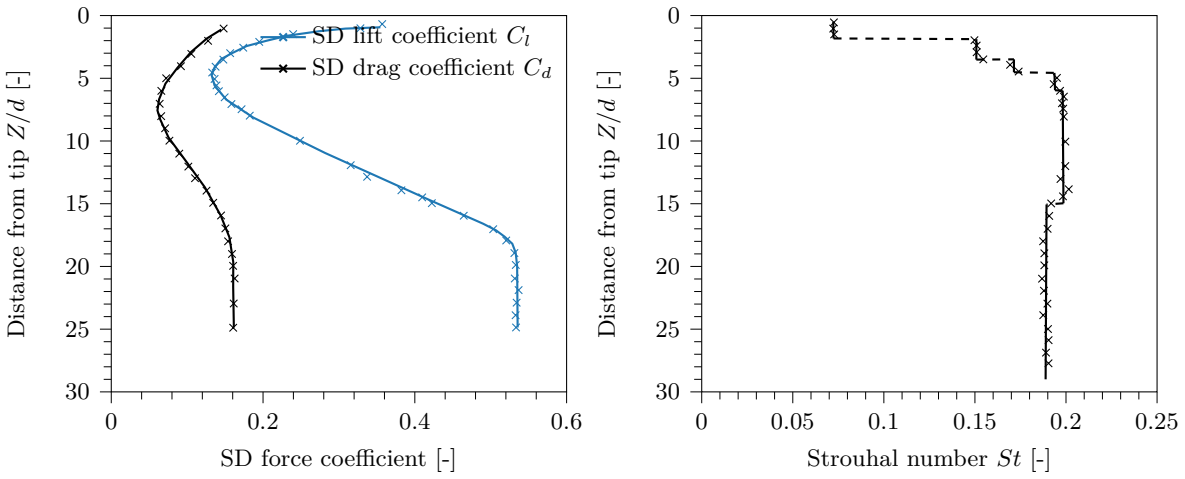

(a) *3D SD force coefficients.*

(b) *3D Strouhal number.*

Figure 2.10: *SD lift coefficient and Strouhal number for a circular cylinder with aspect ratio of 30 at a Reynolds number of* $Re = 4.4 \cdot 10^4$ *using the experimental data of Fox and Apelt [44].*

from the tip increased, the SD force coefficients increased to their maximum values near 18 diameters. From this point the SD force coefficients are nearly constant.

The Strouhal number changes differently than the forces: It's greatly decreased near the tip and increases to something close to the 2D values near 5 diameters from the tip as figure 2.10b shows. In addition, the variation in Strouhal number with height has several discrete jumps and regions of constant shedding frequency are found; this behavior can be related to vortex-cells. The decreased Strouhal numbers and increased SD forces near the tip is caused by the same phenomena: Tip vortices are dominated by low frequency components with higher bandwidth which disrupts the regular 2D vortex-shedding and gives higher SD forces. The presented Strouhal number and SD force data are only at sub-critical Reynolds numbers but the changes with height at super-critical Reynolds numbers should be similar to how the mean drag changed i.e. mostly a scaling [34, 44, 69, 71, 77, 78].

Fox and Apelt [78] showed that the aspect ratio affects the 3D forces. When the aspect ratio λ (ratio of height to diameter) is less than 7, regular vortex-shedding is suppressed. When the aspect ratio is between 7 and 13, the aspect ratio affected the forces differently in two separate regions: Near the tip, the unsteady force characteristics are independent of aspect ratio whereas they are dependent and varied with it nearer to the base. At aspect ratios larger than 13, the magnitude of unsteady forces are larger and varies with height like shown in figures 2.9 and 2.10 regardless of the aspect ratio. As can be seen, the force coefficients approach the 2D values as the distance from the tip becomes large enough. Aspect ratio affected the Strouhal number less and it becomes aspect ratio independent when $\lambda > 10$. At these aspect ratios, the vortex-shedding develops the cell-like behavior shown in figure 2.10b.

Coherence and correlation

The coherency between two sensors, e.g. using the wake fluctuations, is measured in frequency domain using the coherence function defined as

$$C_{xy}(f) = \frac{|G_{xy}(f)|^2}{G_{xx}(f)G_{yy}(f)}, \tag{2.6}$$

and indicates how "correlated" two signals are in frequency domain [80]. This statistic is often missing from the literature and it's possible that it's confused with the correlation. Here, G denotes auto-spectral densities which is the cross-spectral density when the subscripts mismatch.

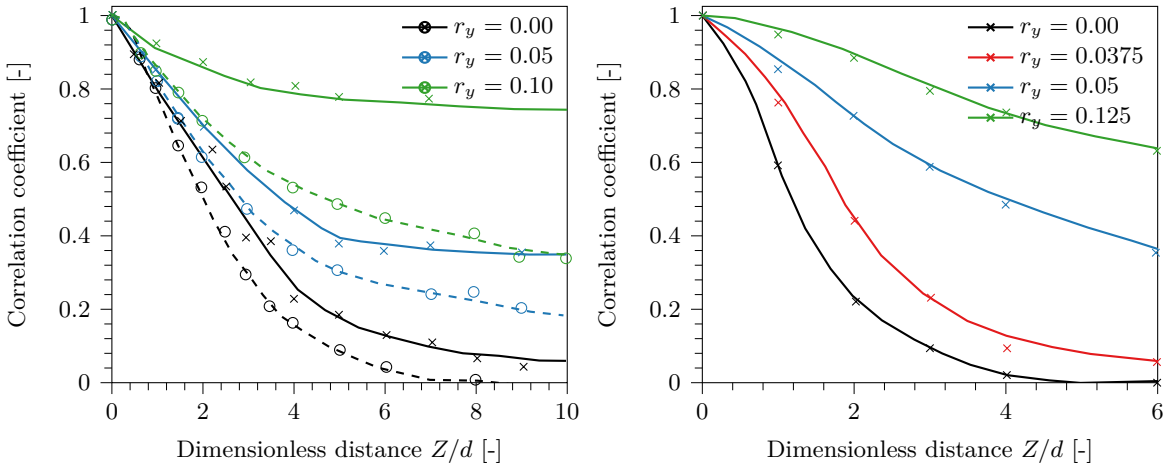

(a) *2D cylinder [43].* **(b)** *3D cylinder [85].*

Figure 2.11: *Spatial correlation coefficient for ciruclar, 2D cylinders in uniform (solid lines and ×) and turbulent (dashed lines and ∘) flow [43] and 3D cylinder placed in a turbulent boundary layer at different dimensionless amplitudes of motion [85].*

Only the coherence at the vortex-shedding frequency ($C_{xy}(f_s)$) between two sensors is plotted and this should be at the maximum coherence unless coherent shedding is missing at a given point; to be sure that the coherence is near the vortex shedding frequency, bandwidth filters are applied. To calculate the coherency between two sensors, the inbuilt coherency function from the SciPy signal package is used.

At any given frequency, the coherency C_{xy} is real valued, in the range [0, 1] and is expected to drop as distance between sensors increase. This means that it does not include the phase difference directly which is important when integrating the force along the length. If using fixed sensors, the maximum number of tested separation distances are (N choose 2)+1 where N is the total number of sensors, choose signifies unique combinations and the +1 is due to self comparison.

Coherence is less investigated in the literature than the correlation and this might have been due to the extra computing power needed or because it's confused with the correlation. It might still be possible to infer the coherence from the length of the vortex-cells shown in figure 2.10b as it's measured in frequency domain and cells with similar dominant vortex-shedding frequency should be more coherent.

Correlation between two sensors, e.g. using the wake fluctuations, is measured in time domain using the Pearson's r correlation function defined as

$$R(x, y) = \frac{cov(x, y)}{x_\sigma y_\sigma}. \tag{2.7}$$

Here, *cov* is the covariance between two recordings and $x_\sigma y_\sigma$ is the product of the standard deviation (SD) of each sensor. The correlation ρ_{xy} is real valued, in the range [-1, 1] and is expected to drop quicker with distance than the coherence.

The shedding characteristics vary along a cylinder's height and forms cells with similar characteristics. The length, correlation and coherence of these cells increases with the degree of motion which in turn changes and increases the total aerodynamic force [34, 44, 78, 81–84].

Vortex cells and vertical correlation and coherence

The correlation as a function of separation is shown in figure 2.11a for a circular cylinder with no end-effects (mounted with end-plates or spanning the width or height of a wind tunnel) using

the experimental data of Novak and Tanaka [43]. When the amplitude of motion r_y is low, the correlation drops like a negative exponential function with distance. As the amplitude of motion increases, so does the correlation at most distances and it drops slower with the distance. The effect of turbulence on correlation is to reduce it at all amplitudes.

For cylinders of finite-length, the correlation is reduced and drops quicker with distance than the 2D correlation as shown in figure 2.11b using the data of Howell and Novak [85]. This reduction in correlation could be related to end-effects and be similar to how the 3D forces changed for finite-length cylinders. The effect of motion is somewhat different for 3D cylinders than 2D: The correlation changes little when the amplitude of motion is low ($r_y < 0.05$) but is greatly increased and more similar to the 2D correlation when the amplitude is higher.

The location of the reference sensor is important. This was found by Howell and Novak [85] when measuring the correlation on a stationary 3D cylinder in a "shallow" boundary layer (i.e. low turbulence intensities at all heights and low turbulence and speed gradients). Howell and Novak reasoned that the spatial correlation was mostly due to tip vortices near the tip, due to turbulence near the bottom and due to 2D vortex-shedding near the middle. In a vortex-induced vibration model created by Ruscheweyh [49], the vortex-lift correlation along a cylinder was specified similarly to these findings with a maximum value near 75% of the height and near zero vortex correlation near the tip and bottom.

2.1.5 What's missing?

Several findings on the fluid dynamics around a cylinder has so far been presented in addition to the effect roughness and turbulence. While studied, the unsteady pressure and resulting unsteady forces (strength and frequency spectrum) needs to be better understood. The current data on unsteady lift (in terms of SD lift and characteristic frequency) is too scattered at super-critical Reynolds numbers making it difficult to determine the correct values. Furthermore, the Strouhal numbers from the literature was scattered at the super-critical Reynolds number regions and it needs to be determined if it should be closer to 0.2, in the range $St \in [0.25, 0.3]$ or if both Strouhal numbers present at super-critical Reynolds numbers.

The literature shows that triggered super-critical Reynolds number flow is different from that over a smooth cylinder in uniform flow. With a better understanding of the unsteady forces and pressure distribution on smooth, stationary cylinders, better ways of simulating super-critical Reynolds number flows using a combination of roughness and turbulence can be verified with the goal of recreating the correct force characteristics. Finally, to get the correct 3D force characteristics, realistic coherence and correlation is needed. Much of the correlation and 3D force data on cylinders are limited to sub-critical Reynolds numbers and the data on coherence is mostly missing or confused with correlation. Accurate measurements of these statistics at super-critical Reynolds numbers would be necessary to determine if the 3D force characteristics at simulated super-critical Reynolds numbers are correct.

2.2 Fundamentals of vortex-induced vibrations

2.2.1 A short introduction to vibrations and aeroelasticity

The main mechanics that make up the field of aeroelasticity are shown in figure 2.12. Depending on the coupling, different physical phenomena can be observed [6, 86]. For chimneys, there are three main causes of vibrations and deformation: 1) Static aeroelasticity and divergence, 2) turbulence-inudced vibrations and forced response (mechanical vibrations) and 3) vortex-induced vibrations (aeroelasticity). The mechanical vibration branch can be helpful in modeling vortex-induced vibrations as it can be reduced to a random vibration or harmonic vibration problem if the circumstances are correct (no nonlinearities). These types of models have simple

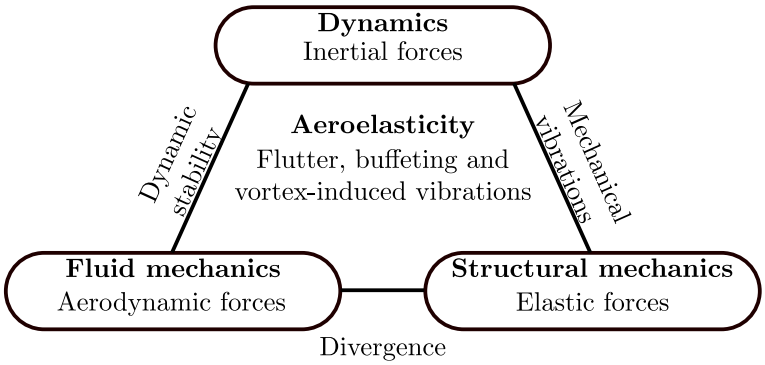

Figure 2.12: *Collar's aeroelasticity triangle [86].*

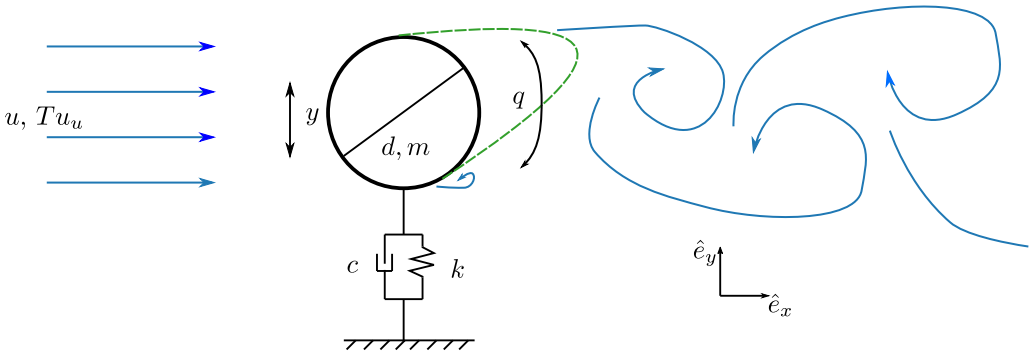

Figure 2.13: *2D model of vortex-induced vibrations.*

solutions (either known solutions of ordinary differential equations of simple transfer functions) and are useful when, for example, only interested in the maximum [7, 32, 49, 86–88].

Flutter is an example of dynamic aeroelasticity and there are many different kinds. For example, it led to the collapse of Tacoma Narrows bridge and many aircraft wings. Flutter is related to a positive feedback loop between dynamic forces and coupled modes of motion (e.g. coupled plunge and rotation motion) that adds energy to the system. This is often seen in the eigenvalues which represent both the oscillation frequency and the growth rate of motion. When eigenvalues merge, the vibration frequency of the involved modes are the same and one or more vibration modes have a positive growth rate which amplifies the vibrations instead of damping them. If there are no nonlinearities, these vibrations would grow unbounded [6, 86, 89, 90].

2.2.2 2D model of vortex-induced vibrations

Vortex-induced vibrations has similarities to flutter as shown by de Langre [91] and Zhang et al. [92]. The phenomenon is a self-excited aeroelastic instability that's the result of a coupling between structural motion and fluctuating lift due to vortex-shedding and is complex to model [7]. This means that there are no analytic method based on basic flow principles that fully represents the behavior of elastic bodies experiencing vortex-shedding [90, 93, 94]. Instead, phenomenological and empirical models that captures the essence of vortex-induced vibrations are used [7]. Some of these only give the maximum response while some others only give an amplitude response when the structural damping is in a specific range. Both of these model types will be further discussed in section 2.4.

Instead of a plunge and rotation model like in flutter, vortex-induced vibrations can better be modeled as a plunge and vortex dynamics model. This is illustrated in figure 2.13 which shows some of the fluid and structural parameters involved in 2D vortex-induced vibrations on

circular cylinders. Firstly, a cylinder is placed in a one dimensional flow with mean speed u and turbulence intensity Tu_u. This cylinder can only move perpendicular to the flow ($\hat{e}_y$ only), has a diameter d and mass m and is connected to a mass-damper with stiffness k and damping coefficient c. Due to the flow, alternating vortices are shed from the top and bottom of the cylinder ($\theta = \pm 90°$) which leads to a self-excited and limited vortex-shedding process q. This nonlinear process is often modeled as a van der Pol or Rayleigh oscillator and the resulting unsteady pressure distribution gives an oscillating lift force. For a real and more involved 2D model, more parameters need to be included such as the effect of motion and loading in other flow directions (e.g. $\hat{e}_x$). Like in flutter, the structural motion and vortex-shedding process are coupled which gives a nonlinear flutter-like behavior during vortex-induced vibrations.

2.2.3 Lock-in of vortex-shedding

Simple forced vibration models with harmonic forcing have a linearly increasing frequency of motion. This is not the case for vortex-induced vibrations and the nonlinear change in forced frequency is one of its defining features. This nonlinear change in frequency due to a synchronization between the shedding process and structural motion is illustrated in figure 2.14a. When below the natural frequency, the vortex-shedding frequency increases linearly with the fluid speed according to the Strouhal law (equation (2.5)). When close to the natural frequency, between the green dashed lines in figure 2.14a, the shedding frequency can jump to the structure's natural frequency and the vortex-shedding frequency "locks-in" with it. As the fluid speed is further increased, the vortex-shedding frequency "locks-out" from the natural and the vortex-shedding frequency again increases linearly. The speeds at which the frequency jumps occurs at depend on the amplitude; this means that lower mass and damping gives longer lock-in [6, 7, 33, 61, 84–86, 90, 92, 95–105].

Lock-in is different for forced oscillations and freely oscillating cylinders. The former should lead to more stable vortex-induced vibration-like behavior and the latter will have stable vortex-induced vibrations if the incoming flow is stable and if the damping is low. If the flow is not stable or the damping is high, it's likely that the vortex-induced vibrations will be intermittent and alternate between high amplitude vortex-induced vibration and low amplitude turbulence-induced vibrations. This is exemplified in figure 2.14b where the lock-in range is shown to increase with the structural amplitude. This can be measured in forced oscillation tests by simply increasing the amplitude but in free-vibration tests the damping and mass needs to be low to get high amplitudes. Lock-in in freely, vibrating structures have added complexity and hysteresis in that it can have two amplitude response branches that can coexist at the same speed. The resulting solution branch depends on the existing vibration amplitude but should only be observed with low mass and damping [96, 99–102, 106].

2.2.4 Amplification of forces with motion

In addition to changing the vortex-shedding frequency, the aeroelastic effect leading to lock-in amplifies the unsteady forces. While the effect of vortex-induced vibration on SD drag is less explored (mere mentions of it increasing [33]), its effect on mean drag is better studied. Many experimental studies have found that vortex-induced vibrations increases the mean drag on circular cylinders though the results of Jones et al. [24] showed no noticeable increase in drag for a cylinder oscillating close to the vortex-shedding frequency. The exact relation between mean drag and structural motion is unknown but the drag has been related to the SD vibration amplitude using empirical curve fits which are nontrivial to include in time domain models [6, 14, 33, 61, 70, 98, 99, 101, 104–106]. While increasing the mean drag might seem unimportant for vortex-induced vibrations, it does affect response: The mean drag adds an aerodynamic damping component to the structure by adding a velocity and drag component in the $\hat{e}_y$ direction [14].

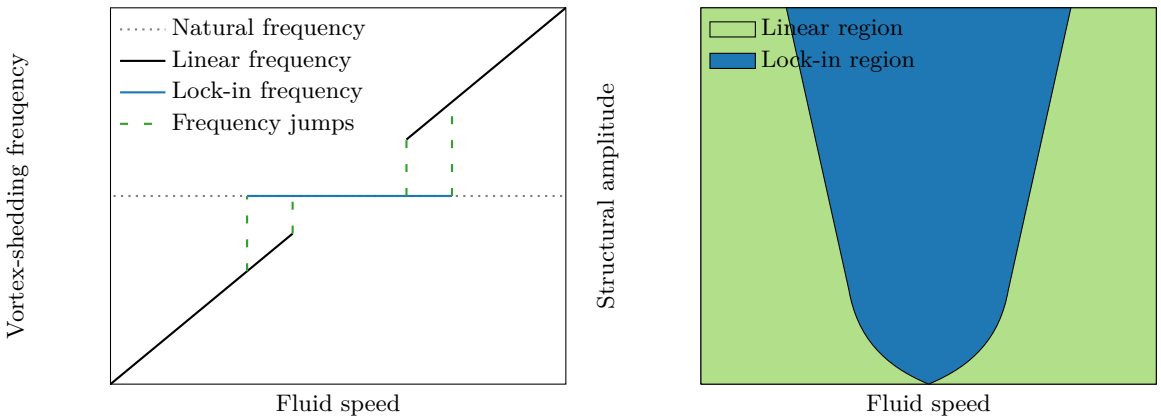

(a) *Behavior of shedding frequency with speed.* **(b)** *Changes in lock-in range with amplitude level.*

Figure 2.14: *Changes in vortex-shedding frequency and lock-in range with speed and amplitude level for a cylinder with prescribed motion [6, 33, 85, 104, 105].*

The effect of lock-in on the unsteady lift force is well studied and motion greatly amplifies the lift when the shedding frequency is close to the natural frequency of motion. A mathematical analogy to what happens is a forced limit cycle oscillator experiencing resonance [7, 14, 33, 98, 104]; this kind of model will have frequency entrainment (lock-in) when the driving frequency is close to the linear natural frequency and an increased amplitude during it [95]. This force amplification is due to the vortex-shedding process becoming stronger and more stable during lock-in. This in turn leads to a different unsteady pressure distribution that increases the steady and unsteady forces. If SD drag is amplified similarly to the lift, it should be possible to model it as a limit-cycle oscillator as well [107].

2.3 Vortex-induced vibrations of slender structures

The simple 2D model consisted of a disk connected to a spring and damper but 3D models are more complex with infinitely many modes of motion and with a stiffness and damping that depends on the structural material and shape. Vortex-induced vibrations can then instead be modeled like in figure 2.15. Broadly speaking, the 3D model differs from the 2D model in 3 key areas: 1) The incoming wind has 3 speed and turbulence components that varies with height; 2) the structure has a global mass, stiffness and damping, a diameter that can vary with height, several mode shapes with their own modal mass, damping, stiffness and displacement which determine the global displacement; and 3) vortex-shedding characteristic and forces that are a function of height. While the sketch in figure 2.15 only shows the dominant mode shape for vortex-induced vibrations of chimneys (1st mode shape), the structure can simultaneously move in the $\hat{e}_x$, $\hat{e}_y$ and $\hat{e}_z$ directions and be dominated by other modes.

2.3.1 Incoming wind

The incoming wind in figure 2.15 can, at any height, be characterized as a mean speed vector with an added unsteady flow vector. These speed vectors make up the atmospheric boundary layer can vary in both direction and magnitude with both height and can be reduced to a speed profile and a turbulence intensity profile. The speed profile is simply the mean speed as a function of height and should increase monotonically in the heights of interest for industrial chimneys. The turbulence intensity profile is the ratio of the speed's standard deviation and mean value. Unlike the mean speed, it decreases monotonically with height in the theoretical models; in real life it starts by increasing and then reaches a height where it starts decreasing

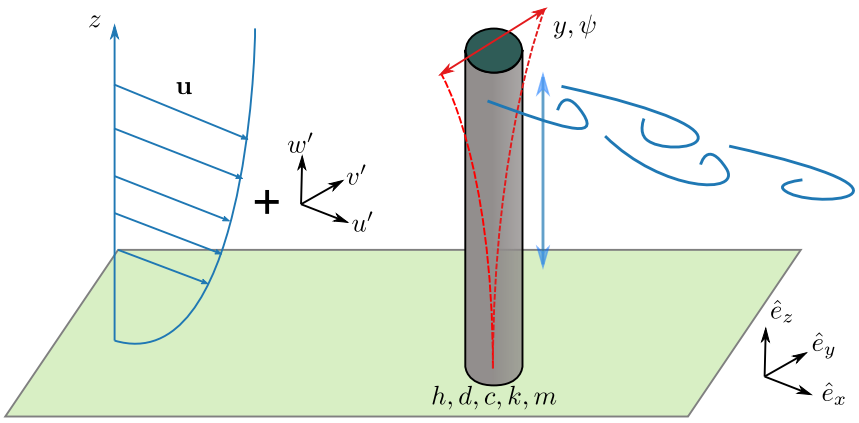

Figure 2.15: *3D model of vortex-induced vibrations.*

with height [5, 90, 108].

The statistical boundary layer profiles are based on long-term and high wind speed measurements and are modeled using 1) the friction or shear speed near the ground, 2) an assumed relationship between the mean speed and standard deviation and 3) a law describing the profiles as a function of height. The shear speed is low even with very large mean wind speeds and is related to the shear stress near the ground. This shear stress depends on the surface roughness, described by the roughness height, and increasing it increases the friction experienced by the wind which reduces the wind speeds near ground [90, 108].

There are two popular laws for estimating the profiles: power laws like in the CICIND model code [55] and logarithmic laws like in the Eurocode [5]. The power laws are empirical fits of the wind profiles and are simpler than the logarithmic law. The logarithmic boundary layer profiles are more mathematically rigorous as they're based on an approximate boundary layer solution of the full Navier-Stokes equations for atmospheric flows; this approximate solution is called the turbulent Ekman layer. By assuming that the SD values are proportional to the mean speeds and a turbulence coefficient, the turbulence profile becomes the inverse of the speed profile times a constant. This is because the turbulence intensity is the ratio of SD value to mean value [5, 6, 55, 90, 108]. A description of terrain types, the boundary layer produced and how to reproduce it in wind tunnels are prescribed in design codes [5, 55].

2.3.2 Structural parameters

For flexible structures and coupled linear equations of motion, it's much simpler to solve the equations of motion after a modal decomposition. This method separates a coupled system into a new set of uncoupled equations. These new sets of equations don't model the physical system directly but rather the degree of motion for the various modes shapes which prescribe the motion. Each of these mode shapes have their own modal mass, stiffness, damping and forces and all are dependent on the mode shape in question and the global parameters. For vortex-induced vibrations of industrial chimneys, the main mode of interest is the first bending mode and the derived quantities involving mass, frequency and damping are based on it.

There are several ways in which the mode shapes and modal masses can be estimated. For simple beam like structures (which some simple chimneys can be approximated as), analytic solutions can be found using beam theory (e.g. Euler-Bernoulli or Timoshenko-Ehrenfest). For more complex structures, finite element methods (FEM) can be used to calculated the mode shapes and corresponding mass but one can also use experimental methods [86, 87].

In experiments, the mode shape can be found by normalizing the acceleration at a several points along the chimney/cylinder with a reference measurement. This can be done using free-response, ping tests or forced harmonic vibration tests [87]. The experimental modal mass m_g

can be found by assuming that the stiffness k and mode shape are unchanged when adding tip mass to the cylinder. Using $\omega_i^2 = k/m_i$ (where subscript 1 is tests without added mass and 2 with), $m_2 = m_1 + m_{add}$, the modal mass can be estimated from equation (2.8). For vortex-induced vibrations on industrial chimneys, the equivalent mass per unit height m_e (given in (2.9)) is often more useful than the modal mass alone.

$$m_g = m_{add}\frac{\omega_2^2}{\omega_1^2 - \omega_2^2}, \tag{2.8}$$

$$m_e = \frac{m_g}{\int_0^1 \psi(z)^2 dz}. \tag{2.9}$$

If the mass per unit height or equivalent mass without added mass is known, then the equivalent mass can be calculated using equation (2.10). This equation is much more general and the sum at the end is the summed effect of all N point masses placed at z_i.

$$m_e = \frac{\int_0^1 m(z)\psi(z)^2 dz + \sum_{i\in N} m_{add,i}\psi(z_i)^2}{\int_0^1 \psi(z)^2 dz} = m_{e,0} + \frac{\sum_{i\in N} m_{add,i}\psi(z_i)^2}{\int_0^1 \psi(z)^2 dz}. \tag{2.10}$$

Similar to the mass and mode shape, damping is an important parameter for the response. Unfortunately, there's no good analytic or numerical method for calculating damping and the modal damping needs to be determined experimentally. As the damping coefficient changes greatly with the system parameters, it's more convenient to use the viscous damping factor ζ (or just damping factor) as in equation (2.11) which is more similar across experiments and scales. This value scales the damping coefficients using the critical damping coefficient (which is determined by the mass and natural frequency). Another way of representing the damping is through the logarithmic decrement δ. This value is based on the reduction in vibration amplitude over n periods of oscillations and the natural frequency. For structures with low damping, the critical damping coefficient and logarithmic decrement are related by $\delta = 2\pi\zeta$ [87].

$$\zeta = \frac{c_{damping}}{2m\omega_n}. \tag{2.11}$$

2.3.3 Derived parameters

Structural parameters

While the modal and equivalent mass are useful, a dimensionless version should be more useful as experiments at all scales can be compared. This can be done using the mass-ratio μ (given in equation (2.12)) which relates the equivalent and added mass to the displaced fluid. From simple vortex-induced vibration models, it's clear that the mass has a direct effect on the response by scaling the forces. When the mass-ratio is low, e.g. in oceans, there's an important addition from fluid-added mass (from inertial effects) [14, 101, 106, 109]. For higher mass-ratio, e.g. in air, the added mass tends to be small compared to the equivalent mass.

$$\mu = \frac{m_e + \frac{\pi\rho d^2 C_M}{4}}{\rho d^2}, \tag{2.12}$$

$$r_y = \frac{|Y|}{d}, \tag{2.13}$$

Similarly, it's useful to present the vibration amplitudes in the form of dimensionless amplitudes instead as it makes it easier to compare differently sized models and chimneys. Here, the dimensionless amplitude due to cross-wind vibrations (turbulence and vortex-induced) is denoted by r_y (equation (2.13)) and comes from assuming a harmonic response in the form $y = r_y sin(\omega t)$ for 2D configurations or at the tip for 3D cantilevered or flexible support configurations.

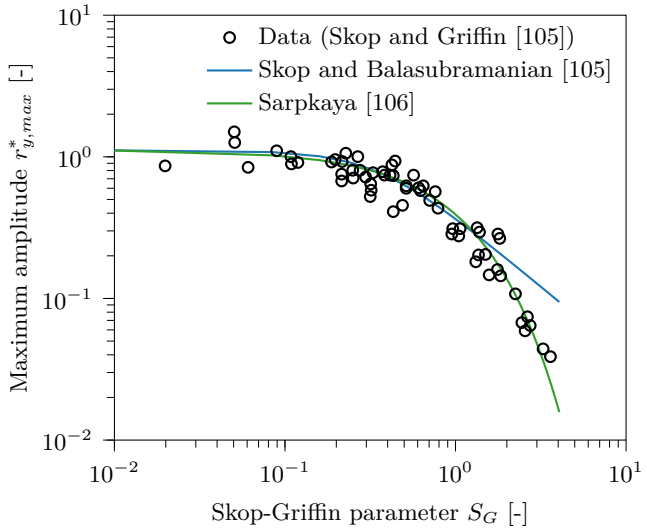

Figure 2.16: *Mode shape corrected maximum response and emperical fits of it [105, 106].*

$$Sc = \frac{4\pi m_e \zeta}{\rho d^2} = \frac{2m_e \delta}{\rho d^2}, \tag{2.14}$$

$$S_G = 2\pi^3 St^2 \zeta \mu. \tag{2.15}$$

A third useful dimensionless structural parameter is the Scruton number Sc (equation (2.14)) which is a mass-damping parameter. The Skop-Griffin parameter S_G (in equation (2.15)) is an alternative that includes the fluid added mass and some of the vortex-shedding behaviors by including the mass-ratio and the Strouhal number. These mass-damping parameters are scaled versions of each other if the added mass is much lower than the equivalent.

The usefulness of mass-damping parameters are debatable in predicting vortex-induced vibration. Several researchers have fitted the maximum amplitude as a function of the Scruton number but the results are mixed (cf. the article of Khalak and Williamson [101] or reviews of Sarpkaya [106] and Williamson and Govardhan [109]). Several models predict an independent effect [109] and several maximum amplitudes can be found at a Scruton number [106, 109] which led Sarpkaya to conclude that "there is no compelling reason to combine the mass with damping" [106]. What is agreed upon in the conflicting reviews and shown by Blevins and Coughran [98], is that mass-ratio has a larger effect on the extent of lock-in than damping does in water.

$$r^*_{y,max\ SB} = \frac{0.35}{\sqrt{0.12 + S_G^2}}, \tag{2.16}$$

$$r^*_{y,max\ S} = 1.12e^{-1.05 S_G}. \tag{2.17}$$

While it's use in predicting response has been debated, plotting the maximum response as a function of mass-damping parameters like in figure 2.16 using the Skop-Griffin parameter can be useful when comparing similar experiments [6, 85, 101, 105, 106]. This figure compares the measured mode shape corrected maximum response[4] $r^*_{y,max}$ with the empirical least-square fits of Skop and Balasubramanian (equation (2.16)) [105] and Sarpkaya (equation (2.17)) [106]. Both fitted functions match the data when using log scales and, according to Sarpkaya, this makes it plausible for $\ln(r^*_{y,max})$ to be a linear function of S_G [106]. This *doesn't* mean that amplitude *is* a

[4]Scaled by $1/\Lambda$ where Λ is 1.0 for rigid cylinders, 1.291 for pivoted cylinders, 1.305 for cantilevered beams and 1.155 for tight cables and simply supported beams [6, 106].

linear function of a mass-damping parameter nor that Sarpkaya's skepticism was unfounded. To quote Mar's law, "[e]verything is linear if plotted log-log with a fat magic marker" [110]. Similar plots and empirical fits can and have been made using the Scruton number which is used more in chimney design [5, 55, 111].

Fluid parameters

Just like how dimensionless structural parameters are useful for comparing experiments and structures of different sizes, so are dimensionless fluid parameters. Two examples of useful dimensionless fluid parameters are already defined and are the Reynolds number and the Strouhal number in equations (2.1) and (2.5) respectively. These two numbers are useful for the fluid dynamics but less useful for the structural response. The response is more dependent on the incoming wind speed and the frequency of motion. A good and general dimensionless speed should then be the reduced speed U_R given in equation (2.18). This dimensionless speed is good for buildings which can experience vortex-induced vibrations, galloping and flutter and is akin to the inverse reduced frequency more traditionally used in unsteady aerodynamic theory (with the frequency set to the natural) [6, 86, 89, 90].

$$U_R = \frac{U}{f_n d}, \tag{2.18}$$

$$\omega_q = \frac{\omega_s}{\omega_n} = \frac{U}{U_{crit}} = U_R St. \tag{2.19}$$

If the focus is on response due to vortex-induced vibrations only (e.g. for mathematical modeling or vortex-induced vibration experiments), it's better to use a dimensionless speed or frequency like the one given in equation (2.19). This dimensionless speed or fluid/structure frequency ratio (ω_q) combines the reduced speed U_R with the characteristic shedding frequency. The benefit of this value instead of the reduced speed, is that the vortex-induced vibrations are centered around 1 (with maximum amplitude at a dimensionless speed greater than one) instead of being in the range $U_R \in [4, 6]$ depending on the Strouhal number [5, 32, 49, 55, 112, 113].

2.3.4 Previous full-scale tests

While important for validation of mathematical and wind tunnel models, full-scale experiments on large chimneys and chimney-like structures are rare and exhaustive pressure data from them even rarer. Instead, the field studies end to present acceleration, strain and wind speed data which is much simpler to gather. The existing full-scale experiments without significant pressure data can be separated into two groups: those that aggregate and use displacement data for validation of predictive models [114–120] and those examining the temporal statistics of vortex-induced vibrations [121–124]. The response statistics papers tend to focus on the structural and wind characteristics by examining the response as a function of wind speed or Reynolds number and the probability of seeing a specific response level at a speed.

The remaining 6 full-scale chimney tests include measurements of circumferential pressure but only four where at super-critical Reynolds numbers. All full-scale tests have a few things in common. The first is that the dimensionless amplitudes are low ($r_y = \mathcal{O}(10^{-3})$ [125, 126]). The second is that there's a transduced limitation and only a limited amount of pressure taps can be used at the same time. The experiments with the most pressure data used 18 pressure taps at four different levels [127]. For some chimneys pressure can be measured at more levels and with more taps per level but the lack of transducers means only be a limited number of taps can be connected at the same time.

Christensen and Askegaard [128] investigated the mean and SD pressure distribution on a Danish chimney, using 14 pressure taps at two heights at a time, but the presented data are only for a few selected wind speeds. The mean pressure distribution was found to be similar to that

of Roshko [8] but the minimum and wake pressure coefficients were larger on the chimney than in the wind tunnel experiments. In addition to the pressure, the response and bending moment as a function of wind speed was investigated for the Danish chimney using accelerometers and strain gauges. Hansen [129] extended the work of Christensen and Askegaard by calculating the lift force spectrum and comparing it with the theoretical Gaussian spectrum of Vickery and Clark used in the vortex-induced vibration model further discussed in section 2.4.1. The theoretical and experimental spectra match qualitatively but only after fitting the experimental turbulence bandwidth parameter to the theoretical model.

Waldeck [130] found the super-critical pressure distribution in the rear to be larger than Christensen and Askegaard's when measuring the pressure distribution on a South African chimney using 16 taps at 3 different heights. In a separate study, Waldeck [126] also compared the experimentally obtained lift spectrum to the same theoretical lift spectrum. The findings suggest that the theoretical and experimental spectra are similar near the vortex-shedding frequency when curve fitting the experimental data the theoretical spectrum's shape. This was done by fitting 1) the lift due to vortex-shedding alone 2) the variance resulting from vortex-shedding 3) the mean vortex-shedding frequency and 4) the turbulence bandwidth parameter.

Sanada, Suzuki and Matsumoto [125] found mean rear pressure distributions in between those of Christensen and Askegaard, Ruscheweyh and Waldeck when investigating a Japanese chimney using 16 pressure taps at a single height [126, 128, 131]. Their results differ from the other investigations in that they found a better theoretical lift spectrum than the Vickery and Clark spectrum. According to them, the lift force spectrum better fits a combined Dryden- and von Kàrmàn type wind spectrum as it includes both the vortex-shedding peak and the low frequency lift components [125]. A similar sentiment was expressed by Scherer [124] who found that the vortex-shedding spectrum doesn't follow a Gaussian distribution.

Ruscheweyh [131] investigated the circumferential pressure distribution on a television tower at super-critical Reynolds numbers using 12 pressure sensors at a single height. The pressure data was gathered over two years and sporadic vortex-shedding was observed but only for periods where the average separation point and flow conditions were steady. The measured mean pressure distributions were similar to those found by Christensen and Askegaard making them larger in the rear than Roshko's wind tunnel experiments [8, 19, 132]. The last field experiment, is the test chimney of Aachen Technical University. While it was fitted with several pressure taps, only 50 taps could be simultaneously connected to the pressure transducers and the analysis focused more on the aerodynamic admittance and response than the pressure distribution [127]. Additionally, the diameter (0.91 m) and height (28 m) were smaller than the other full-scale tests and only low critical Reynolds numbers were reached.

The last full-scale experiment is that of Zuo [133] who used a 7.62 m long horizontal cylinder mounted 6 m above ground meaning that there's no atmospheric boundary layer effect. This cylinder was fitted with a 32 pressure taps in a single at a location with mostly 2D flow. As the cylinder's diameter was only 0.3 m, only sup-critical and low critical Reynolds numbers could be reached. Still, this experiment was a natural experiment on the effect of turbulence intensity and the results suggest that the effect of free stream turbulence is overblown.

2.3.5 What's missing from literature

Currently, there are several things missing on the aeroelastic behavior of cylinders due to vortex-shedding. As shown in section 2.1.1, much of the correlation and 3D force data on cylinders are limited to sub-critical Reynolds numbers and the data on coherence is mostly missing. There are several potential ways to get this missing data. For instance, a full-scale field test on a large diameter chimney that's fitted with several pressure taps (and sensor banks) and accelerometers could measure the vertical correlation, coherence and 3D force characteristics. If the vibration amplitudes are high, it will differentiate itself from the literature that's mostly from chimneys

with low levels of vibrations.

Methods for recreating vortex-induced vibration of flexible structures at super-critical Reynolds numbers are lacking. The effect of surface roughness and turbulence are more well studied for 2D cylinders and a high-fidelity field tests can serve as a validation case for 3D wind tunnel tests and numerical simulations.

2.4 Predicting vortex-induced vibrations

As mentioned earlier, there are no accurate methods for predicting vortex-induced vibrations using equations based on basic principles. Some attempts have been made at deriving equations of motion based on first principle but they rely on assuming a form for the aerodynamic force [7, 90, 93, 94]. Instead, assumptions are made regarding the spectrum of vortex-lift force, the type of motion during lock-in and the form of the nonlinear aerodynamic force (e.g. as a structural term or as a separate equation). In this section, some useful models for predicting vortex-induced vibrations of circular cylinders and chimneys will be presented.

2.4.1 Spectral model

Derivation of model

The spectral model of Vickery and Basu [32, 88], used in the Eurocode and CICIND model code, is based on random vibration theory. The sectional power spectrum of vortex-lift force is found using two assumptions: 1) the correlation of fluctuating lift as a function of distance can be expressed as equation (2.20) (with correlation length being l) and 2) the power spectra can be approximated using a Gaussian distribution with variance related to the turbulence intensity Tu through the bandwidth $B \approx 0.1 + Tu$ as in equation (2.21). For assumption two, the frequency components far from the vortex-shedding frequency are ignored and the lift spectrum on a cylinder is found from equation (2.22) by evaluating the spectrum near $f = f_n$ [32, 88, 134]. The assumed correlation is based on the 2D correlation found by Novak and Tanaka and is not changed in the full 3D model [32, 43, 88].

$$R(z_1, z_2) = \cos\left(\frac{2r}{3l}\right) \exp\left[-\left(\frac{r}{3l}\right)^2\right], \; r = \frac{2h \mid z_1 - z_2 \mid}{[d(z_1) + d(z_2)]}, \tag{2.20}$$

$$S_C(f) = \frac{C_{l\sigma}^2 \rho d U^2}{\sqrt{\pi} B f_s} \exp\left[-\left(\frac{1 - f/f_s}{B}\right)^2\right], \tag{2.21}$$

$$S_{C_l,viv}(f) = h^2 \int_0^1 \int_0^1 \sqrt{S_C(f)|_{z_1} S_C(f)|_{z_2}} R(z_1, z_2) \psi(z_1) \psi(z_2) dz_1 dz_2. \tag{2.22}$$

When accounting for all 3D effects [32], the linearized damping factor becomes

$$\zeta_A = -\left(\frac{\rho d_0^2}{m_e}\right) \left[\frac{\int_0^1 K_a(z) \psi^2 dz}{\int_0^1 \psi^2 dz} - \frac{\int_0^1 K_a(z) (d(z)/d_0)^2 \psi^4 dz}{\int_0^1 \psi^2 dz} \left(\frac{r_y}{a_L}\right)^2\right], \tag{2.23}$$

where K_a is an experimentally determined aerodynamic damping coefficient [32]. When K_a is simplified using a Raleigh oscillator, it can be simplified to $K_a = K_{a0} \dot{y}(1 - a\dot{y}^2)$. This added damping should induce a limit cycle oscillation when the linear damping is negative. As there's no current method for including nonlinear terms in standard random vibration theory [86, 87], this nonlinearity was approximated using a limiting amplitude ($a_L d$) and a statistical SD amplitude. Using an added damping of this form is debatable and Kareem [135] conjectured that it's disingenuous to reduce motion induced forces to linear parameters as they're too complex.

Vickery and Basu [113] further simplified the response calculation for slender structures by assuming that: 1) the aerodynamics over the top one third of the structure dominates and that

an average value over it can be used, 2) tapering can be ignored unless 20% or more and 3) the extra lift force due to the turbulence spectrum can be ignored. With this, the spectral vortex-induced vibration model can be simplified to

$$r_{y,\sigma} = \frac{\frac{C_{l\sigma}}{8\pi^2 St^2}\frac{\rho d^2}{m_e}\left(\frac{\sqrt{\pi}l}{2\lambda}\right)^{0.5}\phi(\omega_q, B)}{\left[\int_0^1 \psi^2(z)dz\right]^{0.5}\left[\zeta - K_{a,0}\frac{\rho d^2}{m_e}\left(1 - \frac{r_{y,\sigma}}{a_L}^2\right)\right]^{0.5}}, \tag{2.24}$$

$$\phi(\omega_q, B) = \frac{\omega_q^{3/2}}{B^{1/2}}\exp\left[-0.5\frac{\left(1-\omega_q^{-1}\right)^2}{B^2}\right], \tag{2.25}$$

where the first contains the constant terms, the latter the variable forces and ω_q is the dimensionless speed defined in equation (2.19). The solution to equation (2.24) in terms of $r_{y,\sigma}$ can be found by rewriting it to a bi-quadratic equation. For design purposes, the solution can be further simplified by only calculating maximum $r_{y,\sigma}$ found at $\omega_q \approx 1.1$ [113]. To convert the standard deviation of the amplitude to the statistical maximum amplitude, $r_{y,\sigma}$ is multiplied by a peak factor k_p defined as [5, 32, 55, 88, 113]

$$k_p = \sqrt{2}\left(1 + 1.2\tan^{-1}\left(0.75\frac{Sc}{4\pi K_{a,0}}^4\right)\right) \tag{2.26}$$

A major model issue

There is a region where equation (2.24) gives high amplitude response independent of $\phi(\omega_q)$. By focusing on the damping terms, the linear stability can be derived as

$$\zeta - K_{a,0}\frac{\rho d^2}{m_e} > 0 \;\rightarrow\; Sc > 4\pi K_{a,0}. \tag{2.27}$$

When the relation is unfulfilled, the linear damping is negative and amplitude response is determined by the nonlinear damping and not the variable force. The effect of this on total damping (structural + aerodynamic) as a function of the Scruton number is shown in figure 2.17 and it decreases linearly when $Sc > 4\pi K_{a,0}$; in this region the nonlinear damping is negligible. As the Scruton number further decreases, the linear damping approaches negative values and the nonlinear damping needs increase to compensate for it. The effect of the nonlinear damping on the total is so great that the total damping increases as the Scruton number (and linear damping) decreases past $Sc = 7 - 9$. Due to the form of the nonlinear damping, this requires a constant high amplitude at all ω_q.

There have been attempts at overcoming the negative linear damping. For example, the Danish annex of the Eurocode fixed it by making $K_{a,0}$ a function of the dimensionless frequency ω_q [5]. Another fix is to change the aerodynamic damping term completely. Experiments by Lupi et al. [59] found that the aerodynamic damping better fits an equation in the form $a\exp(-y_\sigma b)y_\sigma^c$ than $K_{a,0}(1-a\dot{y}^2)$ during forced response tests. Maximum amplitude predictions with this damping form were better than the original but requires numerical methods and only the maximum response can be calculated [59, 115]. Philosophically, the modified model of Lupi et al. has another problem: It's getting so far removed from the original random vibration model of Vickery and Basu that it becomes a new empirical model based on curve fitting.

2.4.2 Correlation length model

According to Ruscheweyh [49], it's only necessary to calculate maximum response in most cases and this formed the basis for a model to calculate maximum modal amplitude assuming harmonic motion that's used in the Eurocode [5]. In the spirit of simplicity, tip effects are neglected and

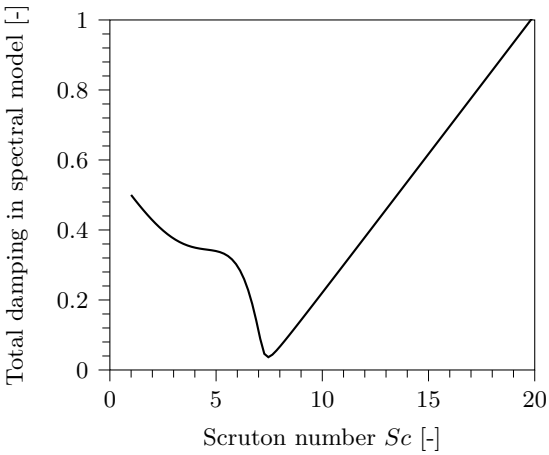

Figure 2.17: *Total damping in the spectral model (denominator of equation* (2.24) *without the mass and diameter scalar).*

only the correlation length (which affects the force's strength) and lock-in effects are considered. Based on these assumptions, the equation for the mode shape's SD amplitude becomes

$$r_{y,\sigma} = \frac{\pi \rho U^2 \int_0^h c_{lat}(z)\psi dz}{2\omega_n^2 m_g \delta}, \tag{2.28}$$

where damping is expressed using the logarithmic decrement δ.

Equation (2.28) can be simplified by assuming that the force coefficient is constant over the correlation length, L'. This constant lift coefficient, c_{lat}, depends on the Reynolds number and is experimentally determined from an envelope of available experimental data, i.e. assumed to be a worst case force [136]. Using the definitions of the Scruton number, Strouhal number and equivalent mass given in equations (2.14), (2.5) and (2.9), equation (2.28) can be rewritten to:

$$r_{y,\sigma} = \frac{c_{lat}}{ScSt^2} K_\xi K_W^*, \tag{2.29}$$

$$K_\xi = \frac{\int_0^1 \psi dz}{4\pi \int_0^1 \psi^2 dz}, \tag{2.30}$$

$$K_W^* = \frac{\int^{L'} \psi dz}{\int_0^1 \psi dz}. \tag{2.31}$$

In equation (2.30), K_ξ represents a mode shape constant and K_W in equation (2.31) is the correlation length factor. To calculate the maximum response rather than the standard deviation, equation (2.29) is multiplied by a peak factor C. This factor is incorporated by modifying equation (2.31) so that the integral is over the length L_e (effective correlation length) rather than L' as in equation (2.32):

$$K_W = C \cdot K_W^* = \frac{\int^{L_e} \psi dz}{\int_0^1 \psi dz}. \tag{2.32}$$

By combining equations (2.29), (2.30) and (2.32), the model becomes

$$r_{y,max} = \frac{c_{lat}}{ScSt^2} K_W K_\xi. \tag{2.33}$$

To solve equation (2.33), L_e needs to be defined and it can be approximated using

$$L_e = 2d_0 \exp\left(1 + 1.4 r_{y,max}\right), \quad r_{y,max} \leq 0.6$$

Table 2.1: *Simplified calculations of correlatin length L_e/d_0 based on dimensionless amplitude.*

$r_{y,max} \leq 0.1$	$0.1 < r_{y,max} < 0.6$	$r_{y,max} \geq 0.6$
$\frac{L_e}{d_0} = 6$	$\frac{L_e}{d_0} = 4.8 + 12 r_{y,max}$	$\frac{L_e}{d_0} = 12$

This equation has an upper limit to the amplitude and the explanation for it is simple: Aerodynamic nonlinearities will limit the maximum limit cycle amplitude [136]. At low amplitudes, the effective correlation length is mostly due to random vibrations and a constant effective correlation length can be assumed. The correlation length between the high and low amplitudes can be approximated using linear interpolation and L_e was simplified to the function given in table 2.1 [49]. As the correlation requires the amplitude and amplitude the correlation, the maximum amplitude needs to be solved for by iteration.

To fully transform the model into what's used in the Eurocode [5], there is one step left: Assume a constant mode shape for similar structures and solve the integral in equations (2.30) and (2.32). For chimneys, and other tall cantilevered structures, the assumed mode shape is y^2 and K_ξ reduces to 0.133 [5, 55]. When evaluating the integral in equation (2.32) from $(h - L_e)$ to h and using the same mode shape, K_W becomes [49, 136]

$$K_W = 3\frac{L_e d_0}{\lambda}\left[1 - \frac{L_e d_0}{\lambda} + \frac{1}{3}\left(\frac{L_e d_0}{\lambda}\right)^2\right] \tag{2.34}$$

2.4.3 Simiu and Scanlan's design approximation

Simiu and Scanlan [90] derived a design approximation based on a nonlinear representation of vortex-induced vibrations using a power series of $\dot{y}$ terms with odd exponential. This equation depends on experimentally determined coefficients and most of these are zero during lock-in. When averaging the model over a cycle of oscillation, it can be approximated to the equation (2.35) which only gives the maximum response and has a similar form to the empirical fit of Skop and Balasubramanian in equation (2.16) [105]. While the equation could be useful for roughly estimating the maximum response amplitude in experiments, it should not be used for final designs.

$$r_y = \frac{1.29}{\left[1 + 0.43(8\pi^2 St^2 Sc)\right]^{3.35}} \tag{2.35}$$

2.4.4 Coupled wake oscillator models

Coupled wake oscillator models can model both the vortex-induced vibrations and the oscillating lift and are often based on the observations of Bishop and Hassan [33] and model of Birkhoff and Zarantonello [7, 137, 138]. In these models, the structural motion (linear) and lift force due to vortex-shedding (nonlinear) are modeled in separate but coupled equations of motion. Due to the nonlinear nature of these equations, they are often solved numerically at several dimensionless frequencies or approximated by for example assuming a harmonic form and by neglecting higher order harmonics or by averaging them [139].

Skop and Griffin [104] derived an early coupled wake oscillator model where the fluid forces were modeled using a van der Pol oscillator and arbitrarily coupled with structural speed (dissipation coupling). The wake oscillator model of Tamura and Amano [112] was less arbitrary and was based on an oscillating Magnus-lift which again was modeled as a van der Pol oscillator with structural acceleration and speed couplings. The Tamura model was later extended to a 3D model though it's much more complex than the 2D model, contain more assumptions on the forces and is less user-friendly [140]. Both of these coupled wake oscillator models have

characteristics first found by Bishop and Hassan [33] such as lock-in with amplified forces and unsteady lift being limit-cycle oscillation-like.

A third wake oscillator model is that of Facchinetti et al. [14] who argued that the wake should be coupled to structural acceleration if limited to a single coupling term. This form is similar to what Meliga and Chomaz found using an asymptotic, multiple-scale analysis of the Navier-Stokes equations which gives credence to the coupling choice. The wake coupling can be improved and Meliga and Chomaz specified that an extra coupling in the form of the structure's jerk or integral of motion could improve the response predictions [94]. The simple wake oscillator model of Facchinetti et al. is described in equations (2.36) and (2.37) where q is the wake variable which drives the oscillating lift. The total structural damping factor D, equation (2.38), consists of the structural and a drag induced damping due to cylinder's motion.

$$\ddot{y} + D(\omega_q)\dot{y} + y = \omega_q^2 M q, \tag{2.36}$$

$$\ddot{q} + \epsilon\left(q^2 - 1\right)\dot{q} + \omega_q^2 q = A\ddot{y}, \tag{2.37}$$

$$D(\omega_q) = 2\zeta + \frac{\gamma}{\mu}\omega_q. \tag{2.38}$$

Two of the coefficients in the model needed to be experimentally determined and 12 and 0.3 were found to be good values for A and ϵ respectively using forced response experiments [14]. Ogink and Metrikine [141] found that different values better match free-vibration experiments and concluded that the best coefficient values depend on the experimental configurations. The remaining model parameters depend on the aerodynamic forces and are the strength F, the mass-scaled force M and the stall parameter γ; all three are defined in equations (2.39)–(2.41). The stall parameter includes a factor of 5/3 and this is a simplified method for including the mean drag amplification during high amplitude vortex-induced vibrations. This stall parameter is also scaled by the mass-ratio in the total damping which helps limit the amplitude growth associated with low mass-ratios and damping ratios.

$$F = \frac{C_{l0}}{16\pi^2 St^2}, \tag{2.39}$$

$$M = \frac{F}{\mu}, \tag{2.40}$$

$$\gamma = \frac{5}{3}\frac{C_d}{4\pi St} \tag{2.41}$$

A benefit of coupled wake oscillator models, is how customizable they are. For instance, it's quite simple to add noise to the model either as white noise or in the form of turbulence with varying dimensionless speed [142–146]. In addition, they can easily be combined with other phenomena to improve the predictions e.g. vortex-induced vibrations in two directions [107] or added tuned-mass dampers [7, 87]. Some customization of the models can be regarded as general improvements, e.g. Srinil and Zanganeh [107] improved the amplitude response predicted by Facchinetti et al.'s model by adding a nonlinear stiffness and Ogink and Metrikine [141] added a frequency dependent coupling term. While these changes improved the predictions, the changes added new nonlinearities that made the system harder to solve for. Of the coupled wake oscillator models, the model that's shown to be the easiest, most consistent and best to use is that of Fachinetti et al. (with modified parameter values) and it will form the basis for a new, simple and effective predictive model for predicting the amplitude response in later chapters.

2.4.5 How to improve predictions of vortex-induced vibrations

There are ways to improve the predictive models presented. For instance, the correlation length model can be improved by finding more accurate lift force coefficients as a function of the

Reynolds number. The spectral model can be improved by better including the effect on nonlinear damping like in the work of Lupi et al. Instead of modifying the damping directly in the transfer function, it would be better to include a better description of the aerodynamic damping directly in the structural equation of motion. The downside to this is that a method for deriving nonlinear transfer functions needs to be created. Another way to improve the model is to get better measurements of the aerodynamic damping and the lift spectra as suggested by Sanada, Suzuki and Matsumoto and Scherer [124, 125].

There are several things that can be improved for the wake oscillator models beyond finding better coefficient and parameter values. Firstly, one of the best ways of getting the amplitude response is to do computationally expensive numerical simulations. Better nonlinear approximations of the amplitude response would eliminate the need for this time consuming task. Secondly, there's no simple equation for the maximum structural response due to vortex-induced vibrations. An equation for the maximum response could aid in designing chimneys. Lastly, it needs to be determined if and when the model is better than the design code models at predicting the response of 3D structures.

2.5 Original contributions of this work

To improve the prediction of vortex-induced vibrations on industrial chimneys using wind tunnel experiments and mathematical models, several studies have been made. Each of these have incrementally improved our understanding and can be separated into three groups: 1) Improved understanding of 2D unsteady pressure distribution at super-critical Reynolds numbers; 2) Improved understanding of vortex-induced vibrations of finite length cylinders; and 3) Improved models for predicting vortex-induced vibrations and understanding of when to use them.

The first gap filled, is the lack of good unsteady pressure distributions around a smooth and stationary circular cylinders at super-critical Reynolds numbers. Experiments on a large, smooth, circular cylinder in a high speed wind tunnel was performed and its results are presented in chapter 3. These tests are supplemented by a small-scale test campaign that aimed to recreate the unsteady pressure distributions seen at large Reynolds numbers but at much lower Reynolds numbers. These results are discussed in chapter 4. The comparison and new super-critical data focuses on the Strouhal number obtained from the unsteady pressure data and the wake characteristics, the global force statistics (i.e. mean and SD values) and the main spatial and temporal unsteady pressure distributions using the bi-orthogonal decomposition (BOD).

The knowledge gained from the 2D stationary tests are used to determine the response and wake characteristics for flexible cylinders of finite length with smooth and rough surfaces in chapter 5. These tests will show the effect of a finite length on the aerodynamics and if the added roughness can adequately simulate super-critical Reynolds numbers when using an atmospheric boundary layer. In addition, the effect of the added atmospheric boundary layer is tested by repeating the tests without it. To help verify these small-scale wind tunnel tests, a full-scale field experiment on a custom designed chimney is presented in chapter 6. This field test campaign shows how the atmospheric boundary affects the response and verifies some of the findings from the small-scale tests.

The last point of improvement is in mathematically predicting vortex-induced vibrations. This is done by comparing the design code models with an approximated nonlinear wake oscillator model that doesn't require numerical simulations; the approximation of this model is described in chapter 7. In addition to deriving an expression for the amplitude response, a simple equation for the maximum amplitude and the lock-in region as a function of mass-ratio and damping are defined and discussed. This predictive model is finally compared with the existing design codes in chapter 8 using the experimentally obtained amplitude responses and the maximum amplitude of chimneys from the literature. Using these results, the best model for a given chimney is defined using the Scruton number and Reynolds number region.

Part II

2D wind tunnel experiments on stationary cylinders

Chapter

3 Wind tunnel results up to super-critical Reynolds numbers

Chapter summary

This chapters details the work done to characterize the super-critical flow around a smooth circular cylinder in uniform flow. For this super-critical cylinder, several measurements are made such as the unsteady pressure distribution and the wake characteristics. These measurements are used to calculate the Strouhal number (using both wake and pressure), the unsteady 2D forces and the steady and unsteady pressure distributions. Additionally, the effect of roughness ribs (with low relative roughness) on the flow at high Reynolds numbers was investigated. The results from these experiments should be significant as two Strouhal numbers were discovered for the smooth cylinder. One of these Strouhal numbers was found to be related to the unsteady pressure distribution that gives most of the unsteady lift force while the other was associated with a pressure distribution with spatial energy focused post separation.

3.1 Background

As mentioned in chapter 2, the Reynolds number plays a large role in the fluid dynamics over circular cylinders. Unfortunately, it's hard to achieve super-critical Reynolds numbers (order of 10^6) in wind tunnels without altering the flow medium (e.g. high pressure, cryogenic) or by using flow speeds large enough to get compressibility effects [8, 16, 17, 19–24]). In addition, the existing smooth, super-critical Reynolds number data has a large amount of scatter which makes it challenging to use (cf. the scatter in unsteady lift from Fung [29], Schmidt [38, 39] and Jones et al. [24]). In addition to the scatter in lift coefficient, there's a qualitative difference in the Strouhal number presented in the literature: Some researchers present a value in the range 0.25 to 0.27 [8, 13, 21, 23–25, 36, 56] whereas others give a value near 0.2 [17, 54]. In addition, the presented pressure distributions are focused on the mean and sometimes the SD pressure distribution but not on decomposing them to more informative spatial pressure distributions (using e.g. the bi-orthogonal decomposition (BOD) method).

Overall, there's a lack of good experimental data (both for wake measurements and unsteady pressure distributions) for smooth cylinders at super-critical Reynolds numbers without flow or surface modifications. This makes it harder to accurately determine if a smaller experiment (e.g. with maximum Reynolds number around 10^5) reaches the correct unsteady pressure distributions and forces with added roughness or uniform turbulence. This chapter introduces some experimental results on a large, circular, steel cylinder ($d = 0.5$ m) in a large, high-speed wind tunnel. This circular cylinder was tested in four configurations where one is a nominally smooth cylinder and with attached ribs. The smooth cylinder tests will give a good baseline for the strength of the unsteady forces, their frequency and the pressure distributions which most strongly affect the unsteady forces on a super-critical cylinder. The tests with added roughness elements show if there are differences when testing a rough cylinder at large scales and at small scales.

3.2 Experimental methodology

3.2.1 Wind tunnel description

The wind tunnel tests were performed in CSTB's climatic wind tunnel, i.e. the Jules Verne wind tunnel. The aerodynamic test section, 6x5 m^2, can reach a maximum wind speed of 70 m/s when operated in the high speed mode and as low as 5 m/s in the low speed mode (though with some irregularities). The wind speed was calibrated based on the location of the cylinder's stagnation point and at the height the pressure taps using a fast response Pitot tube, a pre-calibrated average Pitot tube and three Cobra probes (used for wake measurements).

The turbulence intensity was found in all three main velocity components using the Cobra probes. It was estimated to be 1.5 % in the inward direction (u component of velocity), 1.0 % in lateral direction (left-right or v component) and 1.5 % in longitudinal direction (up-down or w component). The turbulence intensity was slightly higher at lower speeds but quickly converged to the given values as the speed increased.

The wind tunnel mode was changed by changing the fans' rotational speed; this was used to have the smoothest flow at low speeds and high speeds. The low speed fan mode was used for speeds in the range 4 to 24 m/s and the high speed mode for speeds between 20 and 70 m/s. This gave a transition region for wind speeds between 20 and 24 m/s made it possible to verify that the transition between the wind tunnel modes were smooth.

3.2.2 The test model and setup

The test model and setup is sketched shown in figure 3.1. Figure 3.1a shows an annotated photo of the smooth cylinder along with explanations of where the various sensors and equipment were placed, the height at which the added roughness elements were placed and their length. The test model was a circular steel cylinder with diameter 0.5 m and was mounted vertically in the wind tunnel and extended the entire height. This should have given good 2D conditions at the measurement location (mid-height or 2.5 m from floor). The cylinder's and wind tunnel's dimensions made the blockage ratio 8.3% and its effect on the forces and Strouhal number should be small [147]. With this setup setup and structural characteristics, the cylinder had a damping ratio of 36.4% and a damped first natural frequency of 64 Hz. These structural characteristics made the maximum measured acceleration and vibration amplitude negligible and motion should not impact the measured pressure distributions. The coordinate system used and relative positions of the Cobra probes and cylinder in the x-y plane is shown in figure 3.1b.

To measure the unsteady pressure distribution, sixty uniformly spaced pressured taps were drilled at mid-height. The first pressure tap was placed at $\theta = 0^\circ$ (purely in drag direction) with the rest spaced out uniformly with a separation of $\theta_4 = 6^\circ$. These taps were connected to two pressure scanners using vinyl tubing with length 1.0 m. Figure 3.2a shows the location and numbering scheme of the pressure taps in relation to the added roughness and figure 3.2b shows the location of all added roughness elements. To investigate the effect of roughness spacing, specific ribs were removed to increase the spacing as shown the figure 3.2.

Three four-hole Cobra probes were installed behind the cylinder to measure the wake characteristics. These were mounted at different heights and placed 2 diameters behind the cylinder and 0.25 diameter to the side of the cylinder's center for smooth tests, 1 m and 0.125 m measured from the cylinder's rear and center respectively. When testing with roughness, the cobra probes were moved 0.25 diameter further to the side as the strong wake fluctuations caused bad measurements at the original location. A focused side view of the Cobra probes' locations is sketched in figure 3.1c and from the top in figure 3.1b. The upper probe's (D) location was 1 diameter above the pressure tap arrangement, the next (B) 1 diameters below probe D (near height of pressure taps) and the last (A) 2.5 diameters below probe D (1.5 diameters below the pressure taps). These locations were chosen to minimize any adverse interactions between the

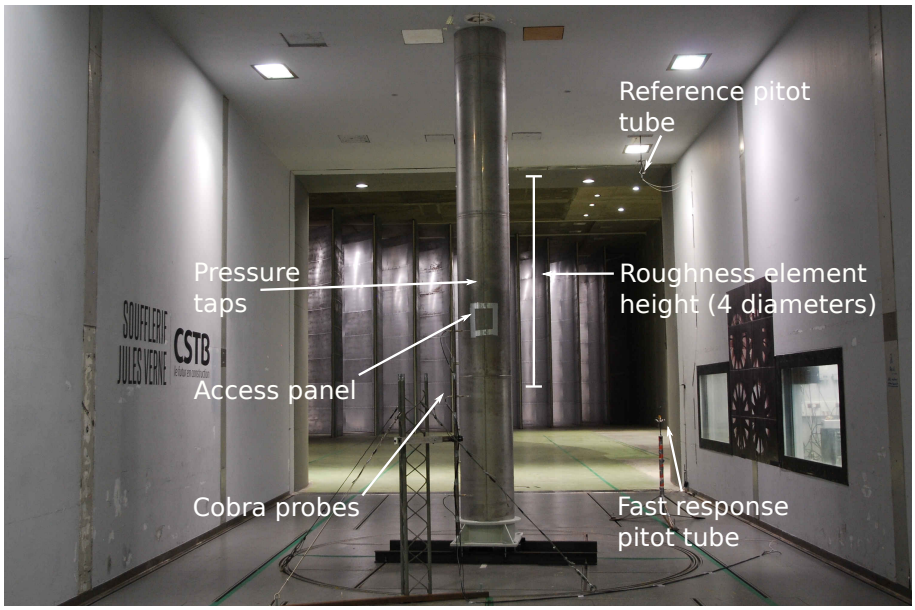

(a) *Picture of experimental setup for smooth tests with annotated explanations.*

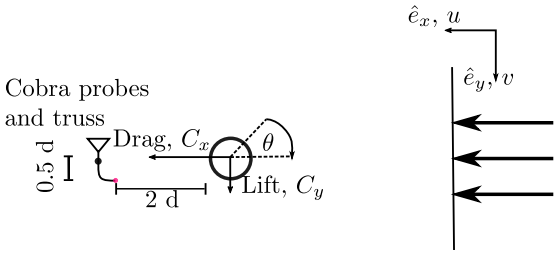

(b) *Sketch from top with coordinate system.*

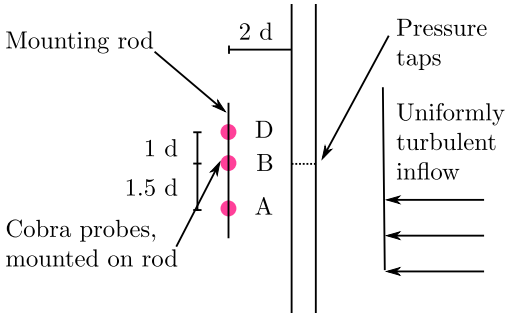

(c) *Side sketch focused on location of cobra probes.*

Figure 3.1: *Figures showing experimental setup, relative locations and coordinate system.*

Cobra probes and the pressure taps. Two different types of Cobra probes were used and only one was rated up to 70 m/s (probe D) while the other two were rated up to 35 m/s. This means that only probe D worked at super-critical Reynolds numbers when using the smooth cylinder.

The last pieces of measuring equipment were two Pitot tubes used to measure the reference wind speed and turbulence intensity. One of these was a fast response Pitot tube that was rated up to 45 m/s and it was placed 4 diameters to the side of the cylinder (2 diameters from the wall), at a height of 1.1 m (2.2 diameters) and slightly ahead of the model. This position was chosen to characterize any freestream flow changes after installing the model. The second, reference Pitot tube was mounted to the roof of the front section of the wind tunnel and rated for all speeds tested. The location was 0.35 m from the roof and 0.87 m from the wall. Both of the Pitot tubes were calibrated based on the wind speed at the location of pressure tap 1 ($\theta = 0°$).

3.2.3 Roughness elements

Surface roughness was added to the circular cylinder using laser-cut, acrylic ribs with rectangular cross-sections with heights of either 0.5 mm or 1.35 mm; this corresponds to relative roughness, $Rr = k_\delta/d$, of $1 \cdot 10^{-3}$ and $2.7 \cdot 10^{-3}$ respectively. These rib elements had a width of 3 mm and a total length of 2 m (4 diameters). This length was the result of lining up 3 rib pieces (2x0.5 m and 1x1 m) and with joints 1 diameter (0.5 m) from the pressure taps. The ribs were glued on at regular intervals by attaching either 30 (θ_1=12° spacing) or 14 (θ_2=24° spacing)

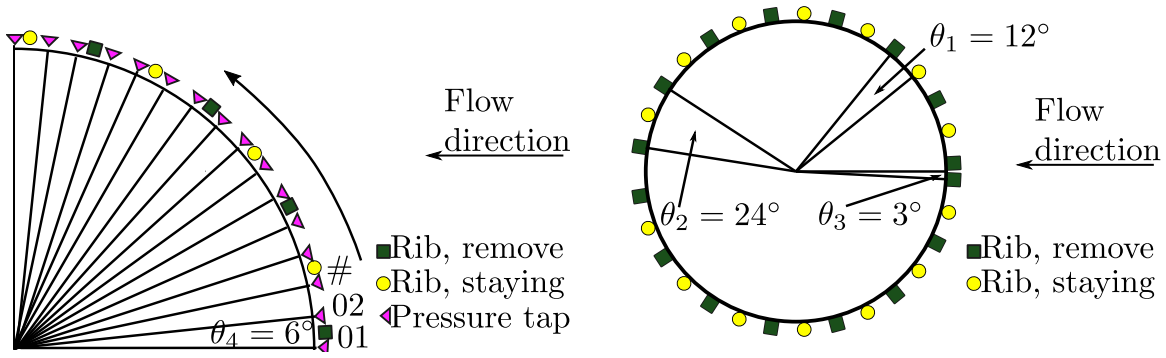

(a) *Pressure tap and rib distribution.* **(b)** *Rib distribution.*

Figure 3.2: *Sketches showing distribution of pressure taps and ribs.*

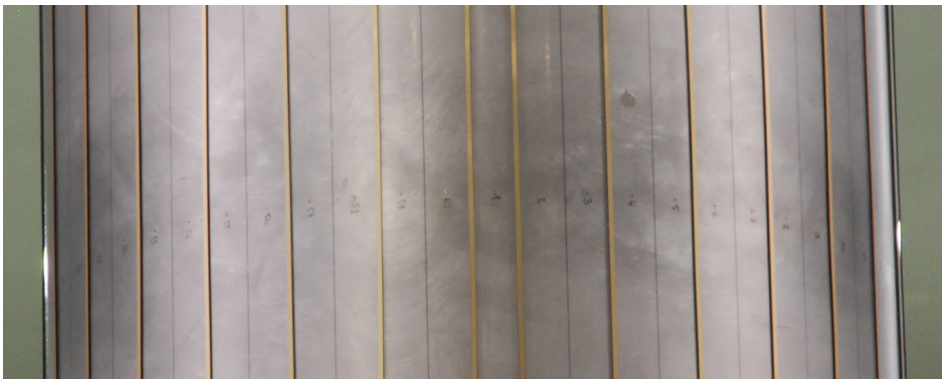

Figure 3.3: *Picture of added roughness elements and pressure taps taken from the front of the cylinder.*

lengths as shown in figure 3.2b. The separation angle between the ribs were different near the stagnation point and rear of the cylinder due to the location and of the pressure taps and to keep it symmetric around the $\hat{e}_x$ axis (the first removable ribs were placed at $\theta_3 = 0 \pm 3°$ and the last at $180 \pm 9°$). Figure 3.3 shows a frontal picture of the cylinder with the $2.7 \cdot 10^{-3}$ roughness elements attached every 12° and how they're positioned relative to the pressure taps.

3.2.4 Instrumentations and measurements

Two separate measurement systems were used as outlined in figure 3.4: One measured the unsteady pressure while the other focused on wind velocity. Both systems used the same recording frequency (400 Hz) and recording length (180 s) but with a slight time-shift between them.

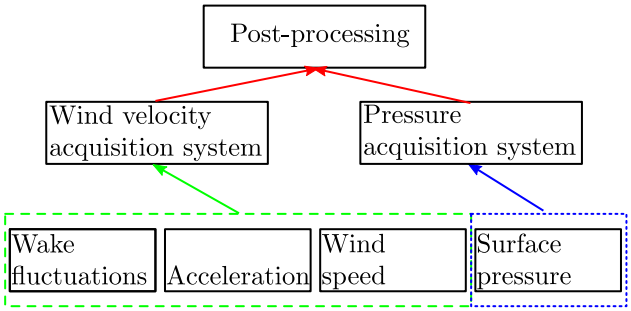

Figure 3.4: *Diagram of wind and pressure data acquisition chains.*

Wind velocity acquisition system

Three things were measured in the wind velocity acquisition system: 1) the reference wind speeds from the Pitot tubes; 2) the cylinder's acceleration using two internally mounted accelerometers and 3) the wind velocities in the wake using Cobra probes. While the Cobra probes measured all velocity components, the main component of interest was the lateral fluctuations v which should be the most affected by vortex-shedding. Not all Cobra probe recording were good and the recorded velocities for many experiments had corrupted data points when the inflow angles were large ($\approx 15°$)[5]. Even with this limitation, there were enough good samples in succession to perform spectral and statistical analyses of the wake's lateral component. To calculate the power spectrum (PSD) of a given wake component (used to identify the vortex-shedding frequencies), an algorithm based on Welch's method with 50% overlap and with a segment length of 8192 points was created. This was implemented in Python using a customized function and the inbuilt Fourier transform function from NumPy.

Pressure acquisition system

The second acquisition system recorded the unsteady surface pressure distribution by connecting the pressure taps with 1 m vinyl tubing to two 32 channel pressure scanners (32HD ESP pressure scanners from Pressure Systems, Inc.) with multiplex frequency of 70 kHz. Both pressure scanners were rated up to 7000 Pa and should have static errors within $\pm$ 0.03%. To correct for the resonance and damping effects caused by the tubing, a proprietary and CSTB developed theoretical transfer function based on the work of Bergh and Tijdeman [148] was used. The theoretical transfer function is well tested for the tubing length, the tube fitting and pressure scanners used. In other words, the temporal unsteadiness should be recovered and correct unsteady forces and pressure distribution can be calculated. The power spectrum of the pressure distributions were calculated using the same algorithm as for the Cobra probes.

3.2.5 Tested wind speeds

The wind tunnel experiments were performed at different speeds depending on the surface roughness configurations. When using the smooth cylinder configurations, the wind tunnel tests were performed at speeds between 4 and 70 m/s whereas tests with ribs were performed at speeds between 4 and 60 m/s. For all configurations, the wind speed was increased by increments of 2 m/s. Additionally, two tests are performed at 20, 22 and 24 m/s as this is where the wind tunnel mode was changed from low to high speed mode. This corresponds to testing Reynolds numbers between $1.33 \cdot 10^5$ and $2.33 \cdot 10^6$, at increments of $6.7 \cdot 10^4$ and with the overlap region around $7.5 \cdot 10^5$.

3.2.6 Characteristic dimensions

The characteristic dimension for the Reynolds number and force coefficients used here is the diameter of the smooth cylinder. While adding surface roughness to the cylinders effectively increases the diameter by 2 times roughness height, this value is not used due to the goal of the test: The goal of the tests was to simulate super-critical Reynolds numbers at speeds below what it should be for a smooth cylinder with diameter d. It should therefore be more philosophically correct to use the diameter of the model both here and in the small-scale tests. In addition, the use of roughness height in creating equivalent Reynolds numbers and force coefficients has been shown to be inadequate in section 2.1.3 as it does not include the effect of flow changes nor the use of discrete roughness elements like ribs [10, 13, 28, 37, 48, 53, 58, 62]. Instead

[5]This is one of the reasons for why the probes were moved for the tests with ribs.

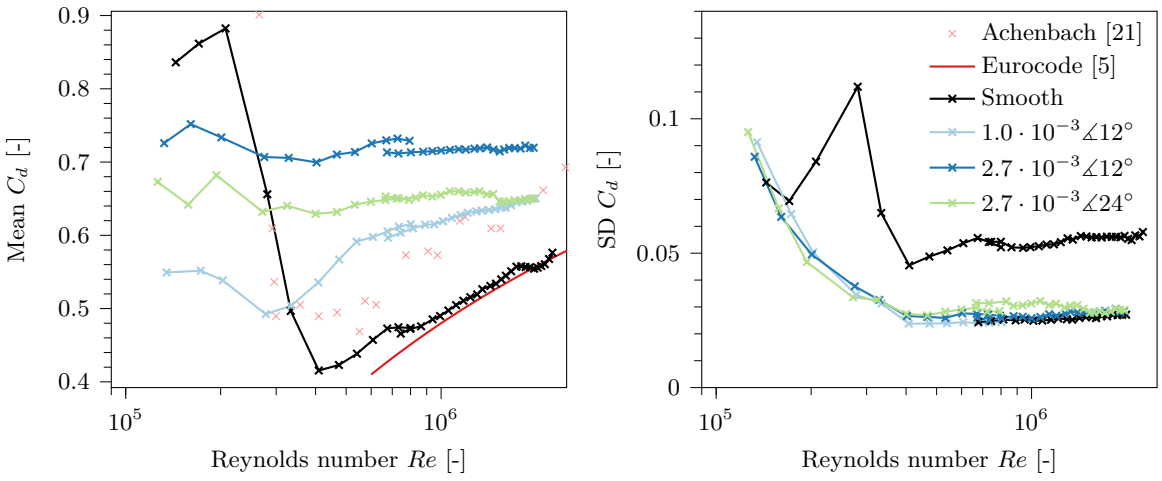

(a) *Mean drag.* **(b)** *SD drag.*

Figure 3.5: *Experimentally obtained drag coefficient compared with the smooth results of Achenbach and Heinecke [21] and analytic drag for the smoothest cylinder in the Eurocode [5].*

Table 3.1: *Reynolds numbers and roughness configurations from large-scale 2D tests identified as being at super-critical Reynolds numbers.*

Rib configuration	Speed [m/s]	Reynolds number [-]
Smooth surface	67.6	$2.25 \cdot 10^6$
$1.00 \cdot 10^{-3} \measuredangle 12°$	24.1	$8.02 \cdot 10^5$
$2.70 \cdot 10^{-3} \measuredangle 12°$	21.8	$7.28 \cdot 10^5$
$2.70 \cdot 10^{-3} \measuredangle 24°$	22.0	$7.33 \cdot 10^5$

of comparing similar effective Reynolds numbers, configurations at similar Reynolds number regions are compared based on the flow/drag description in section 2.1.1.

3.3 Aerodynamic forces

3.3.1 Unsteady lift and drag forces

When comparing the present results with those of Achenbach and Heinecke [21] (figure 3.5a), it can be seen that the mean drag has a similar shape for the smooth cylinders but that Achenbach and Heinecke [21] found higher drag coefficients. There are two differences in the arrangement which could have led to this discrepancy: 1) Achenbach and Heinecke's higher blockage ratio (16.7%) was uncorrected which should increase the drag coefficient and 2) their high-pressure tunnel had a lower turbulence intensity (0.45% instead of 1.5%). Of the two, the difference in blockage ratio is the likely culprit for the difference.

As the mean drag coefficient data match well with the Eurocode [5] formula with the smoothest surface, the present data should be good and the effect of blockage low. The effect of adding ribs on mean drag was also similar to the previous literature and the Eurocode formula [5, 10, 13, 17, 19–23, 26, 27, 31, 40, 58, 62, 63]: Increasing the height of the ribs increased the drag and caused earlier Reynolds number transitions and decreasing the spacing had the opposite effect (lower roughness). Based on the mean drag data, it's assumed that the surface flow over the cylinders reaches good super-critical Reynolds numbers at the values given in table 3.1.

While the added roughness increased the mean drag, it greatly decreased the SD drag as shown in figure 3.5b. At the same time, changing the roughness barely affects the SD drag

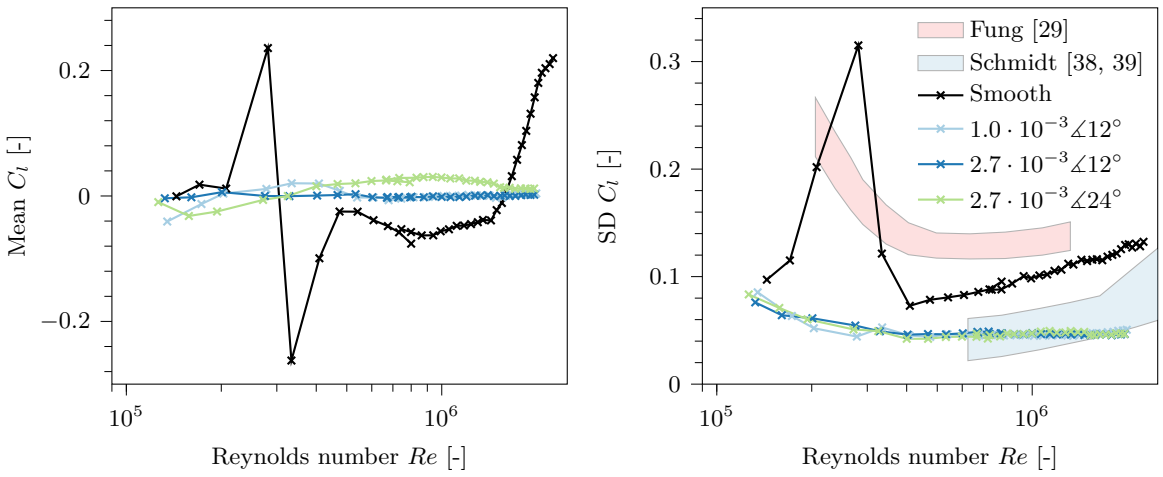

(a) *Mean lift.* **(b)** *SD lift.*

Figure 3.6: *Experimentally otained lift coefficient compared with smooth results of Fung [29] and Schmidt [38].*

and their change with Reynolds number is similar; the increased SD drag at low speeds should be due to low speed effects in the wind tunnel. The smooth cylinder has a more significant Reynolds number effect; there's a reduction in SD drag at critical Reynolds numbers which slightly recovers to a plateau value at super-critical Reynolds numbers.

Figure 3.6 shows that the mean lift was near zero for configurations with ribs, but the smooth cylinder had significant mean lift at high Reynolds numbers. This could either be due to a separation bubble or geometric imperfections and cylinder deformations at high dynamic pressures as in the work of van Hinsberg [22]. The SD lift for the smooth cylinder was closer to the results of Fung [29] and approaches upper values found by Schmidt [38] at higher Reynolds numbers; based on the evolution of Fung's result with Reynolds number, it's possible that these results also would approach the upper values given by Schmidt. A possible reason for why the present results better match Fung's, is that the wind tunnel and experimental configurations are more similar [29, 38, 39]. Contrary to Basu's analysis [13], the configurations with added roughness ribs have lower SD lift coefficients in the Reynolds number range of interest and match best with Schmidt's smooth cylinder results [38, 39]. Additionally, changing the rib height or spacing barely changes the SD lift similar to the SD drag.

3.3.2 Correlation and coherence

The correlation and coherence, defined in section 2.1.4, are shown in figure 3.7 for the configurations with roughness at simulated super-critical Reynolds numbers using the speeds specified in table 3.1. As a reminder, the correlation and coherence for the smooth cylinder at actual super-critical Reynolds number could not be calculated due to only one Cobra probe functioning at these speeds. An example of the coherence between the Cobra probes are shown in figure 3.8 and its the values at the vortex-shedding peaks that are presented in figure 3.7. The locations of the Cobra probes used to calculate the coherence and correlation are given in figure 3.1c.

The correlation, figure 3.7a, was similar for the rib configurations at distances less than 1.5 d but has a rib height based difference when the distance reaches 2.5 d. Additionally, the correlation initially drops and then increases for all configurations. This behavior is more similar to the correlation used in the spectral model (see equation (2.20) in section 2.4.1) than the correlation found by Novak and Tanaka [43]. There's another difference between the previous literature result and the current: The correlation is much stronger in the literature. There are two possible explanations for this. Either the wake correlation is weaker than the one from

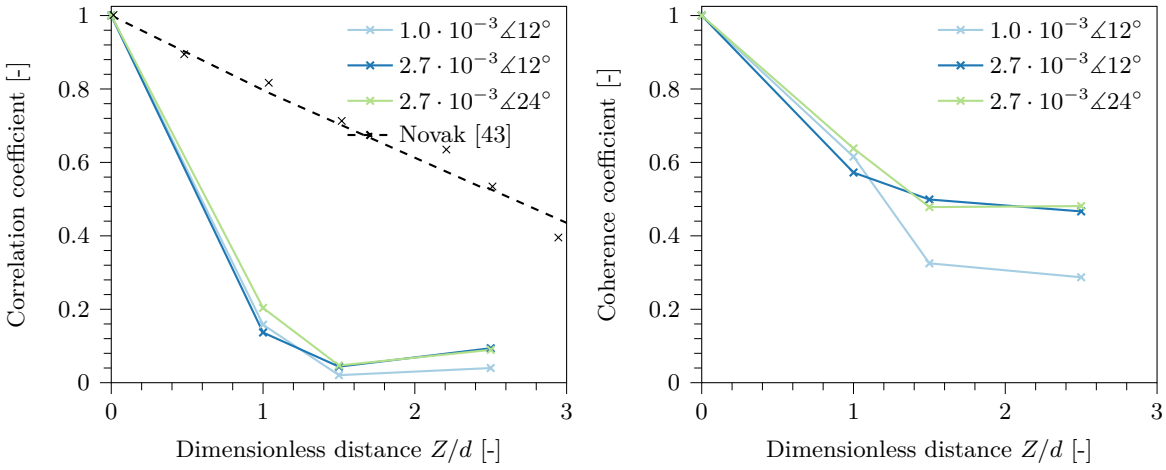

(a) *Correlation.* **(b)** *Coherence.*

Figure 3.7: *Comparison of correlation and coherence at super-critical Reynolds number configurations.*

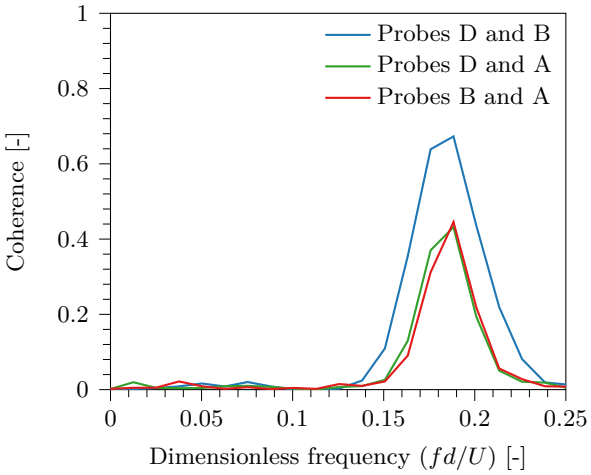

Figure 3.8: *Example of coherence between Cobra probes using the cylinder with* $2.70 \cdot 10^{-3} \measuredangle 12°$ *roughness attached. Note that the resolution was decreased for visualization purpuses.*

unsteady pressure or correlation and coherence is confused in the literature. As the correlation given by Novak and Tanaka is that much greater, the latter explanation is more plausible.

The maximum coherence, figure 3.7b, is different from the correlation in that it's much stronger. A possible reason for this, is that the coherence shown is for the vortex-shedding process only instead over all frequencies like in the time domain. Like for the correlation, the maximum coherence is independent of roughness size at low distances (1 d) but the coherence is significantly higher with larger roughness height at higher distances (1.5 and 2.5 d). The coherence evolves differently with distance than the correlation: It drops significantly slower with distance and then plateaus between distances of 1.5 and 2.5 d. The difference between coherence at low and high distances might be because there's a different vortex-cell when the distance is greater than 1.5 d. While the wake correlation was different from the pressure correlation of Novak and Tanaka, the coherence was more similar to it. Because of this and as it focuses on a narrow band frequency, the coherence idq a much better measure of vortex-cells and flow similarity along the height.

For the highest measured Reynolds numbers using 3 Cobra probes with the smooth cylinder (critical Reynolds numbers), the correlation coefficients are fairly constant with distance and is approximately {1 d: 0.08, 1.5 d: 0.01 , 2.5 d: 0.0}. Similarly, the coherence coefficients

are approximately {1 d: 0.17, 1.5 d: 0.03 , 2.5 d: 0.01}. These coefficients are mentioned because it shows that the coherence is higher than the correlation and because many of the rib configurations have a similar coherence and correlation trend with Reynolds numbers: At critical Reynolds numbers the correlation and coherence coefficients are smaller and increases at super-critical Reynolds numbers. As the smooth cylinder's coefficients are smaller at critical Reynolds numbers than for the rough cylinders' and as decreased roughness height reduces coherence, it's possible that the smooth cylinder's coherence and correlation coefficients are lower at super-critical Reynolds numbers as well.

3.4 Unsteady pressure distributions and their effect on the forces

3.4.1 Bi-orthogonal decomposition

Definition

The unsteady pressure data are decomposed into orthogonal spatial (topos) and temporal (chronos) pairwise components using the bi-orthogonal decomposition (BOD) [46, 149]. When transforming the continuous BOD method to discrete, the pressure field of a single ring of pressure taps is defined as the sum of the following eigenvalue scaled orthogonal fields

$$p(\theta, t) = \sum_{i=1}^{n} \Psi_i(\theta)\alpha_i\Phi_i^{\mathrm{T}}(t).$$

If the pressure data is arranged in matrix form with one dimension as time and the other as sensor location, the discreet BOD method resembles the singular value decomposition (SVD). Because of the size of the data matrix, directly applying a SVD routine is ill advised and may fail (e.g. RAM shortage). Instead, it can be shown that the topos is identical to the eigenvectors of the signal's spatial correlation matrix the corresponding eigenvalues are equal to the BOD eigenvalues squared ($\alpha_{corr} = \alpha_{BOD}^2$). As the BOD components are pairwise orthogonal, the chronos can be recovered from in matrix form using

$$\mathbf{\Phi}(t) = \mathbf{P}(\theta, t)\mathbf{\Psi}(\theta)\mathbf{A}^{-1},$$

where $\mathbf{\Phi}$ and $\mathbf{P}$ are the chronos and pressure data (m by n matrices), $\mathbf{\Psi}$ is the topos (n by n matrix) and $\mathbf{A}$ the eigenvalues (n by n diagonal matrix). The dimensions m and n are the number of time samples and sensors respectively. The sign of a given chronos or topos can be changed arbitrarily (for the reconstruction and visualization), provided both chronos and topos in the pair have their signs changed.

One of the important factors in the BOD methods, is the energy each orthogonal topos and chronos pair contributes to the total energy of the signal. As the total energy of the signals should increase with the dynamic pressure, it'll be much more informative to compare the relative energy from each BOD pair to the total energy. This is done by dividing energy from each BOD pair with the total energy which is found from the trace of the spatial or temporal correlation matrices [46] or by diving the individual eigenvalues by the sum of eigenvalues as shown in equation (3.1). The focus later will be on the first four manually sorted BOD pairs; these pairs contain between 99.7 and 99.9% of the total energy of the signals measured using the eigenvalues. Most of this energy will be contained in the mean BOD pair and it's better compare the energy of the fluctuating pairs using equation (3.2); this is analogous to calculating the conditional probability given an event.

$$\alpha_{r,i} = \frac{\alpha_i}{\sum_{j=1}^{n} \alpha_j} \tag{3.1}$$

$$\tilde{\alpha}_{r,i} = \frac{\alpha_{r,i}}{1 - \alpha_{r,1}} \tag{3.2}$$

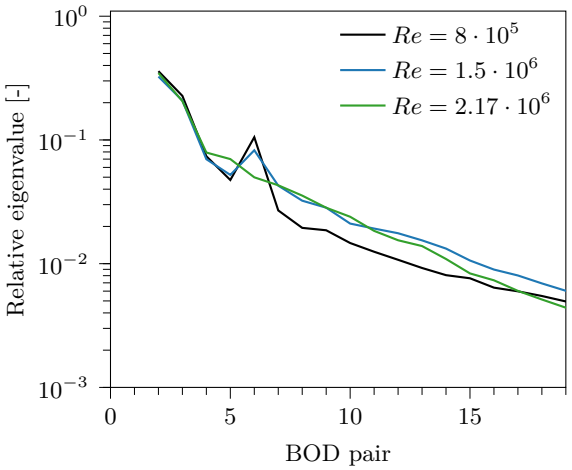

Figure 3.9: *Comparison of relative eigenvalues for the smooth cylinder at three Reynolds numbers.*

Relative contribution to forces

To compare the forces from each BOD pair to the total force, the ratio of root mean square (rms) force from pair i is compared to the total rms force [46]. The rms is defined as

$$x_{rms} = \sqrt{\frac{1}{T_2 - T_1} \int_{T_1}^{T_2} [x(t)]^2 dt},$$

which, when the mean (over-bar) and standard deviation (σ subscript) are known, simplifies to

$$x_{rms} = \sqrt{\bar{x}^2 + x_\sigma^2}.$$

Using this, the rms ratios are defined as

$$p_{rms}(i) = \frac{x_{rms,\ i}}{x_{rms,\ total}}.$$

From this, it's clear that a large nonzero mean force will strongly affect the rms ratios and increase the relative importance of the first BOD pair (mean forces). Therefore, it's better to compare the contribution to the fluctuating forces by removing the mean contribution similar to how the mean energy was removed from the relative energy in equation (3.2).

3.4.2 Smooth cylinder's topos and Reynolds number effect

The energy of the signals

The relative energy for the first 19 fluctuating BOD pairs are shown in figure 3.9 for the smooth cylinder at three Reynolds numbers (from the critical region to super-critical). This was done by removing the mean component using equation (3.2). As can be seen, much of the energy was contained in the first three fluctuating BOD pairs and there's a steady decrease in energy as the rank of the BOD pairs increases. The exception is a jump in the relative eigenvalues for pair six with the two critical Reynolds number cases. This is due to a manual sorting of the BOD pairs based on physical meaningfulness towards vortex-shedding instead of purely on energy levels. The pair that's manually moved up in the order, is the fourth BOD pair which contains a period and oscillating frequency component found in the wake; this was done to better compare the same physical phenomena. Finally, it can be seen that as the Reynolds number increases, the relative energy of the pairs higher than 4 increases but that the relative energy of the first four BOD pairs are similar regardless of the Reynolds number.

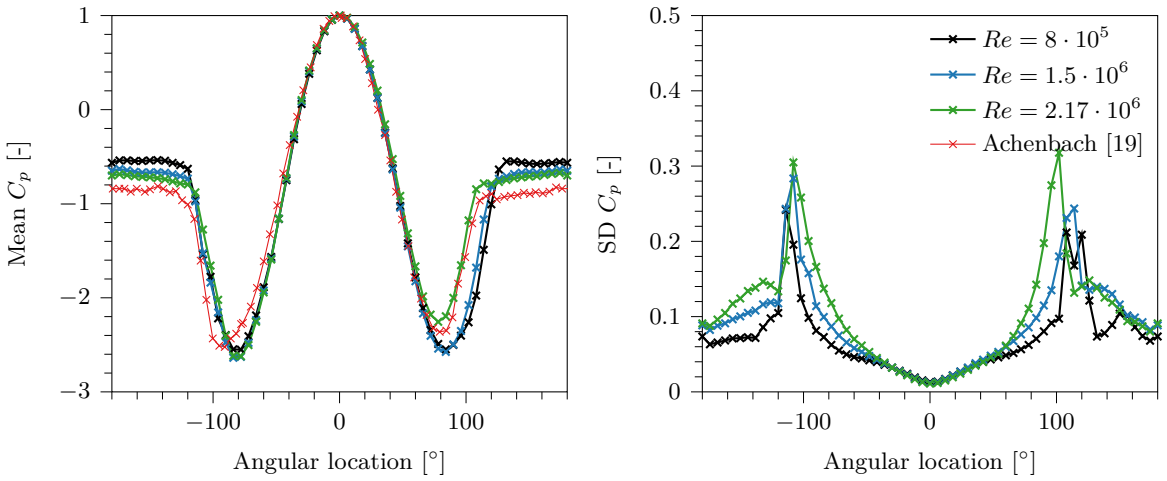

(a) *Comparison of mean C_p.*

(b) *Comparison of SD C_p.*

Figure 3.10: *Comparison and evolution of the mean and SD pressure coefficient with Reynolds number for the smooth cylinder and with the mean results of Achencbach [19].*

Spatial energy and unsteady pressure

The distribution of the mean pressure distribution on the smooth cylinder was similar to that found by Achencbach [19] as shown in figure 3.10a. While unintentional, the mean pressure distributions are not just similar in terms of values, but also similar in having asymmetry with a higher minimum pressure coefficient at positive angles. A second difference is the higher pressure coefficient post separation for the rough cylinder which should explain the lower drag coefficient in the current experiment. While not directly compared, the SD pressure coefficient has a similar shape as that found by West and Apelt [41] (shown in figure 2.3) though the peak value is smaller and further in the rear and the current results are missing both the second high peak in the rear and the high rear SD pressure coefficient.

The spatial energy (topos) of the first four BOD pairs are related to the mean and SD pressure distribution. This is shown in figure 3.11 which compares the first four topos at three Reynolds numbers. It should be immediately clear that the first BOD pair in figure 3.11a, the most energetic BOD pair, has a topos containing the mean pressure distributions and its chronos is flat with time. As the Reynolds number increases from critical to super-critical Reynolds numbers, the separation point (flat region) moved towards earlier separation (lower angular locations) and the pressure in the rear becomes lower. This is consistent with the literature description given in section 2.1.1.

The asymmetry is less consistent. Due to surface imperfections (deformations at high speeds) or a separation bubble [15], the low pressure peak on one side of the cylinder was larger than the other at super-critical Reynolds numbers; this caused the nonzero mean lift. The super-critical pressure distribution of Achenbach [19] ($Re = 3.6 \cdot 10^6$) have a relative lower pressure coefficient in the rear (which can explain the higher drag) but is similar to the present super-critical mean pressure distribution.

The second BOD pair, figure 3.11b, has a spatial distribution which should strongly contribute to the unsteady lift and will be referred to as the "vortex-lift" pair. This is because its shape has low energy levels at most locations except $\theta \in \pm[90, 110]$ where there are anti-symmetric peaks. The energy in these locations contributed greatly to the SD pressure peaks but contributes much less elsewhere. As the Reynolds number increases, the spatial energy peaks of the vortex-lift move to lower angles similar to how the shedding point moves forward for the mean BOD pair. While mostly anti-symmetric, one side has more energy. This was on the side with smaller negative peaks in the mean distribution and it's possible that the separation bubble

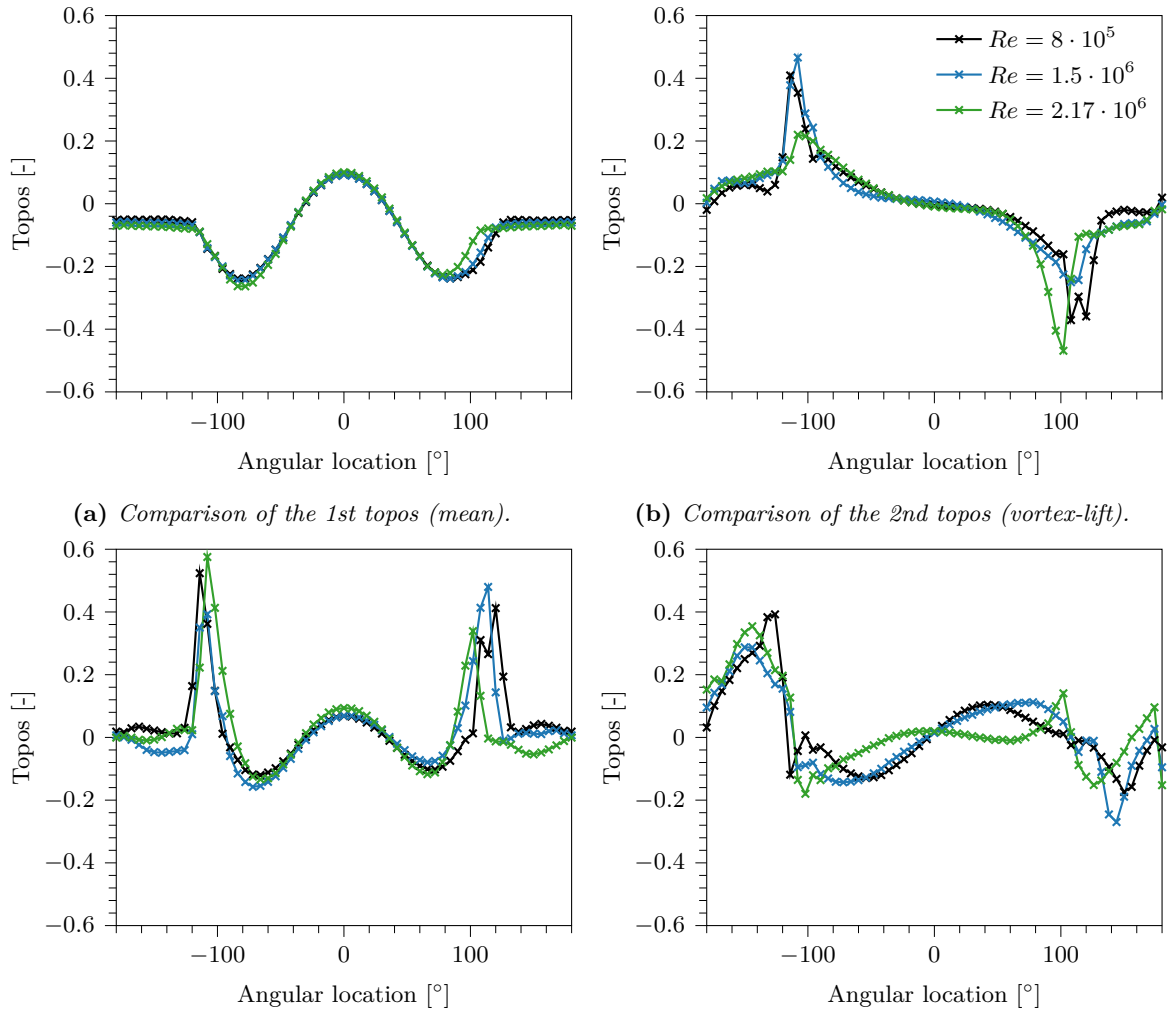

(a) *Comparison of the 1st topos (mean).*

(b) *Comparison of the 2nd topos (vortex-lift).*

(c) *Comparison of the 3rd topos (vortex-drag).*

(d) *Comparison of the 4th topos (second vortex-lift).*

Figure 3.11: *Comparison and evolution of first four topos with Reynolds number for the smooth cylinder.*

or surface deformation gave a more energetic fluctuating lift force on this side.

The third topos has peaks at the same location as the vortex-lift pair but with the same sign at both locations. This makes it more symmetric though the side with stronger lift has a lower energy peak. In addition, there's higher energy levels between $\theta = \pm 90$ which has a similar shape as the mean BOD pair; these spatial peaks move forward with increasing Reynolds numbers. If anything, this spatial energy should contribute to the unsteady drag and SD pressure between $\theta = \pm 110$ with the largest relative effect on SD pressure between $\theta = \pm 90$. Because of this shape, it'll be referred to as "vortex-drag".

The fourth BOD pair, here dubbed "second vortex-lift", has a peculiar shape which is reminiscent of the vortex-lift pair until the shedding point where there's an abrupt change in the spatial and a change of sign; this could be related to super-critical surface flow separation. Because of the shape, this BOD pair should be contributing to the SD pressures in the cylinder's rear and will contribute both to the unsteady lift and drag. As the shape of the fourth topos is more chaotic, it's harder to conclude on how it changes with the Reynolds number. It's likely that the changes in topos are highly dependent on the separation point which in turn is dependent on the surface imperfections and formation of separation bubbles.

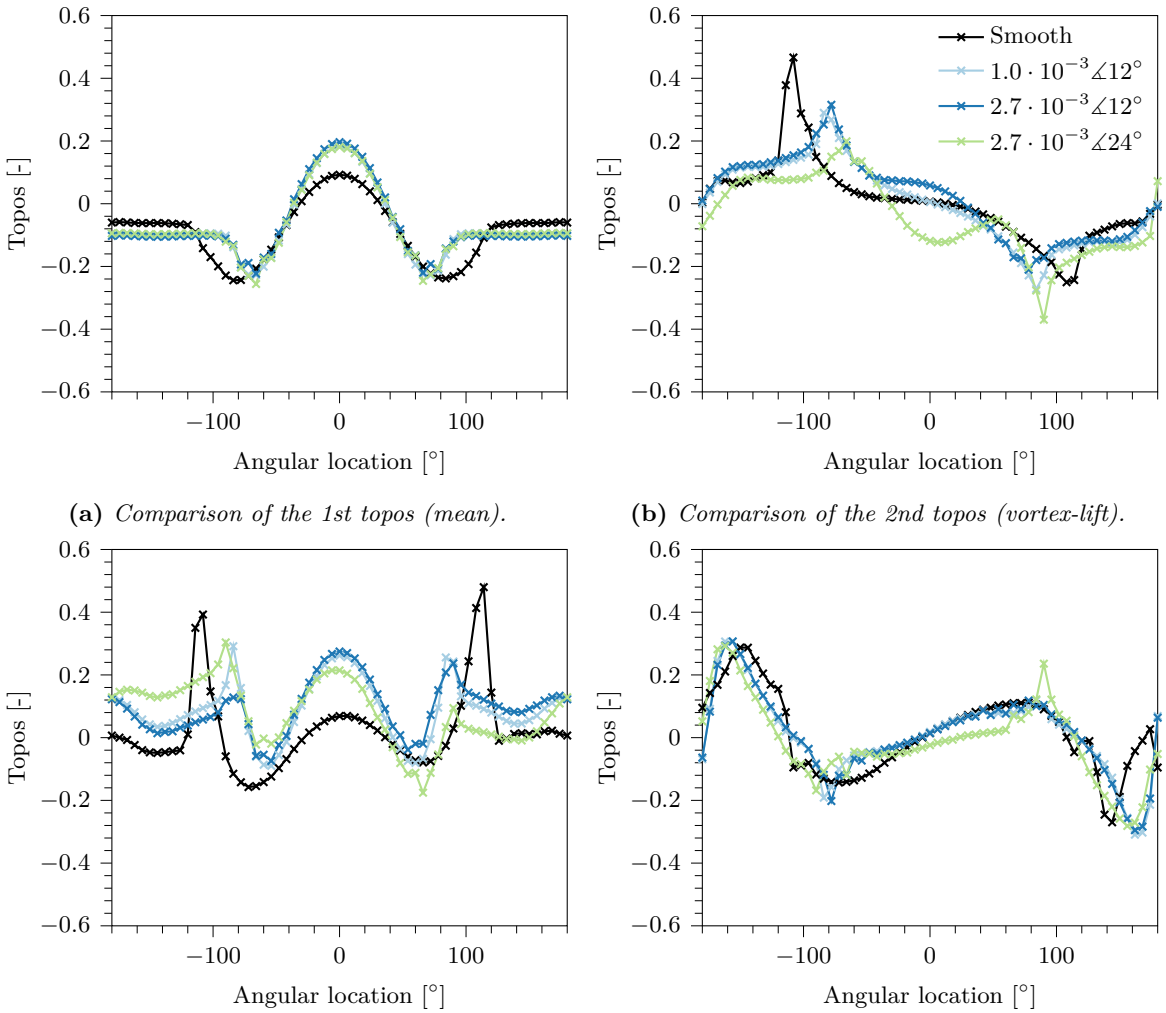

(a) *Comparison of the 1st topos (mean).*

(b) *Comparison of the 2nd topos (vortex-lift).*

(c) *Comparison of the 3rd topos (vortex-drag).*

(d) *Comparison of the 4th topos (second vortex-drag).*

Figure 3.12: *Smooth and rough configurations compared at a Reynolds number of* $1.5 \cdot 10^6$.

3.4.3 The effect of roughness and simulated super-critical Reynolds numbers

Spatial energy

The spatial energy changes not only with the Reynolds number but also with the surface roughness. When comparing the spatial energy of the first four BOD pairs at a Reynolds number of $1.5 \cdot 10^6$, figure 3.12, differences can be seen between the smooth and rough cylinders at simulated super-critical Reynolds numbers. Firstly, it can be seen that the mean distributions (in figure 3.12a are more symmetric with roughness ribs, that the separation occurs earlier and that the relative energy in the rear is lower but higher in the front. This could be explained by the ribs causing an earlier separation or that the ribs are at effectively higher Reynolds numbers than the smooth cylinder; for instance, the smooth cylinder may not have fully reached stable super-critical flow.

Like for the mean distribution, the earlier separation point was noticeable when comparing the vortex-lift topos in figure 3.12b. Overall, the spatial energy distributions were similar but the rough configurations were slightly less asymmetric, had their stronger peak and the other side of the smooth's and a bit more energy in the rear. Like the vortex-lift, the peaks near the separation point were at lower angular locations with roughness than the smooth's for the second vortex-lift pair and the energy peaks in the rear was at higher angular locations as shown in

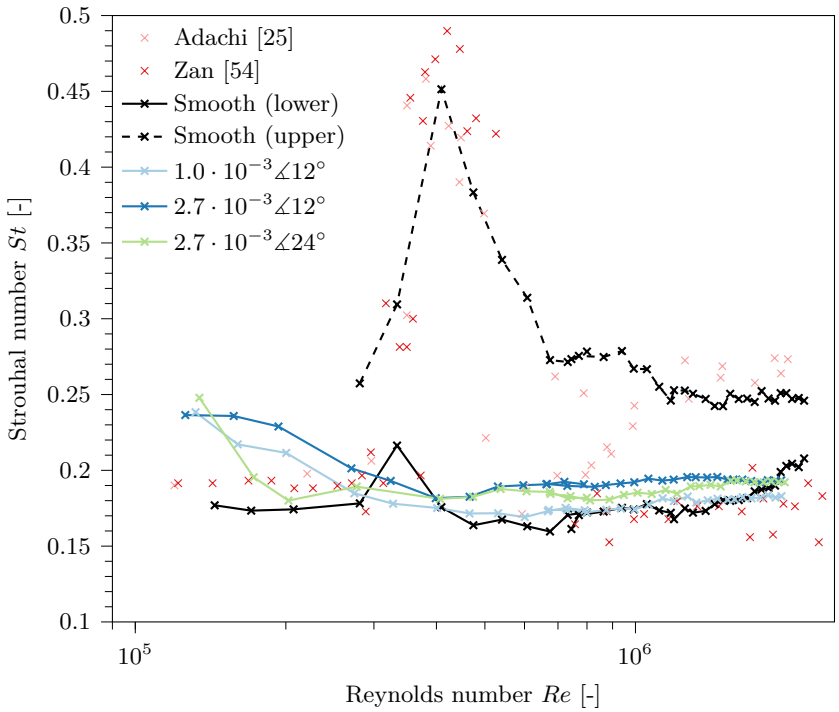

Figure 3.13: *Wake Strouhal numbers using the configurations in table 3.1 and compared with the smooth results of Adachi [25] and Zan [54].*

figure 3.12d. This could indicate that the rear vortex-shedding process is different when adding the ribs. The vortex-drag BOD is compared in figure 3.12c and has the largest visual differences between smooth and rough configurations. When adding the ribs, the peaks near the shedding points becomes less important and the spatial energy becomes more concentrated near the stagnation point and in the cylinder's rear.

3.5 Wake and lift Strouhal number

There are three ways the vortex-shedding frequency and the Strouhal number can be determined with this experimental setup: 1) the wake fluctuations, 2) the unsteady lift and 3) pressure oscillations from a single pressure tap. As the unsteady lift can be noisy, the chronos of the BOD pairs contributing the greatest to the shedding process (vortex-lift and second vortex-lift) are used instead. The frequencies obtained from a pressure tap near $\theta = 90°$ match the frequencies from the vortex-lift BOD pair while the frequencies obtained from a pressure tap near $\theta = 155°$ match the 2nd vortex-lift BOD pair; these results are not shown. Them matching makes sense as most of the spatial energy contributing to it is in this area.

Figure 3.13 shows the Strouhal number calculated using the lateral velocity component from the high speed Cobra probe (D). These results are compared with the results of Adachi [25] on a smooth and rough cylinder (uniform relative roughness of $Rr = 2.54 \cdot 10^{-3}$) using wake measurements. As can be seen, there's not one but two dominant wake shedding frequencies for the present smooth cylinder and therefore twin Strouhal numbers. The upper Strouhal number found was consistent with most of the literature $St \in [0.24, 0.25]$ [8, 21, 25] and the lower value was consistent with the pressure measured Strouhal number of Zan [54] and Shih [17] $St \in [0.2, 0.21]$.

An example PSD of the lateral wake component with a large window is shown in figure 3.14 using the smooth cylinder configuration at three different Reynolds numbers. The two dominant dimensionless shedding frequencies are shown with the upper Strouhal number having more

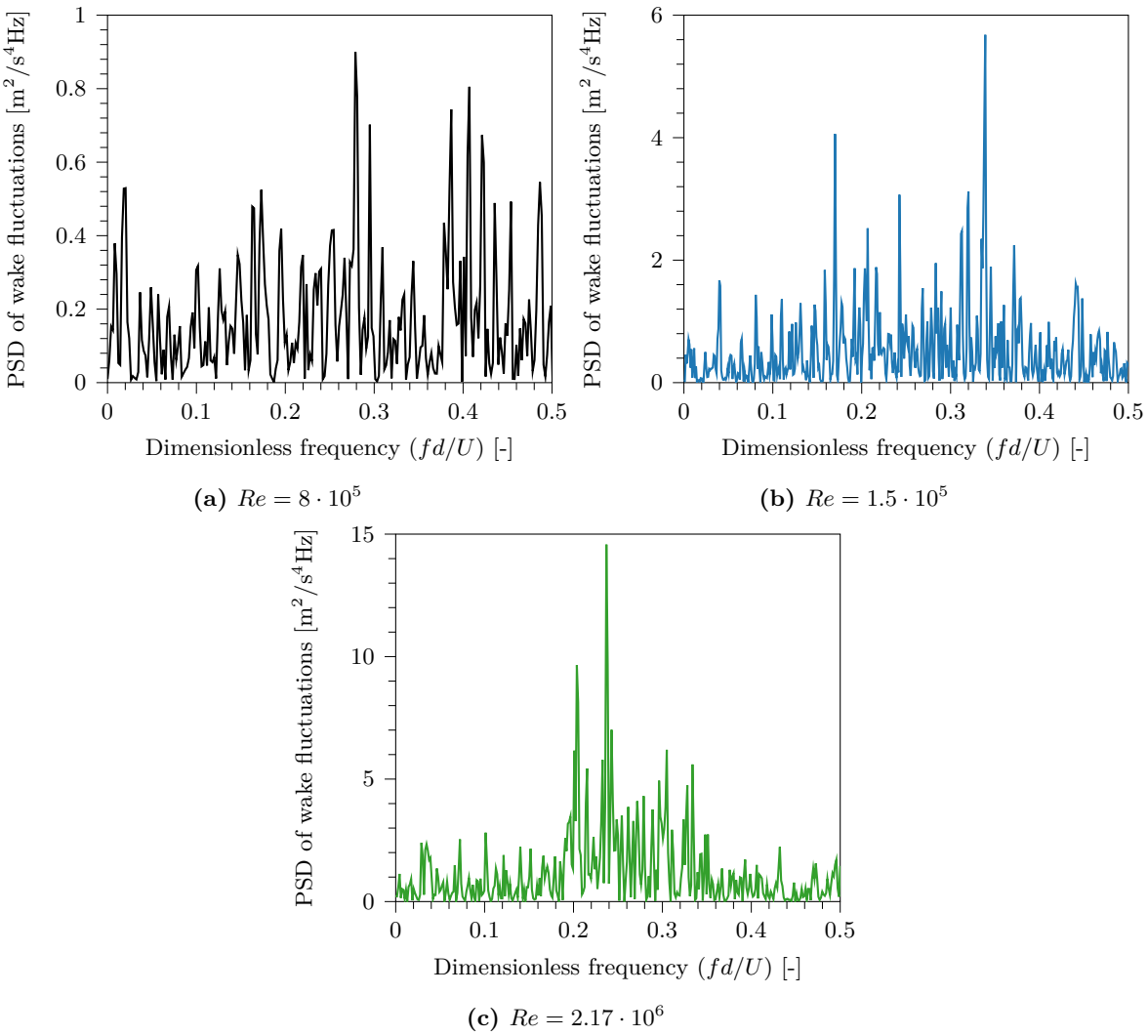

(a) $Re = 8 \cdot 10^5$ **(b)** $Re = 1.5 \cdot 10^5$

(c) $Re = 2.17 \cdot 10^6$

Figure 3.14: *PSD of wake fluctuations using the smooth cylinder at three Reynolds numbers.*

energy than the lower which is consistent among smooth tests. When reducing the window size of the PSDs, it becomes clear that the double frequency phenomena is bi-stable. Depending on the window, the lower frequency can either be dominant, missing or small compared to the upper like in figure 3.14. Similarly, there are windows where the upper frequency is indeterminate. The PSD of the wake fluctuations does differ from the PSD of the chronos in figure 3.15b in one important aspect: In the wake the second Strouhal number is the strongest whereas in the BOD, the first Strouhal number has more energy due to being found in the vortex-lift BOD pair with a higher eigenvalue.

When adding the rib elements, the wake Strouhal number is consistently lower and more consistent as figure 3.13 shows. For all three roughness configurations, the Strouhal number was close to 0.195 at super-critical Reynolds numbers which is close to the lower Strouhal number for the smooth cylinder (approaches 0.21) and the results of Zan [54]; the rough results of Adachi gave higher Strouhal numbers [25]. This Strouhal number was slightly decreased when reducing the degree of surface roughness by either increasing the spacing or decreasing the roughness height. As the upper shedding frequency is unobserved with added roughness, it's possible that the added roughness smooths out the instability that leads to the second vortex-shedding frequency.

The lower Strouhal number was found in the second BOD pair or the vortex-lift pair as shown in figure 3.15b; it was also found in a pressure tap located on the top. Unlike the wake

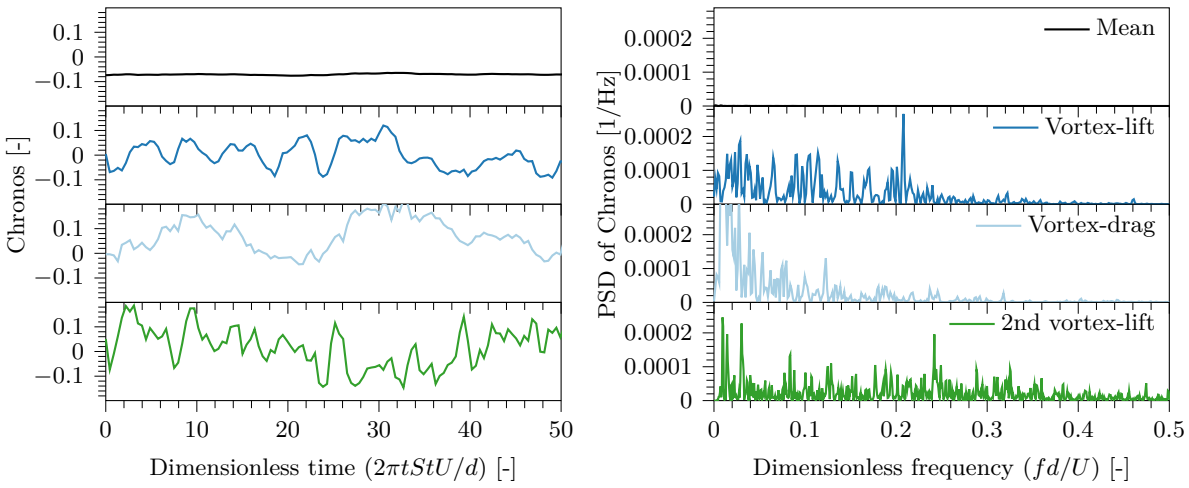

(a) *Evolution of chronos.* **(b)** *PSD.*

Figure 3.15: *Comparison of temporal signal and PSD of chronos for the first four BOD pairs using the smooth cylinder at a Reynolds number of* $2.17 \cdot 10^6$.

fluctuations, this pair was the most energetic of the fluctuating the BOD pairs meaning that the lower Strouhal number had a strong, single PSD peak. In other words, the lower Strouhal number is associated with the vortex-lift whereas the upper is associated to another vortex-shedding process. The PSD contain a lot of low frequency noise, as seen in figure figure 3.15a, which explains why the PSD doesn't have a singular peak.

The classical characteristic vortex-drag frequency (two times the Strouhal number) is not readily observed for any of the temporal distributions[6]. Instead, its temporal distribution is like the third plot of figure 3.15a. It has slowly oscillating components but the temporal energy tends to have the same sign with time. The PSD of the chronos also shows that low frequency components are dominating the temporal energy fluctuations and the unsteady drag caused by this BOD pair might be dominated by flow conditions rather than vortex-shedding.

The fourth BOD pair contains the second Strouhal number as seen in the last plot of figure 3.15b. This pair's temporal variation has a dominant frequency component at a dimensionless frequency near 0.25 and should be due to the secondary separation in the rear of circular cylinders; this frequency peak was also found with a pressure tap located near the rear. When viewed in time domain (figure 3.15a), it can be seen that there's a slow change in sign in addition to the dominant frequency component. This extra vortex-shedding process might explain the lack of a dominant shedding frequency at twice the Strouhal number.

When combining the spatial information on the second and fourth BOD pair, it's clear that the lower Strouhal number is associated with the main unsteady lift process whereas the higher Strouhal number is associated with a combined lift and drag process focused in the rear that has a lower total impact on the total unsteady force. Based on this, a good Strouhal number for vortex-induced vibrations could be close to 0.2 at super-critical Reynolds numbers like it is at sub-critical [55]. The wake Strouhal numbers from the smooth cylinder are directly compared with the Strouhal numbers obtained from the BOD analysis in figure 3.16 for all tested Reynolds numbers and configurations. From it, it can be seen that the lower Strouhal number match with the vortex-lift BOD pair for all Reynolds numbers and the higher with the second vortex-lift.

Similar to the smooth results matching, the Strouhal number from the wake and BOD pairs are more or less identical with roughness. In addition, the vortex-lift and second vortex-lift have the same dominant frequencies with added roughness. This makes it plausible for roughness

[6]In small-scale tests for a smooth cylinder it was found in the BOD pair with a similar topos as the third pair (vortex-drag).

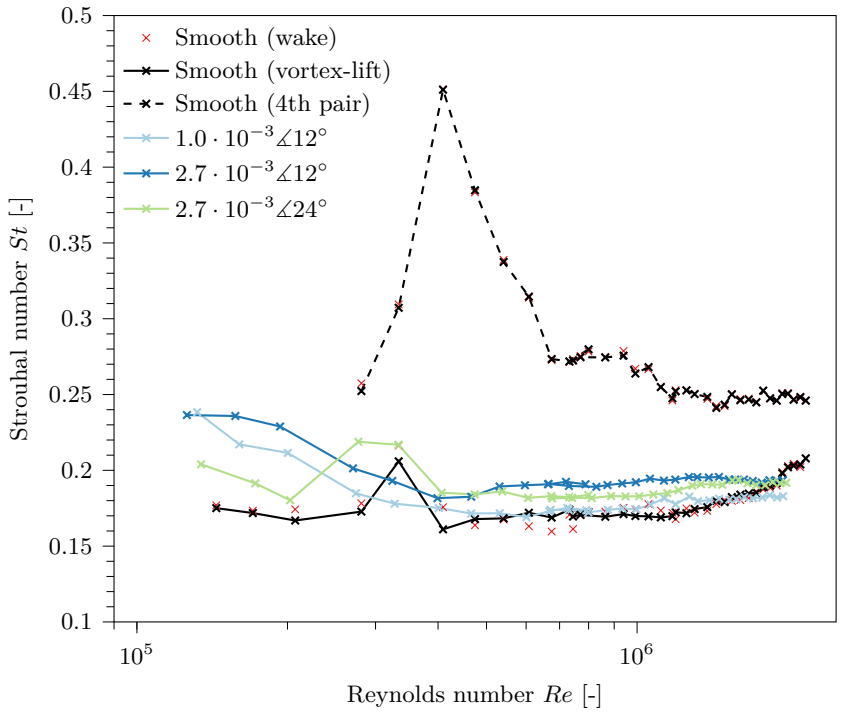

Figure 3.16: *Chronos Strouhal numbers using the configurations in table 3.1 and compared with smooth wake results from figure 3.13.*

to reduce the instability that caused the secondary vortex-shedding process in the rear, and thereby the wake, to have a higher dominant frequency.

3.6 Summary of large-scale results

This chapter has presented a super-critical Reynolds number experiment on smooth and rough circular cylinders and the main results are summarized in table 3.2. The mean drag on the smooth cylinder was found to be similar to the literature (though with a blockage related scaling) and the effect of roughness was as expected. For most configurations and Reynolds numbers, the mean lift was close to zero but not for the smooth cylinder when approaching super-critical values. Here, the cylinder experienced a mean lift due to a separation bubble or a surface deformation. Also like in the literature, the SD drag was found to be much smaller than the SD lift and follow a similar trend as the mean drag. What might be more unexpected, is the fact that added surface ribs decreased the SD lift and drag at these scales and Reynolds numbers but changing rib spacing and size did not.

As vortex-induced vibration is a 3D phenomenon, the correlation and coherence along the height is important. For the rough cylinders, the correlation was found to be much smaller than the correlation found in literature using unsteady pressure but the coherence was found to be much closer to it. Overall, the coherence should be a better measure for vortex-induced vibrations as it focuses on the frequency bandwidth containing the vortex-shedding process instead of the entire time signal. While not measured directly, the correlation and coherence for the smooth cylinder had a similar pattern at critical Reynolds numbers as the rough cylinders. If following the same pattern at super-critical Reynolds numbers, the correlation and coherence coefficients would have the same shape as the rough cylinders' but have smaller values.

In addition to the global forces, the pressure distributions were investigated using its statistics and a decomposition (BOD). The first BOD pair, most energetic, was identified as being the mean pressure distribution and was the dominating relative force if the mean value was nonzero.

Table 3.2: *Summary of results at actual or simulated super-critical Reynolds numbers.*

	Smooth	$1.00 \cdot 10^{-3} \measuredangle 12°$	$2.70 \cdot 10^{-3} \measuredangle 12°$	$2.70 \cdot 10^{-3} \measuredangle 24°$
Mean C_d	0.55	0.615	0.732	0.651
SD C_l	0.127	0.046	0.049	0.046
St_1	0.2	0.17	0.19	0.18
St_2	0.25	N/A	N/A	N/A
$C_{p,\ min}$	-2.5	-1.27	-1.15	-1.43
Location min	80°	72°	66°	66°
SD $C_{p,\ max}$	0.3	0.095	0.078	0.097
Location max	110°	84°	78°	90°
Φ_2	at St_1	at St_1	at St_1	at St_1
$\Psi_{2,\ max}$	110°	84°	78°	90°
Φ_4	at St_2	N/A	N/A	N/A
$\Psi_{4,\ max}$	140°	156°	156°	162°

The second BOD pair (vortex-lift) was anti-symmetric and contained most of the peak SD values but had low spatial energy outside a narrow region. This pair was recognized as the dominating unsteady lift pair and had a temporal oscillation at one of the Strouhal numbers for the smooth cylinder.

Two Strouhal numbers were identified for the smooth cylinder and correspond to the two conflicting literature results. The lower value (closer to 0.2) was found in the vortex-lift BOD pair whereas the higher value (close to 0.25) was due to a different shedding or reattachment process focused in the rear of the cylinder. While the vortex-lift was a stronger BOD pair than the second vortex-lift, it's the latter which was dominating in the wake. The vortex-drag BOD pair was found to not contain any noticeable higher frequency terms (mostly low frequency components) and the mean BOD pair had a flat temporal energy distribution.

With the unsteady pressure distribution characterized for a smooth cylinder at super-critical Reynolds numbers, it's possible to test and validate methods of recreating it in smaller wind tunnels. This is the focus of the next chapter where ribs and turbulence are used to recreate super-critical Reynolds numbers at lower ones.

Chapter

4 Simulation of super-critical Reynolds numbers in a smaller wind tunnel

Chapter summary

This chapter presents the methods that were found to be the best at simulating super-critical flow around a smooth circular cylinder at smaller scales (lower Reynolds numbers). The experiments were done in smaller atmospheric wind tunnel than in the previous chapter but without the boundary layer generator. The effect of roughness ribs was found to be different at this scale when compared with the large-scale results. The effect of turbulence intensity on the unsteady forces was found to be low on SD forces but great on mean drag and Strouhal number with the tested intensities. Similarly, the roughness height was found to have a significant effect on the mean drag and Strouhal number but not on the SD forces. Increasing the rib spacing, on the other hand, greatly affected the SD forces, mean drag, Strouhal number and the unsteady pressure distributions. The optimal surface condition found (all things considered) will later be used to simulate super-critical flow for a 3D experiment.

4.1 Background

Having determined the correct unsteady pressure distributions and force characteristics (strength and frequency) for a smooth circular cylinder at super-critical Reynolds numbers, the next steps of the investigation can be discussed: How to recreate these characteristics at smaller scales. As mentioned in section 2.1.3, there have been attempts at reducing the Reynolds number to measurements of the diameter and relative roughness height of added uniform surface roughness. This can prematurely trigger super-critical flow [10, 21], but does not produce satisfactory unsteady forces [13, 62]. A better method might be the use of roughness ribs which, according to Ribeiro, should be the best at simulating the super-critical flow around a smooth cylinder [28, 37, 48]. The main problem with this research, is that there's no guideline for designing the ribs other than "use the smallest ribs able to simulate super-critical Reynolds numbers as larger ones can distort the surface flow" [28, 37].

This leads to the goal of the current chapter. What's the best strategy for simulating super-critical Reynolds numbers for a smooth cylinder at lower speeds and in a smaller wind tunnel? As rib elements seem like the best roughness type for inducing super-critical Reynolds numbers, this roughness type is investigated in addition to the turbulence intensity. The goal is to find the best roughness dimensions for simulating super-critical Reynolds numbers at smaller scales and to investigate the effect of turbulence intensity and spacing on it.

4.2 Experimental methodology

4.2.1 Wind tunnel description

The small-scale experiments aimed at simulating super-critical Reynolds numbers were performed in CSTB's atmospheric wind tunnel, i.e. the NSA wind tunnel. The aerodynamic test section, 2x4 m^2, can reach a maximum wind speed of 30 m/s without the uniform turbulence generating grids and 19 m/s with it. The grid used to generate turbulence is shown in figure 4.1a and consists of semi-circular lengths of PVC tubing with the circular side facing the inflow and the flat side downstream. The grid components have a width of 0.05 m and the distance between two parallel lengths are 0.2 m when measured from the center of each. This grid was mounted 3.1 m upstream from the test model.

The wind speed was calibrated at the measurement locations using a fast response Pitot tube, a pre-calibrated average Pitot tube and three Cobra probes. With the Cobra probes, the turbulence intensity in the three principal directions (u, v and w) and the vertical velocity gradient was characterized. When not using the turbulence generator (uniform flow), the turbulence was somewhat high at low wind speeds but quickly converged to 1% in the u component and 0.8% for the v and w components of velocity. When adding the turbulence generating grid, the turbulence intensity was determined to be 6% for the u component of velocity and 3% in the other two directions. The vertical gradient was found to be negligible with both configurations.

4.2.2 The test model and setup

The test model was a carbon fiber tube with a diameter of 0.055 m. Two sketches of the setup and a photo of the mounted test model is shown in figure 4.1. As can be seen from the photo in figure 4.1a, the test model was a circular carbon fiber tube that extended the height of the wind tunnel with a reference Pitot tube beside it and with Cobra probes behind it. To make sensor and model installation easier, the model was separated into three sections which were mounted flush. One of the sections was shorter than the rest (only 0.1 m long) and had 30 pressure taps drilled uniformly (12° spacing) at mid height. This part was placed in the middle of the model (marked in blue in figure 4.1c).

The rest of the model consisted of two carbon fiber tubes, each 0.95 m long, where the bottom contained the 1.5 m long vinyl tubes connecting the pressure taps to the pressure scanner. As the size of the model was small compared to the wind tunnel, the blockage ratio was negligible. When mounted in place, the circular cylinder had a first damped natural frequency of 25 Hz and a damping ratio of 21.4% which made the vibration amplitude negligible. In addition, the small size made the blockage negligible.

Three Cobra probes were mounted in the wake. The positions of their tips relative to the cylinder were 2 diameters behind it and 0.25 diameters to the side as shown in 4.1b. This corresponds to 0.11 m and 0.014 m measured from the rear of the cylinder and center respectively. The vertical locations of the Cobra probes in relation to the pressure taps are shown in 4.1c and The upper probe's (A) location was 1 diameter below the pressure tap arrangement, the next (B) 2 diameters below and the last (C) 3.5 diameters below the pressure taps. These locations were chosen to minimize any adverse effect between the Cobra probes and the pressure taps. When calibrating, the Cobra probes' tips were moved to where the cylinder's center would be when mounted and raised up by 2 diameters.

The last part of the experimental setup, was a fast-response Pitot tube used to measure the reference wind speed at the height of the pressure taps. This Pitot tube was placed 5 diameters to the side of the cylinder (opposite side of the Cobra probes, see figures 4.1a and 4.1b) with its tip aligned with the cylinder's center.

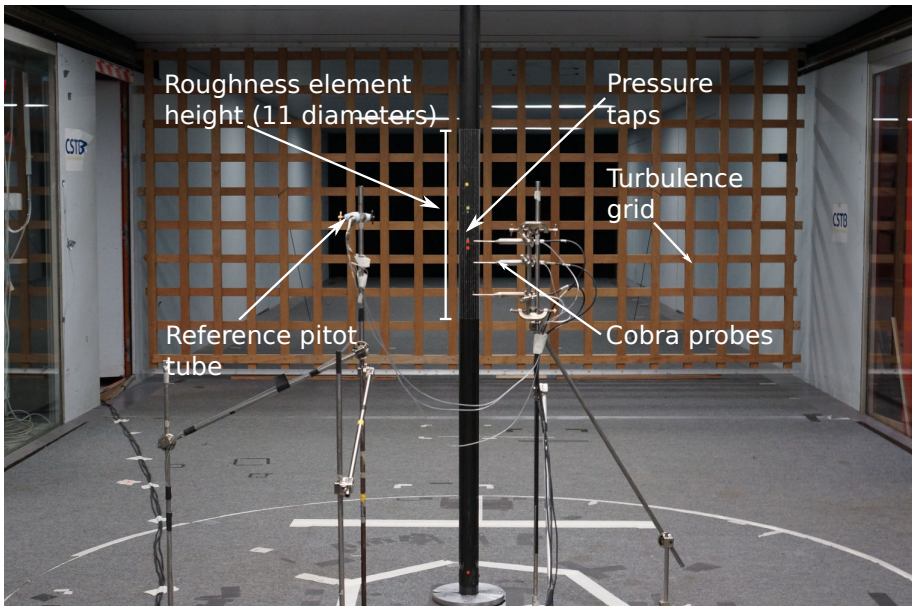

(a) *Picture of experimental setup for with attached ribs, turbulence generating grid and annotated explanations.*

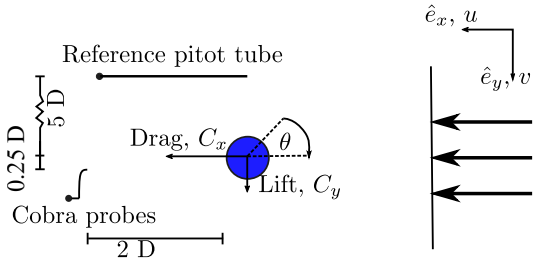

(b) *Sketch from the top with coordinate system.*

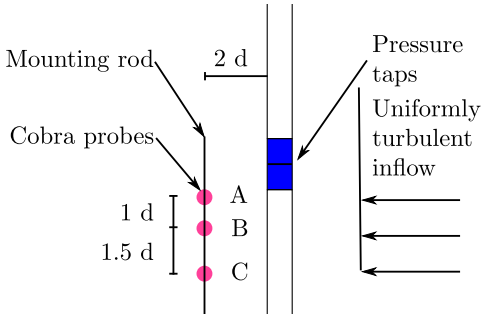

(c) *Side sketch focused on location of cobra probes.*

Figure 4.1: *Figures showing experimental setup, relative locations and coordinate system.*

4.2.3 Roughness elements

To simulate higher Reynolds numbers, the cylinders were fitted with surface roughness in the form of ribs with rectangular cross-section (cut using a circular saw). These ribs were placed at regular intervals (either $\theta_5 = 12$ or $\theta_6 = 24°$ spacing between them) to make them symmetric around the cylinder and their locations relative to the pressure taps is sketched in figure 4.2. When using the smaller rib spacing, the angular distance between the first rib and the stagnation point (pressure tap 2), is 6° and it's the same at the rear. When using the larger spacing, the ribs closest to $\theta = 0$ and 180° were removed and then every other rib (green rectangles in figure 4.2) leaving only 14 ribs (yellow circles). This was done to preserve the rib symmetry around the 0–180° and the 90–270° lines. The photo in figure 4.3 shows a cylinder configuration mounted with 30 ribs and how they're placed in relation to the pressure taps.

Four differently sized roughness ribs, with lengths of 0.6 m ($\approx 11d$), were tested. The smallest had a height of 0.2 mm (relative height of $Rr = 3.64 \cdot 10^{-3}$), the second smallest 0.4 mm ($Rr = 7.27 \cdot 10^{-3}$), the second largest 0.5 mm ($Rr = 9.09 \cdot 10^{-3}$) and the largest had a height of 1.0 mm ($Rr = 1.82 \cdot 10^{-2}$). The three largest ribs had a width of 0.8 mm (relative width of $1.45 \cdot 10^{-2}$ when compared with the diameter) whereas the smaller ones were 0.7 mm ($1.27 \cdot 10^{-2}$). Of these roughness sizes, only the results from the two best sizes are presented in this chapter ($Rr = 9.09 \cdot 10^{-3}$ and $1.82 \cdot 10^{-2}$); results using all roughness elements are presented in the appendix. To differentiate the rib configurations, they are presented in the form $Rr\measuredangle xx°(U/T)$

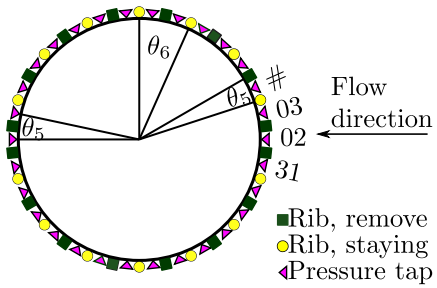

Figure 4.2: *Distribution of ribs and pressure taps on the cylinder's surface.*

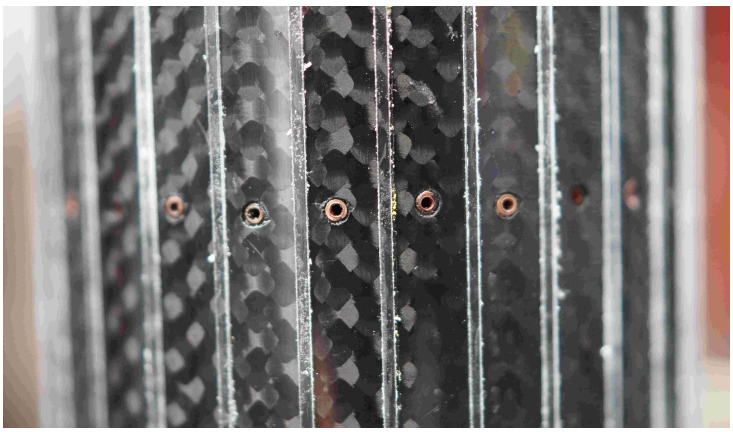

Figure 4.3: *Focused picture of mounted ribs and their relative location to the pressure taps.*

where Rr is the relative height of the ribs and xx is the spacing between them and U/T marks uniform or turbulent flow.

4.2.4 Instrumentations and measurements

Like for the large-scale tests, the measurements were separated into two separate recording systems. A difference was that both systems recorded the reference wind speeds as shown in figure 4.4. Two other differences are the recording length and acquisition frequency: Both the wind and pressure measurement systems had a recording frequency of 512 Hz and recording length of 60 s. This combination produced ergodic time series based on the first 10 BOD pairs (see appendix B.1).

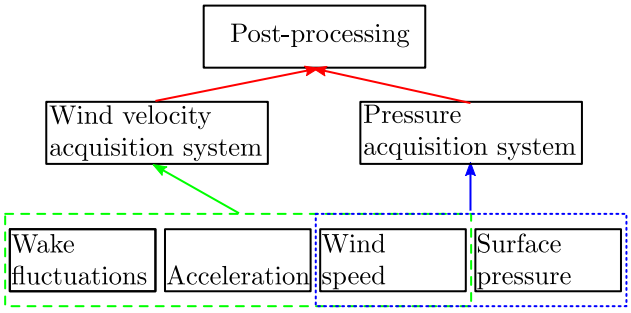

Figure 4.4: *Diagram of wind and pressure acquisition chains.*

Wind velocity acquisition system

The small-scale wind tunnel tests used three four-hole Cobra Probes to both determine the flow field and the lateral wake characteristics behind the cylinder. This is similar to what was done in the large-scale tests but there's a difference in the sensors: For the small-scale tests, all three sensors had a maximum rated speed of 45 m/s which was above the maximum wind speed of the tunnel. While the sensors worked at all speeds, they had the same limitation as in the large wind tunnel: Inflow angles above $\approx 15^\circ$ caused individual, corrupt samples. Like previously, the wake data was analyzed spectrally using the PSD calculated using a Welch's method and statistically using the coherence and correlation defined in section 2.1.4.

Also like before, reference wind speed from the Pitot tube and acceleration from an internally mounted accelerometer was recorded in the wind velocity acquisition system. As the wind velocity acquisition system was limited to signals of strength $\pm$ 5 V, the highest wind speeds in the wind tunnel could not be recording using the Pitot tube.

Pressure acquisition system

As the pressure system was not limited to $\pm$ 5 V, the reference wind speed was measured in both acquisition system as shown in figure 4.4. The pressure taps were connected to a 32 channel pressure scanner using 1.5 m vinyl tubing and tubing effects were corrected for using the same proprietary method as in chapter 3. This pressure scanner was similar to the ones used in the large wind tunnel but only rated for pressures up to 2500 Pa. Figure 4.2 shows the location and numbering scheme of the pressure taps in addition to the location of added roughness elements. The pressure tap numbering starts at 2 as sensor 1 was reserved for the Pitot tube measuring the wind speed.

4.2.5 Tested wind speeds

The wind tunnel experiments were performed at different speeds depending on the turbulence intensity. When using the uniform flow configuration (no grid), the wind tunnel tests were performed at speeds between 5 and 30 m/s. In terms of Reynolds numbers, this corresponds to values between $1.83 \cdot 10^4$ and $1.10 \cdot 10^5$. The turbulent experiments were only performed for wind speeds up to 19 m/s as the turbulence grid started to vibrate noticeably at higher speeds; this speed corresponds to a Reynolds number of $6.97 \cdot 10^4$. For all tests, the speed was increased by increments of 1 m/s or Reynolds number increments of $3.67 \cdot 10^3$.

4.3 Aerodynamic forces

4.3.1 Strouhal number

Two examples of power spectral densities at super-critical Reynolds numbers with added roughness ribs are shown in figure 4.5. The PSD of the lateral wake component using a Cobra probe is shown in figure 4.5a and can immediately be seen to be different from the wake PSD from the smooth cylinder: Like with roughness at large scales, there's only one strong spectral component in the lateral PSD with added roughness at super-critical Reynolds numbers. This spectral peak is similar to the one obtained from the vortex-lift BOD pair in figure 4.5b and should be the lower Strouhal number. The second vortex-lift has a peak at the same location but is more spread out with extra, small peaks near dimensionless frequencies of 0.39 and 0.43; these should be close to the oscillation frequency of the drag. Both the vortex-drag and mean BOD pairs' spectral densities were dominated by low noise and mean value terms making the spectrum low valued at most frequencies of interest.

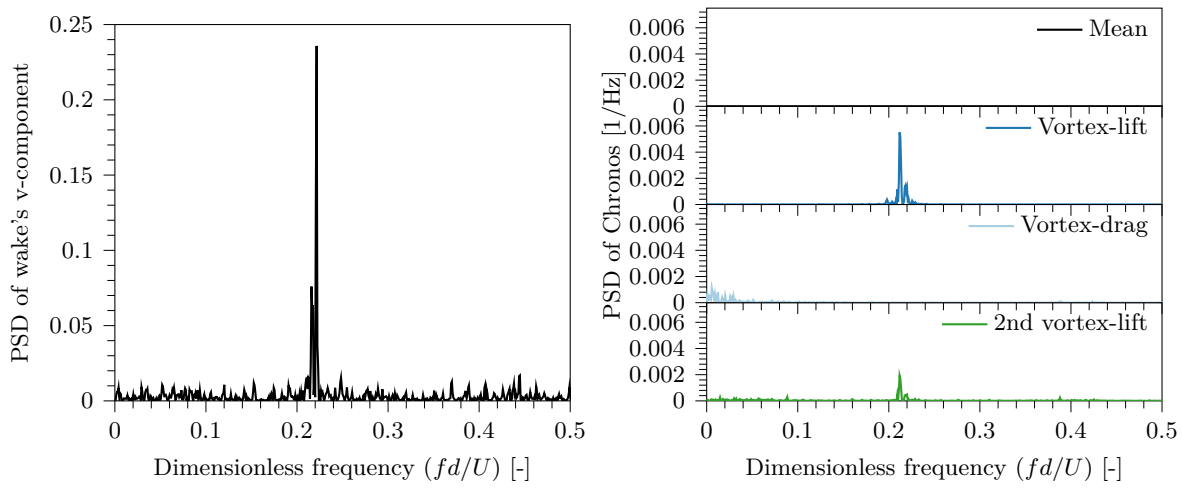

(a) *Lateral wake component*

(b) *First four chronos*

Figure 4.5: *Power spectral density of lateral wake component and chronos using same rib roughness configuration (*$9.09 \cdot 10^{-3} \measuredangle 12°$ *(U)) and Reynolds number (*$6.22 \cdot 10^4$*).*

The similarities in shedding frequency and vortex-shedding process in the wake and unsteady lift can be further seen in figure 4.6. For most configurations and speeds, the wake Strouhal number was slightly larger than the vortex-lift BOD pair's. This difference was shown to be significant for all tested configurations using Bayesian inference (explained in section A.4) but was negligible and could be due to rounding errors. Similarly, it can be shown that there's little difference between the Strouhal number obtained from a single pressure tap and the BOD pairs (see table B.4).

Like for the smooth, large cylinder results, there's a critical Reynolds number with increased Strouhal numbers followed by a super-critical Reynolds number region with lower and more constant Strouhal numbers. What's different at small and large Reynolds numbers, is that the Strouhal numbers at super-critical Reynolds numbers are greater than the lower smooth Strouhal number with roughness at small-scale. This is contrary to the results with ribs at actual large Reynolds numbers in section 3.5 where the added roughness decreased the Strouhal number compared to the smooth's. It's therefore possible that the effect of added ribs is different for small and large-scale experiments and that this is related to the actual Reynolds number.

In the large wind tunnel, the Strouhal number was similar with a reduction in the degree of surface roughness (spacing and height) but the behavior was different at small scale (results shown in appendix B.2). From figure 4.6 and the inference results in table B.6, it can be concluded that increased roughness height significantly decreases the Strouhal number at small-scale on average. This is consistent with the results of Adachi [25] and Achenbach and Heinecke [21] on the effect of uniform roughness on the Strouhal number.

Similarly, an increase in turbulence can be shown to decrease the Strouhal number and promote earlier transitions to super-critical Reynolds numbers. The latter is consistent with the literature but the former is inconsistent. Some previous experiments gave a higher Strouhal number with increased turbulence but noted that its effect was dependent on the turbulence length scale (not estimated here) [53, 54, 69]. Similarly, the present results go against those of Ribeiro [37] who showed that increasing the turbulence intensity does not significantly affect the Strouhal number when using ribs possibly due to the turbulent flow interacted differently with the added ribs.

Increasing the spacing between ribs reduced the Strouhal number. This is not consistent with the literature as reducing the spacing should reduce the overall surface roughness which should increase the Strouhal number instead of decreasing it [21, 25]. While not consistent with

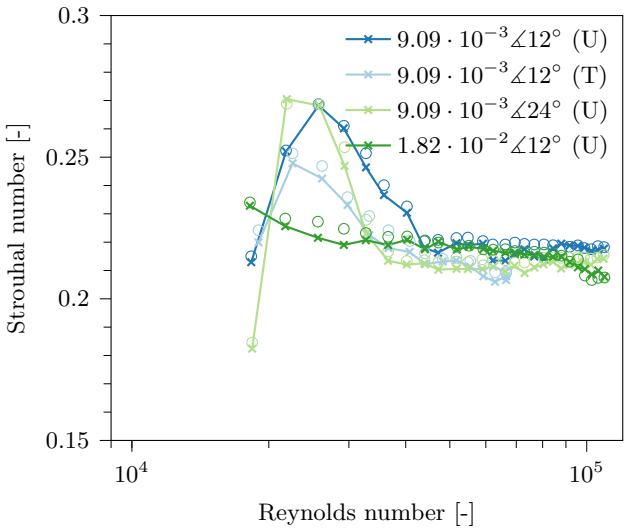

Figure 4.6: *Comparison of Strouhal numbers from wake (∘ marks) and chronos (lines and ×). Turbulent results are marked with (T) and uniform flow with (U).*

the literature, it is consistent with the large Reynolds number tests where a negligible decrease in the Strouhal number was observed with the larger spacing. It's likely that the increased rib spacing introduced a phenomena similar to that observed by Nigim and Batill [65] and Perry, Schofield and Joubert [66]. They found that the ratio of rib spacing to diameter determines the surface flow conditions and the shedding behavior. If the ratio is small, less than 3 for circular ribs, the surface protrusions acts as cavities trapping vortices. With higher ratios, the surface vortices are not trapped and instead interact with the flow over the cylinder giving a different unsteady shedding frequency.

4.3.2 Unsteady lift and drag coefficients

The unsteady drag and lift as a function of the Reynolds number are shown in figures 4.7 and 4.8 respectively. Most configurations have a small, non-zero mean lift (see figure 4.8a) but like for the smooth cylinder at super-critical Reynolds numbers, there can be a significant mean lift for low rib sizes due to either a separation bubble of cylinder deformation (cf. figure B.10a). The general behaviors of the mean drag, SD drag and SD lift are similar to that seen for the smooth cylinder at large Reynolds numbers in that there's a decrease and subsequent increase in the force coefficients at critical Reynolds numbers and a more stable coefficient value at super-critical Reynolds numbers. The exception is the SD lift which tend to have increased values at low simulated super-critical Reynolds numbers and decreased but stables values as the Reynolds number further increases. It's possible that this can be observed for the smooth cylinder if the Reynolds number was further increased but this was not tested.

When comparing the mean drag from the small-scale and large-scale tests, it's clear that increasing the rib height has the overall effect of increasing the drag. This is not the case for SD drag when comparing all the configurations at simulated super-critical Reynolds numbers and the SD drag tends to be similar when changing the rib height (cf. section B.3 and table B.7). The exception is when the height doubles from $9.09 \cdot 10^{-3}$ to $1.82 \cdot 10^{-2}$ where the SD drag reduces. Similarly, the SD lift tends to be similar when increasing the rib height (cf. table B.8) except when increasing from $9.09 \cdot 10^{-3}$ to $1.82 \cdot 10^{-2}$ which again decreases it. These small-scale results seem similar to Ribeiro's and surface ribs should be good at mimicking the super-critical force coefficients of a smooth, circular cylinder using lower Reynolds numbers [28, 37, 48].

The effect of increasing the rib spacing is quite different for the small and large-scale tests.

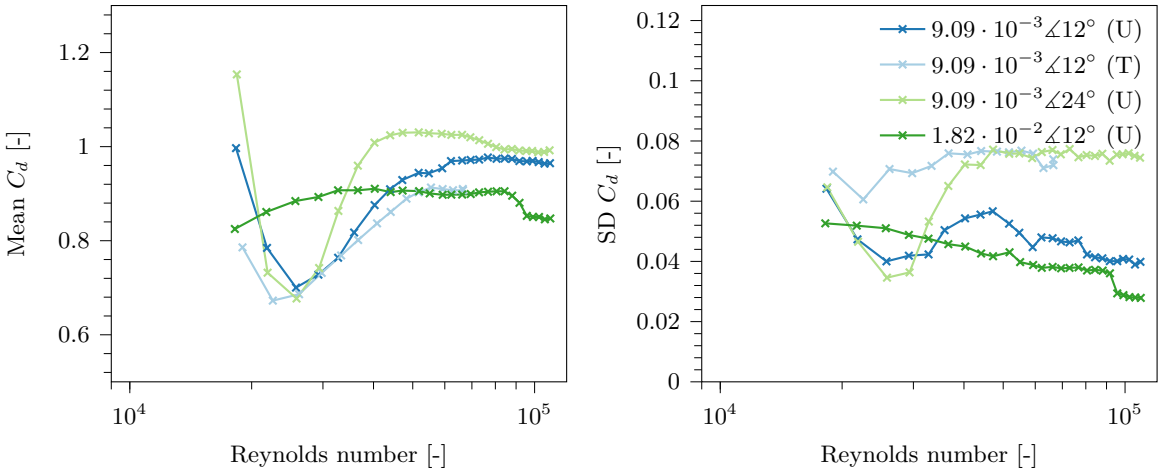

(a) *Mean drag.* **(b)** *SD drag.*

Figure 4.7: *Mean and SD drag coefficient as a function of Reynolds number. Turbulent results are marked with (T) and uniform flow with (U).*

At small-scales, the mean drag is increased when increasing the rib spacing. This doesn't make sense intuitively as it's a decrease in the degree of surface roughness which should give lower drag. The effect is opposite in the large Reynolds number tests and an increase in rib spacing decreases the mean drag. Like the mean drag results, there's a difference in the SD force coefficients at large and small-scales. At large scales and Reynolds numbers, the SD force coefficients are fairly unaffected by the rib spacing tested but at small scales they differ significantly for all configurations (cf. figure 4.8b table B.7 and B.8]. When increasing the spacing, the SD drag coefficient is almost doubled while the SD lift coefficient can be almost tripled. This should be related to the Strouhal number decreasing with increased spacing and how the surface vortices between the ribs interact with the flow over the cylinder. Based on this, the 12° rib spacing better recreates the unsteady force coefficients.

The added roughness strips affect the unsteady forces differently at small and large scales. At large-scale and high Reynolds numbers the SD force coefficients are low and changing the spacing has little effect whereas changing the spacing has a large effect at small scales and the SD force coefficients are higher with all roughness sizes. There are two possible explanations for the behavior difference at large and small-scale: 1) The relative narrower ribs for large-scale tests gives different surface vortex entrapment mechanism than at small-scale [65, 66] or 2) the higher Reynolds number at large-scale makes surface ribs have a different effect. While both of them could affect the aerodynamics simultaneously, it's likely that the larger effect comes from the higher Reynolds numbers.

The turbulence intensity has a different effect on the unsteady forces than the rib dimensions. From the studies Cheung and Melbourne [30] and Blackburn and Melbourne [53], the mean drag coefficient should be lower with increased turbulence intensity at sub-critical Reynolds numbers and SD drag and lift coefficients lower. The variation at simulated super-critical Reynolds numbers is more uncertain with turbulence (due to wind tunnel requirements), but Cheung and Melbourne and Blackburn and Melbourne's results indicate the coefficients can be higher with increased turbulence at critical Reynolds numbers and lower at super-critical [30, 53]. These conjectures have been speculative as their turbulent results don't reach super-critical Reynolds numbers with the exception for some results at 18% turbulence intensity.

The unsteady force results in figures 4.7 and 4.8 show some of the things mentioned by Cheung and Melbourne and Blackburn and Melbourne but is at the same time different. When increasing the turbulence intensity from 1 to 6%, the mean drag was indeed lower at simulated super-critical Reynolds number but was also lower at critical Reynolds numbers instead of higher.

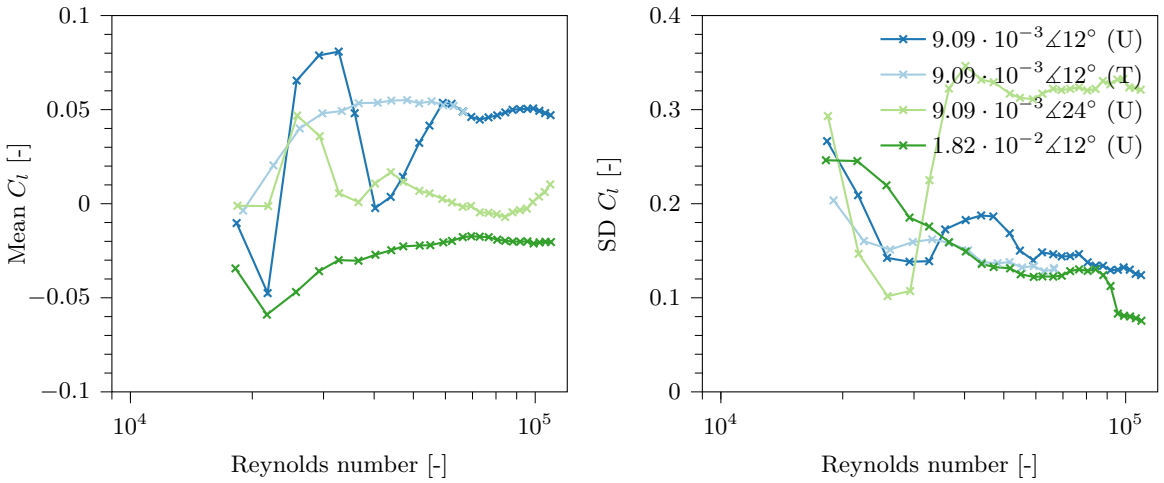

(a) *Mean lift.* **(b)** *SD lift.*

Figure 4.8: *Mean and SD lift coefficients as a function of Reynolds number. Turbulent results are marked with (T) and uniform flow with (U).*

Table 4.1: *Reynolds numbers and roughness configurations from small-scale 2D tests identified as being at simulated super-critical Reynolds numbers.*

Configuration	Speed [m/s]	Reynolds number [-]
$9.09 \cdot 10^{-3} \measuredangle 12°$ (U)	17.0	62 200
$9.09 \cdot 10^{-3} \measuredangle 12°$ (T)	15.1	55 500
$9.09 \cdot 10^{-3} \measuredangle 24°$ (U)	14.9	54 800
$1.82 \cdot 10^{-2} \measuredangle 12°$ (U)	11.0	40 300

This reduction in mean drag is undeniable for all rib configurations (as per the inference in table B.7) as is the increase in SD drag which for the smaller spacing increases towards the values seen with the larger spacing; this goes against the previously mentioned literature. The SD lift changes differently from the SD drag and can be shown to be slightly (but significantly) lower when using the higher turbulence intensity. This is supported by several studies where turbulence was found to interfere with the vortex-lift [30, 37, 67–69].

There's one similarity between the present results and the literature on turbulence and surface roughness: The added turbulence caused the flow over the cylinder to transition to super-critical at lower Reynolds numbers similar to how the increased surface roughness caused an earlier transition. Table 4.1 shows when the configurations discussed here transitioned to well-developed super-critical Reynolds number and corresponds to when the mean drag in figure 4.7a plateaus. A fuller discussion of when super-critical Reynolds number flow occurs and its characteristics are given in section 2.1.1.

4.3.3 Correlation and coherence

It can immediately be seen that the correlation and coherence with ribs in these small-scale tests (figure 4.9) are different from the large scale (figure 3.7). Still, the correlation was smaller than that given by Novak and Tanaka [43] and has a different evolution with distance (here the correlation starts flattening out or increasing at distances of 1.5 d). The second major difference between the small and large scale tests with ribs is that the correlation and coherence drop slower with distance. These points should be an indication of a vortex-shedding process and vortex-cells that are more similar along the height both over a narrow band of frequencies (coherence) and over all frequencies (correlation).

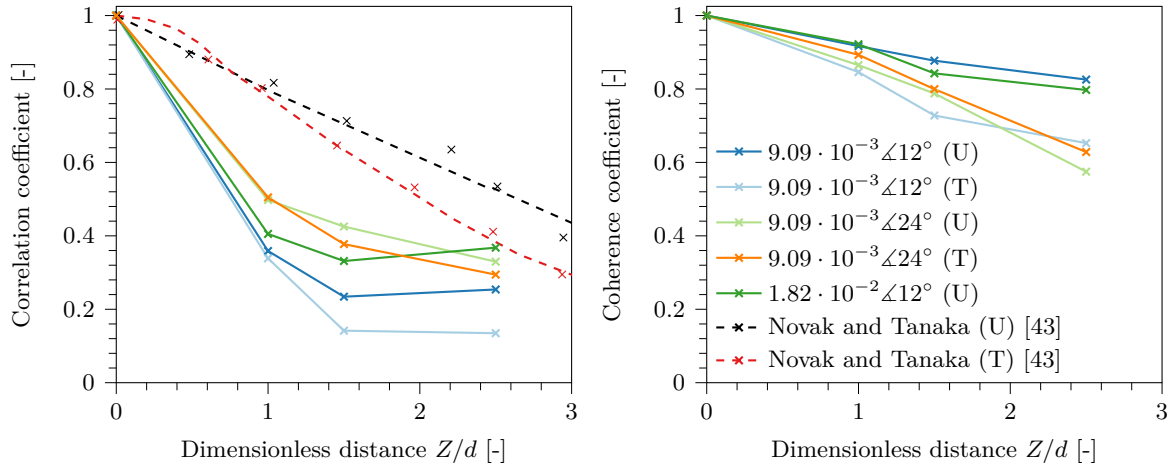

(a) *Correlation.* **(b)** *Coherence.*

Figure 4.9: *Comparison of correlation and coherence at the simulated super-critical Reynolds number configurations given in table 4.1.*

Taller ribs gave higher correlation and coherence on average as shown in figure 4.9 (with the exception of the coherence for the $1.82 \cdot 10^{-2}$ configuration). For most configurations with low spacing, the effect of turbulence was also predictable and it reduced both statistics. The more surprising increase in correlation is when increasing the rib spacing. This might be due to the large spacing giving a more correlated noise at the price of a less coherent vortex-shedding process as seen in figure 4.9. Another surprise with the larger spacing was that increasing the turbulence reduced the correlation and increased the coherence. This suggests that there's a qualitative difference in how the turbulence and flow interacts with cylinder when using 24° spacing instead of 12°.

There are good possible reasons for why the correlation was low and coherence high. The correlation is measured in time domain (over all frequencies) and there are a lot of possible noise sources that can make the signal less similar across distances. The coherence, on the other hand, is measured in frequency domain near the vortex-shedding frequency with a small bandwidth. Due to vortex-cells, it might be easier for it to have a high value across distances. So while there might be noise that makes the flow less correlated along the height, the vortex-shedding process (which the coherence measures) can be more "correlated" than the total flow.

4.4 Simulated super-critical unsteady pressure distributions

4.4.1 Topos and eigenvalue changes with Reynolds number

The mean and SD pressure distributions (figure 4.10a) was fairly consistent with the Reynolds number for the rough cylinder like the smooth (figure 3.10a). The exception to this is at the lowest Reynolds numbers where the minimum pressure coefficient was much lower which is consistent with Achenbach [19] results at critical Reynolds numbers. The same can be seen for the SD pressure distribution in figure 4.10b. In addition to being more consistent, the rough cylinder's pressure distributions are different from the smooth's in the pressure coefficients distribution and values. With the rough cylinder, the separation point and point of minimum pressure coefficient was earlier than for the smooth and the minimum pressure coefficient and rear pressure coefficients were larger; a comparison of this can either be based on the mean pressure coefficient or the topos shown in figure 4.11a.

The changes with simulated Reynolds numbers are smaller for the mean and vortex-lift distributions in figures 4.11a and 4.11b respectively. For these two distributions at super-critical

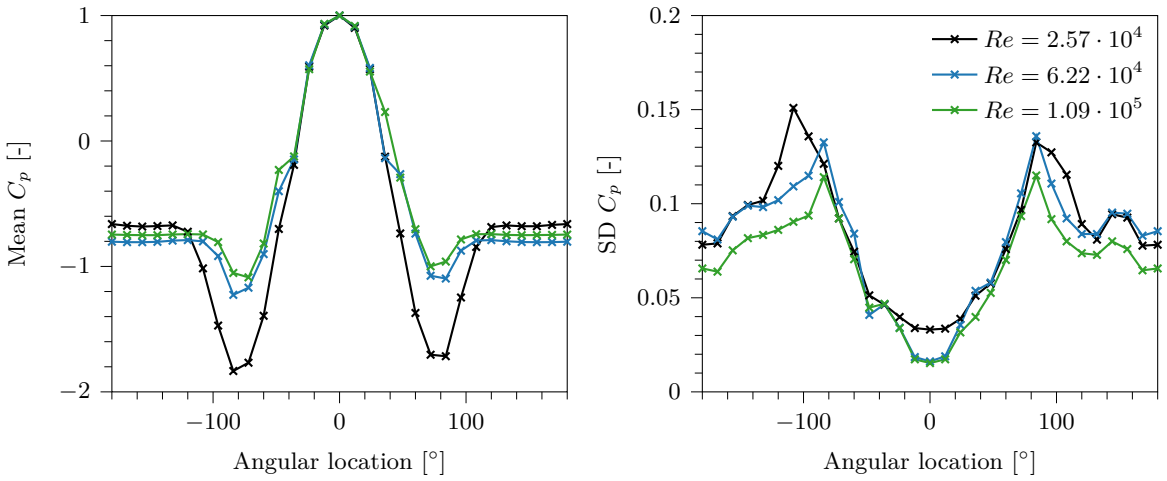

(a) *Mean C_p distribution.* **(b)** *SD C_p distribution.*

Figure 4.10: *Comparison and evolution of mean and SD pressure distibution with Reynolds number for the $9.09 \cdot 10^{-3} \measuredangle 12°$ cylinder configuration.*

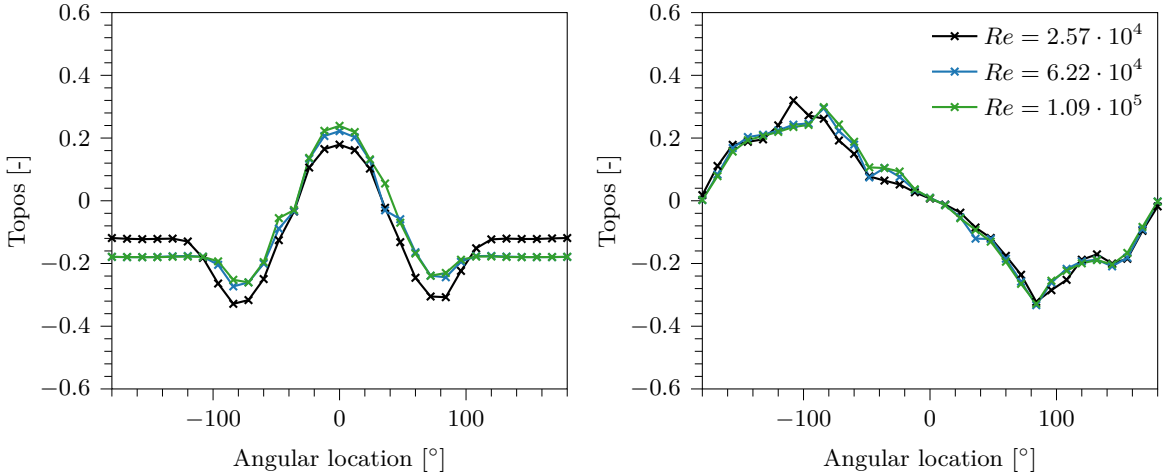

(a) *Comparison of the 1st topos (mean).* **(b)** *Comparison of the 2nd topos (vortex-lift).*

Figure 4.11: *Comparison and evolution of first and second topos with Reynolds number for the $9.09 \cdot 10^{-3} \measuredangle 12°$ cylinder configuration.*

Reynolds numbers, the main difference when increasing the Reynolds number was to slightly reduce the energy near the stagnation point and to slightly increase the energy in the rear. Other than that, they are similar. The critical Reynolds number configurations are again different. As the flow separation point is at significantly larger angles, the energy near the front is much lower than the super-critical configurations and the energy in the rear much higher. Similarly, the vortex-lift peaks in the second topos are at a higher angular location though this is visible only on one side of the cylinder.

The evolution of the relative fluctuating eigenvalues (found using equation (3.2)) are different at simulated critical and super-critical Reynolds numbers as shown in figure 4.12. At critical Reynolds numbers, the energy of vortex-lift BOD pair (2) was lower than at simulated super-critical; this made the relative energy for the higher BOD pairs larger at a Reynolds number of $2.57 \cdot 10^4$. This clear qualitative difference with the Reynolds number was not seen as clearly for the smooth cylinder in figure 3.9.

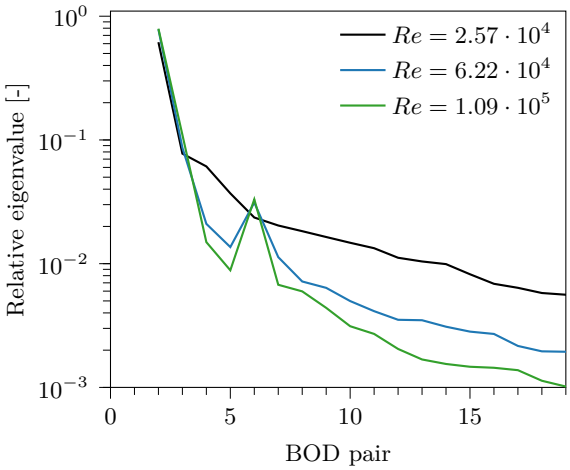

Figure 4.12: *Comparison of relative eigenvalues with Reynolds number for the* $9.09 \cdot 10^{-3} \measuredangle 12°$ *cylinder configuration.*

4.4.2 Spatial energy distribution at simulated super-critical Reynolds numbers

When comparing the topos of the mean distributions (figure 4.13a) from the rough cylinders at simulated super-critical Reynolds numbers with the smooth large scale reference cylinder, immediate differences can be found. Firstly, it can be seen that the small-scale configurations have more energy both in the front of the cylinder and in the rear. While the increased energy in the front might be to counteract the energy in the rear, the more negative energy in the rear should be due to the surface flow separation occurring at lower angles. The amplified energy in the rear and front of the cylinder (more negative in the rear and more positive in the front), should be related to why the configurations with ribs have increasing mean drag.

The second difference in the mean topos with added ribs, was the jaggedness in the spatial distribution when increasing the rib spacing. This jaggedness was present for all four topos presented in figure 4.13 and should be a result of how the entrapped surface flow interacts with the flow over the cylinder. It's possible that these jagged spatial distributions were partly responsible for why the mean drag and SD forces increased with the spacing and why the Strouhal number decreased which is inconsistent with previous results [21, 25].

There are two similarities in the vortex-lift topos shown in figure 4.13b between the smooth cylinder at large-scale and rough cylinders at small-scale and one major difference. The main similarities, are the anti-symmetric shapes and spatial energy peaks near the separation point. For the rough cylinders, the separation point and the point of peak vortex-lift were at smaller angular locations which was a minor difference. The major difference was in the rear of the cylinder where there's a secondary energy peak not found with the smooth, large cylinder. This second peak might be related to the secondary vortex-lift seen for the smooth cylinder in the fourth pair and could help explain why the secondary shedding process was negligible with ribs. The increased spatial energy in the rear was also seen with ribs at large scales but to a lesser extent.

The largest differences between the rough cylinder and the smooth reference case were for the third and fourth BOD pair. While there were qualitative similarities in the second vortex-lift topos between the rough and smooth cylinders, the spatial energy distributions had several differences as shown in figure 4.13c. For instance, the peaks in the rear for the rough cylinders at simulated super-critical Reynolds numbers were at larger angular locations, narrower and were stronger and the spatial energy in the front had a different shape; it's reminiscent of the smooth cylinder's spatial energy distribution, but with different values. It's possible that the

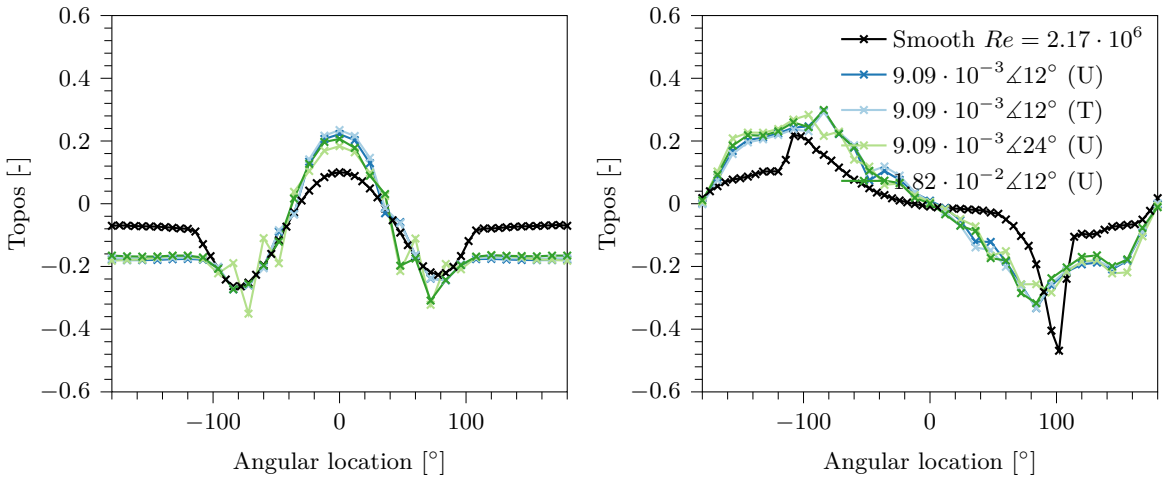

(a) *Comparison of the 1st topos (mean).*

(b) *Comparison of the 2nd topos (vortex-lift).*

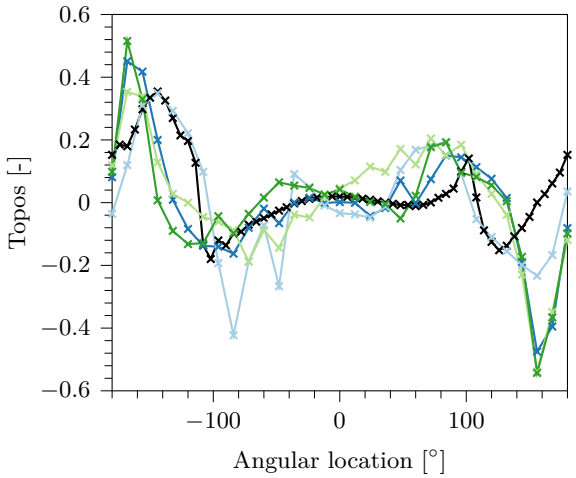

(c) *Comparison of the 4th topos (second vortex-lift).*

Figure 4.13: *Comparison of first four topos from smooth and rough experiments at the actual and simulated super-critical Reynolds numbers defined in table 4.1.*

dissimilitude in the fourth topos can be ignored as the fourth BOD pair was important for the shedding process on the smooth cylinder but not the rough ones and as some of the rear spatial energy was included in the vortex-lift pair. When comparing the vortex-drag topos for the rough and smooth cylinders, the rough cylinders were found to be wildly different and are not shown.

4.4.3 MAC comparison of topos

The differences in spatial energy distribution, or topos, can be assessed using the modal assurance criterion (MAC) described in section A.3 using the definition of Pastor, Binda and Harčarik [150]. Instead of relying purely on a visual comparison, this parameter gives a numerical quantification of how similar two topos are while ignoring the scaling. When comparing the MAC values, anything above 90% should be considered fantastic and anything over 75% good. To be able to compare the results from the smooth cylinder at large-scale (60 pressure taps) with the rough cylinders at small-scale, the pressure distribution from the smooth cylinder was down sampled by ignoring every other pressure tap starting from $\theta = 0°$.

When comparing the mean BOD pair in figure 4.14, the MAC values can be seen to be high for all compared configurations. While the comparisons with the smooth cylinder consistently have lower MAC values, they are still above 83% for all rib configurations indicating a good

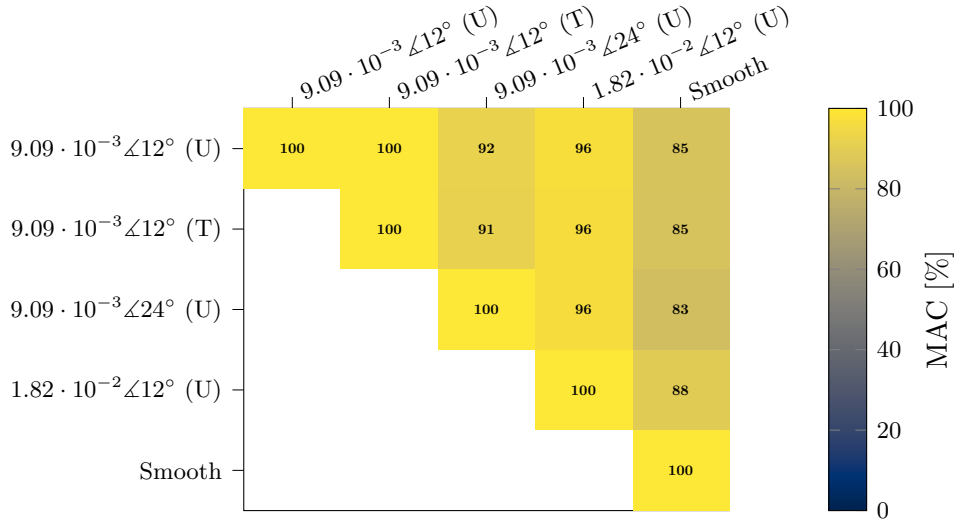

Figure 4.14: *MAC value comparison for the mean topos at super-critcal Reynolds numbers.*

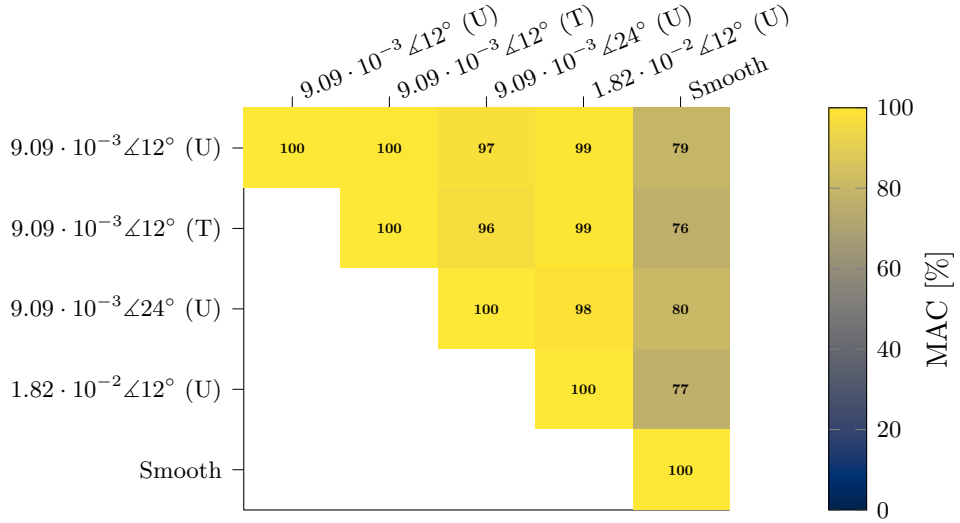

Figure 4.15: *MAC value comparison for the vortex-lift topos at super-critcal Reynolds numbers.*

match. This signifies that most of the visual topos differences for these configurations could be a scaling difference and most of the actual energy differences might be near the separation point and the suction peaks or due to the asymmetry for the smooth cylinder.

The similarity of the vortex-lift topos was almost as good as the mean distribution. Figure 4.15 shows that the MAC values and similarity was high between the rib configurations but that the similarity with the smooth cylinder was lower. As the vortex-lift distributions with ribs had a secondary and smaller peak in the rear not present in the smooth cylinder's, earlier separation point and was more anti-symmetric, these lower MAC values make sense. Even with these differences, the MAC values are around 75% and the similarity was fairly good.

For the second vortex-lift, in figure 4.16 respectively, the similarity was reduced. While there's some good similarity between the rib configurations, the previously mentioned differences in the second vortex-lift gave low MAC values when comparing the rib configurations with the smooth configuration. The best comparison was the $9.09 \cdot 10^{-3} \measuredangle 12°$ configuration with turbulence which had a topos more similar to the smooth cylinder's; the similarity was especially better in the rear.

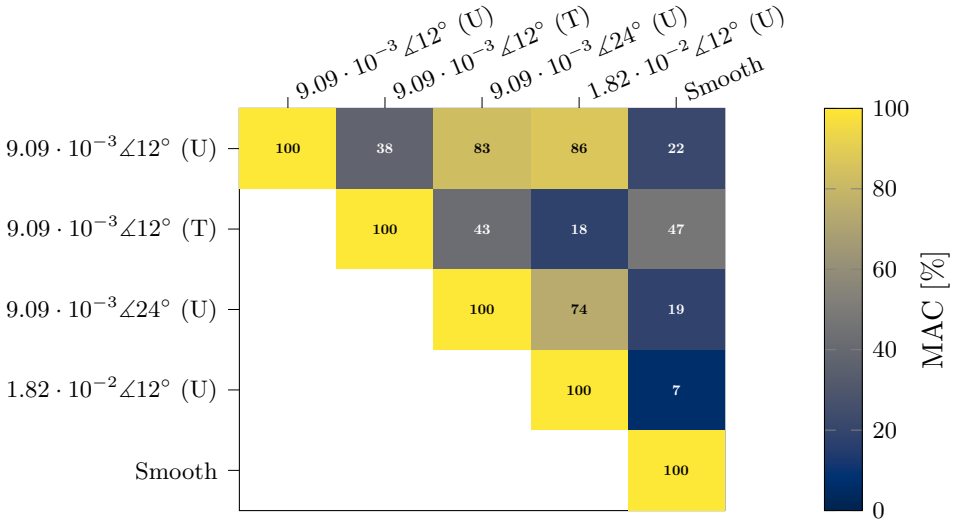

Figure 4.16: *MAC value comparison for the 2nd vortex-lift topos at super-critcal Reynolds numbers.*

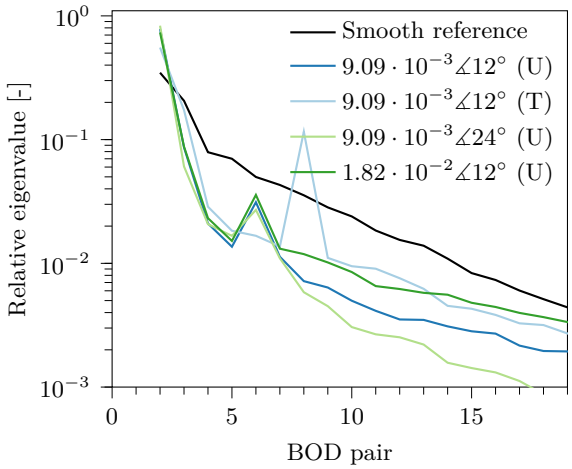

Figure 4.17: *Evolution of relative eigenvalues (using the fluctuating pairs only) with BOD pair rank for the configurations in table 4.1.*

4.4.4 Eigenvalue comparison

Like for the topos, there were differences in the relative eigenvalues between the smooth super-critical cylinder and the rough configurations at simulated super-critical values when only comparing the fluctuating pairs. Firstly, the rib configurations' vortex-lift BOD pair had a much higher relative energy than the smooth reference cylinder. This should indicate that the vortex-lift is relatively stronger for the rib configurations than the smooth. The configuration with the highest spacing had the highest relative lift from the vortex-lift BOD pair. Still, this alone does not explain why the larger roughness spacing gave a stronger SD lift coefficient but the energy in absolute values does: The energy of the vortex-lift BOD pair was 66% higher for the $9.09 \cdot 10^{-3} \measuredangle 24°$ configuration than the $9.09 \cdot 10^{-3} \measuredangle 12°$ configuration at comparable Reynolds numbers.

For the higher rank BOD pairs, the smooth reference cylinder had higher relative eigenvalues which is expected. The higher rank BOD pairs for the rough cylinder has similar relative energies for the first five BOD pairs and the relative energy drops rapidly except for the energy bumps due to the manual sorting of the fourth BOD pair. At BOD pairs greater than five, the relative energy is fairly low and the main difference between the configurations is that the configurations

with relatively higher energy at the vortex-lift pair has lower energy at higher rank BOD pairs.

4.4.5 Chronos comparison

As the simulated super-critical rib configurations had different characteristic and physical shedding frequencies, they are not compared directly. Instead, they can be compared indirectly using the bandwidth of the peaks and a qualitative description of the PSD. For most rib configurations, the PSD of the first four chronos varied like in figure 4.5b and there were differences and similarities with the smooth cylinder's PSD.

While the PSD of the smooth and rough cylinders' mean and vortex-drag chronos were similar (dominated by low frequency components), the vortex-lift and second vortex-lift were different. The vortex-lift's PSD had significant noise at most frequencies below the shedding frequency for the smooth large-scale cylinder. In addition, the peak at the Strouhal number were relatively small giving a very noisy period signal. For the rough cylinders at small-scale, on the other hand, almost all of the temporal energy was focused at the Strouhal frequency and the signal was strongly periodic. The second vortex-lift was more similar for the smooth and rough cylinder in that they both contain more noise than the vortex-lift. Still, they can be differentiated as the rib configurations had more energy focused at the Strouhal number and as the Strouhal number was significantly lower than the upper value found for the smooth cylinder.

Just like the topos, the rib configurations' chronos were different from both the smooth cylinder and each other. This can be exemplified by investigating the half-power bandwidth (point where a PSD peak is reduced by a factor of $\sqrt{2}$) of the vortex-lift chronos' PSD; a higher bandwidth means that the energy is more spread out. Table B.5 shows inference results on the average effect of rib height, spacing and turbulence intensity on the vortex-lift bandwidth at super-critical Reynolds numbers. From this, it can be seen that increasing the turbulence and rib spacing does not significantly affect the Strouhal number bandwidth for the rough configurations but that rib height does: An increase in rib height can be shown to give a narrower Strouhal number bandwidths on average.

4.4.6 Relative forces from BOD pairs

A comparison of the relative strength of the BOD pairs on total force is the last comparison between the small and large-scale experiments. This is shown in figure 4.18. As the relative drag (figure 4.18a) was mean dominated for both the rough and smooth cylinders, the relative drag was quite similar in absolute values. For the higher rank BOD pairs, there were more differences. For instance, the vortex-lift BOD pair had a negligible impact on total drag for the smooth cylinder but was nearly as significant as the vortex-drag BOD pair for the rough. The second vortex-lift pair had some scatter in the relative drag among configurations but was relatively more similar than the other fluctuating force pairs even if its relative drag was higher without roughness. These extra unsteady forces might be due to the significant secondary vortex-shedding process for the smooth cylinder.

The relative lift, in figure 4.18b, had more dissimilarities than the relative drag. While the relative lift on the smooth cylinder was mostly from the mean BOD pair, due to the strong mean lift, most of the relative lift from the rough cylinders were from the vortex-lift pair. The smooth cylinder's lift still had a large relative contribution from the vortex-lift pair but its contribution to the total lift was diminished by the significant mean lift bias. Even when comparing the conditional relative lift (with the mean removed) like in table 4.2, the relative lift from the vortex-lift BOD pairs were higher with the ribs even when removing the mean bias.

For the higher rank BOD pairs, the relative lift changed similar to the relative drag. There were two exceptions to this. The first exception was the smooth cylinder having more relative lift from the vortex-drag and second vortex-lift pairs compared with the rough configurations.

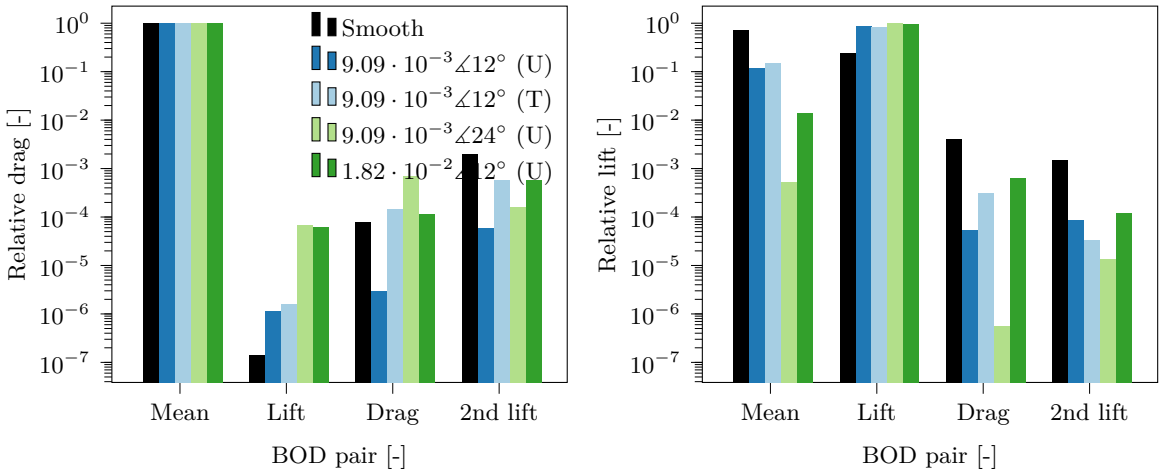

(a) *Relative drag.*

(b) *Relative lift.*

Figure 4.18: *Comparison of relative forces at super-critical Reynolds numbers.*

Table 4.2: *Comparison of conditional relative lift using fluctuating BOD pairs only.*

Configuration	Vortex-lift	Vortex-drag	2nd vortex-lift
Smooth	$9.33 \cdot 10^{-1}$	$1.55 \cdot 10^{-2}$	$5.59 \cdot 10^{-3}$
$9.09 \cdot 10^{-3}\measuredangle 12°$ (U)	$9.99 \cdot 10^{-1}$	$6.18 \cdot 10^{-5}$	$9.79 \cdot 10^{-5}$
$9.09 \cdot 10^{-3}\measuredangle 12°$ (T)	$9.97 \cdot 10^{-1}$	$3.64 \cdot 10^{-4}$	$3.88 \cdot 10^{-5}$
$9.09 \cdot 10^{-3}\measuredangle 24°$ (U)	$9.99 \cdot 10^{-1}$	$5.71 \cdot 10^{-7}$	$1.35 \cdot 10^{-5}$
$1.82 \cdot 10^{-2}\measuredangle 12°$ (U)	$9.97 \cdot 10^{-1}$	$6.62 \cdot 10^{-4}$	$1.23 \cdot 10^{-4}$

The second exception was the $9.09 \cdot 10^{-3}\measuredangle 24°$ (U) configuration which had a relatively lower lift from the vortex-drag and second vortex-lift pairs compared with the relative drag.

4.5 Best configuration for simulating super-critical Reynolds numbers at small-scale

In some regards, the added roughness failed to properly simulate the super-critical Reynolds number flow seen for the smooth reference cylinder as the summary in table 4.3 shows. Firstly, the tests with added ribs had a higher mean drag, SD lift and Strouhal number. Secondly, the minimum pressure coefficient was much greater but was around the same angular location. The maximum SD pressure coefficient, on the other hand, was much higher for the smooth cylinder, at a higher angular location and was asymmetric. The $9.09 \cdot 10^{-3}\measuredangle 24°$ (U) configuration was closer to the smooth cylinder in terms of minimum mean pressure coefficient, max SD pressure coefficient and location of maximum SD pressure coefficient but it gave a much higher SD lift coefficient. While the correlation and coherence is important for getting the correct 3D flow characteristics, a direct comparison with smooth super-critical flow could not be made as it could not be measured for the smooth reference cylinder.

Overall, the tests with the small rib-spacing (12°) and a relative height of $9.09 \cdot 10^{-3}$ had the best balance for simulating super-critical Reynolds numbers at a speed range usable in the wind tunnel and in matching the smooth cylinder's unsteady force characteristics (mean, SD values and frequency) and important pressure distributions (mean, vortex-lift and second vortex-lift). The other small-scale rib spacing and height configurations shown in the appendix had coefficients that were more different from the smooth cylinder and achieved super-critical Reynolds numbers at speeds that were less useful in the wind tunnel. When doing 3D, elastic

Table 4.3: *Reynolds numbers and roughness configurations from large-scale 2D tests identified as being at simulated super-critical Reynolds numbers.*

Roughness	Smooth	$9.09 \cdot 10^{-3}$	$9.09 \cdot 10^{-3}$	$9.09 \cdot 10^{-3}$	$1.82 \cdot 10^{-2}$
Spacing/flow	N/A (U)	$\measuredangle 12°$ (U)	$\measuredangle 12°$ (T)	$\measuredangle 24°$ (U)	$\measuredangle 12°$ (U)
Mean C_d	0.55	0.97	0.913	1.03	0.91
SD C_l	0.127	0.148	0.132	0.313	0.149
St_1	0.2	0.213	0.211	0.211	0.221
St_2	0.25	N/A	N/A	N/A	N/A
$C_{p,\ min}$	-2.5	-1.21	-1.26	-1.75	-1.49
Location min	80°	84°	84°	72°	84°
SD $C_{p,\ max}$	0.3	0.136	0.15	0.257	0.137
Location max	110°	84°	84°	96°	84°
Φ_2 (chronos)	at St_1	at St_1	at St_1	at St_1	at St_1
$\Psi_{2,\ max}$ (topos)	110°	84°	84°	96°	84°
Φ_4 (chronos)	at St_2	N/A	N/A	N/A	N/A
$\Psi_{4,\ max}$ (topos)	140°	168°	144°	156°	156°

tests on circular cylinders, it will be important to have a large range of possible super-critical Reynolds numbers and not just test at the highest speeds available in the wind tunnel.

If the aim is to reproduce the lower Strouhal number from the smooth large-scale tests ($St \approx 0.2$), then the $1.82 \cdot 10^{-2} \measuredangle 12°$ configurations could be the better choice. Unfortunately, the largest rib configurations tended to have other problems and there are three reasons why these configurations should not be used: 1) The behavior of the global force coefficients, correlation and coherence was weird when compared to the other rib configurations; 2) the transition from critical to super-critical could not be verified (the flow might be super-critical at all speeds or distorted into something else); and 3) the topos tended to be less similar to the smooth super-critical cylinder's when compared with the other rib configurations.

4.6 Summary of small-scale results

In addition to finding a good roughness configuration for replicating super-critical Reynolds number at small-scale, several findings were made on how changes in turbulence and roughness affect the aerodynamics of a circular cylinder; all results are summarized in table 4.3. In section 4.3.1, it was shown that increasing the turbulence intensity had a statistically negligible impact on the Strouhal number. Increasing the rib height, on the other hand, was shown to decrease both the Strouhal number and its bandwidth at the super-critical Reynolds numbers. The Strouhal number also decreased when increasing the rib spacing but this didnt affect the bandwidth. Like at large-scale, there were differences in the wake Strouhal number and Strouhal number obtained from vortex lift's chronos but it tended to be small in absolute value.

Increasing the turbulence intensity had a statistically negligible effect on the unsteady lift, but significantly decreased the mean drag as shown in section 4.3.2. The standard deviation of the unsteady forces were also affected by the increased turbulence intensity and the SD lift was shown to decrease while the SD drag increases. The effect of increased rib height on the standard deviation of unsteady forces was found to be more negligible than the increase in mean drag. In addition, it was shown that increasing the rib spacing gave a higher mean drag and greatly increased SD lift and drag. This is contrary to the conventional wisdom and large-scale experiments where lower overall roughness gave lower mean drag.

The coherence and correlation of the vortex-shedding process along the height is related to the unsteady forces; these values give an indication of the 3D forces. This was investigated in section 4.3.3 and the effect of turbulence was to decrease the correlation and coherence

when the spacing was small. When the spacing was large, the added turbulence increased the coherence but decreased the correlation. Increasing the spacing tended to increase the correlation and decrease the coherence for both turbulence intensities. With the exception of the $1.82 \cdot 10^{-2}$ configurations, the effect of increased rib height was to increase both the correlation and coherence.

Increasing rib spacing caused the spatial energy distributions of unsteady pressure (BOD topos) to have more jagged shapes. The effect of increased turbulence was small for most of the pertinent BOD pairs but did introduce a more pronounced and jagged shape for the second vortex-lift topos. Changing the rib height had a much smaller effect on the relative forces and topos than the other two changes.

For most speeds, the relative drag from the BOD pairs was dominated by the mean distribution and relative lift by the vortex-lift distribution. There were speeds where other BOD pairs contributed greatly to the total lift and this tended to be due to asymmetric pressure distributions or when two physical BOD pairs were combined into new conflated shapes. This was clearest when the mean lift was non-zero and the lift rms had a bias associated with the mean pressure distribution.

Part III

Aeroelastic experiments

Chapter

5 Small-scale aeroelastic wind tunnel experiments

Chapter summary

This chapter presents a 3D aeroelastic wind tunnel experiment on elastic circular cylinders of finite height. To simulate the response of a full-scale structure at super-critical Reynolds numbers, the best roughness configuration from the previous chapter was used to simulate the super-critical flow. The results from these experiments showed that the Strouhal number, correlation and coherence (with and without motion) was significantly lower than the small-scale 2D results. Additionally, it's shown that increasing the roughness reduced the response. This should indicate that something akin to the super-critical Reynolds number region, where the lift force is weaker compared to sub-critical values, was reached for the rough cylinder. Additionally, removing the boundary layer increased the response meaning that it's an important parameter when it comes to the coherence, force amplitude, and response.

5.1 Background

The scaling and Reynolds number issue for circular cylinders subjected to vortex-induced vibrations can be aptly summarized using the claim of Vickery and Clark [4]: The loads due to vortex-induced vibrations may be overestimated by as much as 400% when large structures are scaled down in wind tunnels. This is hard to verify as, according to the investigation of Belloli et al. [27], there are no super-critical vortex-induced vibrations experiments on circular cylinders where the cylinder is free to move and relatively few experiments at critical Reynolds numbers (c.f. the works of Ding et al. [151], Raghavan and Bernitsas [103] and Swithenbank et al. [152]). Many of the previous experiments in the literature have an additional limitation which makes them less applicable when testing chimneys and other tall, slender structures with circular cross-section: The previous experiments tend to use quasi-2D cylinder (end plates) with the motion limited to one degree of freedom and with a fixed, rigid mode shape or use cables with large aspect ratios ($\lambda > 100$) [27, 103, 151, 152].

There is an additional factor that needs to be considered when scaling wind tunnel experiments: The effect of an atmospheric boundary layer and turbulence intensity on the response. Batham [60] reported that an atmospheric boundary layer was enough to experimentally recreate the response of a chimney at super-critical Reynolds numbers. The caveat to this is that Batham was simulating the response due to random vibrations but it does raise an interesting question: Is a turbulent atmospheric boundary layer enough to simulate the super-critical response of circular cylinders of finite height?

The experiment presented in this chapter deals with these issues by doing the following. Firstly, the response and wake characteristics for a slender cylinder of finite height was measured for a smooth sub-critical cylinder and a rough cylinder at super-critical Reynolds numbers. These tests will show if the Reynolds number effect is as large as proclaimed in 3D tests. Secondly, the same measurements will be repeated with and without an atmospheric boundary layer. These

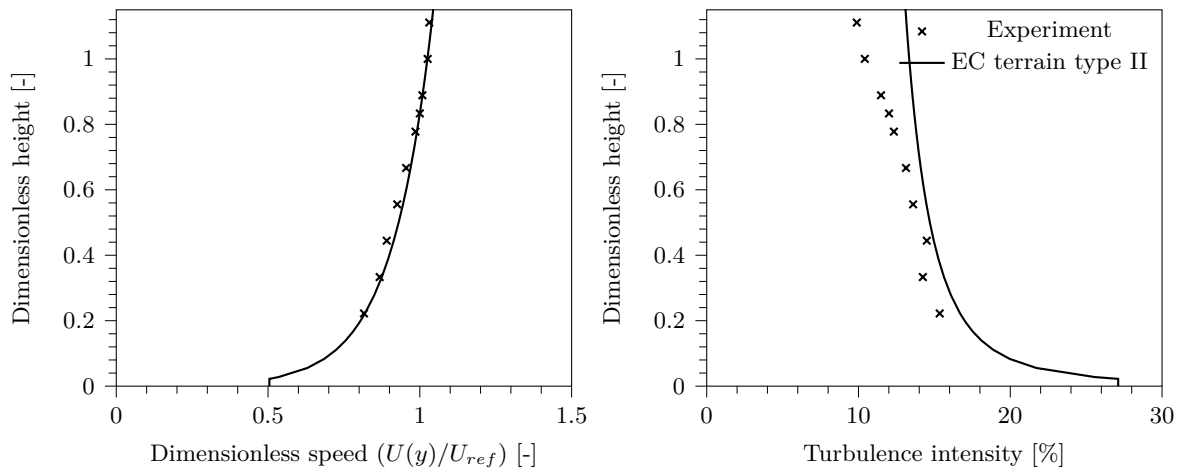

(a) *Speed profile with $U_{ref} = U(z = 0.83)$.* **(b)** *Turbulence profile (legend in figure 5.1a).*

Figure 5.1: *Comparison of experimentally obtained wind profile (at 1:100 scale) with full-scale wind profile generated by the Eurocode using terrain category II [5].*

tests will show if surface roughness is needed to simulate the super-critical flow over a 3D cylinder or if it adds unnecessary complexity.

5.2 Experimental methodology

5.2.1 The generated atmospheric wind

The aeroelastic tests were performed in the same small-scale wind tunnel described in chapter 4. The difference between these tests and the previous, was that some of the aeroelastic tests were performed with an artificial atmospheric boundary layer generated upstream of the model. To calibrate the gradient and wind speed at the dimensionless reference height (z=0.83), a fast response Pitot tube and a pre-calibrated average Pitot tube was used. By varying the height of the fast response pitot tube, the wind gradient (turbulence intensity and speed) was measured in relation to the calibrated average Pitot tube.

Figure 5.1 shows the wind gradient produced in the wind tunnel. The measured speed profile (figure 5.1a) matches the Eurocode speed profile but the measured turbulence (figure 5.1b) matches less; the turbulence was lower at most heights and with an increasing difference with height. As mentioned in chapter 4, the turbulence intensity was measured to 1% using a Cobra probe (1%, 0.8% and 0.8% for the u, v, w components of velocity respectively) when testing without the boundary layer and with negligible height gradient.

5.2.2 Test model and setup

The test models were two carbon fiber tubes and both had an external diameter of 0.055 m (d), internal diameter of 0.051 m and length of 0.9 m. One of these tubes were fitted with the best roughness from chapter 4, ribs with relative roughness height $9.09 \cdot 10^{-3}$ and a spacing of 12° between them (30 ribs), to trigger usable, super-critical Reynolds numbers. These tubes were mounted to a steel diabolo support, as shown in figure 5.2a, which in turn was securely bolted down below the wind tunnel. This arrangement gave better control of the natural frequency and damping of the model at the expense of the mode shape.

To increase the damping, the diabolo support could be further modified by adding polyurethane foam in the gap between the wind tunnel's floor and the model. An example of this added damping arrangement is shown in figure 5.2b. This increased the damping ratio near uniformly in the

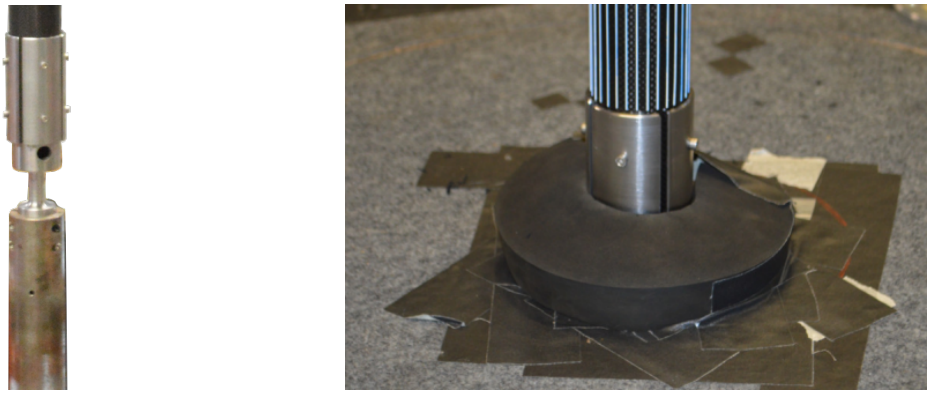

(a) *Diabolo support.* **(b)** *Added polyurethane foam.*

Figure 5.2: *Pictures of diabolo support used to mount the cylinders and the polyurethane foam used to add structural damping.*

$\hat{e}_x$ and $\hat{e}_y$ directions with little effect on the natural frequency.

The experimental setup is pictured and sketched in figure 5.3. Figure 5.3a shows the experimental setup (rough test model and aerodynamic sensors) with the equipment used to produce the atmospheric boundary layer in the background. The relative locations of the hot-film sensors and the fast Pitot tube is given in figure 5.3b with the Pitot tube placed 10 diameters to the side of the cylinder (0.55 m), at a height of 7.5 diameters (z=0.83 or Z=0.75 m) and with its tip aligned with the cylinder's front. The hot-films were placed 4 diameters behind the cylinder's rear (0.22 m) and 0.5 diameters off the cylinder's centerline (0.0275 m).

Figure 5.3b shows the relative height of the hot-film sensors. The first and upper hot-film (1) was placed 1 diameter below the cylinder's tip, the second (2) 2 diameters below the tip, the third (3) 3.25 diameters and the last and lowest (4) 4.75 diameters below the tip. This made the distances between sensors 1 and 2, 2 and 3 and 3 and 4 1, 1.25 and 1.5 diameters respectively. Finally, a 3D accelerometer was placed inside the cylinders on a level mounting bracket at a height of 15.55 diameters (Z=0.855 m or z=0.95) or 0.82 diameters from the model's tip.

5.2.3 The first mode shape

The experimentally obtained first mode shape was determined from tests without added mass by using two accelerometers (one reference and one movable) and is compared with two often assumed mode shapes [5, 55] in figure 5.4. The two assumed mode shapes are the straight $\psi(z) = z$ (flexible support) and parabolic $\psi(z) = z^2$ (cantilevered support) mode shapes. As figure 5.4 shows, flexible support mode shape has a closer shape to the experimentally obtained mode shape than the cantilevered. This makes sense as most of the bending was concentrated in the diabolo support with some additional bending of the cylinder.

5.2.4 Model configurations and parameters

A simplifying assumption was needed to estimate the equivalent mass per unit length (m_e) for all configurations: It's assumed that the mode shape was similar when adding extra mass and damping and when testing without the roughness strips. Part of this assumption was that the modal stiffness of the cylinder stayed constant. With these assumptions, the modal mass for the cylinders without added mass was estimated from equation (2.8) by first adding a calibrated mass and then comparing the natural frequencies. From this, the equivalent mass without added mass was found using equation (2.9) using the mode shape integral from the best fitted mode shape and the equivalent mass with added mass using equation (2.10).

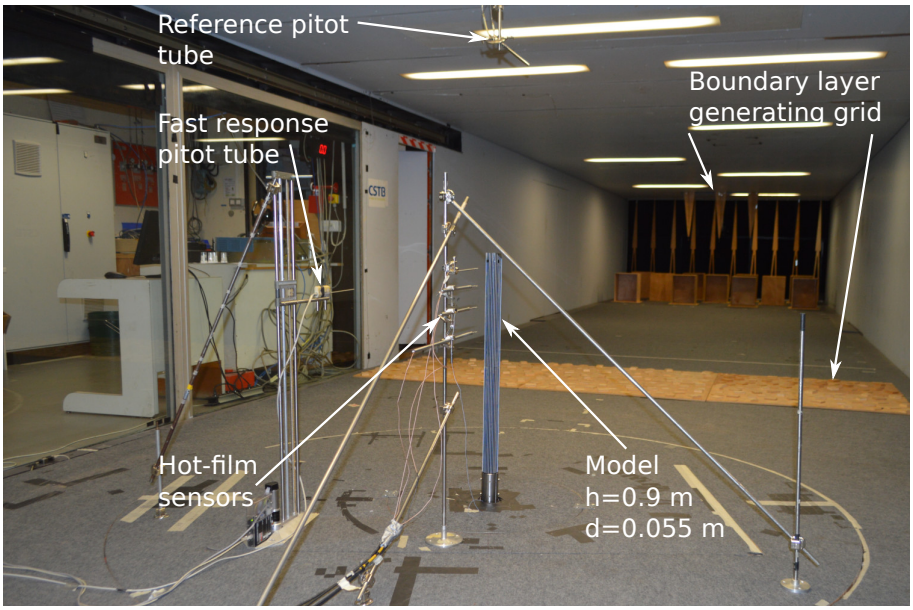

(a) *Picture of setup with explanations.*

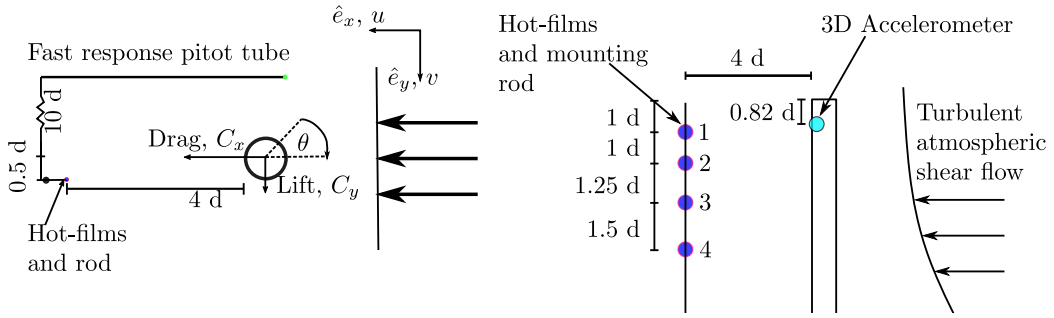

(b) *Sketch from top with coordinate system.*

(c) *Sketch from side focused on hot-film locations.*

Figure 5.3: *Sketches of experimental setup, relative locations and coordinate system used.*

The resulting equivalent masses, m_e, for each test case are given in table 5.1 along with: cylinder surface condition, mass added near the tip (m_{add}), dimensionless mass-ratio μ (defined in equation (2.12)), natural frequency (f_n) in the across-wind direction ($\hat{e}_y$), damping ratio (ζ) in across-wind direction, Scruton number Sc (mass-damping parameter defined in equation (2.14)), Strouhal number St and the Reynolds number giving vortex-induced vibrations using the best estimate of the constant Strouhal numbers in figure 5.5. For all configurations, the natural frequencies and damping ratios were characterized before and after testing a configuration to verify that the structural parameters remained the same.

Two of the configurations in 5.1 are marked with an asterisk. They were tested without the atmospheric boundary layer generator shown in figure 5.3a. These tests showed how the atmospheric boundary layer affected the response at sub-critical and simulated super-critical Reynolds numbers.

5.2.5 Instrumentation and measurements

Unsteady pressures are not recorded for these tests as the tubing connecting the pressure taps to the sensors adds significant damping. Instead, there's just one acquisition chain measuring tip acceleration using an 3D accelerometer (with $\hat{e}_x$ aligned in the along wind and $\hat{e}_y$ in the across wind direction), wind speed using a reference fast-response Pitot tube and the wake characteristics using four hot-film probes placed behind the cylinder. To be sure that the displacement and wake statistics can be properly measured, all time signals were recorded for

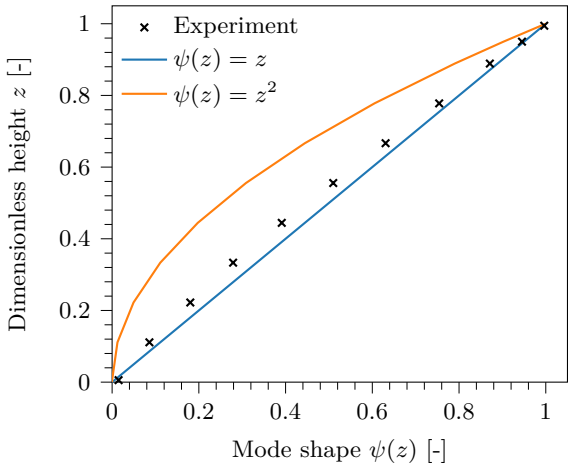

Figure 5.4: *Experimental first mode shape and comparison with two assumed mode shapes [5, 55].*

Table 5.1: *Characteristics of experimental models in the across-wind direction. Asterisk marks tests without atmospheric boundary layer and with low turbulence.*

Surface	m_{add} [kg]	m_e [kg/m]	μ [-]	f_n [Hz]	ζ [%]	Sc [-]	St [-]	Re_{crit} [-]
Rough	0	0.61	168.1	56.3	0.244	5.47	0.182	61000
Rough	0.15	0.75	207.0	42.4	0.265	9.99	0.182	47000
Rough	0.3	0.90	247.8	36.7	0.324	17.2	0.182	40000
Rough	0	0.61	168.1	56.4	0.351	7.87	0.182	61000
Smooth	0	0.60	165.3	56.7	0.209	4.50	0.178	63000
Smooth	0.15	0.74	204.2	42.5	0.257	9.45	0.178	48000
Rough*	0	0.61	168.1	56.0	0.240	5.38	0.176	63000
Smooth*	0	0.60	165.3	56.6	0.278	5.98	0.162	69000

120 s at a frequency of 512 Hz. Note that two of the hot-films (probes 1 and 4, i.e. bottom and upper) broke when changing from the rough to smooth cylinder due to human error.

5.2.6 Analysis of displacement and acceleration

The displacement for each recording, $y(t)$, was calculated from the acceleration signal using the Fourier transform process outlined in section A.1. To eliminate unwanted low-frequency noise, which would become over represented in the displacement signal, a fifth order high-pass Butterworth filter with cutoff frequency of 5 Hz was applied to the acceleration data. This cut-off frequency was well below both the lowest vortex-shedding frequencies and natural frequencies.

The response envelope of displacement was calculated using the Hilbert transform [153]. By separating each recording into 120 segments (each 1 s), the amplitude statistics (mean and maximum) could be estimated with outliers removed (defined as four standard deviations away from mean maximum amplitude). The dominant vibration frequencies were identified from the spectrum $Y(\omega)$ by peak detection but these were mostly at the natural frequency.

These amplitude data were compared using the dimensionless fluid speed ω_q defined in equation (5.1). As this speed includes the Strouhal number, or equivalently the critical vortex-induced vibration speed, the vortex-induced vibrations should be in the same dimensionless speed range regardless of surface and flow configuration. To better compare the experiments across scales, the response amplitudes are shown in dimensionless form r_y using equation (5.2).

$$\omega_q = \frac{\omega_s}{\omega_n} = \frac{U}{U_{crit}} = U_R St, \tag{5.1}$$

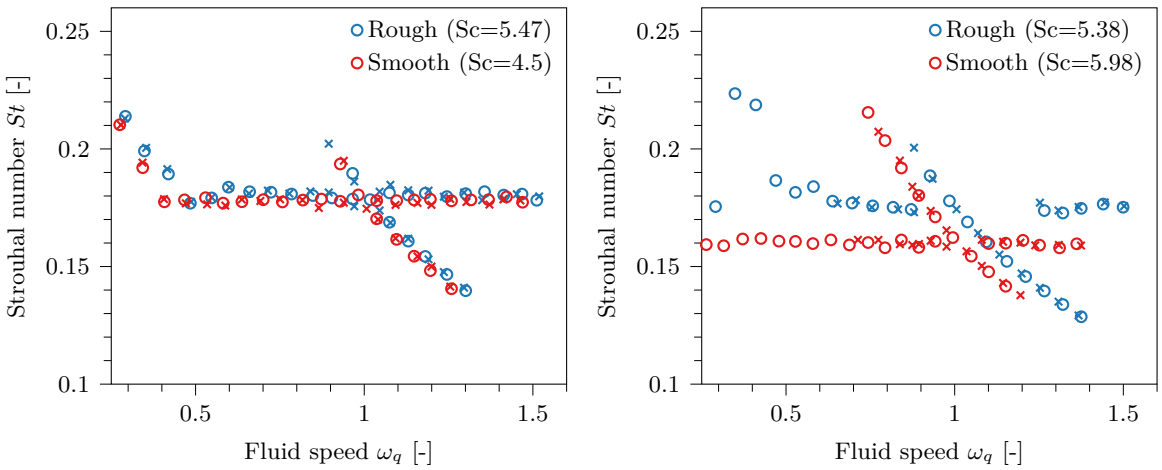

(a) *With atmospheric boundary layer.* **(b)** *Without atmospheric boundary layer.*

Figure 5.5: *Strouhal number for cylinders without added mass and damping (with and without atmospheric boundary layer). ∘ are experiments with increasing speed, × decreasing.*

$$r_y = \frac{|Y|}{d}. \tag{5.2}$$

5.3 Wake and response results

5.3.1 Strouhal number

Two quick conclusions can be made regarding the Strouhal numbers (measured using hot-film sensor 3 at $z = 0.8$) shown in figure 5.5. Firstly, tests with smooth cylinders had lower Strouhal numbers than the rough cylinder. Similar results were seen in 2D tests on similar cylinders (size, material, flow conditions and roughness), but the measured 3D Strouhal numbers were significantly lower than their 2D counterparts (as also shown in the literature presented in section 2.1.4). This reduction should not be due to top effects as the Strouhal numbers were similar when investigating the bottom hot-film probe (4 in figure 5.3c), $y = 0.71$) and the hot-film placed second from the top (2, $y = 0.88$).

The second quick conclusion, was that removing the atmospheric boundary layer (uniform flow) reduced the Strouhal numbers, increased the lock-in region and made the smooth and rough cylinders have noticeably different Strouhal numbers. The latter is in contrast to tests with the turbulent atmospheric boundary layer where the vortex-shedding frequencies were similar for both roughness configurations. This could indicate that adding a turbulent atmospheric boundary layer was enough to simulate or suppress any transition to super-critical Reynolds numbers and that roughness in unnecessary.

The Strouhal number had a significant nonlinear variation with ω_q for the configurations shown in figure 5.5 and two different shedding frequency behaviors were found in the wake. One of these shedding patterns correspond to having a constant Strouhal number (linearly increasing vortex-shedding frequency as for stationary cylinders) whereas the other had a linearly decreasing Strouhal number (constant shedding at the first natural frequency). The latter shedding pattern with ω_q occurs during lock-in and the vortex-induced vibrations should be clearer if there's only one shedding frequency during lock-in. This was seen for the rough cylinder when testing without the atmospheric boundary layer where the linearly increasing Strouhal number was missing for parts of the lock-in region.

Hysteresis was observed for three of the four configurations in figure 5.5. While the smooth cylinder tested with the atmospheric boundary layer showed no hysteresis in figure 5.5a, the rough did have possible lock-in (two vortex-shedding frequencies) at lower speeds when reducing

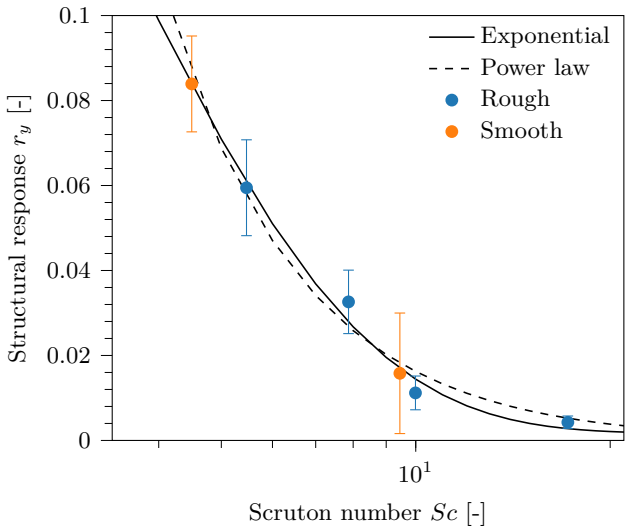

Figure 5.6: *Experimentally obtained maximum response as a function of Scruton number for tests with atmospheric boundary layer. The exponential function is* $r_y \approx 0.00166 + 0.377\exp(-0.339 \cdot Sc)$ *and the power law is* $r_y \approx 1.97 \cdot Sc^{-2.08}$

the speed than when increasing it. This same hysteresis pattern was seen for the rough cylinder without the atmospheric boundary layer in figure 5.5b.

The smooth cylinder had a different hysteresis pattern than the rest when tested without the atmospheric boundary layer. The two frequency region started lower speeds with increasing wind speeds and started at higher speeds with decreasing wind speeds. This is contrary to common sense as one would expect the hysteresis to be a continued lock-in instead of a preemptive lock-in. In addition, this smooth cylinder had Strouhal number evolution different from the rest with more recorded shedding frequencies at the natural frequencies at $\omega_q > 1$ than above; this is the opposite of what's observed for the other three cylinders.

5.3.2 Structural response

Maximum response as a function of the Scruton number

Maximum response as a function of Scruton number is shown in figure 5.6 for the smooth and rough cylinders tested with atmospheric boundary layer. The maximum responses for the rough cylinders droped almost like an exponential or power law function with Sc which is classical but there were some less classical aspects [101, 106, 109]. When increasing the equivalent mass and damping by adding a tip mass ($Sc = 10$ and 17.2), the response seemed to drop slightly differently from when just adding damping (slightly different exponetial functions). It's possible that the equivalent mass either cannot be found by linearly superimposing the added mass or that the effect of damping and mass on maximum amplitude cannot be reduced to a mass-damping parameter which is inline with the view of Sarpkaya [106]. The smooth cylinders' maximum response adds little information as it's only two points but does fit in with the rough cylinder's evolution with Sc.

The response characteristics depended on the Scruton number. This can be inferred from the error bars in figure 5.6 which represent the standard deviation of the maximum amplitude when splitting the signal into 120 segments. When coupled with the time histories, the change in amplitude for the low Scruton number cylinders was seen to be mostly due to an amplitude modulation with time whereas the time history of the high Scruton number cases were more like random vibration. Note that while the low Scruton number cases have the largest SD values, their coefficient of variation were the smallest.

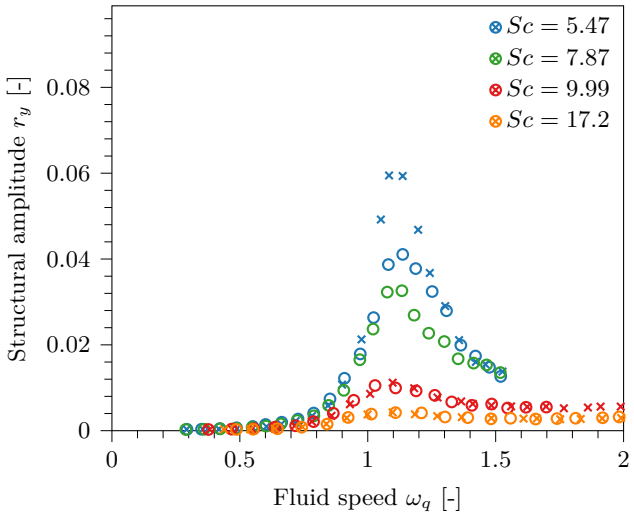

Figure 5.7: *Response for the rough cylinder with atmospheric boundary layer. ∘ marks experiments with increasing speeds and × decreasing.*

Amplitude response of rough cylinders at super-critical Reynolds numbers

Depending on the Scruton number, the response characteristics and shape was quite different. When the Scruton number was low ($Sc < 8$ for the rough cylinders), the response during lock-in was dominated by harmonic vortex-induced vibration. This led to quite high vibration amplitudes as seen in figure 5.7 for $Sc = 5.47$ and 7.87. In addition to the larger vibration amplitudes, the amplitude response had hysteresis. This can be seen for the rough cylinder with $Sc = 5.47$ when decreasing the speed where the vortex-induced vibration amplitudes were higher compared to tests with increasing speeds. There's further hysteresis in the lock-in range and it's more prolonged at $\omega_q < 1$ which is consistent with the Strouhal results in figure 5.5a.

At high Scruton numbers ($Sc > 9$), the rough cylinder's response was greatly diminished as seen in figure 5.7 for $Sc = 9.99$ and 17.2. In addition, the response characteristics changed greatly when increasing the Scruton number from $Sc = 7.87$ to $Sc = 9.99$. This change was large and should be due to the vortex-induced vibrations entering a different vibration regime which matches well with the predictive model of Vickery and Basu where theres a transition from harmonic response to random vibration around $Sc = 9$ [32, 88]. This was also seen in the response time history where the high Scruton number cylinder ($Sc = 17.2$) had a more random change (but still periodic) time history than the low Scruton number cylinder ($Sc = 5.47$) as shown in figure 5.8b.

While the amplitudes were reduced with the Scruton number, the vortex-induced vibration regions had similarities regardless of the Scruton number. The vortex-induced vibrations tended to start at $\omega_q \approx 0.8$ at the same speed and ended at $\omega_q \approx 1.35 - 1.5$ for all tested rough configurations. The end points did reduce with the Scruton number but not nearly as much as the amplitude levels dropped making the vortex-induced vibrations negligible regardless. As the speed increased past this, turbulence-induced vibration took over for the rough cylinders with atmospheric boundary layer but this was only observed for the configurations with added mass and lower natural frequencies.

Amplitude response of smooth cylinders at sub-critical Reynolds numbers

The amplitude response of the smooth cylinders at sub-critical Reynolds numbers were different from the previous super-critical results as shown in figure 5.9. Firstly, the amplitude hysteresis was less noticeable for the smooth cylinder with the lowest Scruton number ($Sc = 4.5$) and tests with decreasing speeds only had slightly higher amplitudes than when increasing it. The

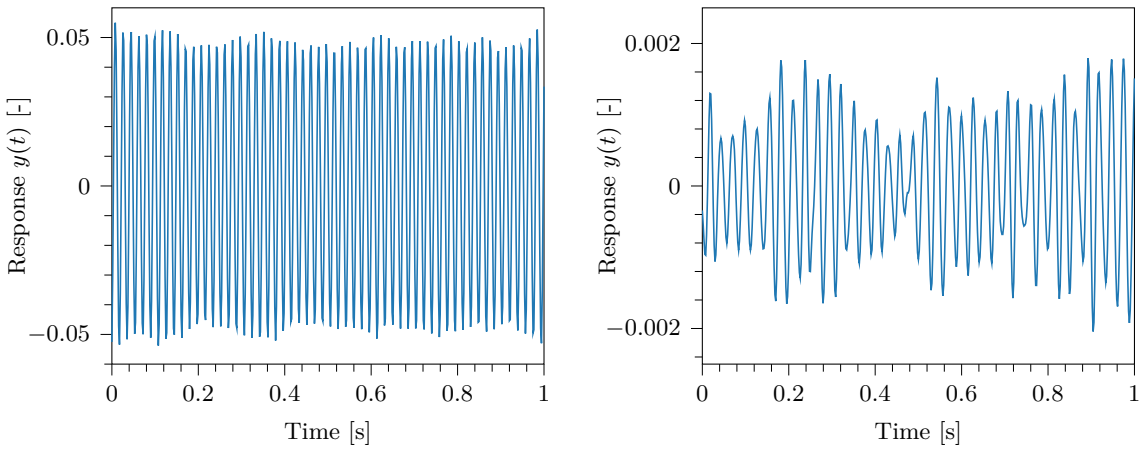

(a) *Low Sc (Sc = 5.47).* **(b)** *High Sc (Sc = 17.2).*

Figure 5.8: *Time histories of cross-wind vibrations for two rough cylinders at relatively high amplitudes of vibrations.*

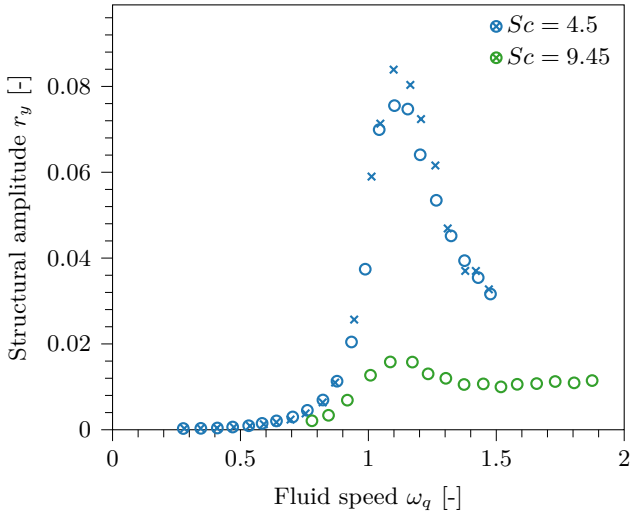

Figure 5.9: *Response for the smooth cylinder with atmospheric boundary layer. ∘ marks experiments with increasing speeds and × decreasing.*

second difference was in the amplitudes and the smooth cylinder experienced higher amplitudes of motion than the rough. As shown in chapters 2, 3 and 4, the SD lift coefficient was larger at sub-critical Reynolds numbers when compared to super-critical which partly explains the higher amplitudes. Another reason for the higher amplitude, was the lower Scruton number.

There might be two causes for the lack of hysteresis. Either there's no conditional lock-in which can lead to hysteresis or the turbulence intensity and stronger vortex-process (compared to rough cylinder) triggered the high amplitude vortex-induced vibration response more easily when $\omega_q \lesseqgtr 1$. The latter can be observed in numerical simulations of a nonlinear, coupled wake-oscillator model (for modeling vortex-induced vibrations) with strong added noise and force (cf. the work of Aswathy and Sakar [142]). Conditional lock-in is here defined as a lock-in region that's sustained when either decreasing or increasing the speed when the vibration amplitude already is high. Conversely, if the amplitude is low when changing the speed, it will remain low.

There were similarities between the amplitude responses of the rough and smooth cylinders. For both, the response was much lower with large Scruton numbers ($Sc > 9$) with more random response time histories even at the highest amplitudes. Additionally, the vortex-induced vibration range was approximately the same when using the dimensionless speed ω_q and can be

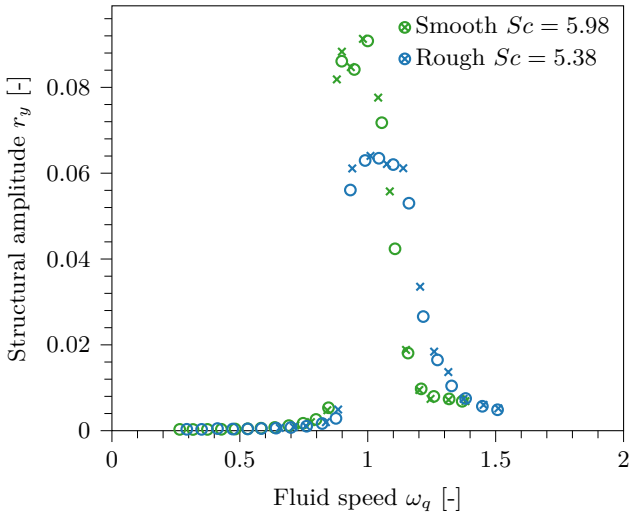

Figure 5.10: *Response for the cylinders without atmospheric boundary layer. ∘ marks experiments with increasing speeds and × decreasing.*

found in the range $\omega_q \in [0.8, 1.4 - 1.5]$. The general behavior with increasing speed was also the same. Overall, this speaks volumes about the usefulness of this dimensionless fluid speed (which is similar to the vortex-induced vibration speed ratio in design codes [5, 55]) and should be preferred over the reduced speed given in (2.18) when dealing with vortex-induced vibrations.

Overall, the effect of roughness on the amplitude response was smaller than expected when compared to the statement of Vickery and Daly (loading up to 400% greater) [4]. As the Strouhal numbers also were quite similar for the rough and smooth configuration (see figure 5.5b), it might be enough to add an atmospheric boundary layer when simulating super-critical flow for a model of this size, scale and aspect ratio.

Amplitude response without an atmospheric boundary layer

The response increased for both the smooth and rough cylinders when removing the atmospheric boundary layer. This should be due to a stronger vortex-shedding process and larger SD lift coefficient as shown in chapter 4 when reducing the turbulence. This effect and subsequent increase in the response was stronger for the smooth cylinder were the response increased even if the Scruton number was 33% higher. As seen in figure 5.10, the highest amplitudes for the rough cylinder was in the range $\omega_q \in [0.9, 1.2]$ but some degree of vortex-induced vibration can be found in the range $\omega_q \in [0.8, 1.4]$. This vortex-induced vibration range was slightly smaller but consistent with the range found using an atmospheric boundary layer. What's more interesting about the response, and really differentiates it from the results with an atmospheric boundary layer, was the nonlinearity. At $\omega_q = 0.9$, the response shot up and then stayed fairly constant before rapidly dropping starting at $\omega_q = 1.15$ which was in contrast to the more rounded amplitude response with the atmospheric boundary layer.

The smooth cylinder had a similar jump in vibration amplitude at low dimensionless speeds as shown in figure 5.10 but had, like the Strouhal number evolution in figure 5.5b, an odd amplitude response. For the smooth cylinder, the flatter, high amplitudes were in the range $\omega \in [0.85, 1]$ and was followed by a gradual but rapid decrease in vibration amplitude. A possible explanation for this odd Strouhal number and amplitude response is that the Strouhal number measured at low vibration amplitudes was different from the linear Strouhal number with high amplitude vortex-induced vibrations. A higher Strouhal number would push the amplitude response towards higher dimensionless speeds and make the amplitude response more similar to the rough cylinder's.

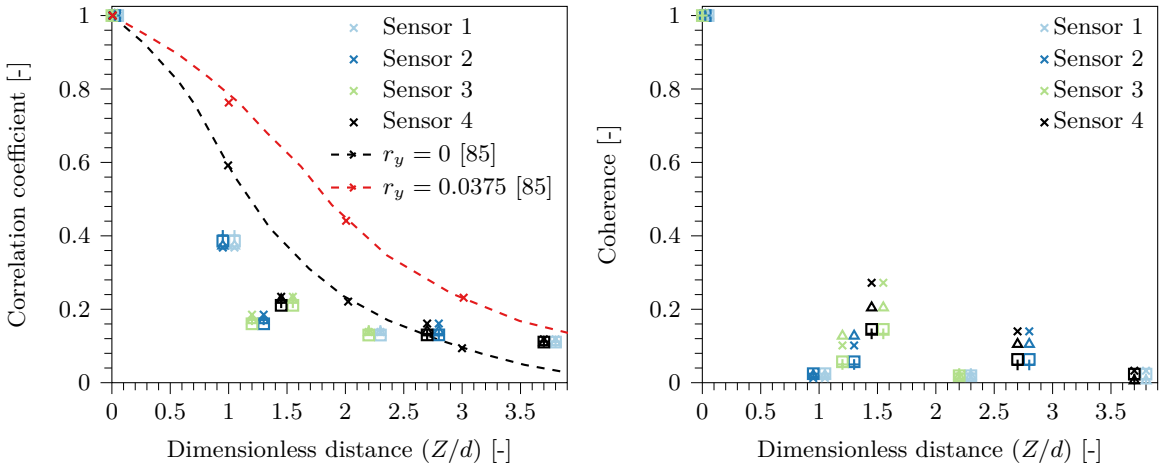

(a) *Correlation compared with the results of Howell and Novak [85].*

(b) *Coherence.*

Figure 5.11: *Coherence and correlation at different amplitudes but the same dimensionless speed ($\omega_q = 1.14$). The amplitudes are $\times = 0.059$, $\triangle = 0.041$, $\square = 0.0062$ and $+ = 0.0028$.*

When combining the results for tests with and without the turbulent atmospheric boundary layer, it becomes clear that there's a roughness or simulated Reynolds number effect when testing without the boundary layer but this disappears when adding it. This was seen for both the vortex-shedding frequencies and the amplitude responses which were quite similar when testing without the atmospheric boundary layer but different without it. In other words, adding a Eurocode terrain category II atmospheric boundary layer could be enough to simulate the super-critical Reynolds number response due to vortex-induced vibrations of cylinders with similar aspect ratios and scales. This matches the results of Batham [60] who found that a turbulent boundary layer was enough the recreate the random response of a full-scale chimney (super-critical Reynolds numbers).

5.3.3 Correlation and coherence

The correlation and coherence (defined in section 2.1.4) as a function of distance (measured in diameters) is shown in figure 5.11. As a reminder, sensor 1 is placed 1 diameter below the tip, sensor 2 is placed 2 diameters below the tip, sensor 3 is placed 3.25 diameters below the tip and sensor 4 is placed 4.75 diameters below the tip. The results are from the rough cylinder with atmospheric boundary layer and is compared at four different amplitudes using the same wind speed. As 3D effects can affect the correlation and coherence, the reference sensors used to calculate the statistics are marked by color. This way, the sensors used to calculate the statistics at a given distance can be identified by two differently colored markers placed next to each other.

The correlation, shown in figure 5.11a changed little with amplitude. Most of the changes in correlation were related the distance between two sensors and the correlation dropped near exponentially with distance. This drop was consistent with the 3D pressure correlation results of Howell and Novak [85] but their correlation was higher even without motion. While lower, the differences between the present wake measurements and pressure correlation were less for these elastic 3D cylinders than for the stationary 2D cylinders presented in chapters 3 and 4.

Unlike the correlation, the coherence at a given location is increased with the amplitude as figure 5.11b shows. Even with the increase, the wake measured coherence was significantly lower than the correlation at most distances and amplitude levels. This goes against the 2D results at large and small-scale (chapters 3 and 4) where the coherence was consistently greater than the correlation which implies that the vortex-cells are smaller and vortex-process weaker. The

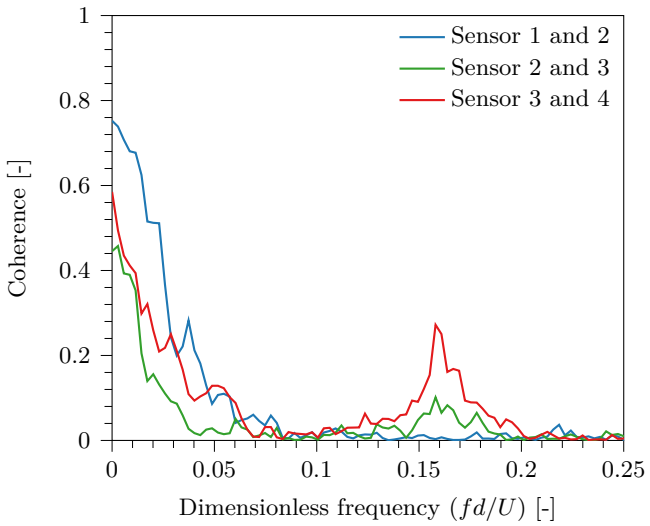

Figure 5.12: *Response for the cylinders without atmospheric boundary layer. ∘ marks experiments with increasing speeds and × decreasing.*

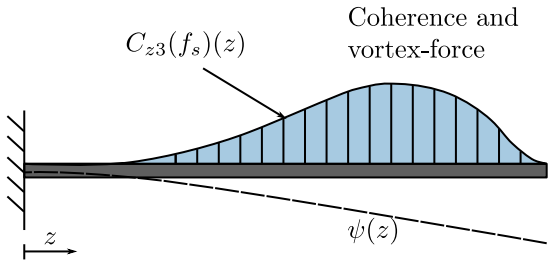

Figure 5.13: *Possible shape of maximum coherence. Inspired by sketch by Ruscheweyh [49].*

exception to the change in coherence with amplitude is when using sensor 1 (near the tip) as the reference. With sensors 1 as the reference, the coherence barely changed with amplitude. As this sensor is near the tip, tip effects and tip shedding could dominate and suppress the more regular vortex-shedding seen at other sensors. An example of the coherence is shown in figure 5.12 for the rough configuration with a Scruton number of 5.47 at a speed of 19 m/s (× in figure 5.11).

While the correlation almost dropped like an exponential function, the coherence did not (with the exception of when sensor 1 was used as reference). Instead, the coherence along the 3D cylinder should be more like what's shown in figure 5.13. Because of end-effects, regular vortex-shedding should be absent near the tip (tip-vortex instead) and the point of maximum vortex-lift force (and best reference point for coherence) lower down. This point was a few diameters from the tip (around $y = 0.7$ or 0.8 or 3-5 diameters from the tip) and was similar to what Howell and Novak [85] and Kareem et al. [35] observed and expressed for pressure and lift correlation. With more measurement points, or a moving set of sensors, the exact shape of the 3D coherence could be determined. From this maxima, the coherence and force strength as a function of position should drop like a bell shaped curve ($\sim$ log normal[7]).

This vertical coherence pattern is not accounted for in spectral model of Vickery and Basu [32, 88] but is similar to what was found by Ruscheweyh [49] for forces on cantilevered cylinders due to vortex-induced vibrations. It's therefore possible that the spectral model can be improved by using a coherence (or correlation) function with this kind of shape instead of the one that is currently used in the model. The coherence is not included in most wake oscillator models

[7] An alternative function, is an exponential function multiplied by a sine function with origin at the tip.

as they tend to be limited to 2D models and this finding could help in analytically deriving 3D parameters used in the model (e.g. the wake forcing strength and nonlinear damping).

5.4 Summary of small-scale aeroelastic results

The response and wake characteristics was measured for several flexible, 3D cylinders in an atmospheric wind tunnel using 1:100 scale models. The models were tested with two surface roughness conditions, with the rough giving super-critical Reynolds numbers and the smooth sub-critical, and two boundary layer configurations, Eurocode terrain category II and none. The wake characteristics were shown to be dependent on both the surface and flow conditions where both surface roughness and a realistic atmospheric boundary layer increased the Strouhal number independently.

When testing with the Eurocode type II boundary layer, the Strouhal number and response become more similar for the smooth and rough configurations than without it. This means that it's possible that several aspects of super-critical vortex-induced vibrations can be captured by a smooth cylinder when similar cylinders, scales and boundary layers are used. This can be related to the small-scale 2D experiments on stationary cylinders (chapter 4) and the results of Cheung and Melbourne [30] where strong added turbulence "smooths out" the force evolution with Reynolds number. When removing the boundary layer, there was a significant amplitude difference between the rough and smooth cylinder which should be due to the rough cylinders being at prematurely triggered super-critical Reynolds numbers with a lower unsteady lift and higher Strouhal numbers than the smooth sub-critical cylinder.

When increasing the Scruton number, there's a qualitative difference between low values (with harmonic vibrations) and higher values (dominated by random vibrations). In these experiments, the transition threshold was when increasing the Scruton number from 7.87 to 9.99 and the maximum amplitude was much lower beyond it. The presented result might be skewed as the highest Scruton number tests are with added mass which could have affected the equivalent mass (and thereby the Scruton number) differently than expected. Another possibility is that the response is not a function of Scruton number alone, as it's often presented as, but rather a combined function of mass, damping and aerodynamics rather than the singular Scruton number.

In addition to the 2D forces, the correlation and coherence along the cylinders' height is important. This was measured in the wake using the rough cylinder with atmospheric boundary layer only. Both of these statistics were found to be significantly lower at all distances when compared to their 2D counterparts. While lower, the 3D correlation was much closer to the 3D pressure correlation found in literature than for the 2D results. Even if the coherence grew with the amplitude, the correlation (which was fairly constant with amplitude) was higher than the correlation at all measured amplitudes of motion. This is different from the 2D results where the coherence was larger than the correlation.

The last correlation and coherence finding, was that the correlation dropped like an exponential function that's independent of the reference sensor but that the coherence was highly dependent on the reference sensor. If the coherence was measured along the entire height using a single reference point, it's likely that the shape would be a log normal probability distribution with the best reference point being 3-5 diameters from the tip for this cylinder.

Chapter

6 Field tests: The Bouin chimney

Chapter summary

This chapters presents a field-experiment on a custom-made 35.5 m tall chimney placed in real atmospheric wind near the Atlantic coast of France. These experiments supplement the wind tunnel experiments and the dimensionless response of this real chimney was higher than that measured with the wind tunnel models. This amplitude difference is mostly due to the lower Scruton number. There are two other related findings from the field tests: The response and incoming atmospheric boundary layer was dependent on the direction of the incoming wind. When the wind came from inland, the speed gradient was the greatest with height and the turbulence intensity the lowest and both profiles matched poorly with the statistical Eurocode boundary layer. This turbulence intensity reduction should be accounted for in design models as it should cause stronger vortex-shedding and larger response.

6.1 Background

To supplement the 2D and 3D wind tunnel experiments on pressure distribution around a cylinder and its response, a full-scale field chimney was designed and erected. As the Reynolds number and turbulence incoming flow impacts the pressure distributions and response, it's important to have actual data on vortex-induced vibrations of slender structure in an atmospheric boundary layer [5, 32, 49, 121]. As shown, the vortex-shedding at super-critical Reynolds numbers is re-established and strengthened in smooth flow but is this the case in the field?

Continuous measurements from monitored industrial chimneys are found in the literature [121–123, 125, 126, 128, 129] but the monitoring is often limited to acceleration data and a reference velocity. This is often due to limited access and opportunity to install extra sensors as the chimneys are in use. Additionally, these chimneys have been designed to or treated to limit vibrations meaning that the observed vortex-induced vibrations were small.

For other more well-studied field-experiments on circular structures, there are problems with the structural dimensions. Due to their smaller size, the high amplitude vortex-induced vibrations were at sub-critical or critical Reynolds numbers rather than super-critical [127, 133, 154]. The same problem was observed in wind tunnels where the speed required to reach super-critical wind speed was large (cf. the experiments of Belloli et al. on a rough cylinder [27]). This often required a higher natural frequency which should reduce the degree of motion (cf. the spectral vortex-induced vibration model in section 2.4.1).

To remedy the above (and to validate the design methodology and the wind tunnel experiments), a custom-made 35.5 m steel chimney was erected on a monitored wind field, in Bouin (near the Atlantic coast of France), and instrumented with several sensors. This chimney was designed to have a low Scruton number ($Sc < 2$) and to experience super-critical vortex-induced vibrations at moderate wind speeds ($U < 10$ m/s).

Figure 6.1: *Experimental chimney in the monitored field with the wind anemometer mast slightly visible (see figure 2 for details). Photo by Lilian Vezin.*

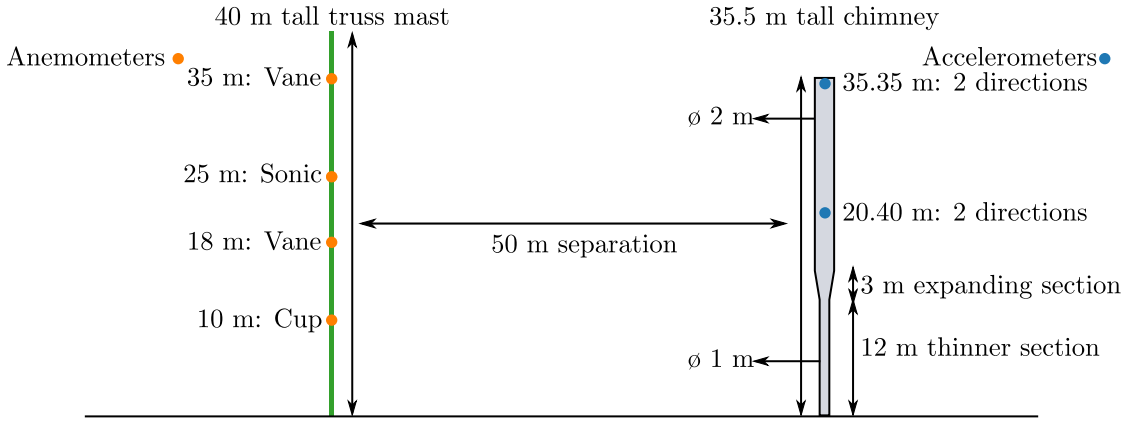

Figure 6.2: *Sketch with the dimensions of the chimney and wind anemometer mast as well as locations of anemometers and accelerometers.*

6.2 Chimney design and methodology

6.2.1 Structural characteristics of the chimney

The chimney used in this field-test was designed, manufactured and erected by Beirens (Poujoulat group) during the summer of 2020 and figure 6.1 shows it mounted in the field. This custom-made steel chimney had a height h of 35.5 m, a bottom diameter d_{bottom} of 1 m for the first 12 m and a tip diameter d_{tip} of 2 m for the last 20.5 m. In between these two sections, there's a 3 m long tapered section connecting the elements (see figure 6.2 for the setup).

This shape is unusual for a chimney and was chosen specifically for this experiment. Two of the criteria for the chimney were to have vortex-induced vibrations in the super-critical Reynolds number range ($Re > 10^6$) and that this would be at moderate wind speeds ($U < 10$ m/s) likely to be seen in the field. To achieve this, the larger diameter upper part was used to achieve a high Reynolds number, as this is the area where the vortex-lift should be most important, whereas the smaller diameter section added the necessary rigidity and support for a low critical wind speed. Structural characteristics of the chimney as measured after erecting the chimney (i.e. at

Table 6.1: *Structural characteristic of the chimney (as identified at the start of the experiment).*

d_{tip} [m]	d_{bottom} [m]	h [m]	$h_{d=2\ m}$ [m]	m_e [kg/m]	f_1 [Hz]	ζ_1 [%]	Sc [-]	Re_{crit} [-]
2	1	35.5	20.5	322.6	0.78	0.22	1.82	1.16e6

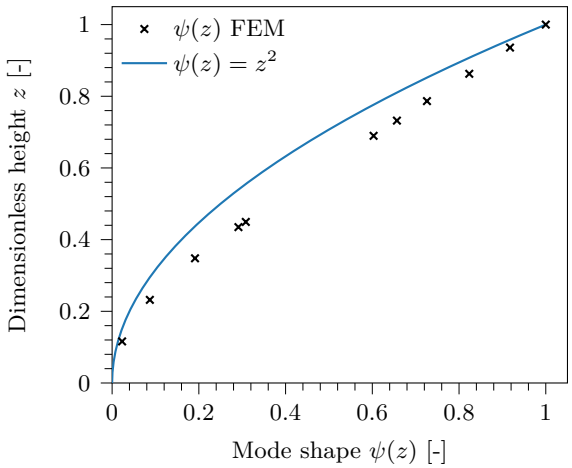

Figure 6.3: *Mode shape of chimney and simplified mode shape used in models [5, 55].*

the start of the experiments are given table 6.1). Both the first natural frequency (f_1) and the damping factor (ζ_1) were estimated from free vibration tests.

The equivalent mass, m_e, was calculated by the chimney designers using an equation similar to (2.9) and using the mode shape ($\psi(z)$) and modal mass found during the design phase using CAD and FEM tools. Figure 6.3 shows the mode shape found using FEM tools and is compared to an often used approximation of a chimney's mode shape ($\psi \approx y^2$) [5, 55]. From it, it can be seen that the assumed and FEM mode shapes have similar shapes but different relative deflection at most heights. As they are fairly close, the simpler to use assumed mode shape will be used in later sections involving the predictive design code models instead of the discrete FEM mode shape.

The low Scruton number, calculated using equation (2.14), should give a high amplitude response if there's well organized vortex-shedding. The maximum dimensionless amplitude (in tip diameters) was predicted to be either 0.31 using Eurocode's method 1 (Ruscheweyh's correlation length model [5, 49]) or 0.53 using Eurocode's method 2 (Vickery and Basu's spectral model [5, 32, 88]). When using aerodynamic values from the Eurocode ($St = 0.18$) [5], the critical wind speed for vortex-induced vibrations (when $f_s = f_n$) should be close to 8.7 m/s which made the critical Reynolds number $Re_{crit} \approx 1.16 \cdot 10^6$. This fulfills the requirements of vortex-induced vibrations at low wind speeds but at super-critical Reynolds numbers.

It is important to note that due to a damaged bolt, the natural frequency decreased to around 0.71 Hz. This was a reduction of almost 9% which affected the amplitude response and the dominant frequency of motion. It's suspected that this increased the damping factor of the first mode (ζ_1) but was not measured.

6.2.2 Field-test location and instrumentation

The chimney was mounted in a monitored wind field located in Bouin near the Atlantic coast of France (GPS coordinates 46,975, -1,998). According to the Eurocode [5], this area is in a wind zone category with 26 m/s as the 50-year reference wind speed. The site is surrounded by farmland with sparse gatherings of trees which makes the terrain category type II. Due to the remote location of the field, and the lack of nearby structures, the model chimney has been

designed without fear of loss or damage of human life, animal life or nearby structures.

The chimney was instrumented with two bi-directional accelerometers, one at 20.4 m and one at 35.35 m (near the top) as shown in figure 6.2. Their measuring range was ±2 g and the acquisition frequency was set to 10 Hz. Wind velocity was measured at four heights using wind anemometers mounted to the 40 m tall truss mast located 50 m northwest of the chimney (see figure 6.2). Vane anemometers, measuring velocity, were placed at heights of 18 and 35 m and a cup anemometer (speed only) was located at 10 m. These anemometers only recorded wind statistics (e.g. mean and standard deviation of speed and direction) over a 10-minute period.

In addition to the wind statistics, the unsteady velocity (three components) was measured using an additional sonic anemometer located at a height of 25 m height. The acquisition frequency of this sensor was 5 Hz. While the sonic anemometer's recording frequency was different from the accelerometers, the recordings were time synchronized. The locations of the sensors and relative locations of the mast and chimney are sketched in figure 6.2.

6.2.3 Data analysis process

The vibration and wind results shown in the present study are based on 1872 ten-minute records gathered at 35 m over a sequential 13-day period in September 2020. Additional wind data, gathered using all anemometers, were used to plot the mean wind gradient.

Each ten-minute sample was analyzed by first finding the mean velocity and dominant wind direction. This was used for two things: 1) to transform the acceleration and displacement to across and along wind directions and 2) to sort and group the response and dominant vibration frequencies calculated from the top bi-directional accelerometer. The displacement $y(t)$ was calculated from the acceleration $a(t)$ following the method outline in section A.1 which uses the inverse Fourier transform of the frequency corrected acceleration spectrum $A(\omega)$. To eliminate low frequency noise, a fifth order high-pass Butterworth filter with cutoff frequency of 0.3 Hz was applied to the acceleration data. The response envelopes of the displacement were calculated using the Hilbert transform [153]. From this envelope, the response amplitude statistics (e.g. the mean and maximum) were calculated for each 10-minute recording.

A statistical analysis was performed, using all 1872 samples, to plot the probability distribution of the vibration amplitudes and associated dominant frequency as a function of wind velocity and direction. These probability distributions were calculated using a statistical kernel function [155] and plotted as violin plots with added box plots. The kernel used here, is the standard kernel used in Python's Matplotlib package (versions 3.7.0 and 3.2.2 respectively).

6.3 Wind characteristics

6.3.1 Distribution of wind speed and direction

The top vane anemometer was used to create the wind rose shown in figure 6.4a which shows the distribution of wind speeds and directions. Northwesterly and northeasterly were the two most frequent wind directions and the most frequent speed range was 4 to 6 m/s. When ignoring the direction, the distribution of all wind speeds resembled a discrete log-normal probability distribution (see figure 6.4b) or a negative binomial distribution with a long tail at high speeds and short at low. The probabilities of a specific wind direction were found using the relative frequencies shown in the wind rose (figure 6.4a) and were: S–4,4%, SW–1,5%; W–1,9%; NW–29,5%; N–16,8%; NE–31,4%; E–11,4% and SE–3,1%.

Using the measured wind speeds and $U_{crit} = 8.7$ m/s, the probability of seeing a speed above $0.8 \cdot U_{crit} \approx 7$ m/s (Eurocodes recommendations for the onset of vortex-induced vibration), is 12.9%. As vortex-induced vibrations are only observed in a specific speed range, an upper limit to the investigated wind speed range can be added. This speed is here defined as $1.2 \cdot U_{crit} \approx 10.5$

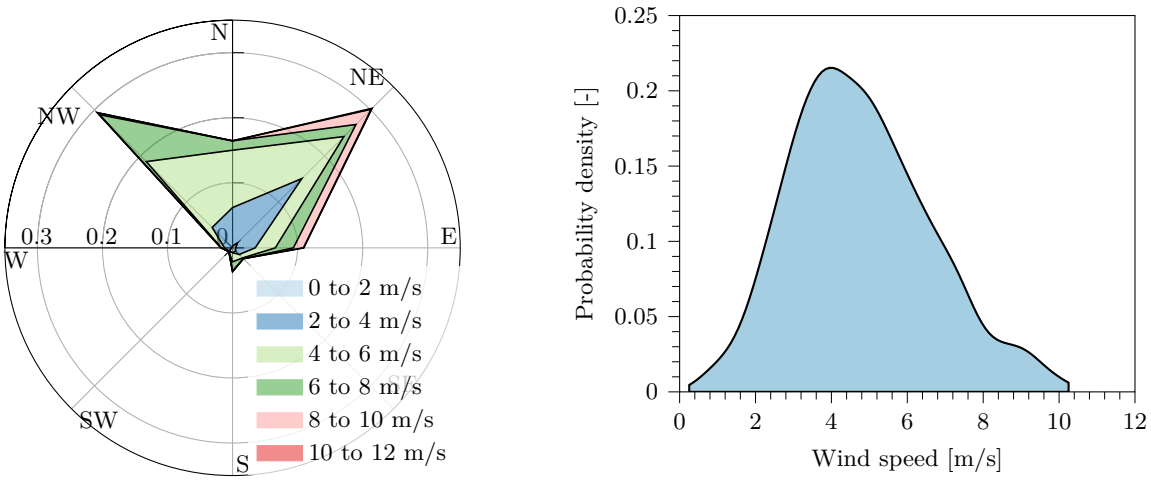

(a) *Wind rose with relative frequencies.* **(b)** *Probablity distribution of wind speed.*

Figure 6.4: *Wind rose showing wind distribution and probability distribution of observed wind speeds.*

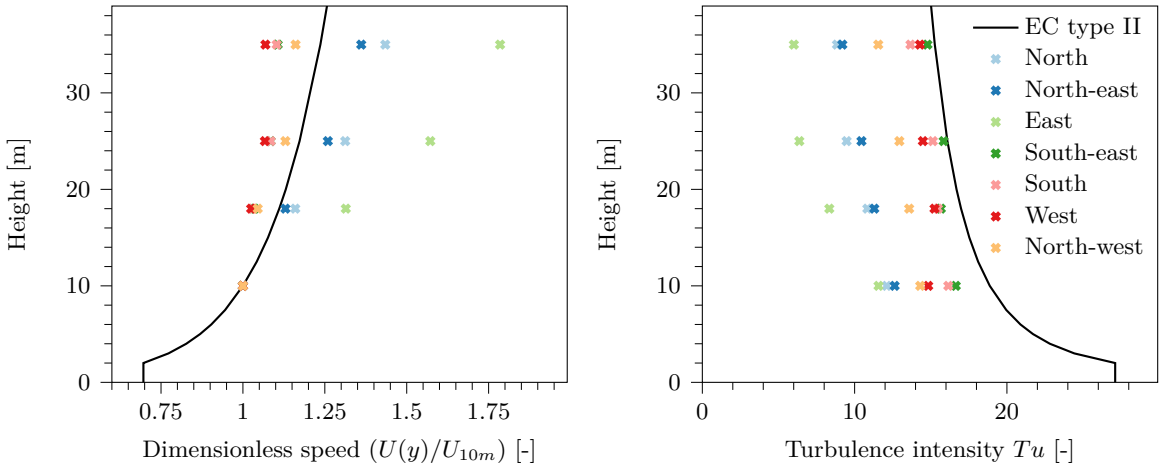

(a) *Speed profile.* **(b)** *Turbulence profile.*

Figure 6.5: *Mean wind profile for the cardinal and ordinal directions compared with the terrain category II wind profile from the Eurocode [5].*

m/s which is when one of the Eurocode design methods gives the highest amplitude [5]. This gave the same observation frequency because 10.44 m/s was the maximum observed mean wind speed.

6.3.2 Mean incoming wind profiles

The mean wind speed and turbulence intensity as a function of height are shown in figure 6.5 for all eight cardinal and ordinal directions. These mean profiles were based on all 10-minute wind samples with a mean wind speed greater than 5 m/s at 35 m. The turbulence intensity $I(z)$, is defined as the standard deviation of speed at a given height divided by the corresponding mean speed. The Eurocode's mean wind speed and turbulence profiles for terrain category II are also plotted in figure 6.5.

It is evident that the mean speed and turbulence profiles strongly depended on the wind direction. While the Eurocode type II mean speed profile was close to a median profile in comparison with the experiments, the Eurocode type II turbulence profile overestimates the turbulence intensity for all directions. A direct comparison with Eurocode atmospheric boundary

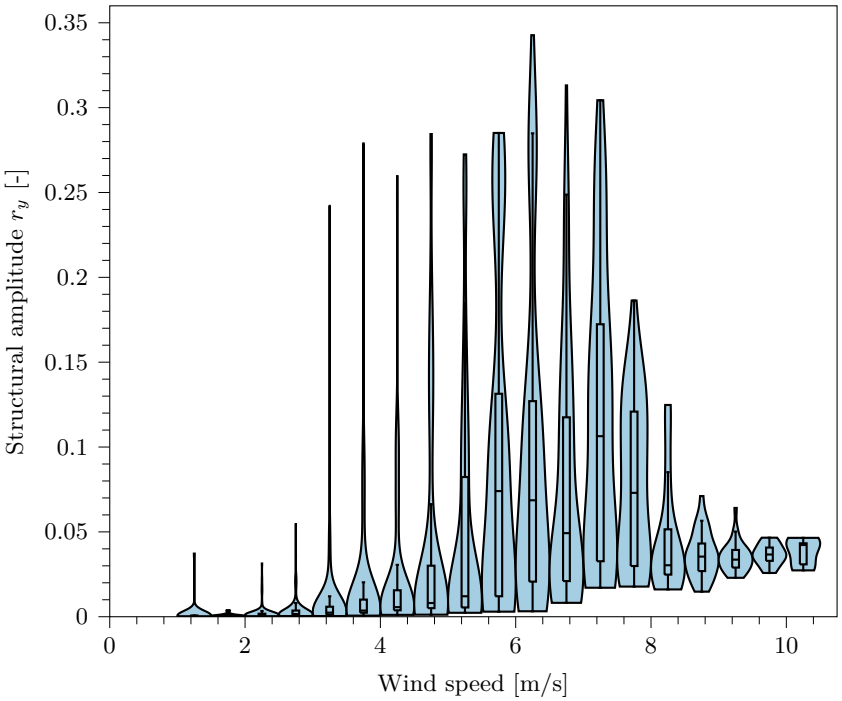

Figure 6.6: *Probability distributions of maximum dimensionless amplitude (using d_{tip}) at a given speed range. The interior rectangle and lines are box plots showing summary statistics.*

layer profiles should then be considered with some caution as they're related to the reference 50-year wind speed (ten-minute at 10 m) and not the instantaneous. Nevertheless, this low-to-moderate wind speed campaign highlights relevant information on the incoming wind useful for vibration analysis.

Northwesterly wind, which has the highest probability of occurrence, had a mean speed profile close to the Eurocode type II model but a lower turbulence intensity (slightly less than 12% at 35 m vs. 15% for the Eurocode). The easterly wind, accounting for 11.4% of the observed wind and much of the vortex-induced vibrations of the chimney, was characterized by the largest speed gradient with height and the lowest turbulence intensity (around 6% at 35 m). In other words, the wind coming from inland and headed towards the ocean had the strongest shear and lowest mean turbulence intensity at the heights measured.

6.4 Cross-wind vibrations

Following the data analysis process in section 6.2.3, a statistical analysis of the chimney's cross-wind vibration was performed. Statistical distributions of the maximum dimensionless amplitude of vibration (r_y with d_{tip} for normalization) and associated dominant frequency (normalized with f_1), are plotted in figures 6.6 and 6.8 as a function of wind speed and direction in figure 6.7.

The results are reported using violin plots as a function of discrete wind speed groups (speed ± 0.25 m/s) using mirrored probability distributions of the data along the y-axis. The exceptions are for 1.25 and 10.25 m/s grouping all speeds below 1.5 and above 10 m/s respectively. In addition to the violins, box plots with summary statistics (median and quartiles) are shown. One benefit of violin plots over box plots is that they show the distribution of the data. This is particularly useful for multimodal processes where the most likely value, associated with the widest point of the violin/density, can differ from the median value [156]. Note that the mirrored probability distributions shown in figures 6.6–6.7 are scaled to a fixed width for all speeds and direction for visibility. Moreover, the tails of the probability distributions contains artifacts of

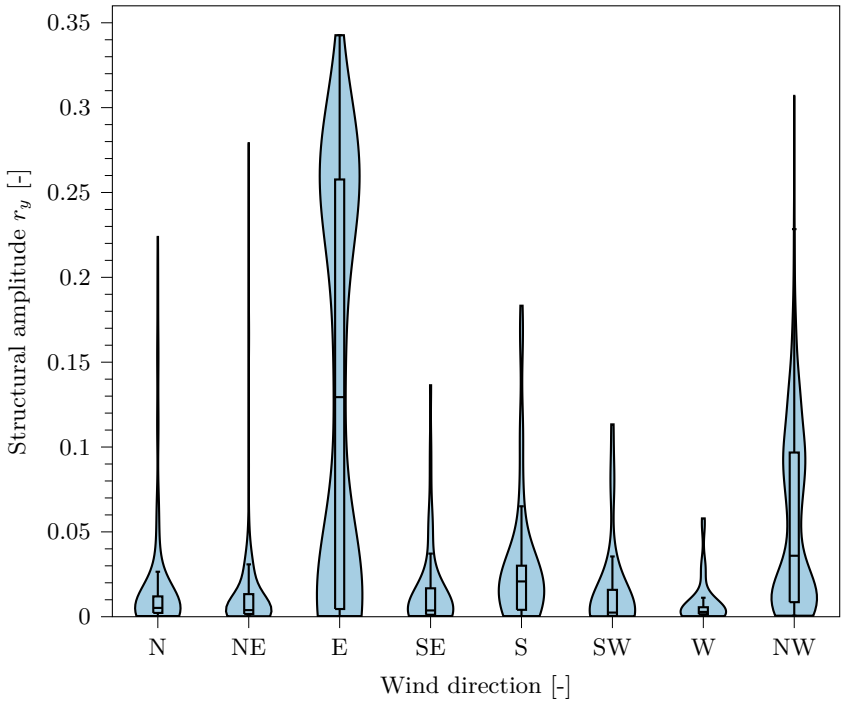

Figure 6.7: *Probability distributions of maximum dimensionless amplitude (using d_{tip}) for different directions ±22.5°. The interior rectangle and lines are box plots showing summary statistics.*

the kernels used and were removed.

As pointed out in section 6.3, the wind direction strongly affected the mean wind speed and turbulence intensity profiles. The wind direction should therefore have a significant impact on the chimney's cross-wind vibration. Statistical distributions of the maximum dimensionless amplitude of vibration are therefore plotted in figure 6.7 as a function of wind direction. The directional groups used in figure 6.7 are the cardinal and ordinal directions ±22.5°, with 0°±22.5° defined as northerly wind and 90° ± 22.5° as easterly.

6.4.1 Amplitude response

Figure 6.6 clearly shows that high amplitude cross-wind vibrations were observed at wind speeds between 5 and 8.5 m/s. The maximum amplitude, up to 35% of the diameter (0.7 m), was observed at speeds between 6 and 6.5 m/s. This maximum amplitude was close to the one calculated using Eurocode's method 1 (based on Ruscheweyhs approach [49]) and 35% lower than the one calculated using Eurocode's method 2 (based on Vickery and Basus approach [32, 88]). However, this maximum amplitude was observed at a wind speed 2 m/s lower than the one suggested by Eurocode. This suggests that the Strouhal number might be higher at these high Reynolds numbers ($Re \approx 8.3 \cdot 10^5$ at $U = 6.25$ m/s), that the natural frequency was lower than measured at the start of the experiments or a combination of the two.

There were cases of amplitudes greater than 20% of the diameter at speeds below 5 m/s. In most of these cases, the vibration amplitudes were already high and the mean speed was slowly reducing from the lock-in speed region over several 10-minute recordings (see hours). This low speed, high amplitude response continued until the mean wind speed reached as low as 3.3 m/s. Similar conditional lock-in phenomena were observed in the wind tunnel experiments, detailed in chapter 5, when decreasing the speed. For other cases (1-2 samples), the high amplitudes were due to the speed increasing to the lock-in range at the end of the 10-minute interval.

Lower amplitude levels (less than 15% of diameter) were frequently observed in the wind speed range 5 to 8.5 m/s. Based on the violin plots, the lower amplitude vibrations are more likely

than the high amplitude vibrations (higher conditional probability). The probability densities of maximum amplitude as a function of the wind direction, shown in figure 6.7, suggest that most of the low amplitude vortex-induced vibrations are associated with northwesterly wind. This wind direction was the most frequently observed direction and has a high likelihood of low amplitude vibration. Similarly, the high amplitude vortex-induced vibrations were most likely and frequent for the easterly wind with the lowest turbulence.

No vibration amplitudes greater than 7.5% of the diameter were observed for wind speeds higher than 8.5 m/s. From 8.5 m/s to 10.25 m/s (which groups all speeds above 10 m/s), one can observe that the probability distributions of the maximum amplitude are more centered with a median value that gradually increases with the speed. The vibrations should therefore be due to turbulence-induced vibrations.

6.4.2 Frequency of motion

At speeds above 8.5 m/s the probability distributions of dominant frequency were more surprising than the response. For turbulence-induced vibrations, a dominant frequency close to the first natural frequency of the chimney is expected ($f/f_1 \approx 1$). Instead, the shape of the violin plots reveals two highly likely dominant frequencies (see for example figure 6.8 at $U = 8.75$ m/s): one with normalized frequencies between 0.9 and 1 and the other with normalized frequencies between 0.8 and 0.9. As reported in section 6.2 a damaged bolt was observed at the end of the test campaign. A check of the random vibration data showed that the chimney's first natural frequency decreased by 9% towards 0.71 Hz. This could explain the peculiar distribution of the dominant frequencies during turbulence-induced vibration regime.

While the probability of high amplitude vortex-induced vibration was low for speeds below 5 m/s, the evolution of the dominant frequency's probability distribution with speed (seen in figure 6.8) is interesting. Up to 4.75 ± 0.25 m/s, two distinct frequency groups were found. The first group contains the median frequencies which increases almost linearly with the wind speed. The second group contains normalized frequencies between 0.9 and 1 and its conditional probability increases with speed. The first group is clearly related to vortex-shedding while the second is due to a combination of turbulence-induced vibrations and vortex-induced vibration at lock-in for a few recordings (conditional lock-in). At speeds between 5 and 8.5 m/s, the dominant frequency was mainly clustered around 0.9 and should be related to lock-in (frequency entertainment) and vortex-induced vibrations. Instead of 12.8% of the observed wind speeds, this lock-in region makes up 37.7% which is almost three times as much.

6.4.3 Directional response statistics

Relevant information on the directional response statistics is found in figure 6.7. Easterly winds (low turbulence) were the most favorable to generate high amplitude vortex-induced vibrations ($> 30\%$ of tip diameter). This wind direction also has the highest conditional probability of maximum amplitudes greater than 15% of the diameter (near 50% of the maximum amplitudes were above 15% of the diameter).

For southerly wind, vibrations up 18% of the diameter were observed but the conditional probability of high amplitudes were low. Instead, the shape of the violin plot for southerly directions shows a high conditional probability for vibrations lower than 5% of the tip diameter, even if much of the incoming wind in this direction is in the vortex-induced vibration speed range, and this could be turbulence-induced vibration. According to figure 6.5b, the turbulence intensity is high for this direction, close to 15% at 35 m height, giving stronger turbulence-induced vibrations. Vortex-induced vibrations were also observed with the more turbulent northwesterly winds, but tended to be at significantly lower amplitude of vibrations.

The conditional probability of wind speeds in the range 5 to 8.5 m/s was highest for easterly, northwesterly and southerly winds (59.6% for northwesterly wind, 47.6% for southerly and 42.7%

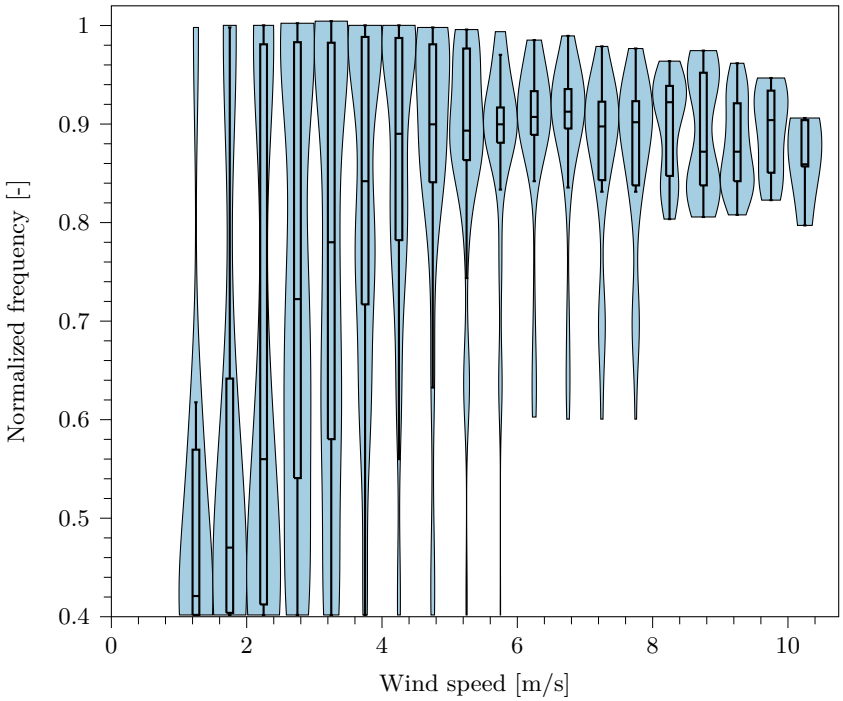

Figure 6.8: *Probability distributions of dominant frequency of motion (using f_1) at a given speed range. The interior rectangle and lines are box plots showing summary statistics.*

for easterly wind, see figure 6.4a for visual). For northerly and northeasterly wind, on the other hand, it's much more likely to see speeds below 5 m/s and low amplitudes. This might explain why some of these directions have higher conditional probability for high amplitude vortex-induced vibrations. Easterly winds (wind towards the ocean) also had the strongest speed gradient with height (figure 6.5a) and the lowest turbulence intensity (seen to be less than 6% at a height of 35 m in figure 6.5b compared to 12% for the northwesterly wind).

While the full impact of shear flow on vortex-shedding and vortex-induced vibration isn't fully understood, it's known that vortex-induced vibrations are stronger for low turbulence 2D flows [32, 37, 78, 88, 90]. This was also shown in the present study due to the atmospheric boundary layers (see speed and turbulence intensity) naturally varying with the direction.

6.5 Summary of field-test results

A custom-made chimney with a large tip diameter (2 m) and low Scruton number ($Sc = 1.82$) was erected in a monitored wind field, near the Atlantic coast of France. Preliminary vibration results and wind characteristics obtained from this chimney during a sequential 13-day period in September 2020 were presented. The amplitude and frequency responses were reported in terms of probability distributions and plotted as a function of both wind speed and direction. As expected two types of cross-wind vibrations were observed, turbulence-induced vibrations and vortex-induced vibrations.

Vortex-induced vibrations with significant amplitudes were mostly observed for wind speeds between 5 and 8.5 m/s with a maximum amplitude near 6.25 m/s. This vortex-induced vibration range was lower than expected and there are two likely culprits: the reduced natural frequency (from 0.78 to 0.71 Hz) and a higher Strouhal number. When using a Strouhal number of 0.3 and a natural frequency of 0.71, the new critical speed becomes 4.73 m/s ($Re \approx 6.3 \cdot 10^5$) which doesn't fit with the literature. Vickery and Basu estimated that the maximum amplitude is when $U = 1.1 \cdot U_{crit}$ [113, 120] and Ruscheweyh when $U = 1.2 \cdot U_{crit}$ [49] but both are lower

than found here (maximum at $U \approx 1.3 \cdot U_{crit}$).

Vortex-induced vibrations were observed at low ($< 15\%$ of the diameter) and high ($> 30\%$ of the diameter) amplitudes of vibration in the speed range $U \in [5, 8.5]$ with the lower amplitudes being more likely. The results also showed that easterly winds with low turbulence were responsible for the highest amplitudes of vibration ($> 30\%$ of the tip diameter) while the low amplitude vortex-induced vibrations were mainly due to northwesterly and southerly winds with higher turbulence intensities. The wind directions giving high vibration amplitudes had wind profiles different from the Eurocode's and the lower turbulence intensities seen in the field could indicate that the Eurocode isn't as conservative it needs to be for vortex-induced vibrations. As the response changed with the direction and boundary layer profile, it's therefore safe to conclude that the atmospheric boundary layer has a significant effect on the response just like in the small-scale aeroelastic tests.

The goal of this test chimney was to gather vortex-induced vibration data at super-critical Reynolds numbers in real atmospheric winds. This has been accomplished but the test platform can be used for more. These preliminary results will help forecast specific vortex-induced vibration events which can be used when performing unsteady pressure measurements along the height of the chimney at super-critical Reynolds numbers with and without vortex-induced vibrations. This extra data will help strengthen the present results and improve our understanding of 3D vortex-shedding, pressure loading and vortex-induced vibrations at super-critical Reynolds numbers with different turbulence conditions.

Part IV

Predicting the response due to vortex-induced vibrations

Chapter

7 Mathematical modeling of response

Chapter summary

This chapters presents a new analytic approximation of a well-studied vortex-induced vibration model. The approximation is based on Facchinetti et al.'s wake oscillator model and was found to match well with numerical simulations. From this approximation, several new findings on the amplitude response were derived. For instance, an equation for the speeds giving an absolute lock-in region (high amplitude only) and two conditional lock-in regions (high and low amplitudes possible) was derived and the effect of mass-ratio and damping on it were investigated. In addition, an equation for the maximum response using the approximated model was postulated and its results match well with both the numerical simulations and the correlation length model from design codes.

7.1 Background

As shown in the field test chapter, chapter 6, the design models for vortex-induced vibrations used in the Eurocode predicted different amplitudes with one of them over predicting the response greatly. This behavior is not good and is partly why the Eurocode design models will exclude the correlation length in the next iteration[8]. But is the spectral model really the best model for predicting vortex-induced vibrations?

While critics might say that Ruscheweyh's correlation length model is a maximum response model only (assuming purely harmonic vibration), the same is true for the spectral model for most practical purposes and many Scruton numbers [5, 32, 49, 55, 88, 113]. With the spectral model, the amplitude response can only be calculated if the Scruton number is high enough (dominated by random vibrations) or if empirical corrections are applied. The former has a second adverse effect on the response: As the Scruton number decreases, the linear damping becomes negative and the response needs to greatly increase to create a positive total damping. There are attempts at fixing this damping issue, but they mostly end up reducing the full model from an amplitude response model to a simple maximum amplitude model.

In an attempt to create a better predictive vortex-induced vibration model, that doesn't require numerical integration or simulation, an existing nonlinear coupled wake oscillator model was approximated. These vortex-induced vibration models tend to be based on harmonic vibrations (which should be better at predicting response compared with the spectral model when the Scruton number is low (e.g. $Sc < 8 - 9$)) and use coupled, harmonic differential equations describing the applied force and response separately where one or more are nonlinear. The model focused on, was the wake oscillator model of Facchinetti et al. [14] as it's easy to work on and well-studied. From it, approximations of the amplitude response and the dimensionless speeds giving vortex-induced vibrations were derived as a function of mass-ratio and damping

[8]The CICIND design code already uses only the Spectral model.

factor in addition to a maximum amplitude equation.

7.2 A new amplitude approximation

7.2.1 Approximation of amplitudes and phase

The first step in approximating the coupled wake oscillator model of Facchinetti et al. [14], was to rewrite equations (2.36) and (2.37) (which define the system as per section 2.4) so that each equation only contains one acceleration term; this made the work easier. This is shown in equations (7.1) and (7.2) with the total structural damping given in equation (7.3) and using dimensionless time $\tau = t\omega_n$. From these equations, it can be seen that the structural acceleration coupling term in the wake has a different impact on the system when coupled with an elastic structure. Instead of being a single term coupling structural acceleration to the wake, the effect of structural motion on the wake is to reduce the natural frequency of the wake oscillator and to force it through a dissipative term dependent on damping and a reactive coupling term (structural speed and displacement respectively).

$$\ddot{y} + D(\omega_q)\dot{y} + y = \omega_q^2 M q, \tag{7.1}$$

$$\ddot{q} + \epsilon\left(q^2 - 1\right)\dot{q} + \omega_q^2(1 - AM)q = -AD(\omega_q)\dot{y} - Ay, \tag{7.2}$$

$$D(\omega_q) = 2\zeta + \frac{\gamma}{\mu}\omega_q. \tag{7.3}$$

Instead of numerically integrating this system of equations, equations (7.1) and (7.2) were approximated using a nonlinear approximation method like the Method of Averaging outlined in section A.5. This method assumes that the amplitude and phase of a differential equation slowly changes over a cycle and that they can be found by averaging a rewritten form of the differential equations over one cycle of oscillation; this reduces the solution process to solving two integrals involving trigonometric function which is trivial. When applied to this system, it reduced the system to equations (7.4)–(7.6) at steady-state conditions (amplitude and phase derivatives are zero) [157] as shown in section A.5.

$$r_y = \frac{\omega_q^2 M}{D} r_q \sin(\theta), \tag{7.4}$$

$$r_q = 2\sqrt{1 + \frac{\omega_q AM \sin(\theta)}{\epsilon D}\left(\sin(\theta) - D\cos(\theta)\right)}, \tag{7.5}$$

$$0 = \omega_q^2(1 - AM) - 1 + \omega_q^2 AM \sin^2(\theta) + \left(\frac{D}{\sin(\theta)} + \frac{\omega_q^2 AM}{D}\sin(\theta)\right)\cos(\theta), \tag{7.6}$$

In these equations, θ is the phase difference between the wake and structural motion and r_q and r_y are the wake and structural oscillation amplitudes. The total damping in the structural equation is frequency dependent but was this badly implemented with this approximation. Setting the frequency in $D(\omega_q)$ to $\omega_n = 1$ simplified the approximation and gave better results as shown in figure 7.1. As the aerodynamic drag term should only be notable during lock-in (the predicted amplitudes are low outside of lock-in), setting the frequency in $D(\omega_q)$ to a constant makes sense: During lock-in and high amplitude vibrations, the forced frequency should be at the natural frequency instead of the linearly increasing vortex-shedding frequency [33, 106, 157].

Equations (7.4) and (7.5) are trivial to solve once θ is known. By using trigonometry and algebra, an analytic closed-form solutions for θ was found by rewriting equation (7.6) to

$$0 = c_3 x^3 + c_2 x^2 + c_1 x + c_0, \; x = \sin^2(\theta)$$

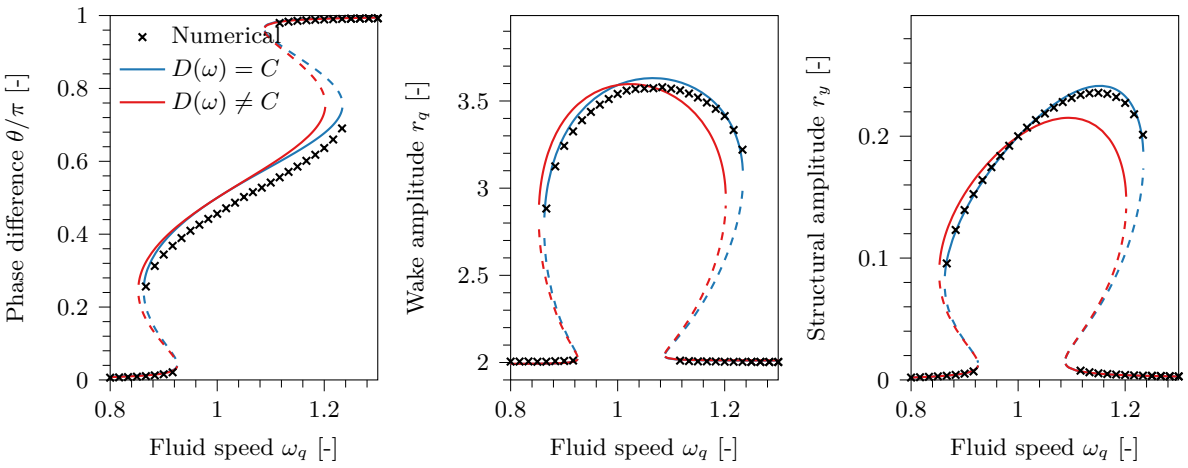

Figure 7.1: *Comparison of simulations of equations* (2.36) *and* (2.37) *and the approximations using: ϵ=0.3, A=12, γ=0.442, F=0.04, ζ=0.0019 and μ=72.9. Solid lines represent stable solutions and dashed unstable.*

$$c_3 = \omega_q^4 A^2 M^2 \left[1 + D^{-2}\right],\ c_2 = 2\omega_q^2 AM \left[\omega_q^2 (1 - AM) - 1\right] + 2\omega_q^2 AM - \frac{\omega_q^4 A^2 M^2}{D^2},$$
$$c_1 = \left[\omega_q^2 (1 - AM) - 1\right]^2 - 2\omega_q^2 AM + D^2,\ c_0 = -D^2. \tag{7.7}$$

This is a bi-cubic equation with three roots. Depending on the parameters and dimensionless speed, the solution for θ can have either three real number solutions or one real number and two complex number solutions. As the complex number solutions are non-physical, they are ignored.

The approximations are compared with numerical simulations of the differential equations (at several fluid speeds) in figure 7.1 with variable and constant frequency in the total damping $D(\omega_q)$. It shows that the approximation with constant damping frequency was similar to the numerical integration, but with extra solution branches and higher phase difference during lock-in, and that the approximation with variable damping frequency was different (smaller lock-in region). At two dimensionless speed regions, three solution branches were found whereas the numerical simulations only have two. To find out which solution branches are physically meaningful, a stability analysis was performed.

7.2.2 Stability of solutions

The system stability can normally be found by first rewriting the equations of motion in state-space form and then formulate the Jacobian ($\mathbf{J}$) using these state-space equations, find all fixed points, evaluate the Jacobian at all fixed points ($\mathbf{A} = \mathbf{J}|_{\mathbf{y}=\tilde{\mathbf{y}}}$) and finally solve the eigenvalue problem $[\mathbf{A} - \alpha\mathbf{I}]\,\mathbf{v}e^{\alpha t} = 0$. For the solution to be asymptotically stable (shrinking perturbations), all eigenvalues need to be negative. If one of the eigenvalues for a given fixed point is positive, then the point is asymptotically unstable (growing perturbations).

For equations (7.1) and (7.2), there's a simpler way of evaluating the stability. According to Balanov et al. [95], the stability of a forced van der Pol equation can be found from the phase difference equation by finding its derivative with respect to the phase. In other words, by taking the derivative $\mathrm{d}/\mathrm{d}\theta$ of equation (7.6), the stability of the approximated system in equations (7.4)–(7.6) can be evaluated. The equation governing the stability is given in equation (7.8) and was solved for all real number solutions of θ.

$$\alpha(\theta) = \frac{\omega_q^2 AM\cos(2\theta)}{2D} - \frac{D}{2}\csc^2(\theta) + \frac{\omega_q^2 AM}{2}\sin(2\theta) \tag{7.8}$$

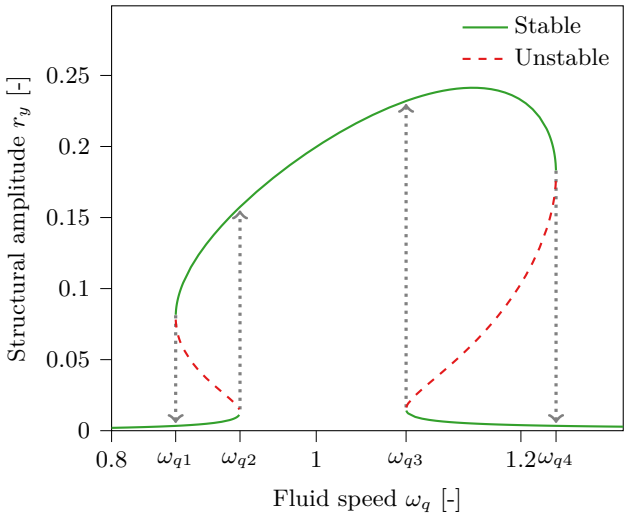

Figure 7.2: *Stability and boundaries of synchronization for given parameters. Dotted lines with arrows mark the jumps when sweeping ω_q.*

From figure 7.2, it can be seen that there were two stable amplitude branches, an upper and a lower structural amplitude branch, and an unstable amplitude branch in between them. The corresponding extra solution branches were also shown for the wake variable and the phase difference in figure 7.1 as dashed lines. These solution branches were not obtained in the numerical simulations as they would require perfect initial conditions and no oscillating force.

The unstable solutions do serve a purpose: They mark the amplitude thresholds for transitions to low or high amplitude solutions and regions with conditional lock-in. If at some point the structural amplitude is above the dashed line, the amplitude should grow until the high amplitude branch is reached. The same is true for low amplitudes and the lower branch. As the existence of this unstable amplitude branch seems to mark where synchronization and lock-in occurs, it's further investigated to find an analytical expression for the lock-in regions rather than finding them visually.

7.3 Predicting when vortex-induced vibrations occurs

7.3.1 Defining the lock-in regions

In the current design codes, the methods for determining when lock-in and high amplitude vortex-induced vibrations occurs are lacking. As a practical use case, a good lock-in definition enables designers to quickly estimate the speeds giving high amplitudes of vibrations and how the regions changes with the parameters. de Langre previously defined the lock-in region to be between $\omega_q = (1 \pm \sqrt{AM})^{-1}$ by linearizing the same system of equations as investigated here. This linearization was done by neglecting all damping terms and reduced the problem to a coupled-mode flutter problem [91]. The coupled-mode flutter analogy matches with the results of Zhang et al. who found that vortex-induced vibrations at higher dimensionless speeds ($\omega_q \in [1.11, 1.38]$) was similar to coupled-mode flutter [92]. Another lock-in definition based on the same set of equations was created by Denoël [144]. This was done using Cardano's formula and gave an approximation for the upper and lower bound of the three solution region.

The new lock-in definition was based on the approximate phase difference in cubic form, i.e. equation (7.7), which is similar to Denoël's approach. Instead of approximating the outer bounds of lock-in from Cardano's formula, the number of real solutions of this equation was

found from the discriminant[9] of equation (7.7). When the discriminant passes zero, it changes from having one to three real solutions (two stable and one unstable). This property was used to define the lock-in region as a function of ω_q and gives up to five amplitude regions: two conditional lock-in regions with two stable solutions, one absolute lock-in region with the high amplitude solution branch only and two locked-out region with low amplitudes.

Setting the discriminant of equation (7.7) to zero gives a bi-sextic equation in terms of ω_q which is two more than expected. Luckily, two of the solutions were trivial and could be ignored as they provide no physically meaningful solutions ($\omega_{q5,6}^2 = (D^2+1)/(1-AM)$). The start and end of the synchronization regions can then be found from the solutions of the bi-quartic equation system

$$\begin{aligned}
0 &= a_8\omega_q^8 + a_6\omega_q^6 + a_4\omega_q^4 + a_2\omega_q^2 + a_0 \\
a_8 &= (1-AM)^2[A^2M^2 - 4D^2(1-AM)], \\
a_6 &= 2[D^2(1-AM)(A^2M^2+8) + A^2M^2(AM+1)], \\
a_4 &= A^2M^2(D^2-1)^2(D^2+1)^2 - 4AMD^2(5D^2+1) - 8D^2(D^2+3), \\
a_2 &= 8D^2(AM+2)(D^2+1), \\
a_0 &= -4D^2(D^2+1)^2,
\end{aligned} \tag{7.9}$$

where only the positive solutions are kept; the negative solutions are mirrored with negative speeds instead of positive. The positive solutions of equation (7.9) are identical to the locations marked ω_{q1}–ω_{q4} in figure 7.2. An analytic solution to the quartic roots exists and was found using a symbolic solver. Due to the increased complexity and number of terms involved[10] the analytic solutions to this quartic equation are not presented.

7.3.2 Changes in lock-in region with mass-ratio and damping

If we assume that aerodynamic conditions are fixed, the two defining characteristics of this new lock-in region definition are the structural damping ratio ζ and the mass-ratio μ which scales the force M and the stall parameter γ in the total drag. As the lock-in region changes greatly at low mass-ratios[11], it is instead investigated by changing the mass-scaled force M. Changing both the mass-scaled force and the damping ratio produces a 3D plot of the lock-in regions. Instead of a 3D plot, the lock-in regions are investigated in figure 7.3 using slices with constant damping ratio or constant mass-scaled force. The total damping D was inferred from the mass-scaled force by keeping the drag and lifts coefficients and Strouhal number constant.

Figure 7.3a shows how the lock-in regions changes with mass-scaled force M. As seen, the solutions of equation (7.9) gives three different lock-in regions: a small conditional region for low values of M and $\omega_q < 1$, an ever-growing region of absolute lock-in and a region of conditional lock-in that persists with increasing M at $\omega_q > 1$. The small conditional region disappears quickly with increased mass-scaled force M and damping ratios ζ (see figure 7.3b) and therefore less likely to be observed in experiments. Still, if the model is adequate in predicting vortex-induced vibrations, the conditional lock-in region at lower ω_q shouldn't be ignored in wind engineering applications. Due to the relatively higher mass-ratios and low damping ratios, high amplitude vortex-induced vibrations could occur at lower fluid speeds than expected like in the experiments detailed in chapters 5 and 6.

The upper conditional region is different from the lower one. Like the lower, its extent grows at very low values of M before decreasing once M reaches a value of 0.002–0.004. Unlike the lower region, the extent of the upper region is relatively large when the shrinking starts and

[9] For a cubic equation, the discriminant is defined as $\Delta = 18c_3c_2c_1c_0 - 4c_2^3c_0 + c_2^2c_1^2 - 4c_3c_1^3 - 27c_3^2c_0^2$.

[10] When printed in the form root$_i$=... and using $AM = C$, the solutions consisted of 476683 characters.

[11] This makes the changes with mass-ratio less noticeable at higher mass-ratio.

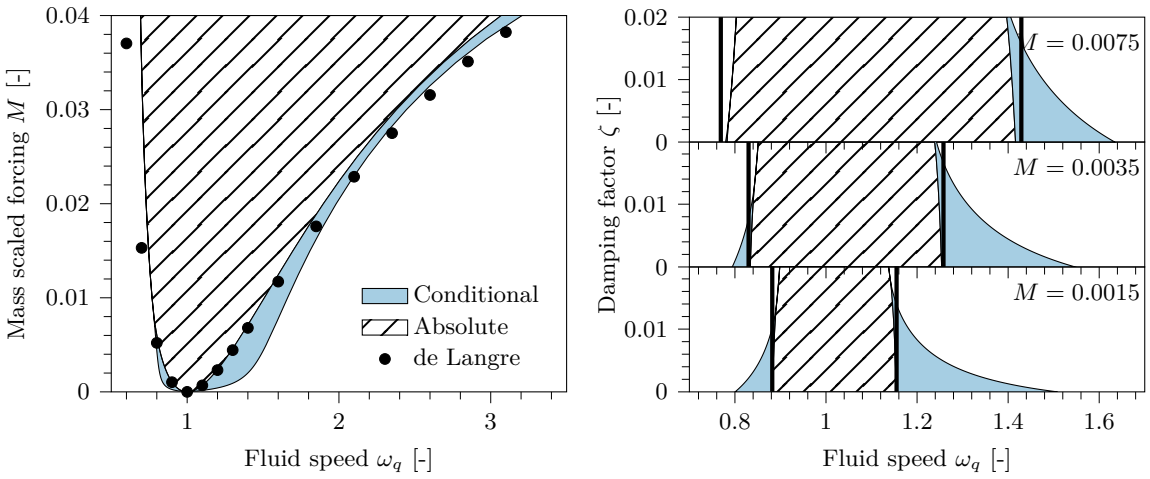

(a) *Lock-in region for changing $M = F/\mu$.*

(b) *Lock-in region for changing ζ.*

Figure 7.3: *Lock-in regions in terms of ω_q, M and ζ using: ϵ=0.3, A=12, γ=0.442, F=0.04, ζ=0.0019 and a variable mass-ratio μ.*

begins growing again when M reaches a value of 0.03 as figure 7.3a shows. While interesting, this growing region is unlikely to be experimentally observed for cylinders in air at super-critical Reynolds numbers as it requires a mass-ratio close to 10. This upper conditional lock-in region was previously detected experimentally for cylinders in cross-flow [33] and for freely rotating airfoils at high angles of attack [97] but was less noticeable in the experiments detailed in chapters 5 and 6. It's possible that method for calculating the response statistics (using the maximum amplitudes) obfuscated the region in the wind tunnel and field experiments.

For low damping ratios, the upper lock-in region is significant and should be accounted for in structural design and experiments. As the damping ratio is increased, the upper conditional region's size and importance decreases as shown in figure 7.3b. This behavior is similar to the lower conditional region. A difference from the lower region, is that the region's size decreases slower with damping ratio when mass-scaled force M is higher; this means that it can persist at significantly higher damping ratios.

The absolute region is the final lock-in region and should be observed regardless of initial conditions. The lines marking it as a function of ω_q has different slopes for ω_q greater or less than one. For $\omega_q < 1$, the slope is reminiscent of a function of the form $f(x) = a(x-1)^2$ (with $a \gg 1$) while the slope is more reminiscent of a higher degree polynomial for $\omega_q > 1$ with a slope that changes sign with ω_q. This shape is different from the forced oscillation lock-in region shown in figure 2.14b and discussed in section 2.2.3 as it does not have the distinct V-shape and by having more different lock-in regions around $\omega_q = 1$.

The absolute lock-in region grows rapidly with mass-scaled force and only decreases with damping once one of the conditional regions disappear. Before the disappearance of the lower conditional region, the absolute region stays fairly constant with the damping ratio as figure 7.3b shows. Once the lower region disappears, the absolute regions starts shrinking noticeably and uniformly with the damping ratio on both sides of $\omega_q = 1$.

The changes in the lock-in regions are compared with the undamped region predicted by de Langre's equation in figure 7.3. The previous definition should only predict the absolute synchronization region and is similar to it when the damping ratio and mass-scaled force are very low. As both parameters are increased independently, de Langre's lock-in region diverges from the new one and becomes wider than the total extent of the new conditional and absolute lock-in regions combined even at low mass-scaled force.

7.4 Predicted maximum response

In the design code models, there's an assumed dimensionless speed ω_q giving the largest response. For the Eurocode models, this is at $\omega_q = 1.1$ for the spectral model and $\omega_q = 1.2$ for the correlation length model [49, 113]. Similarly, the approximated coupled wake oscillator model will be better for design purposes if the speed at which maximum response occurs at can be determined a priori. By inserting the high amplitude analytic root solution for $\theta(\omega_q)$, equation (7.7), and the wake amplitude, equation (7.5), into the structural amplitude, equation (7.4), standard methods for finding the maximum response can be used. This is nontrivial to solve and a simpler method was sought. By inspecting the structural amplitude response and phase differences using different parameter values, the maximum amplitude was found to occur when $\theta_{max} \approx 0.65\pi$ but $\theta_{max} = 0.61\pi$ was found to give better restults at realistic damping values [157]. With this $\theta(\omega_q)$ approximation, the speed at maximum, $\omega_{q,max}$, can be found from equation (7.6) and the equations for maximum amplitude becomes

$$\omega_{q,max} = \sqrt{\frac{D\left[\sin\left(\theta_{max}\right) - D\cos\left(\theta_{max}\right)\right]}{AMD\sin\left(\theta_{max}\right)^3 + AM\cos\left(\theta_{max}\right)\sin\left(\theta_{max}\right)^2 + D\left(1-AM\right)\sin\left(\theta_{max}\right)}}, \tag{7.10}$$

$$r_y(\omega, \theta_{max}) = 2\frac{\omega_q^2 M}{D}\sin(\theta_{max})\sqrt{1 + \frac{\omega_q AM\sin(\theta_{max})}{\epsilon D}\left(\sin(\theta_{max}) - D\cos(\theta_{max})\right)}. \tag{7.11}$$

Figure 7.4 compares the approximated maximum amplitude and speed at maximum with results from numerical integration at several Scruton numbers. As seen in figure 7.4a, the predicted fluid speed at maximum response using the approximation was slightly higher than the numerical integration results at high Scruton numbers and slightly lower at low Scruton numbers. While slightly different, the speeds at predicted maximum response were consistent between the methods. When increasing the damping ratio alone, the speed at which the maximum occurs at was slightly increased for the numerical simulations (better resolution could make it clearer) and this is reflected in the approximation as well.

The predicted maximum amplitudes using the approximation, shown in figure 7.4b, were quite close to the numerical results indicating that the speed difference was negligible for finding the maximum amplitude. The main issue is that the approximated model starts becoming higher than the numerical integration results as the Scruton number decreases below 2. The above is also true when changing the structural damping.

The evolution of maximum predicted amplitude as a function of damping and mass differs between the spectral, correlation length and approximated coupled wake oscillator model. When ignoring the form of the nonlinear aerodynamic damping, the maximum predicting amplitude for the spectral model drops like equation (7.12) with C being a force strength constant. Similarly, the amplitude for the correlation length model drops like equation (7.13) and the new approximated model like equation (7.14) when ignoring the square root term in equation (7.11).

$$r_{y,max} \propto \frac{C_{spectral}}{\frac{m_e}{\rho d^2}(Sc - 4\pi K_a)} \qquad \text{Spectral model} \tag{7.12}$$

$$r_{y,max} \propto \frac{C_{correlation}}{Sc} \qquad \text{Correlation length} \tag{7.13}$$

$$r_{y,max} \propto \frac{2\pi F}{Sc + \pi^2\zeta C_M + \frac{C_D}{2St}} \qquad \text{Wake oscillator} \tag{7.14}$$

From these equations, the predicted maximum amplitude can be seen to be a function of the Scruton number alone or as a combination of the Scruton number and an aerodynamic parameter. The latter is consistent with Sarpkaya's sentiment of the Scruton number alone not

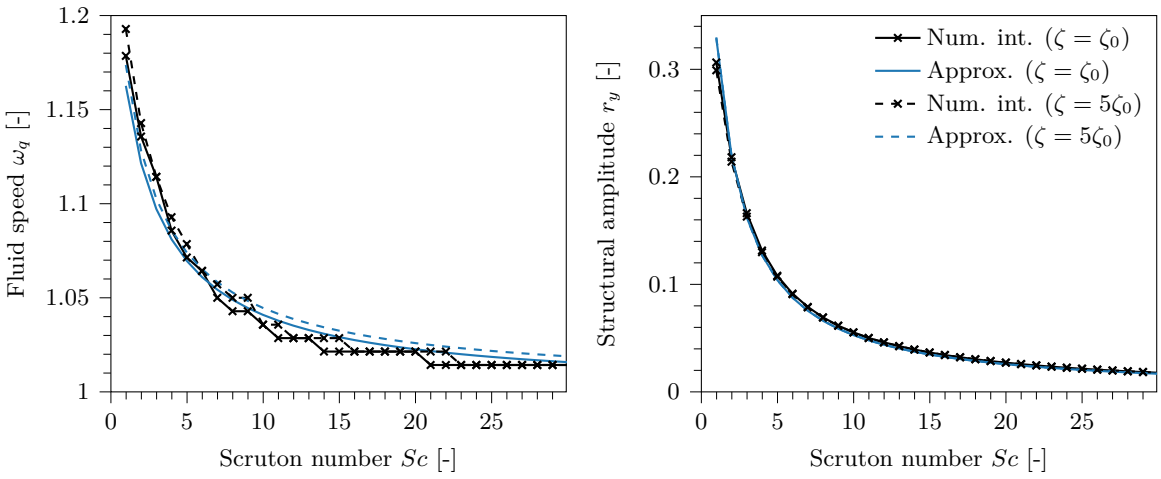

(a) *Speed at maximum amplitude* **(b)** *Maximum amplitude*

Figure 7.4: *Comparison of fluid speed at maximum amplitude and the amplitude from simulation and maximum approximation using: ϵ=0.3, A=12, γ=0.442, F=0.04, ζ_0=0.0019 and μ=72.9.*

being enough for predicting response [106] (see section 2.3.3) which was also observed in the 3D wind tunnel experiments (see section 5.3.2).

The difference in predicted maximum amplitude is shown in 7.5 for a generic chimney with variable Scruton number using the Eurocode implementation of the spectral and correlation length model [5] and the novel approximation of maximum amplitude given in equation (7.11). While the wake oscillator has both a structural and an aerodynamic damping term in the denominator that varies independently of the Scruton number, their values are comparatively small at $Sc \gg 1$. Because of this, the predicted maximum amplitude behaves similarly for the wake oscillator and correlation length models at most Scruton numbers shown in figure 7.5. As the Scruton number is further reduced, the two models starts to predict different amplitudes as the Scruton number independent terms will limit the maximum amplitude in the wake oscillator but not in the correlation length model.

The spectral model, on the other hand, has three different regions of changing amplitudes: When the Scruton number is below 6 it barely changes with the Scruton number, when above 8 it has a moderate linear increase with the Scruton number and when in between there's a large nonlinear change in the predicted maximum amplitude. This is the region where the linear damping becomes increasing negative and the amplitude barely changes with ω_q. At these Scruton numbers, the response is decided by the vibration amplitude required to keep the total damping positive and the forces can be simplified to a constant.

7.5 An approximate summary

A new approximation of a nonlinear vortex-induced vibration model, based on the model of Facchinetti et al. [14], has been presented in this chapter. The model was approximated using the Method of Averaging which produced two simple equations for the wake and structural amplitude and a governing phase difference equation in the form of a bi-cubic polynomial. When setting the total structural damping to a constant value (instead of varying with fluid speed), the approximation was found to match well in terms of wake and structural amplitude but the phase difference could match better. As the goal was to predict the amplitude, the difference in the phase difference is of lesser importance.

From the cubic phase equation, more novel information on vortex-induced vibrations could be gained. As the number of real and stable phase difference solutions depended on the fluid

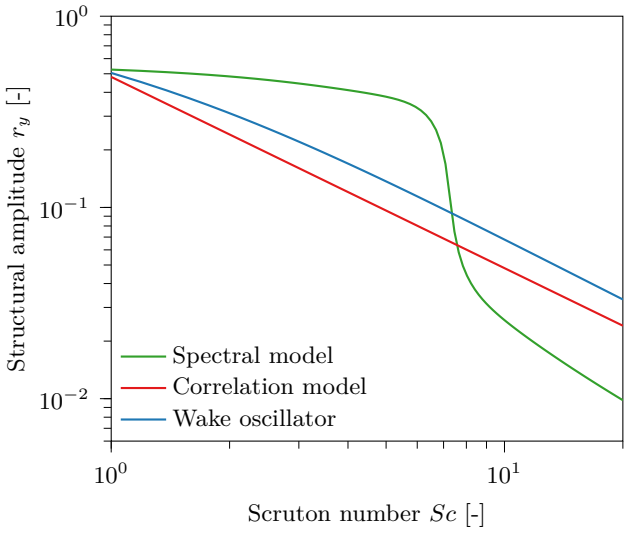

Figure 7.5: *Evolution of maximum amplitude with Scruton number for a generic cylinder (placed in a Eurocode type II terrain) with diameter 3 m, damping ratio of 0.2 % and natural frequency of 1 Hz and variable mass-ratio μ.*

speed, the number of solutions could be used to mathematically define when the lock-in regions started and ended. This was done by finding the discriminant of the cubic equation and by setting it to zero: When the discriminant passes zero, the number of real solutions goes from one to three and this defined the conditional and absolute lock-in regions.

This model has three lock-in regions and two locked-out regions with negligible amplitudes of vibration. The first lock-in region was a conditional region at $\omega_q < 1$(initial conditions determine if the amplitudes are high or low) and this branch existed for a limited range of mass-scaled force and damping ratios but could be observed in wind. The second region was an absolute lock-in region (always high amplitudes) and this region grows with the mass-scaled force with the growth being much stronger at $\omega_q > 1$. The effect of damping ratio on the absolute region was negligible at low damping ratios and only started being noticeable once the lower conditional region disappeared.

The last lock-in region was the upper conditional region. This region was much more noticeable than the lower region and was relatively wide when the mass-scaled force was low and smaller with high. The effect of damping ratio on it was similar to the effect on the lower region, i.e. it decreases with increased damping. Still the upper region persisted at much higher damping ratios than the lower. Additionally, the size of the upper conditional region decreased slower with increased damping when the force's strength was higher.

As designers are often interested in the maximum vibration amplitude only, an expression for the maximum amplitude was derived. This expression was based on the phase difference rather than choosing an arbitrary speed at which the maximum occurs. When investigating the amplitude response, it was found that the phase difference was approximately $\theta_{max} = 0.61\pi$ when the structural response was at its maximum. Using this, an expression for the speed at maximum response was derived and inserted into the structural amplitude equation which match well with numerical integration results. The resulting maximum amplitudes match well with the correlation model when plotting the maximum response as a function of the Scruton number. The wake oscillator model did not match well with the spectral model which predicted significantly higher amplitudes at low Scruton numbers and significantly lower at high Scruton numbers.

Chapter

8 Predictions compared with experimental results

Chapter summary

This chapters compares the predictive powers of the new analytic approximation with two design models. The comparison was done using both the amplitude response (using the results from small-scale tests and the field experiment) and the maximum measured response from a curated list of chimneys. The main finding of this chapter, is that the best model for predicting the maximum response depends on the Scruton number. When the Scruton number is low and amplitudes are high, the best model for predicting the amplitude response was the new approximation while the spectral model was the best when the Scruton number is high and vortex-induced vibrations are relatively low. When predicting the maximum response of real chimneys, the new approximation was found to be closest to the real life measurements on average.

8.1 Background

When designing a chimney or similar structures of circular cross sections, it's useful to know the maximum response and how the response changes with the fluid speed. The former is important when designing the structural supports and the latter is important when designing an effective vibration absorber. Unfortunately, many design codes focus on maximum response only and leave the amplitude response as a curiosity that can be ignored [5, 55].

On the other spectrum, there are models that are more suited for predicting the amplitude response but are less suitable at predicting the maximum response. This class of models includes the wake oscillator approximated in chapter 7 and similar models like the ones presented in section 2.4. The downside is that these models cannot be solved analytically and either need to be approximated, like in the previous chapter, or numerically integrated.

In this chapter, the experimentally obtained amplitude and maximum response are compared with the codified vortex-induced vibration models defined in section 2.4 (Vickery and Basu's spectral model [5, 32, 55, 88] and Ruscheweyh's correlation length model [5, 49]) and with the new approximated wake oscillator model described in chapter 7. This was done by comparing the models with the small-scale aeroelastic tests from chapter 5, the field-test from chapter 6 and the maximum amplitude of several chimneys from the literature [115]. The goal of this was to determine the strength and weaknesses of the various models and to determine the best vortex-induced vibration model for a given situation.

8.2 Model parameters and versions used

8.2.1 Design code models

There are two types of spectral models: those for finding the amplitude response and those for finding the maximum amplitude. Rather than using the approximate maximum amplitude

Table 8.1: *Aerodynamic coefficients, model parameters and Reynolds number region used for all cylinder and boundary layer configurations.*

Configuration	C_l [-]	C_d [-]	St [-]	A [-]	ϵ [-]	Tu [%]	K_{a0} [-]	Reynolds region
Rough w/ ABL	0.125	0.70	0.182	15	0.7	10.5	0.6	Super
Rough w/o ABL	0.150	0.70	0.176	15	1.0	1.0	0.6	Super
Smooth w/ ABL	0.223	1.20	0.178	10	0.7	10.5	1.2	Sub
Smooth w/o ABL	0.247	1.20	0.162	10	1.0	1.0	1.2	Sub

version of the spectral model used in the Eurocode [5], the spectral model used here is based on the fuller but simplified model with variable speed given in equation (2.24) [32, 55, 88, 113, 115]; this is the version shown in section 2.4. The aerodynamic parameters used in the model are based on the Eurocode's [5] and the limiting amplitude a_L is set to 0.4.

Normally, Ruscheweyh's correlation length model [49] is a maximum amplitude model that's based on the statistical maximum observed wind speed. Here, a variable speed is used instead which gives a pseudo amplitude response. The aerodynamic parameters used in these comparisons are the same as those used in the Eurocode and the original work of Ruscheweyh at super-critical and sub-critical Reynolds number [5, 49].

8.2.2 Wake oscillator modification

The amplitude response of the wake oscillator is more centered around $\omega_q = 1$ than the other two models. This can be useful when the turbulence intensity is low and natural frequency is high, but produces an erroneous amplitude response with high turbulence intensities. To remedy this, an empirical turbulence correction is applied to the dimensionless speed used when calculating the wake oscillator's amplitude response: Instead of calculating it for ω_q, the amplitude response will be calculated for ω_q' which is empirically related to ω_q by $\omega_q' = \omega_q \cdot (1 - Tu)$ where Tu is the turbulence intensity. There's no theoretical justification for why this correction should work but, as will be seen, it does.

When calculating the response for full-scale chimneys, the force coefficients (mean drag and unsteady lift) are calculated using the CICIND [55] definition of SD lift and mean drag. To transform the SD lift to amplitudes, the SD values are scaled by $\sqrt{2}$. This is based on the assumption of periodic, sinusoidal oscillations with zero mean where the amplitude is $\sqrt{2}$ times the rms value. Contrarily, the force coefficients found in the 2D, stationary wind tunnel experiments are used when predicting the response of the cylinders used in the 3D wind tunnel tests as the cylinders and surface roughness are the same.

Another issue with the coefficients used in calculating the response with this model is whether or not the more quasi 2D model can be extended to 3D cylinders of finite height. The assumption made here is that the model can be used with finite height cylinders by modifying the empirical wake coefficients (A and ϵ) and by using an aspect ratio corrected lift coefficient. Changing the empirical coefficients based on the aerodynamic conditions does have support in the literature and shows good results (c.f. the work of Ogink and Metrikine [141]).

8.3 Predicting the response from the small-scale wind tunnel

8.3.1 Model configurations and parameters

While the structural characteristics of the small-scale models have already been described in section 5.2.4 and table 5.1, the aerodynamics have not been. The aerodynamic parameters used when comparing the small-scale aeroelastic tests with the predictive models are based on the

surface roughness and the turbulence intensity. The variation with surface and flow conditions are summarized in table 8.1 (using $\rho = 1.225$) and the mode shape used was $\psi(z) = z$.

For the design models, this corresponds to artificially setting the Reynolds number to a super-critical value for the rough cylinders and to sub-critical for the smooth. In addition, the spectral models contain an unsteady lift term. The values used here are the ones measured during the small-scale 2D experiments detailed in chapter 4 using the closest turbulence intensity.

For the approximated wake oscillator model, there are two parameter groups that needs to be determined: the aerodynamic constants and the empirical wake parameters. The aerodynamic coefficients used are the same as for the spectral model, i.e. the ones measured during the 2D experiments. To determine the best wake force coefficient A and wake damping factor ϵ, the lowest Scruton number tests were investigated. This investigation showed that the wake force coefficient A depended on the Reynolds number while the wake damping factor ϵ depended on the turbulence intensity or atmospheric boundary layer. The best values found are shown in table 8.1 and these will also be used when comparing the full-scale measurements.

8.3.2 Structural response

Amplitude response of rough cylinders

Figure 8.1 shows the dimensionless amplitude responses predicted by the models and measured in the wind tunnel using the rough cylinders with the atmospheric boundary layer as a function of dimensionless speed ω_q. For the cylinder with the lowest Scruton number, figure 8.1a, there's an immediate problem with the spectral model: The predicted response overshadows the experimental and other predictions. Including it in the figure would obfuscate the changes in the experimental data and other models. As the spectral model predicts a near constant amplitude of $r_y = 0.370$, including it in the plot would not add extra information.

The wake oscillator model and correlation length model better predicts the amplitude response for the $Sc = 5.47$ cylinder with decreasing speed in figure 8.1a than with increasing speed. After the turbulence correction, the wake oscillator model best captures the highest amplitudes, the extent of the region with the highest amplitudes and the dimensionless speed giving the maximum amplitude but does not predict the full lock-in range. It underestimates the extents of lock-in and instead of starting and ending at 0.8 and 1.5 respectively, it starts and ends around 1.0 and 1.2.

On the other hand, the correlation length model seems to capture the start of the vortex-induced vibration region but as expected, the predicted response does not resemble the experimental amplitude response after reaching the maximum value; it instead stays constant as was expected. The correlation length and wake oscillator models matching the experimental amplitudes at low Scruton numbers makes sense as they assume harmonic vibration like the ones observed experimentally. What could make them differ are different force coefficients.

As the Scruton number is increased, the spectral model becomes increasingly better at predicting the response. The wake oscillator and correlation length models, on the other hand, becomes worse. The transition between for this can be seen in figure 8.1b with a Scruton number of 7.87. The wake oscillator model still predicts the closest amplitude (and a high amplitude range between $\omega_q \in [1, 1.2]$) but the spectral models amplitude response is closer in shape. The main problem for the spectral model is that the predicted amplitudes are consistently higher for all ω_q and this is especially noticeable for $\omega_q \notin [1, 1.2]$.

At even higher Scruton numbers, figures 8.1c and 8.1d with Scruton numbers of 9.99 and 17.2 respectively, the harmonic models poorly predic the response. Neither the correlation length nor wake oscillator models are close to predicting the amplitude responses' shape and the amplitudes are greatly overestimated. The spectral model, on the other hand, does a much better job at predicting the response at high Scruton numbers. This should not come as a surprise as the

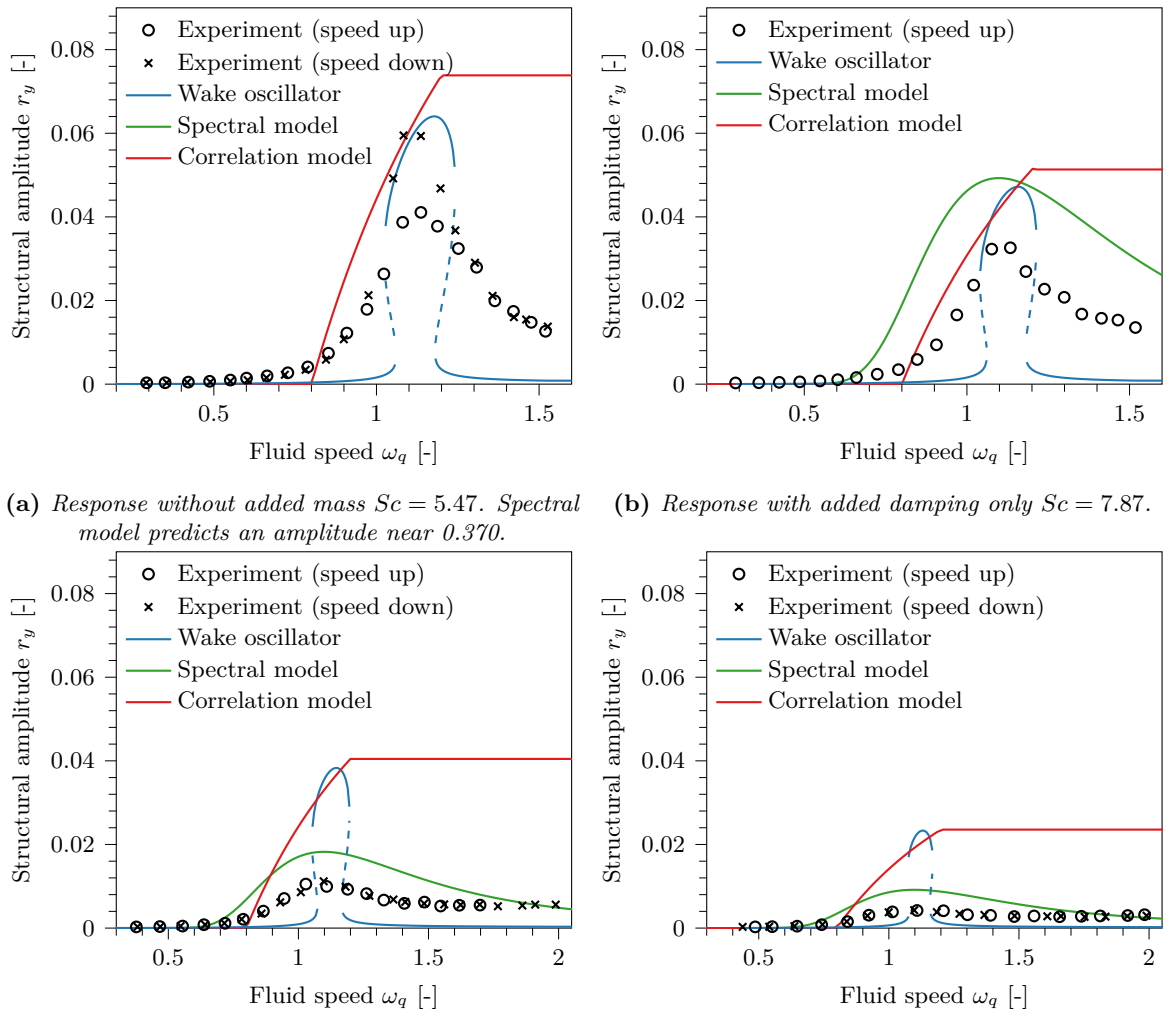

(a) *Response without added mass $Sc = 5.47$. Spectral model predicts an amplitude near 0.370.*

(b) *Response with added damping only $Sc = 7.87$.*

(c) *Response with 150 g added mass $Sc = 9.99$.*

(d) *Response with 300 g added mass $Sc = 17.2$.*

Figure 8.1: *Response for the rough cylinders (super-critical Reynolds numbers) with atmospheric boundary layer. The spectral model is not shown when it predicts a flat response much greater than the rest.*

spectral model was based on random vibration theory [32, 88] and as the response was much more random when the Scruton number was high.

For most of these cylinders, the Eurocode implementation of the spectral model predicts different maximum amplitudes than the speed dependent version plotted. For the lowest Scruton number cylinder, the maximum amplitudes were the same while the Eurocode version predicts an amplitude almost twice as high for the other configurations as shown in table 8.2. The differences in response at higher Scruton numbers was due to the spectral model with variable speed using the lift force measured with the 2D experiments instead of the larger force used in the Eurocode.

Amplitude response of smooth cylinders

Like for the rough cylinders with atmospheric boundary layer, the best model for predicting the response of the smooth cylinders depended on the Scruton number. This is why neither of the smooth cylinders in figure 8.2 ($Sc = 4.5$ and 9.45) are compared with the spectral model. The spectral model predicted a flat response for the smooth cylinder with a Scruton number of 9.45 even if the model predicted a non-flat amplitude response for a rough cylidner with lower

Table 8.2: *Comparison of maximum amplitudes predicted by the spectral model with variable speed and the maximum amplitude formulation given in the Eurocode [5].*

Scruton number	Eurocode (max only)	Spectral (variable speed)
5.47	0.37	0.37
7.87	0.087	0.049
9.99	0.034	0.018
17.2	0.017	0.009

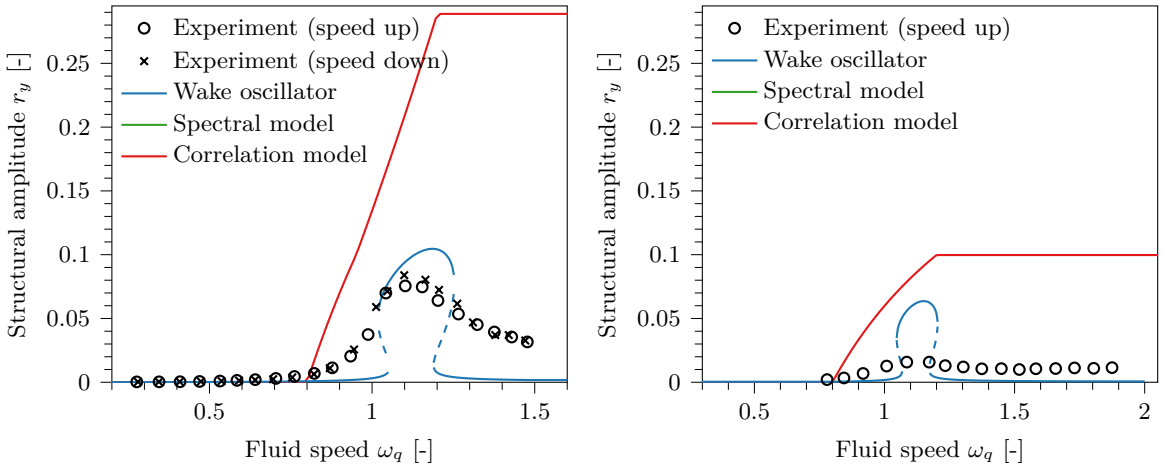

(a) *Response without added mass $Sc = 4.5$. Spectral model and Eurocode version predicts a flat amplitude near 0.477.*

(b) *Response with 150 g added mass $Sc = 9.45$. Spectral model and Eurocode version predicts a flat amplitude near 0.394.*

Figure 8.2: *Response for the smooth cylinders (sub-critical Reynolds numbers) with atmospheric boundary layer. The spectral model is not shown when it predicts a flat response much greater than the rest.*

Scruton number. The reason for this is simple: The negative aerodynamic damping is greater at sub-critical Reynolds numbers than at super-critical which means that the linear damping becomes negative at higher Scruton numbers [5, 55].

For the lowest Scruton number tested, $Sc = 4.5$ shown in figure 8.2a, the wake oscillator model can be seen to best match the response. Just like for the rough cylinders, the wake oscillator predicts high amplitude vortex-induced vibrations between $\omega_q \approx 1$ and 1.2 with amplitudes that are slightly higher than what's measured in this region. Outside this region, the wake oscillator greatly underestimates the response. The biggest change in the correlation length model's predictions is in the amplitudes: The higher lift coefficient greatly increases the predicted response and makes it much greater than the experimental measurements. This is related to why the wake oscillator model and correlation length model predicts different maximum amplitudes: The correlation length model uses a higher SD lift.

Amplitude response without an atmospheric boundary layer

When comparing the predicting models with the rough and smooth cylinder tests without an atmospheric boundary layer, shown in figure 8.3, the wake oscillator model can be seen to be the best. This result matches well with the tests with atmospheric boundary layer. The best model to predict the response of the small-scale cylinders depends on two parameters: The Scruton number and the aerodynamic damping parameter used in the spectral model. When the Scruton number is low, the wake oscillator best predicts the response and when it's high the spectral model is better. Low and high Scruton numbers are ambivalent and this is because the best

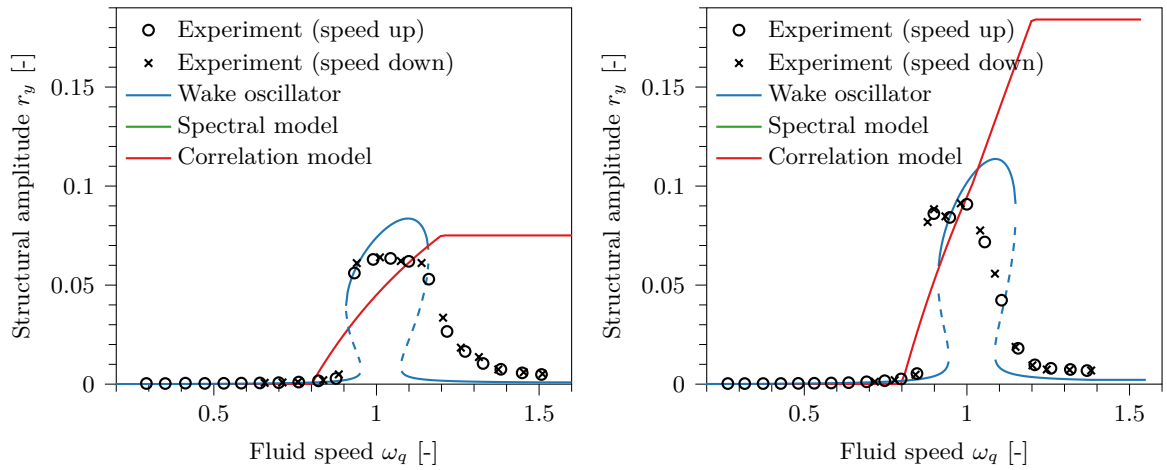

(a) *Response of rough cylinder $Sc = 5.98$. Spectral model predicts a flat amplitude near 0.373.*

(b) *Response of smooth cylinder $Sc = 5.38$. Spectral model predicts a flat amplitude near 0.449.*

Figure 8.3: *Response for the rough and smooth cylinders without atmospheric boundary layer. The spectral model is not shown when it predicts a flat response much greater than the rest.*

Table 8.3: *Modified structural characteristic of the field-test chimney used for amplitude prediction.*

d_{tip} [m]	h [m]	m_e [kg/m]	f_1 [Hz]	ζ_1 [%]	Sc [-]
2	35.5	322.6	0.71	0.22	1.82

model depends on the aerodynamic damping parameter which depends on the Reynolds number. A useful tool for approximating the best model would be equation (2.27): When $Sc > 4\pi K_{a,0}$, the spectral model should be better and the wake oscillator when $Sc < 4\pi K_{a,0}$.

The dimensionless speed modification used in the wake oscillator model does much better without the atmospheric boundary layer. As the peaks were captured when increasing the turbulence intensity, it's possible that the correction used needs an extra term that accounts for the atmospheric boundary layer profile.

8.4 Predicting the field test's amplitude response

8.4.1 Aerodynamic and structural parameters

The structural parameters used to calculate the response of the field-test chimney from chapter 6 are given in table 8.3 (using $\rho = 1.225$) and the mode shape was $\psi(z) = z^2$. These parameters are based solely on the upper part of the structure and use the estimated natural frequency towards the end of the tests. As the aerodynamic parameters affecting the response of the field-test's chimney were not measured, the design codes are used to estimate them. When using the CICIND model code to define the lift and drag on the chimney (using the structural parameters in 8.3 to calculate the critical Reynolds number and aspect ratio), the aerodynamic parameters are those given in table 8.4.

Table 8.4: *Aerodynamic coefficients and model parameters used for the field-test chimney.*

Configuration [-]	C_l [-]	C_d [-]	St [-]	A [-]	ϵ [-]	Tu [%]	K_{a0} [-]
Field-test	0.206	0.68	0.18	15	0.7	6.0	1.0

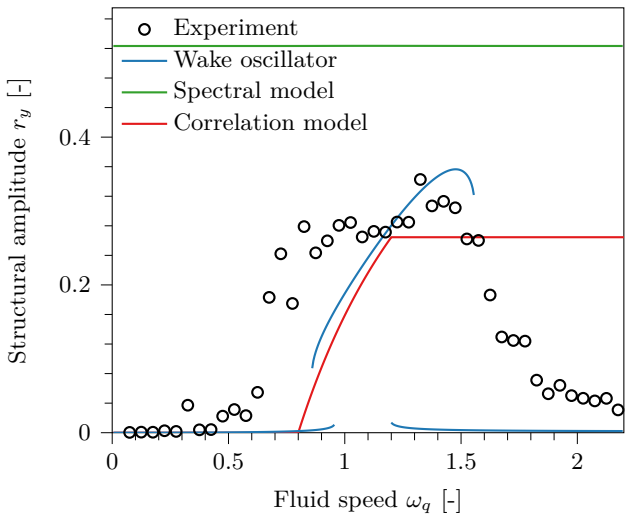

Figure 8.4: *Comparison of mathematical models with the response measured in the field experiment (super-critical Reynolds numbers).*

8.4.2 Comparison of amplitude response

The predicted amplitude responses are compared with the field experiment's response in figure 8.4 and they can be seen to follow the general trends outlined for the small-scale experiments. As the Scruton number is low, the spectral model fails to predict an amplitude response and the predicted amplitude is significantly higher. The correlation length model also gives the same pseudo amplitude response and predicts a maximum amplitude slightly lower than observed. The wake oscillator model does the best job at predicting the maximum response and captures fairly well the end of the high amplitude vortex-induced vibrations region.

The wake oscillator and correlation length models have one thing in common: The predicted high amplitude regime starts later than what's observed experimentally. This makes the predicted high amplitude vortex-induced vibrations regions smaller which was also observed in the small-scale tests to a lesser extent. There are two possible reasons for the mismatch: 1) It's possible that the longer time period used when calculating the response gave an artificially wider response and 2) It's possible that the models and speed correction does not fully capture the full extent of vortex-induced vibrations of a cylinder in an atmospheric boundary layer. Even with this limitation, the wake oscillator model captures the experimental, low Scruton number amplitude response quite well.

8.5 Predicting maximum response

It's been shown that some predictive models are better at predicting the amplitude response. As mentioned, designers are often more interested in the maximum response as this dictates the loads that the chimney, or structure in general, needs to withstand. Therefore, the predicted maximum responses for a collection of real chimneys from the literature are used to compare the Eurocode versions of the spectral and correlation length models and the wake oscillator's maximum amplitude approximation given in section 7.4.

The chimneys used to compare the models are a collection of the 27 chimneys vetted by Lupi et al. [115] and are shown in table D.1 of the appendix. Their collated data include most of the characteristics needed for predicting the response (height, diameter, aspect ratio, equivalent mass, Scruton number and natural frequency) as well as an analysis of how reliable the chimney characteristics are; the 27 chimneys are the most reliable out of a greater collection of 96 chimneys. As it's unknown, the turbulence intensity was set to 10% for all cases as in the

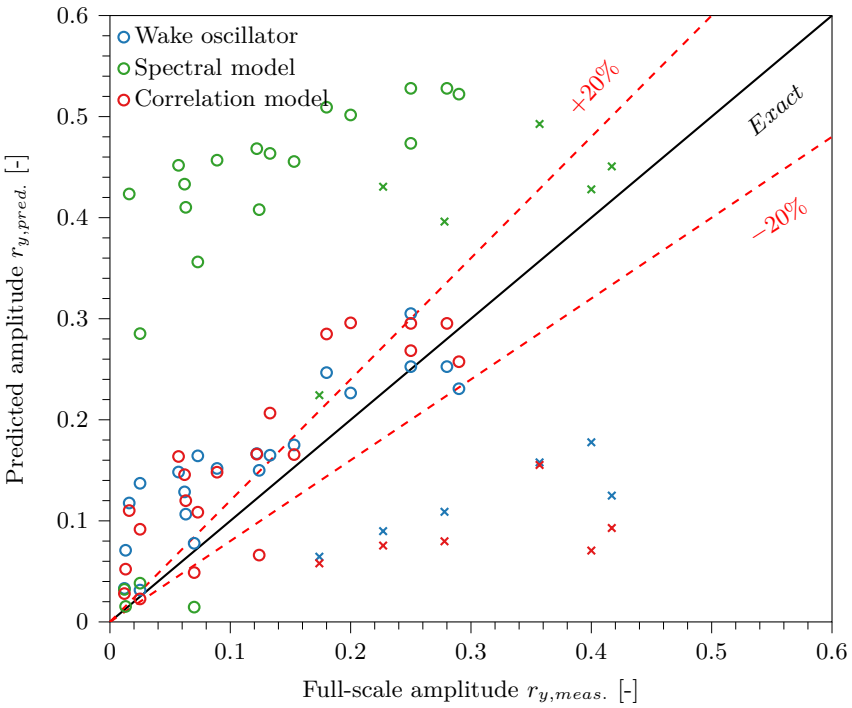

Figure 8.5: *Comparison of mathematical models with maximum amplitudes from the literature [115]. The data points marked with × are chimneys that either are modified, have weird damping behavior or have amplitudes measured by eye.*

work of Lupi et al. The aerodynamic coefficients used in the wake oscillator model was found using the CICIND model code [55] while the correlation length and spectral model uses those given in the Eurocode [5].

The amplitudes predicted by the spectral model are highly dependent on the Scruton number and the Reynolds number. Of the chimneys in figure 8.5, 66.7% had Scruton numbers below $4\pi K_{a,0}$ making the linear damping negative. This made the spectral model near consistently predict dimensionless amplitudes above 0.3 when the Scruton number was low as shown in figure 8.5. Most of these high amplitudes were over predictions with the lowest over predicted amplitude being least 20% greater than what's measured but several of them were over estimated by as much as 300%; this is similar to what Vickery and Daly complained about when using wind tunnels and instead recommended to use this model. Of the remaining seven chimneys, most of them are close to the actual amplitudes except for one that's under predicted.

The correlation length and wake oscillator model also over predicted the vibration amplitude for most chimneys, but the over predictions were less severe which makes these models more economical. In addition, the predicted responses were quite similar for these models. Conceptually, this makes sense: Both models use similar force coefficients, have amplitude dependent forces and predict harmonic resonance at the speed giving the maximum response. For a few of the chimneys, the response was slightly under predicted but still within 20% of the actual amplitude. The major downside of these models, is that the predicted response was significantly lower than the actual response for six of the chimneys which is not only uneconomical but also dangerous. Before dismissing these models as unsafe, these chimneys need further investigation to verify that there's nothing wrong with the measurements.

The under predicted chimneys are numbers 5 and 11–15 of table D.1. Chimneys 11–14 were measured by eye at night during the same extreme event with negligible turbulence intensities (very cold winter and stable atmospheric stratification) [158]. As shown in the small-scale 2D tests in chapter 4 and in the field experiment in chapter 6, the lower turbulence intensities

should have given different force coefficients (vortex-lift and mean drag) than the ones used in the wake oscillator and correlation length model which leads to larger amplitudes. In addition to the very low turbulence and the changed aerodynamics, the cold temperature had an effect on the structural parameters: The cold temperatures increased the density which reduced the mass-ratio and the Scruton number [158]. Outside of the rare event, no significant vibrations were observed making it possible for the average vortex-induced vibration amplitudes to be lower than what's reported.

Chimney 5 was a modified version of number 4 where the top 1/3 of the chimney had a reduced diameter (1 m instead of 1.58 m). While van Koten [118] verified that the listed parameters were correct for the modified chimney, it was found that the vibrations were focused in the upper part with the lower part being mostly rigid. This should have changed many of the parameters like the effective height and mode shape which could give lower equivalent mass, mass-ratio and effective damping which results in a higher response. The last odd chimney was not a chimney but a distillation column. According to Basu [79], the damping of this column was highly uncertain, highly amplitude dependent and should be lower than the one presented. All-in-all, there are reasons for believing that the six under predicting chimneys are anomalies. The correlation length and wake oscillator models could therefore be good at predicting the maximum response but they may need an extreme event modification that prevents the extreme under prediction seen with chimneys 11–14.

In addition to the visual comparison, the models' ability to predict the response should be compared quantitatively. This was done using the sum of squares of residuals (RSS). The RSS error is defined in equation (8.1) where N is the set of chimneys and $r_{y,pred.}$ and $r_{y,meas.}$ are the predicted and measured amplitudes respectively. For the chimneys used, the spectral model had a RSS of 1.79, the correlation length method 0.407 and the wake oscillator model 0.304. Based on these errors and figure 8.5, it's clear that the spectral model had the greatest error (least economical and most conservative). Similarly, the wake oscillator model had the smallest error and should produce the most economical designs provided that the chimneys don't collapse due to rare events.

$$RSS = \sum_{n \in N} \left(r_{y,pred.} - r_{y,meas.}\right)^2 \tag{8.1}$$

8.6 Which model to use?

As mentioned and shown, the experimental amplitude response and maximum responses were compared with predictions from three models. Based on the models' performance, the best model for a given situation could be concluded on. The model that should be less used, is Ruscheweyh's correlation length model as it cannot predict the amplitude response. It's quite good at getting the maximum amplitude but routinely over predicts the maximum response for most cylinders; this was most evident for cylinders experiencing vortex-induced vibrations at sub-critical Reynolds numbers. This makes sense as the model was not made to calculate the maximum amplitude up to a given speed and was made to be a conservative design model.

When increasing the Scruton number, there's a qualitative difference between low values (with harmonic vibrations) and higher values (dominated by random vibrations). In the small-scale experiments, the threshold was when the Scruton number was increased from 7.87 to 9.99 though the exact value was dependent on the surface roughness. These qualitative differences means that the best vortex-induced vibration model is dependent on the Scruton number.

When the damping and mass is high ($Sc > 8$–10)[12], the best model for predicting the response due to vortex-induced vibrations was the random vibration based spectral model of Vickery and Basu. At these Scruton numbers, the experimentally obtained responses were

[12]The exact Scruton number depends on the Reynolds number region and the aerodynamic damping.

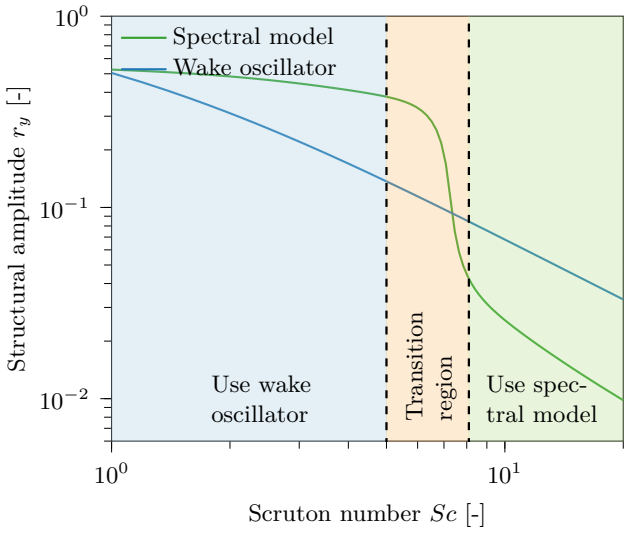

Figure 8.6: *Visualization of best predictive model for a given Scruton number using the imaginary chimney from figure 7.5 at super-critical Reynolds numbers.*

much more random than at low Scruton numbers and the effect of the nonlinear aerodynamics damping was negligible. As the Scruton number was decreased, this random vibration model became increasingly bad at predicting the response and started predict a near flat response at amplitudes up to 7 times greater than the measured response. This transition occurs in a small Scruton number region where the nonlinearity became increasingly important and the response more harmonic than random. This model fault is not unknown and even the creators of the model noted that the predicted response became independent of nominal forcing at low Scruton numbers due to the negative linear damping and form of the nonlinear damping [113]. As mentioned, other versions of the model use a modified nonlinear damping but these don't give an amplitude response (cf. the work of Lupi et al. [59, 115]).

The best model at low Scruton numbers ($Sc < 8$), was the approximated version of Facchinetti et al.'s wake oscillator that's presented in chapter 7. This model is based on harmonic oscillators (where one is nonlinear) which helps explain why it performs well at low Scruton numbers (harmonic vibration region) and badly at high Scruton numbers (random vibration region). As getting the correct amplitude response is more important at low Scruton numbers due to the higher response that needs to be treated, this newly approximated vortex-induced vibration model should be a highly valuable tool when designing chimneys (and similar structures). With this tool, it should also be possible to design better vibration absorbers that suppress vortex-induced vibrations though this would require a third coupled differential equation.

It's possible to further improve the wake oscillator model. Firstly, the predictions will be improved with better force coefficients as a function of the turbulence intensity, atmospheric boundary layer and Reynolds numbers. Secondly, a better dimensionless speed correction should be derived. The current correction makes the speed at maximum amplitude match but does not predict the full lock-in region when using atmospheric boundary layers.

Overall, the best model for a given Scruton number is sketched out in figure 8.6 but needs to be modified for each Reynolds number region. In the transition region, care needs to be taken but it's possible that the model predicting the lowest response is the best.

Part V

Outlooks and conclusion

Chapter

9 General conclusions

9.1 2D wind tunnel experiments on stationary cylinders

This work has presented and tied together several studies aimed at improving the predicted response of industrial chimneys due to vortex-induced vibrations at high Reynolds numbers ($Re > 10^6$, i.e. at super-critical Reynolds numbers). The first step was first to determine the unsteady forces on a stationary circular cylinder at actual super-critical Reynolds numbers in a large wind tunnel. With this baseline, the best roughness configuration for simulating the super-critical Reynolds number flow at lower ones was determined at smaller scales. The requirements for a well reproduced super-critical flow were: 1) To simulate super-critical Reynolds numbers at reasonable wind speeds; 2) To have similar unsteady force characteristics (mean and SD values); and 3) To have a similar characteristic vortex-shedding frequency (Strouhal number).

Two bi-stable Strouhal numbers were found for the smooth cylinder at large Reynolds numbers. When decomposing the unsteady pressure distribution using the bi-orthogonal decomposition (BOD), the two different Strouhal numbers were found to originate from different spatial unsteady pressure distributions (topos). The lower Strouhal number ($St \approx 0.2$) was found to be associated with the vortex-lift BOD pair which had its spatial energy (topos) focused near the "top"; this pair also produced most of the fluctuating lift ($\theta \in \pm[90°, 110°]$). The higher Strouhal number ($St \approx 0.25$), on the other hand, was associated with the "secondary vortex-lift" distribution. Instead of being near the top, the spatial energy of this BOD pair was focused in the rear ($\theta \in \pm[120°, 180°]$) which produced fluctuating lift and drag.

Finding these Strouhal numbers consolidated some conflicting literature on vortex-shedding at super-critical Reynolds numbers: Depending on the measurement type, previous experiments gave a Strouhal number either in the range $St \in [0.25, 0.27]$ or near $St = 0.2$ [8, 13, 17, 21, 23–25, 36, 54, 56]. This work showed that both of them exists in the wake and unsteady pressure measurements and are not a scatter of possible values. The relative strength of these two shedding frequencies (measured in frequency domain) depended on where it was measured. In the wake, the strongest spectral peak was for the higher Strouhal while the lower Strouhal number was relatively weak. In the decomposed unsteady pressure, the lower Strouhal number had a much stronger spectral peak and total energy than the higher Strouhal number.

Adding surface roughness in the form of ribs eliminated the instability that lead to the upper vortex-shedding frequency. The remaining Strouhal number was found in the wake and both the vortex-lift and second vortex-lift BOD pairs. This shedding frequency depended on the roughness configuration and scale. At small-scales and Reynolds numbers, increasing the roughness decreased the Strouhal number. The effect of roughness was different at large-scales and Reynolds numbers where increased roughness at large Reynolds numbers slightly increased the Strouhal number.

The added roughness and scale also changed the correlation and coherence along the height. This was clearly seen when comparing the correlation at small-scale with the large-scale results: The correlation and coherence was much greater when testing with the larger ribs at small-scales. The increased correlation and coherence could partly explain why the standard deviation (SD) of the lift coefficient was larger at small-scales but fails to explain it fully. At small-scales and

Reynolds numbers, increasing the rib spacing decreased the correlation but greatly increased the SD lift and drag coefficients while increasing the rib size barely changed the force but increased the correlation. This indicates that there's a Reynolds number or wind field difference.

The spatial distribution of unsteady pressure was investigated and compared between the smooth large-scale tests and the small-scale tests with roughness. This comparison used the first four BOD pairs which represent (in order of decreasing relative energy) the mean, vortex-lift, vortex-drag and second vortex-lift pressure distributions. The two most important pairs to match were the mean and vortex-lift pressure distributions as they represent most of the fluctuating lift force and energy from the time signals.

Even if the smooth cylinder at actual super-critical Reynolds numbers had an asymmetric mean pressure distribution, it matched well with the rough small-scale cylinders at simulated ones. This asymmetry also caused a bias in the vortex-lift distribution which affected the difference in relative lift for the rough and smooth configurations. This difference was smaller when only considering the unsteady force components but still noticeable. There were two big differences between the vortex-lift topos from the small-scale and large-scale configurations: 1) earlier separation point with the rough cylinders and 2) increased spatial energy in the rear for the rough cylinders. Even with the differences, the agreement of the vortex-lift was good for the rough and smooth configurations as indicate by the high MAC values.

The differences between the smooth and rough cylinders were greater for the vortex-drag and second vortex-lift with the vortex-drag being more or less incomparable. The asymmetry in the mean and vortex-lift should also have affected the second vortex-lift and part of the differences between the smooth and rough cylinders were due to this asymmetry. Still, there were other more prominent differences: Many of the differences in second vortex lift were due to the spatial energy for the rough cylinders being focused further in the rear than for the smooth cylinder and the spatial energy distributions barely match as indicated by the low MAC values.

9.2 Aeroelastic experiments

The response of a flexible cylinder at simulated super-critical Reynolds numbers was determined using the previous investigation on surface roughness and compared with a sub-critical cylinder. In addition, tests were performed with and without an Eurocode type II boundary layer to test the effect of a turbulent atmospheric boundary layer. These tests allowed us to test two hypotheses: 1) The wrong Reynolds number region gives a very different response and 2) Turbulent atmospheric boundary layers can be enough to simulate super-critical Reynolds numbers.

There are three results that make it seem like the added turbulent atmospheric boundary layer was enough for simulating super-critical vortex-induced vibrations making roughness unnecessary. Firstly, the Strouhal numbers were fairly similar for both the super-critical and sub-critical cylinders when testing with the boundary layer; this suggests similar aerodynamics. Secondly, while tests at simulated super-critical Reynolds numbers using roughness did have a different amplitude response than the sub-critical cylinder when testing with the atmospheric boundary layer, the differences were mostly due to a different Scruton number (a mass-damping parameter). This result is also seen when comparing the maximum amplitude for several Scruton numbers and the results from the smooth and rough cylinders seems to be part of the same exponential or power law curve.

Finally, removing the atmospheric boundary layer removes these similarities between the cylinders and the rough cylinder at super-critical Reynolds numbers have different vortex-shedding frequencies and response than the smooth sub-critical cylinder. The effect of the boundary layer on the shedding was also greater for the smooth cylinder than the rough which suggests that the added turbulent atmospheric boundary layer could be enough to simulate super-critical Reynolds numbers of similar experiments.

The small-scale aeroelastic tests were accompanied by a field experiment on a 35.5 m tall

custom-made chimney that had a diameter of 2 m at the top but only 1 m at the base. The only aerodynamic parameter measured in the field was the wind speed at four heights. This chimney was designed to have a low Scruton number and to experience high amplitude vortex-induced vibrations at moderately low speeds. While not measured, the chimney was constructed so that unsteady pressure and forces could be measured at several heights.

The response of this chimney and the incoming wind was recorded over a 13-day period and the data split into 10-minute segments for a statistical analysis. The response followed typical real life response patterns based on the wind speed and frequency of motion. At low speeds, the dominant frequency was either at the linearly increasing Strouhal shedding frequency (vortex-induced vibrations) or natural frequency (turbulence-induced vibration). At high speeds, the response was mainly due to turbulence-induced vibrations.

The response was more interesting at intermediate speeds (5-8 m/s) where the response was either large and due to vortex-induced vibrations or small and due to turbulence. The vortex-induced vibration amplitude depended on the atmospheric boundary layer profiles and this parameter changed with the direction. The wind direction giving the highest amplitudes of motion had a steep speed gradient but low turbulence at all heights. The directions with low response, on the other hand, had high turbulence with height. These atmospheric boundary layers were different from the Eurocode type II boundary layer and the turbulence intensities were significantly lower in the field for all directions.

9.3 Predicting the response due to vortex-induced vibrations

Approximate solutions to a nonlinear wake oscillator model was derived to improve the predictions of vortex-induced vibrations using mathematical models. This new approximation matched well with numerical integration of the same model but required a constant total damping (aerodynamic + structural) in the structural equation instead of a speed dependent. With this approximation, two new investigations on the size of the lock-in regions and the maximum amplitude was performed.

By investigating the stability and phase difference between forcing and motion, a bi-quartic equation for the bounds of 3 lock-in regions in terms of the dimensionless speed was found. At low speeds, there's a conditional lock-in region (needs high existing amplitudes) that only exists with low mass-scaled force M and low structural damping ratio. The next lock-in region was a region of absolute lock-in and this region grew in size with the mass-scaled forcing. When increasing the damping ratio, the absolute region did not start shrinking until the low-speed conditional region disappeared. At this point, further damping decreased the absolute lock-in regions size at high and low dimensionless speeds.

The last lock-in region was a higher speed conditional lock-in region. While the lower region disappeared with increasing force, the upper region persisted: As the force's strength grew, the conditional region grew, then decreased until the force reached a certain value where the upper conditional region started growing again. The effect of damping factor on the upper conditional region was similar to the lower one and it decreased with damping. The main difference between them was that the upper region was larger at low damping which led to the upper region persisting at much higher damping ratios.

Designers often only use the maximum response when designing a chimney and an expression for the maximum response was therefore derived. It was found that the maximum amplitude tended to occur at the same phase difference and an expression for the speed at maximum response was derived from this. This is different from the design models which assumes the maximum occurs at a specific speed. This new expression was compared with numerical simulations at several Scruton numbers and both the speed at maximum and the maximum amplitude matched well.

To be sure that this new model was an improvement to the existing design code models, the

predicted response using this approximated wake-oscillator model, the spectral model and the correlation length model were compared with experimental data. The best model for predicting the amplitude response was found to depend on the Scruton number. When the Scruton number was low, the best model at reproducing the amplitude response was the new approximation while the spectral model was best at high Scruton numbers. This makes sense as the response is more harmonic at low Scruton numbers, which favors harmonic models like the wake oscillator, and more random at high Scruton numbers, which favors random vibration models like the spectral model used in the CICIND model code and the Eurocode.

When comparing the maximum predicted response with that found in the literature, the new approximation was found to be significantly better than the spectral model on average. The exception was for six chimneys where the approximated wake-oscillator model severely under predicted the response. The amplitude for most of these chimneys were measured during the night and experienced a rare event where the density was much higher and the turbulence intensity became negligible. It's possible that the under prediction is not as severe as shown and that a safety factor in the form of an extreme event modifier, or wake parameters that account for variations between chimneys, could alleviate any issues. With this, the approximated wake-oscillator model should still be viewed as the best model for predicting the response at low Scruton numbers.

9.4 Perspectives

While much new knowledge has been gained from this work, there's still a few points that can be improved by continuing the studies made here. Firstly, the chimney used in the field tests was fitted with taps for measuring unsteady pressure at 7 levels. In the current study, this has not done yet. Measuring the unsteady pressure in the field at critical and super-critical Reynolds numbers (with and without motion) could help verify the large-scale 2D tests. Most notably, it can verify whether or not the two Strouhal numbers exists in the field. In addition, the field measurements will give a better idea of how the Strouhal number, correlation and coherence changes with the mean boundary layer profile as it depended on the direction.

The large and small-scale tests at simulated super-critical Strouhal numbers gave very different force characteristics (dimensionless frequency and mean and SD values). This indicates that the actual Reynolds number is important for the flow characteristics when simulating higher Reynolds numbers. There are a few ways to test this claim. Firstly, a large and a small cylinder fitted with ribs of similar dimensionless roughness size should be tested in the same wind tunnel. This will show that the difference in force characteristics at simulated super-critical Reynolds numbers is not due to different wind fields. If the difference in wind tunnels and scales are not the causes, e.g. still gives different force coefficients with different scales in the same wind tunnel, a new 2D test campaign with cylinders of different diameters and similar ribs would be advised. This would help determine the best rib size and spacing combination for a circular cylinder with a given diameter. With enough data, a regression analysis or a look-up table could be created.

The total force experienced by a cylinder depends on both the 2D force coefficients and how coherent it is along the height and was measured in the form of correlation and coherence. This was not measured for a smooth circular cylinder at super-critical Reynolds number and is gap in this work. Determining these statistics will improve any further investigation on the best method of simulating super-critical Reynolds numbers and should be regarded as a vital measurement for this.

In addition to such 2D comparisons, the correlation and coherence should be measured for finite height cylinders and with more turbulent atmospheric boundary layer profiles and surface roughness configurations. By comparing these with field measured correlation and coherence, e.g. using the field experiment mentioned in chapter 6, a conclusion could be reached regarding

whether or not a turbulent atmospheric boundary layer is enough to simulate vortex-induced vibrations at super-critical Reynolds numbers.

The last pieces of improvements are related to predictive models. As the aerodynamic damping. As the nonlinear aerodynamic damping becomes less important at high Scruton numbers, it might be better to combine the good parts of the spectral model with the wake oscillator model. When the Scruton number is low, the best option is to use the wake oscillator as concluded in chapter 8. When it's high, the best course of action might be to combine parts of the spectral and wake oscillator model into one model. This can be done by using the structural definition of the wake oscillator model but a forcing similar the spectral model's instead of the nonlinear wake oscillator force. The difference in the model at high and low Scruton numbers is exemplified in equation (9.1) where F_{rms} is the root mean square of the applied force. Of course, the threshold for harmonic forcing and random forcing depends on both the Scruton and Reynolds number and needs to be better determined.

$$\ddot{y} + D(\omega_q)\dot{y} + y = \begin{cases} Force = \omega_q^2 Mq, & \text{if } Sc \text{ is low} \\ Force_{rms} \propto \sqrt{S_{C_l,viv}(f)}, & \text{otherwise} \end{cases} \tag{9.1}$$

The wake oscillator model can be improved in more ways. As mentioned in chapter 8, the empirical turbulence correction did make most of the predicted vortex-induced vibrations match the observed. But it did not capture the full extent of lock-in and higher amplitude vibrations. A possible fix to the model would be to incorporate turbulence fix in the form of a noise term or a randomly varying speed like added by Denoël [144] or Aswathy and Sarkar [142].

The last mentioned point of improvement for the wake oscillator is to create a more general 3D model. For linear systems, modal decomposition can be used to get the 3D response but this is not possible for nonlinear equations. Instead, it might be useful to assume that the structural oscillator is modeling the response amplitude for a specific mode shape and then use equivalent 3D parameters in the structural and wake equation. To do this, good expressions for the wake force and damping (A and ϵ) need to be defined as a function of wind conditions, Reynolds number and aspect ratio and should be related to the coherence (possibly through a spatial and modal projection of the aerodynamic forces).

Part VI

Appendix

Appendix

A Mathematical tools

> *"Someone told me that each equation I included in the book would halve the sales."*
>
> Stephen Hawking

Following the publishing guide given to Stephen Hawking, much of the mathematical definitions and additional data that might confuse the readers rather than help them further understand the material are moved here.

A.1 Transforming acceleration to response

In a typical vibration modeling framework, it's often assumed that the displacement can be written in the form $y(t) = r_y e^{-i\omega t}$. From this, the speed and acceleration ($\dot{y}$ and $\ddot{y}$ respectively) can be found by taking the derivative of $y(t)$ with respect to time. A similar relationship can be defined in frequency domain for Fourier transforms. When denoting $A(\omega)$ and $Y(\omega)$ as the Fourier transforms of $\ddot{y}(t)$ and $y(t)$ respectively, the relationship between acceleration and displacement in frequency domain can be defined as in equation (A.1). [86, 87]

$$A(\omega) = -\omega^2 Y(\omega) \tag{A.1}$$

From the above, a useful and a not-so-useful property can use used to derive the response of a structure. If the acceleration in time domain is known, the displacement can be found by taking the inverse Fourier transform of the frequency scaled Fourier transform of acceleration. The alternative would be a double time integration of the data. Due to the identity in equation (A.1), it's important to filter the data so that low-frequency noise isn't amplified and so that high frequency components aren't drowned out. [86, 87, 159]

A.2 Hilbert transform

The Hilbert transform ($H[s(t)]$) is, like the Fourier transform, a linear transformation of a time series where the spectral components of a signal is phase shifted by $-\pi/2$ [153, 160] which alone isn't interesting. What's more interesting for vibrations is the analytic signal defined in equation (A.2). From the analytic signal, the instantaneous amplitude can be found from the modulus or magnitude and the instantaneous frequency from the argument of the complex number provided the phase difference is constant; this should hold true for free-response tests but not in forced tests with varying frequency and strength. An example of the response envelope obtained from experimental data is shown in figure A.1.

$$z(t) = s(t) + iH[s(t)] \tag{A.2}$$

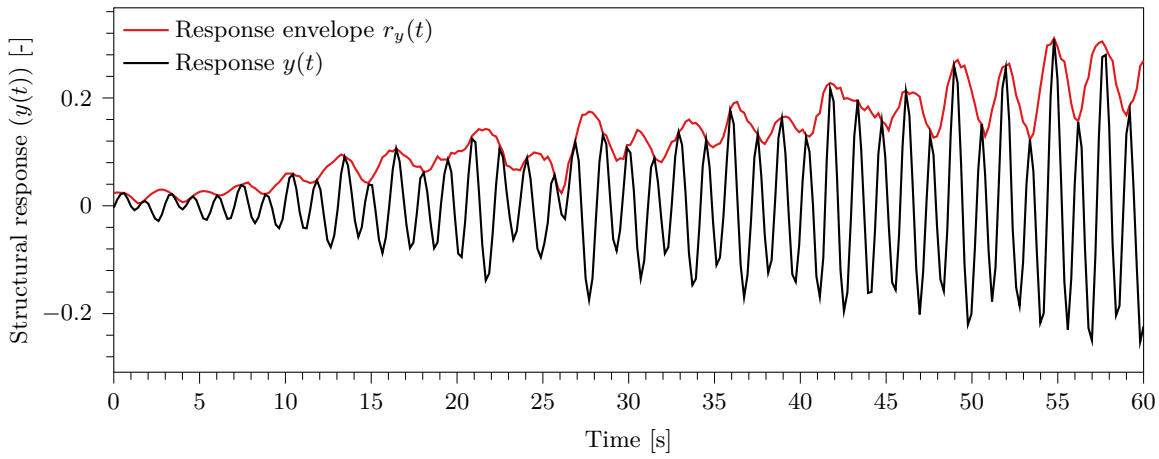

Figure A.1: *Example time history of response response and amplitude envelope from the Hilbert transform.*

Once the instantaneous frequency and amplitude is known, the corresponding damping and natural frequency can easily be found for free-response tests. This is can done by fitting the data to an equation in the form $A(t) = A_0 e^{\zeta \omega_n t}$ and by using the standard relationships between damped natural frequency, critical damping ratio and the natural frequency. Instead of doing a best fit, the natural frequency and damping can be calculated for all amplitudes making their change with amplitude apparent.

A.3 Modal assurance criterion

The modal assurance criterion (MAC) used to calculate how similar the shape of two vectors are (ignoring any scaling factors) and is defined as [150]

$$\text{MAC} = \frac{|\mathbf{v}_i \bar{\mathbf{v}}_j|^2}{(\mathbf{v}_i \bar{\mathbf{v}}_i)\,(\mathbf{v}_j \bar{\mathbf{v}}_j)}, \tag{A.3}$$

where the over score indicates complex conjugate and $\mathbf{v}$ are vectors. There's ongoing discussions on what's the best way of comparing two vectors [161] (e.g. representing mode shapes or related to BOD components) and the form given in equation (A.3) was chosen for its simplicity and ease of use. In the current format, MAC values ranges between 0 and 1 and values greater than 0.9 is considered as consistent correspondence [150]. For ease of use and comparison, the MAC values are scaled by 100 making them percentages.

A.4 Bayesian inference

Bayesian inference is used to test if changes in rib and turbulence configurations have significant effects on the aerodynamics around the cylinder (e.g. in Strouhal number). This Bayesian analysis uses an improper Normal Gamma reference prior (known as "independent Jeffreys prior") where the posterior probabilities are found using Bayes updating [162] as implemented in the R package "statsr" [163]. The prior distribution used is a "non-generative model" meaning the density doesn't integrate to 1 but is still a constant value. As the name implies, samples cannot be drawn from this prior. This distribution is based on setting the sample in the prior distribution in the sample to zero and prior probabilities as uniform. Inference using the posterior probabilities, based the data and prior, then becomes similar to a frequentist based inference using a Student's t-distribution. The difference is that the Bayesian is probabilistic and the frequentist approach is deterministic.

Within this frame work, H_0 is the conservative hypothesis/model (no difference), H_1 is the alternative, P(H_2|data) is posterior probability of H_1 given the data (posterior probability of H_1 is 1-P(H_2|data)) and BF as the Bayes factor which indicates the strength of one hypothesis compared to the other (denoted $BF_{H_i:H_j}$) (defined by posterior and prior likelihood odds). The strength of evidence, Bayes factor, is a numerical value and a value above 3 indicates evidence for the alternative [164]. Values above 20 shows strong evidence and values above 150 indicates very strong evidence for a model. Bayes factors less than 1 indicates evidence for the other model and its strength of evidence is the inverse of the Bayes factor. Exact Bayes factor values are meaningless when one is above 10^4; in these cases, the order of magnitude is given instead.

A.5 Analytic approximation of deterministic equations

Description of the method

The analytic approximation used here, is called the method of averaging; the Krylov-Bogoliubov technique to be more precise. For deeper information of the technique and full derivation, see the textbooks of Nayfeh and Mook [139] or Balanov, Janson, Postnov and Sosnovetseva [95]. As an introduction to the method, first write the nonlinear equations in the form of equation (A.4). Then impose the conditions for y_i and $\dot{y}_i$ given in equations (A.5) and (A.6). If equation (A.6) is to be true, equation (A.7) needs to hold.

$$\ddot{y}_i + \omega_i^2 y = -h(y_i, \dot{y}_i) \tag{A.4}$$
$$y_i = r_{y_i}(t)\cos(\omega t + \phi_{y_i}(t)) = r_y(t)\cos(\Psi_{y_i}(t)) \tag{A.5}$$
$$\dot{y}_i = -\omega r_{y_i}(t)\sin(\Psi_{y_i}(t)) \tag{A.6}$$
$$\dot{r}_{y_i}\cos(\Psi_{y_i}(t)) - r_{y_i}(t)\dot{\phi}_{y_i}\sin(\Psi_{y_i}(t)) = 0 \tag{A.7}$$

From equation (A.6), an expression for $\ddot{y}_i$ can be derived and is inserted into equation (A.4) along with equation (A.5)). The equation of motion are now in terms of r_{y_i}, ϕ_i and their time derivatives. Using the condition in equation (A.7), the equation can be rewritten twice to yield equations for $\dot{r}_{y_i}$ and $\dot{\phi}_i$. Another assumption is now needed: We assume that r_{y_i} and ϕ_i are slowly varying functions when compared to the forced frequency Ψ_i. The equations of $\dot{r}_{y_i}$ and $\dot{\phi}_i$ are then averaged over one cycle of fast oscillation; r_{y_i} and ϕ_i can be regarded as constant as they are invariant over one fast oscillation. This gives equations (A.8) and (A.9). As the equations can be lengthy, the final equations are presented with y_i and $\dot{y}_i$ for brevity.

$$\dot{r}_{y_i} = \int_0^{2\pi} \frac{\sin(\Psi)}{2\pi\omega}\left(h(y_i, \dot{y}_i) + (\omega_i^2 - \omega^2)y_i\right) d\Psi_i \tag{A.8}$$
$$\dot{\phi}_i = \int_0^{2\pi} \frac{\cos(\Psi)}{2\pi\omega r_{y_i}}\left(h(y_i, \dot{y}_i) + (\omega_i^2 - \omega^2)y_i\right) d\Psi_i \tag{A.9}$$

Applying the method

$$\ddot{y} + D(\omega_q)\dot{y} + y = \omega_q^2 M q \tag{A.10}$$
$$\ddot{q} + \epsilon\left(q^2 - 1\right)\dot{q} + \omega_q^2 q = A\ddot{y} \tag{A.11}$$
$$D(\omega_q) = 2\zeta + \frac{\gamma}{\mu}\omega_q \tag{A.12}$$

Equations (A.10) – (A.12) define the system investigated. Here, D is total linear structural damping and $\omega_q = StU_R$ (where St is the Strouhal number and U_R is the reduced speed using

a frequency in Hz). To approximate the system using the method of averaging, the first thing to do is to rewrite equation A.11 using equation (A.10); this gets rid of the $\ddot{y}$ term in equation A.11. Applying equations (A.8) and (A.9) to the system and defining $\theta = \phi_q - \phi_y$ yields the following equations for $\dot{r}_y$, $\dot{\phi}_y$, $\dot{r}_q$ and $\dot{\phi}_q$.

$$\dot{r}_y = \frac{1}{2}\left(\frac{\omega_q^2}{\omega} M R_q \sin(\theta) - D R_y\right) \tag{A.13}$$

$$\dot{\phi}_y = \frac{1-\omega^2}{2\omega} - \frac{\omega_q^2 M r_q}{2\omega r_y}\cos(\theta) \tag{A.14}$$

$$\dot{r}_q = -\frac{1}{2}\epsilon\omega_q r_q\left(\frac{r_q^2}{4} - 1\right) + \frac{A r_y}{2}\left(\frac{\sin(\theta)}{\omega} - D\cos(\theta)\right) \tag{A.15}$$

$$\dot{\phi}_q = \frac{\omega_q^2(1-AM)-\omega^2}{2\omega} + \frac{A r_y}{2 r_q}\left(D\sin(\theta) + \frac{\cos(\theta)}{\omega}\right) \tag{A.16}$$

Using the phase difference ($\theta = \phi_q - \phi_y$) instead of individual phases, equations (A.16) and (A.14) becomes:

$$\dot{\theta} = \frac{\omega_q^2(1-AM)-1}{2\omega} + \left(\frac{\omega_q^2 M r_q}{2\omega r_y} + \frac{A r_y}{2\omega r_q}\right)\cos(\theta) + \frac{AD r_y}{2 r_q}\sin(\theta) = g(\theta) \tag{A.17}$$

To find the amplitudes of motion and phase difference, equations (A.13), (A.15) and (A.17) are solved when the time derivatives are zero. This is during steady state conditions and is assumed to be a valid assumption; either the system is steady-state during lock-in and dominated by $\ddot{y}$ or it is not locked-in and $\ddot{y}$ is negligible. When rewriting the equations for r_q and θ using equation (A.18), the equations governing r_y, r_q and θ are:

$$r_y = \frac{\omega_q^2 M}{D(\omega_q)\omega} r_q \sin(\theta) \tag{A.18}$$

$$r_q = 2\left(1 + \frac{AM\omega_q \sin(\theta)}{\epsilon\omega D(\omega_q)}\left(\sin(\theta) - D(\omega_q)\cos(\theta)\right)\right)^{0.5} \tag{A.19}$$

$$0 = \frac{\omega_q^2(1-AM)-1}{2\omega} + \cos(\theta)\left(\frac{\omega_q^2 AM}{2D(\omega_q)\omega^2} sin(\theta) + \frac{D(\omega_q)}{2sin(\theta)}\right) + \frac{\omega_q^2 AM}{2\omega}\sin^2(\theta) = g(\theta) \tag{A.20}$$

To solve the equation, one simply needs to solve for the possible θs and insert this into the solution for r_q and r_y (or insert equation (A.19) into equation (A.18) and skip a step).

Appendix

B Additional results from small 2D wind tunnel

In addition to the results and configurations shown in chapter 4, the wind tunnel test campaign contained several more roughness configurations. These results are presented here to avoid cluttering the main results chapter. The full list of tested configurations are those given in table B.1.

In addition to the tests with ribs, two experiments were performed with added sand roughness. This roughness was added to the cylinder by gluing on a near uniform layer of sand particles with size between 0.4 and 0.5 mm in the same area as where the roughness ribs were placed. This corresponds to a relative roughness in the range $[7.27, 9.09]\cdot 10^{-3}$.

B.1 Ergodicity of unsteady pressure

To be sure that the unsteady pressure data gathered is good, the ergodicity of it is tested using some 10 minute recordings for the unsteady pressure data. This is done by comparing the MAC values for five experimental configurations at a single speed as shown in figure B.1. As can be seen, there's difference in both the topos and chronos when comparing the long and short recording for higher BOD pairs (BOD pairs>10). The difference between configurations tested at 19 and 20 m/s is turbulence. The results at 19 m/s is for configurations with added turbulence generating grid and 20 m/s is for configurations without it.

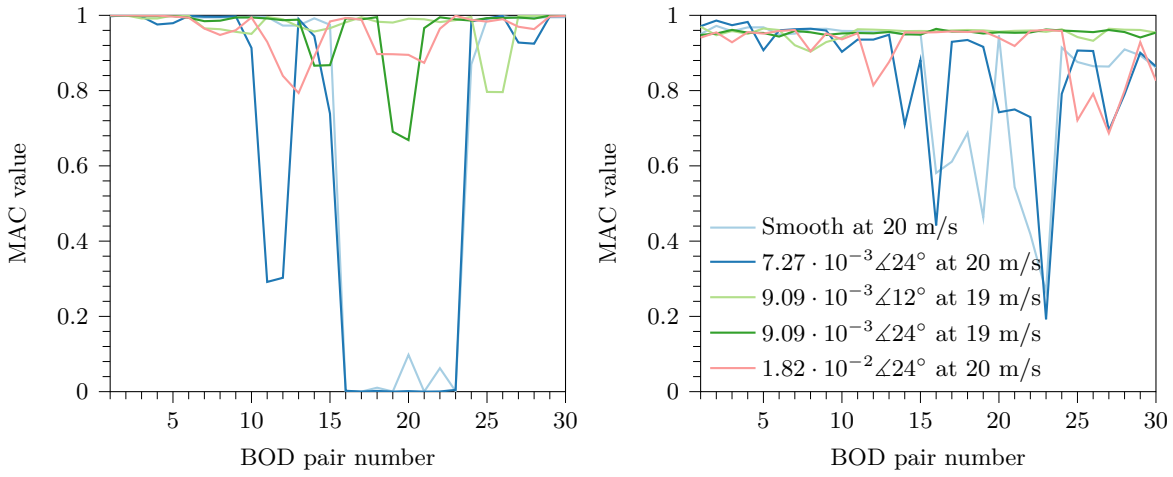

(a) *Topos* **(b)** *Chronos*

Figure B.1: *MAC values for topos and PSD of chronos comparing 10 minutes and 1 minute tests.*

For the topos' MAC values, figure B.1a, shows that the correspondence is excellent for most BOD pairs and experimental configurations. There are some where the correspondence is

Table B.1: *Test details, dates and naming of configurations. Rib dimmensions are height times width and relative roughness height and rib separation angle ($Rr\measuredangle\alpha$).*

Date	Setup	Test details	U [m/s]	$Rr\measuredangle\alpha$
6/12	grad	Wind calibration and characterization	5 speeds	N/A
6/15	azim	Find zero degree inflow	5 speeds	N/A
6/16	Rib01	Ribs 0.2×0.7 and 12° separation	5-28	$3.64 \cdot 10^{-3}\measuredangle 12°$
6/16	Rib02	Ribs 0.2×0.77 and 12° separation (turbulent)	5-19	$3.64 \cdot 10^{-3}\measuredangle 12°$
6/16	Rib03	Ribs 0.2×0.7 and 24° separation (turbulent)	5-19	$3.64 \cdot 10^{-3}\measuredangle 24°$
6/16	Rib04	Ribs 0.2×0.7 and 24° separation	5-28	$3.64 \cdot 10^{-3}\measuredangle 24°$
6/16	Rib05	No ribs (smooth)	5-30	Smooth
6/16	Rib06	No ribs (smooth, turbulent)	5-19	Smooth
6/17	Rib07	Ribs 0.4×0.8 and 12° separation (turbulent)	5-19	$7.27 \cdot 10^{-3}\measuredangle 12°$
6/17	Rib08	Ribs 0.4×0.8 and 12° separation	5-30	$7.27 \cdot 10^{-3}\measuredangle 12°$
6/17	Rib09	Ribs 0.4×0.8 and 24° separation	5-30	$7.27 \cdot 10^{-3}\measuredangle 24°$
6/17	Rib10	Ribs0.4×0.8 and 24° separation (turbulent)	5-19	$7.27 \cdot 10^{-3}\measuredangle 24°$
6/18	Rib11	Ribs 0.5×0.8 and 12° separation (turbulent)	5-19	$9.09 \cdot 10^{-3}\measuredangle 12°$
6/17	Rib12	Ribs 0.5×0.8 and 12° separation	5-30	$9.09 \cdot 10^{-3}\measuredangle 12°$
6/18	Rib13	Ribs 0.5×0.8 and 24° separation	5-30	$9.09 \cdot 10^{-3}\measuredangle 24°$
6/18	Rib14	Ribs 0.5×0.8 and 24° separation (turbulent)	5-19	$9.09 \cdot 10^{-3}\measuredangle 24°$
6/18	Rib15	Ribs 1.0×0.8 and 12° separation (turbulent)	5-19	$1.82 \cdot 10^{-2}\measuredangle 12°$
6/18	Rib16	Ribs 1.0×0.8 and 12° separation	5-30	$1.82 \cdot 10^{-2}\measuredangle 12°$
6/19	Rib17	Ribs 1.0×0.8 and 24° separation	5-30	$1.82 \cdot 10^{-2}\measuredangle 24°$
6/18	Rib18	Ribs 1.0×0.8 and 24° separation (turbulent)	5-19	$1.82 \cdot 10^{-2}\measuredangle 24°$
6/19	Rib19	Sand roughness	5-30	$7.27 - 9.09 \cdot 10^{-3}$
6/19	Rib20	Sand roughness (turbulent)	5-19	$7.27 - 9.09 \cdot 10^{-3}$

nonexistent, see ribs 5 and 9 between pairs 16 and 23, and this could be due to differences in the strength of various higher pairs. It's the lower pairs that are important for vortex induced vibration (pairs 1-5) and the agreement here is excellent. The agreement for PSD of chronos is less corresponding for long and short recording as seen in figure B.1b. For the lower BOD pairs, the agreement is good with MAC values above 0.9 but it's reduced for the smooth cylinder and rib $7.27 \cdot 10^{-3}\measuredangle 24°$ without turbulence between pairs 16 and 23. Overall, the agreement between recording length is consistently acceptable for determining the vortex shedding characteristics around a cylinder and 1 minute recordings are acceptable in getting the global statistics.

B.2 Strouhal number

B.2.1 Strouhal number comparison

In addition to the Strouhal numbers presented in section 4.3.1, the Strouhal number was calculated for all experimental configurations. This is shown in figure B.2 for the configurations with ribs and in figure B.3 for the configurations with sand roughness and smooth surface (no roughness added). Note that the Strouhal number for the configurations with sand roughness are measured with the unsteady pressure only as loose sand could damage the Cobra probes.

B.2.2 Strouhal comparison using single pressure tap and vortex-lift's chronos

The difference in Strouhal number when calculating it using a single pressure tap and the vortex lift's chronos can be estimated similarly to the difference between vortex lift's chronos and wake measurements. Pressure tap 10, located at an angular position of 96° compared to the pure

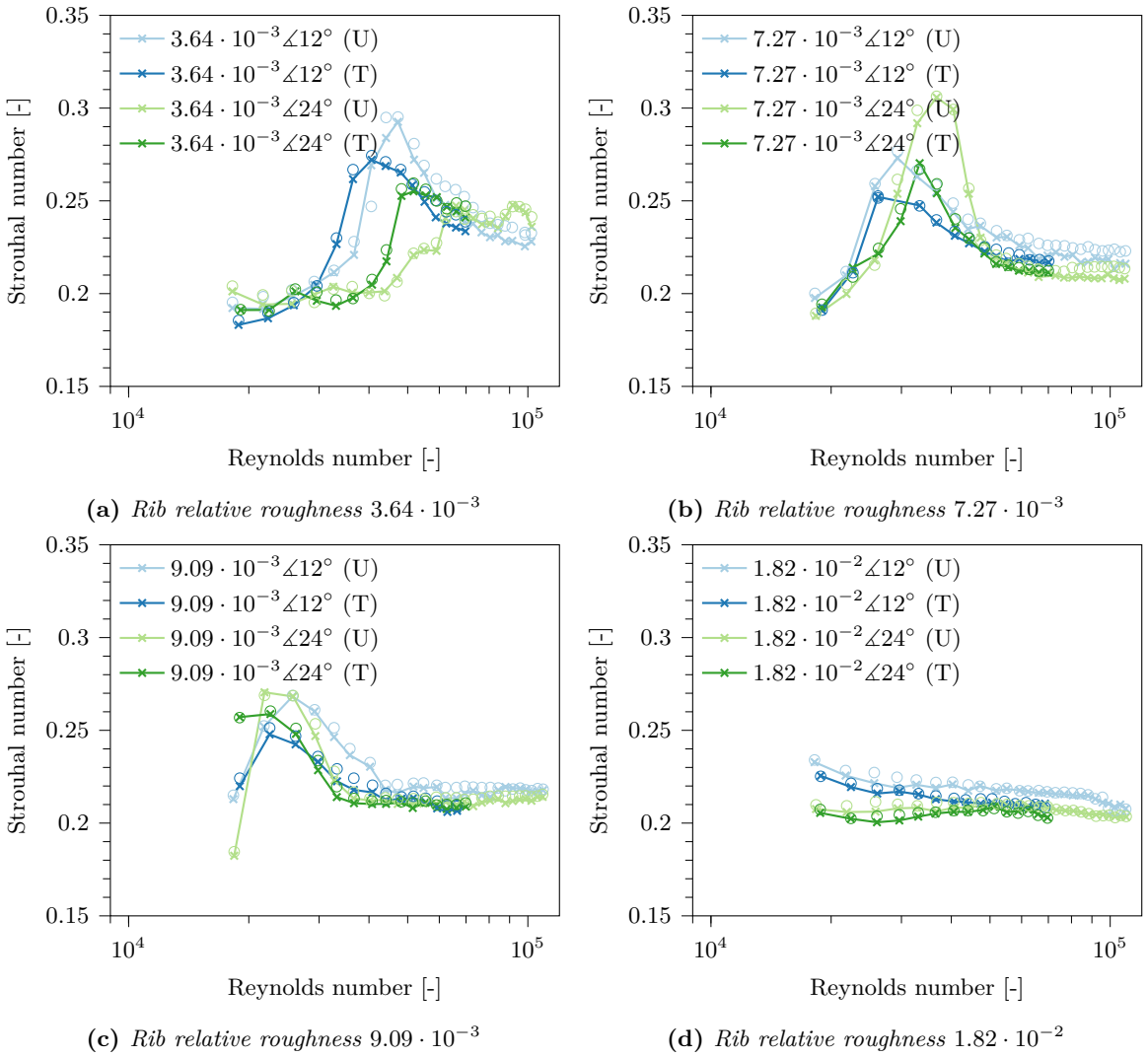

(a) *Rib relative roughness* $3.64 \cdot 10^{-3}$

(b) *Rib relative roughness* $7.27 \cdot 10^{-3}$

(c) *Rib relative roughness* $9.09 \cdot 10^{-3}$

(d) *Rib relative roughness* $1.82 \cdot 10^{-2}$

Figure B.2: *Comparison of Strouhal numbers from wake (× marks) and chronos (lines) using the rib configurations. Turbulent results are marked with (T) and uniform flow with (U).*

drag direction, is chosen for this analysis as it should be experiencing mostly lift and be in a zone of clear vortex-shedding. An example of PSDs from this pressure tap, using the same configurations as in the wake PSD example in figure 4.5a, is shown in figure B.4a. As seen, the absolute PSD values are greater when using the pressure rather than wake fluctuations and there's relatively more frequency content at low frequencies; the PSD at low frequencies have higher values here but relatively lower values at the Strouhal frequency (more noise dominated).

An example of the difference in Strouhal numbers ($St_{chronos} - St_{tap}$ is shown in figure B.4b for the smooth cylinder without turbulence. For most speeds, the difference is minute (either zero or $\sim 10^{-10}$) and the small differences are due to numerical rounding of the wind speeds. For a few other speeds, the difference is greater and the peak frequency (and Strouhal number) has a slightly different value. This difference is only present at certain speeds and additional statistical inference is perform to evaluate the mean differences.

The inference results on the mean difference in peak Strouhal number and the bandwidth is shown in table B.4. As seen the difference is ambiguous and there's no real evidence for either model. For both tests, the probability of the conservative model being correct given the data is slightly higher than the alternative. This gives a small Bayes factor (BF) and poor evidence for either model. There are mean differences in the peak and bandwidth, but the mean differences

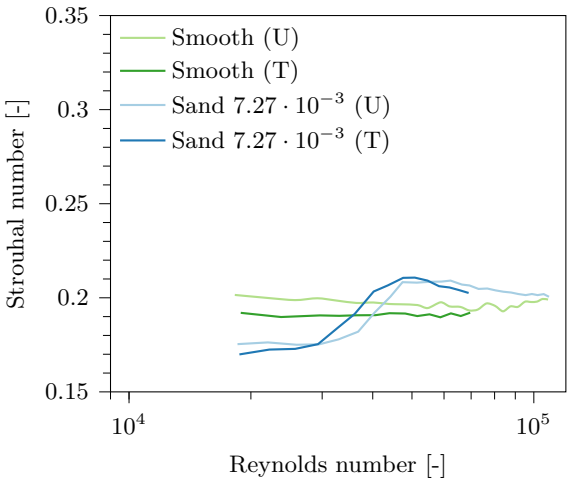

Figure B.3: *Strouhal number from chronos using sand roughness configuration. Turbulent results are marked with (T) and uniform flow with (U).*

are small and the likelihood of the alternative model is less than the conservative.

B.3 Unsteady forces

The mean and SD drag coefficients calculated for all configurations using equation (2.3) are shown in figures B.5 – B.9. Similarly, the mean and SD lift coefficients calculated for all configurations using equation (2.4) are shown in figures B.10 – B.14. Both forces and statistics conform to the discussions presented in chapter 4. The reason for not including all configurations in one plot is because there are too many configurations to compare.

B.4 Super-critical Reynolds numbers

The onset of super-critical Reynolds numbers is defined as in section 2.1.1. I.e., the onset is when the mean drag coefficient (and other force statistics) reaches a steady value with Reynolds numbers post drag crisis. The configurations that reached and the speeds/Reynolds numbers that the configurations reach super-critical Reynolds numbers are shown in table B.2. The configurations marked with N/A in the speed and Reynolds numbers columns does not satisfactorily reach the super-critical region.

B.5 Correlation and coherence

B.5.1 Correlation

The vertical correlation for the cylinder configurations with ribs that reached super-critical Reynolds numbers (per table B.2 are shown in figures B.15a–B.15d. As mentioned, the tests with sand roughness did not use the Cobra probes meaning that no correlation could be measured. As can be seen, the correlation at super-critical Reynolds numbers conform to the trends discussed in chapter 4

B.5.2 Coherence

The vertical correlation for the cylinder configurations with ribs that reached super-critical Reynolds numbers (per table B.2 are shown in figures B.16a–B.16d. As mentioned, the tests

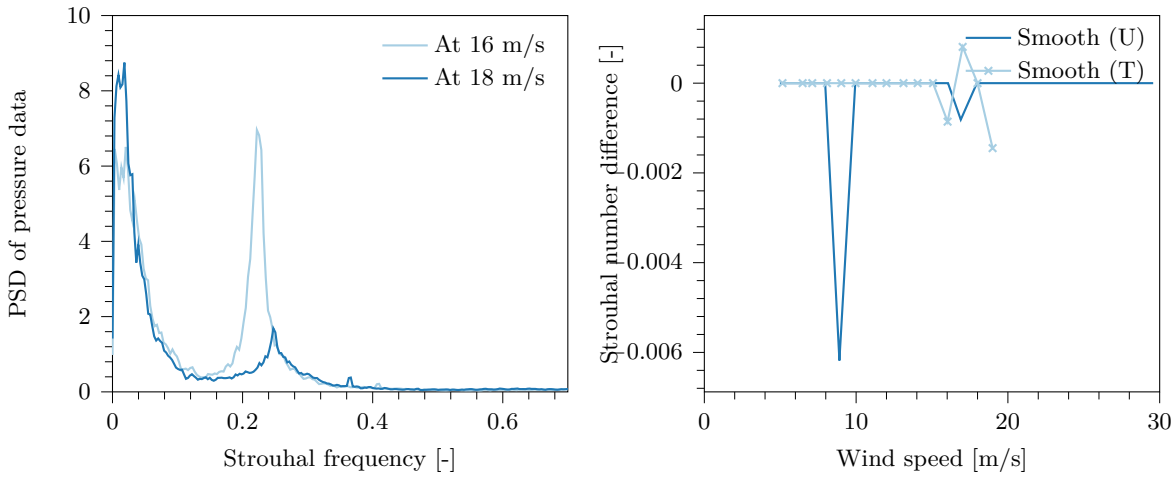

(a) *Example of power spectral densities from pressure tap using two speeds and rib roughnesse configuration* $3.64 \cdot 10^{-3} \measuredangle 24°$.

(b) *Difference in Strouhal number from vortex lift's chronos and a single pressure tap.*

Figure B.4: *Examples of PSD from pressure tap and the absolute difference in Strouhal numbers for topos and pressure tap measurements.*

with sand roughness did not use the Cobra probes meaning that no coherence could be measured. As can be seen, the coherence at super-critical Reynolds numbers conform to the trends discussed in chapter 4

B.6 Topos comparison using MAC

The MAC value comparisons shown in figures B.17–B.20 are an extension of the MAC value comparison in section 4.4.3. This is done by comparing the super-critical topos for all configurations rather than the chosen few in chapter 4.

B.7 Relative forces

The relative forces shown in figures B.21–B.24 extends the relative force comparison done in section 4.4.6 to all roughness configurations reaching super-critical Reynolds numbers. These results conform to the analysis done in chapter 4.

B.8 Inference results

To better compare the force statistic results (e.g. Strouhal number, lift and drag), Bayesian inferences is used to evaluate the significance of any differences between configurations. This procedure follows the technique outlined in section A.4 and the Bayesian inference performed is as follows:

- Differences in Strouhal number between wake measurements and vortex lift's chronos in table B.3.
- Differences in Strouhal number between single pressure tap and vortex lift's chronos in table B.4.
- Differences in Strouhal number between configurations using the vortex lift's chronos in table B.5.

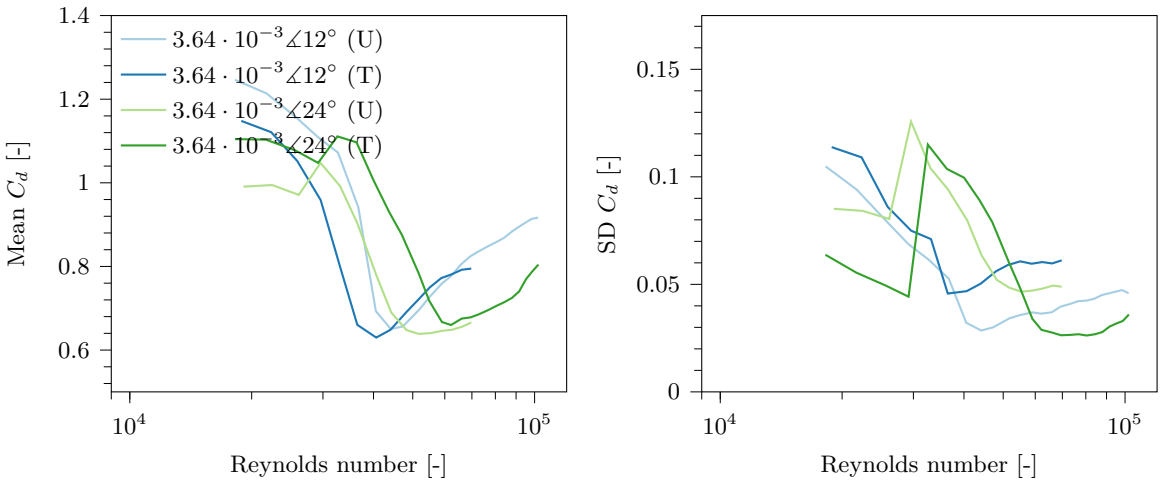

(a) *Mean drag*

(b) *SD drag*

Figure B.5: *Mean and SD drag coefficient for ribs with relative roughness* $3.64 \cdot 10^{-3}$*. Turbulent results are marked with (T) and uniform flow with (U).*

- Differences in Strouhal number between configurations using the wake measurements in table B.6.
- Differences in mean and SD drag between configurations in table B.7.
- Differences in mean and SD lift between configurations in table B.8.

For Bayesian inference result tables, the first column describes the conservative hypothesis (null model in frequentist inference), the second the probability of the alternative model being true given the data and the third and fourth columns are the Bayes factors described in section A.4 which describes how strong the evidence is.

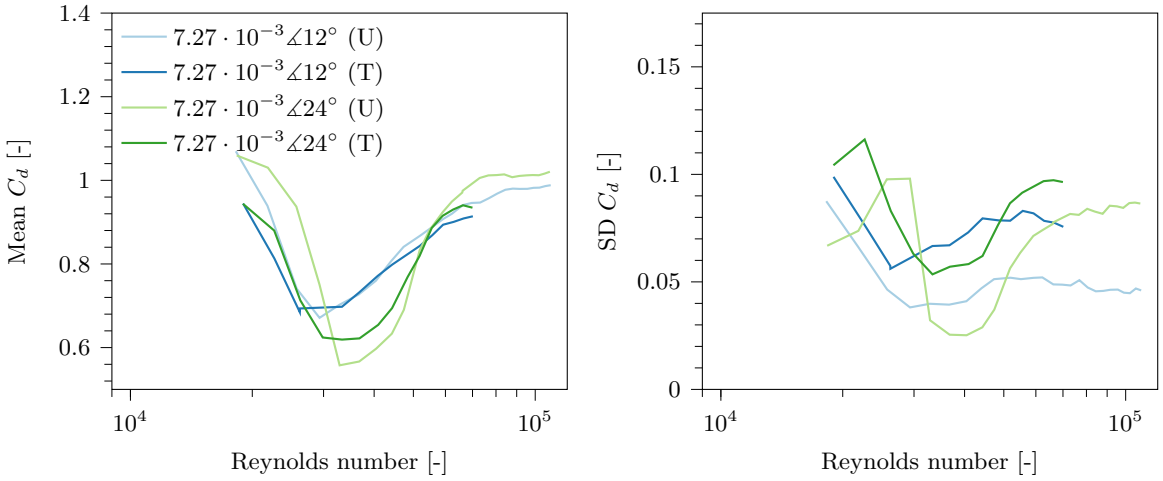

(a) *Mean drag* **(b)** *SD drag*

Figure B.6: *Mean and SD drag coefficient for ribs with relative roughness* $7.27 \cdot 10^{-3}$*. Turbulent results are marked with (T) and uniform flow with (U).*

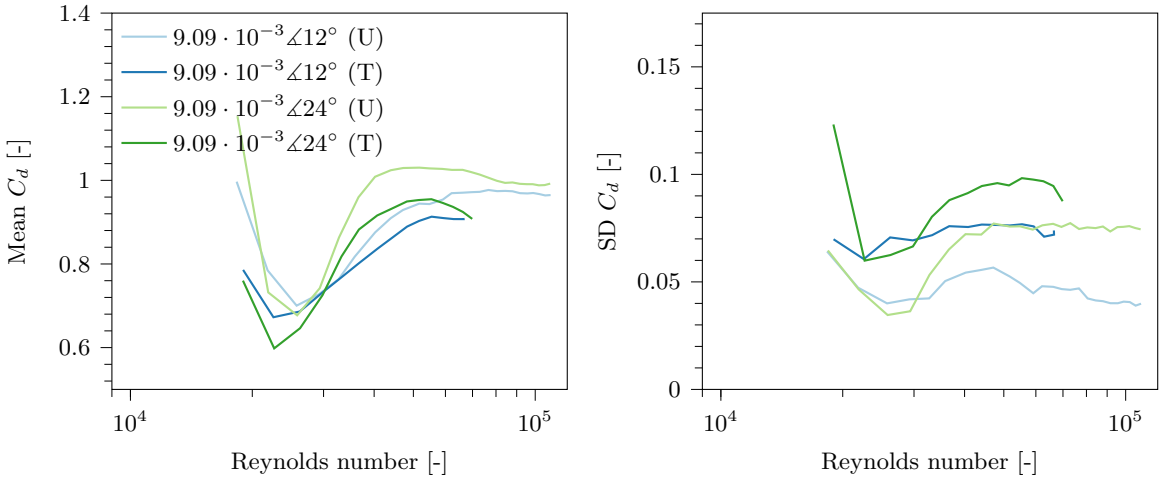

(a) *Mean drag* **(b)** *SD drag*

Figure B.7: *Mean and SD drag coefficient for ribs with relative roughness* $9.09 \cdot 10^{-3}$*. Turbulent results are marked with (T) and uniform flow with (U).*

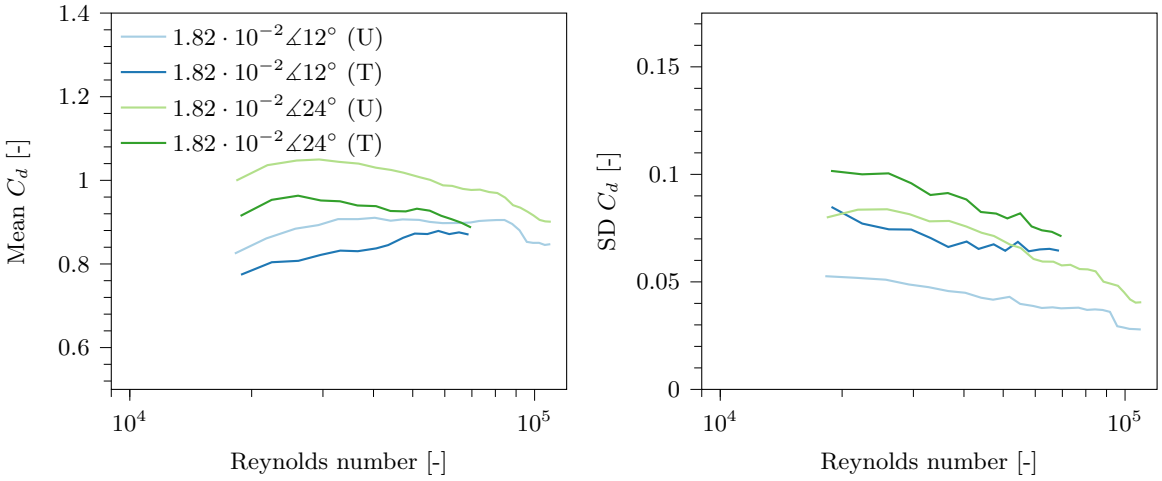

(a) *Mean drag* **(b)** *SD drag*

Figure B.8: *Mean and SD drag coefficient for ribs with relative roughness* $1.82 \cdot 10^{-2}$*. Turbulent results are marked with (T) and uniform flow with (U).*

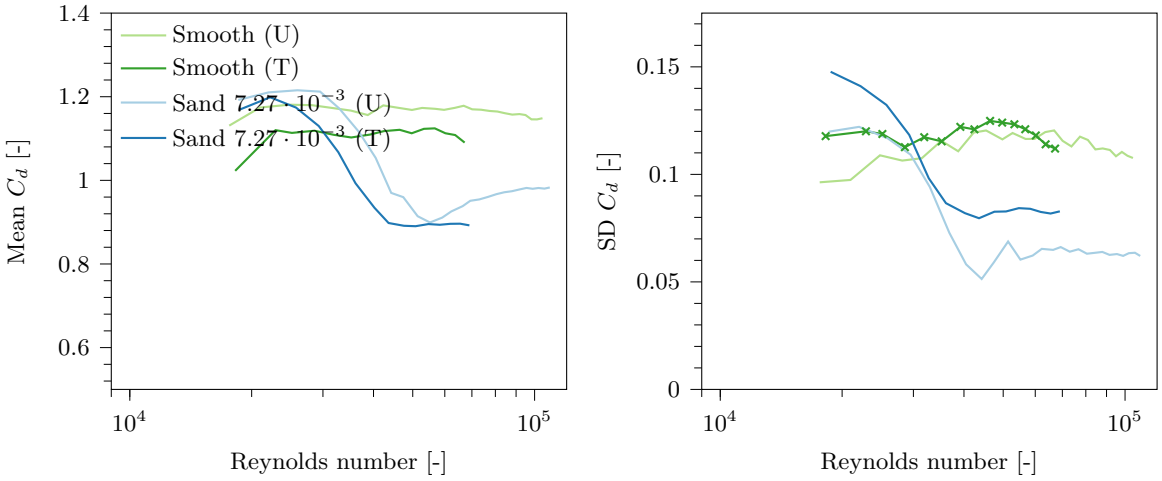

(a) *Mean drag* **(b)** *SD dragt*

Figure B.9: *Mean and SD drag coefficients for sand roughness and smooth surface configurations. Turbulent results are marked with (T) and uniform flow with (U).*

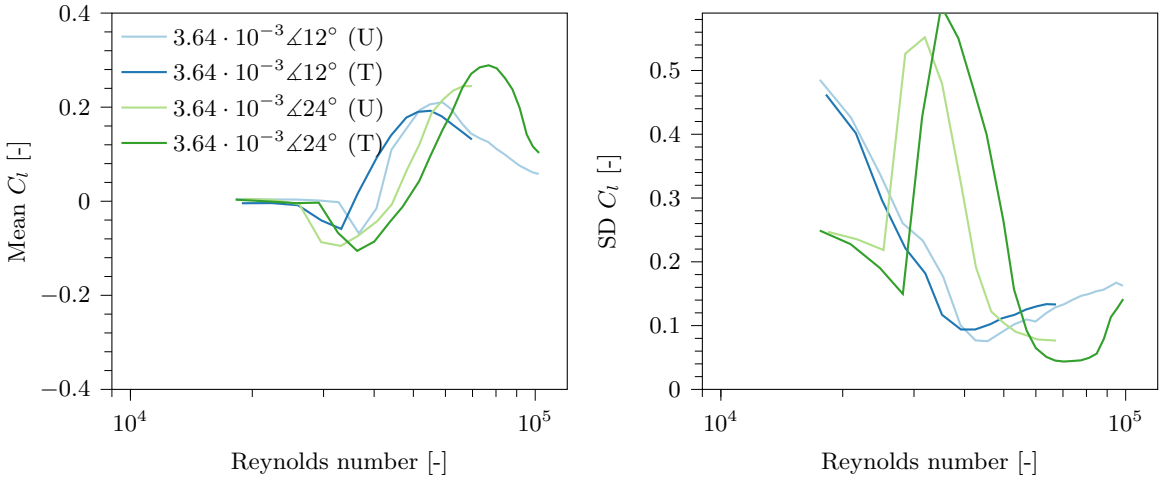

(a) *Mean lift* **(b)** *SD lift*

Figure B.10: *Mean and SD lift coefficient for ribs with relative roughness* $3.64 \cdot 10^{-3}$*. Turbulent results are marked with (T) and uniform flow with (U).*

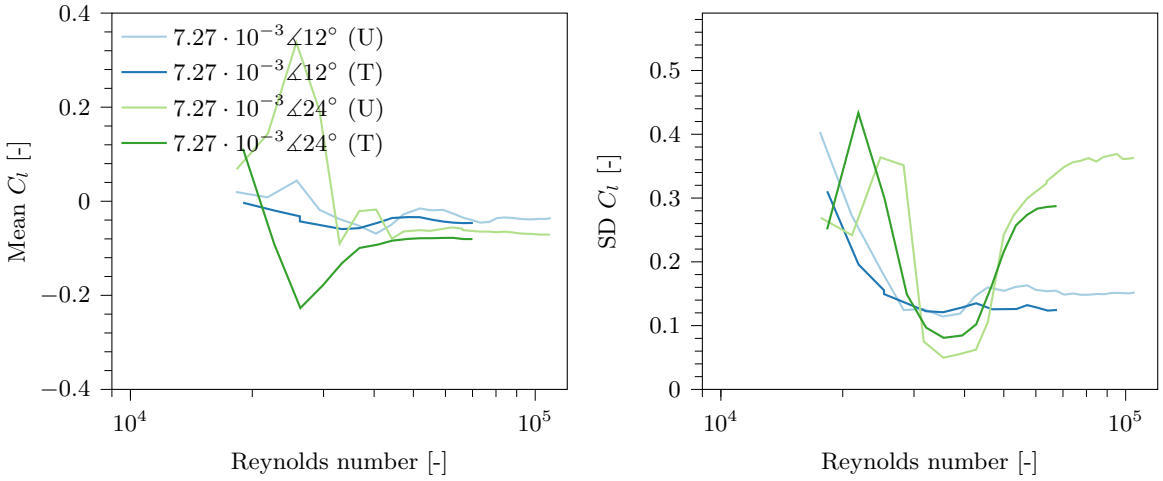

(a) *Mean lift* **(b)** *SD lift*

Figure B.11: *Mean and SD lift coefficient for ribs with relative roughness* $7.27 \cdot 10^{-3}$*. Turbulent results are marked with (T) and uniform flow with (U).*

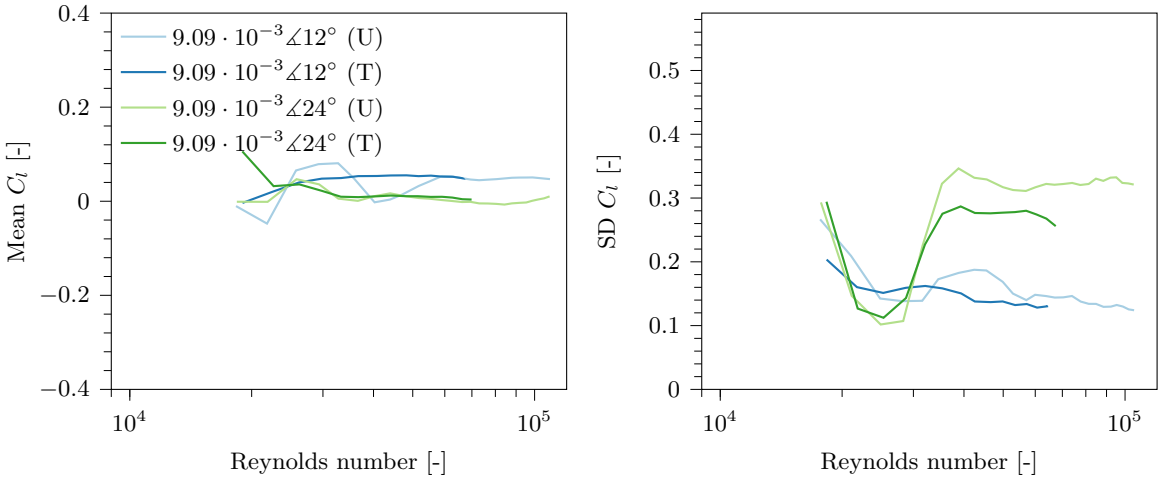

(a) *Mean lift* **(b)** *SD lift*

Figure B.12: *Mean and SD lift coefficient for ribs with relative roughness* $9.09 \cdot 10^{-3}$*. Turbulent results are marked with (T) and uniform flow with (U).*

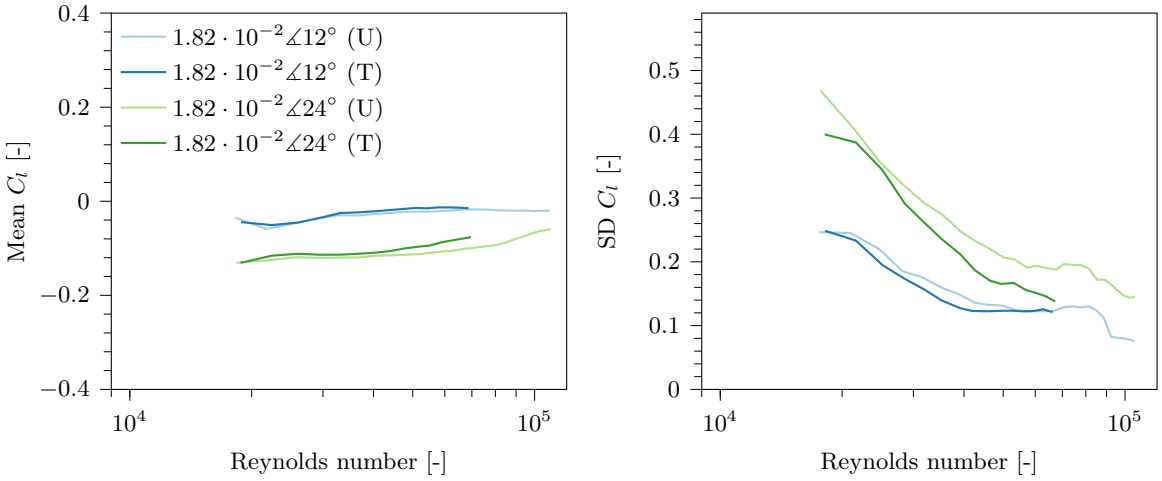

(a) *Mean lift* **(b)** *SD lift*

Figure B.13: *Mean and SD lift coefficient for ribs with relative roughness* $1.82 \cdot 10^{-2}$*. Turbulent results are marked with (T) and uniform flow with (U).*

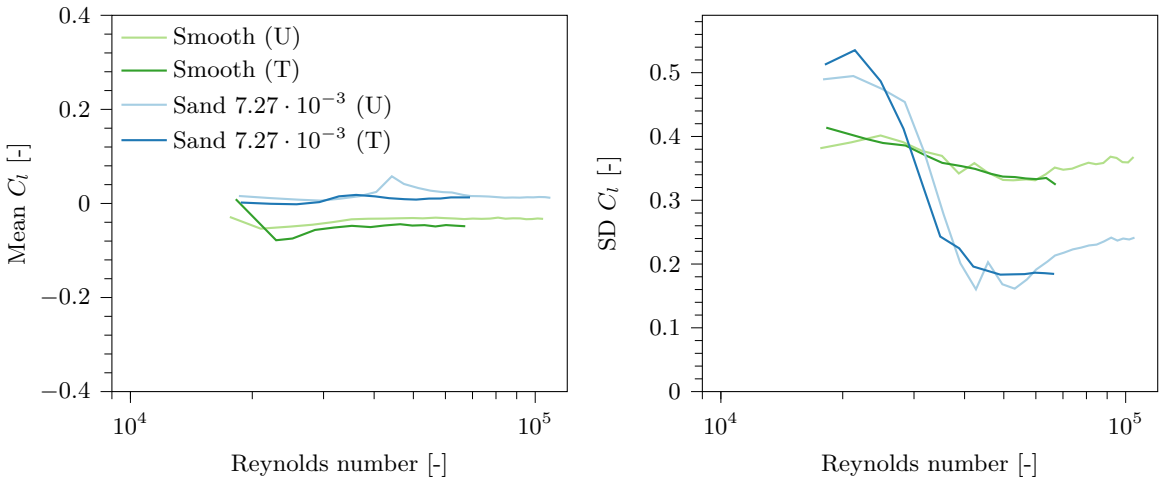

(a) *Mean lift.* **(b)** *SD lift.*

Figure B.14: *Mean and SD lift coefficients for sand roughness and smooth surface configurations. Turbulent results are marked with (T) and uniform flow with (U).*

Table B.2: *Reynolds numbers and roughness configurations from small-scale 2D tests identified as being at super-critical Reynolds numbers.*

Rib #	Configuration	Speed [m/s]	Reynolds number [-]
Rib 01	$3.64 \cdot 10^{-3} \measuredangle 12°$ (U)	27.8	102000
Rib 02	$3.64 \cdot 10^{-3} \measuredangle 12°$ (T)	19.0	69800
Rib 03	$3.64 \cdot 10^{-3} \measuredangle 24°$ (U)	N/A	N/A
Rib 04	$3.64 \cdot 10^{-3} \measuredangle 24°$ (T)	N/A	N/A
Rib 07	$7.27 \cdot 10^{-3} \measuredangle 12°$ (T)	19.1	70100
Rib 08	$7.27 \cdot 10^{-3} \measuredangle 12°$ (U)	23.0	84400
Rib 09	$7.27 \cdot 10^{-3} \measuredangle 24°$ (U)	20.9	76600
Rib 10	$7.27 \cdot 10^{-3} \measuredangle 24°$ (T)	18.1	66300
Rib 11	$9.09 \cdot 10^{-3} \measuredangle 12°$ (T)	15.1	55500
Rib 12	$9.09 \cdot 10^{-3} \measuredangle 12°$ (U)	17.0	62200
Rib 13	$9.09 \cdot 10^{-3} \measuredangle 24°$ (U)	14.9	54800
Rib 14	$9.09 \cdot 10^{-3} \measuredangle 24°$ (T)	14.0	51500
Rib 15	$1.82 \cdot 10^{-2} \measuredangle 12°$ (T)	14.8	54400
Rib 16	$1.82 \cdot 10^{-2} \measuredangle 12°$ (U)	11.0	40300
Rib 17	$1.82 \cdot 10^{-2} \measuredangle 24°$ (U)	8.01	29400
Rib 18	$1.82 \cdot 10^{-2} \measuredangle 24°$ (T)	7.10	26000
Rib 19	Sand $7.27 \cdot 10^{-3}$ (U)	29.7	109000
Rib 20	Sand $7.27 \cdot 10^{-3}$ (T)	14.9	54700
Rib 21	Smooth	67.6	2170000

Table B.3: *Bayesian inference results comparing Strouhal numbers obtained from wake measurements and vortex lift's chronos.*

H_1 (conservative test model)	$P(H_2\|data)$	$BF_{H_2:H_1}$	$BF_{H_1:H_2}$	Interpretation
No difference in mean Strouhal number between wake and vortex lift's chronos	1	$\sim 10^{17}$	~ 0	Very strong evidence against H_1
No difference in mean Strouhal number bandwidth between wake and vortex lift's chronos	0.587	1.42	0.704	No evidence worth mentioning for H_1

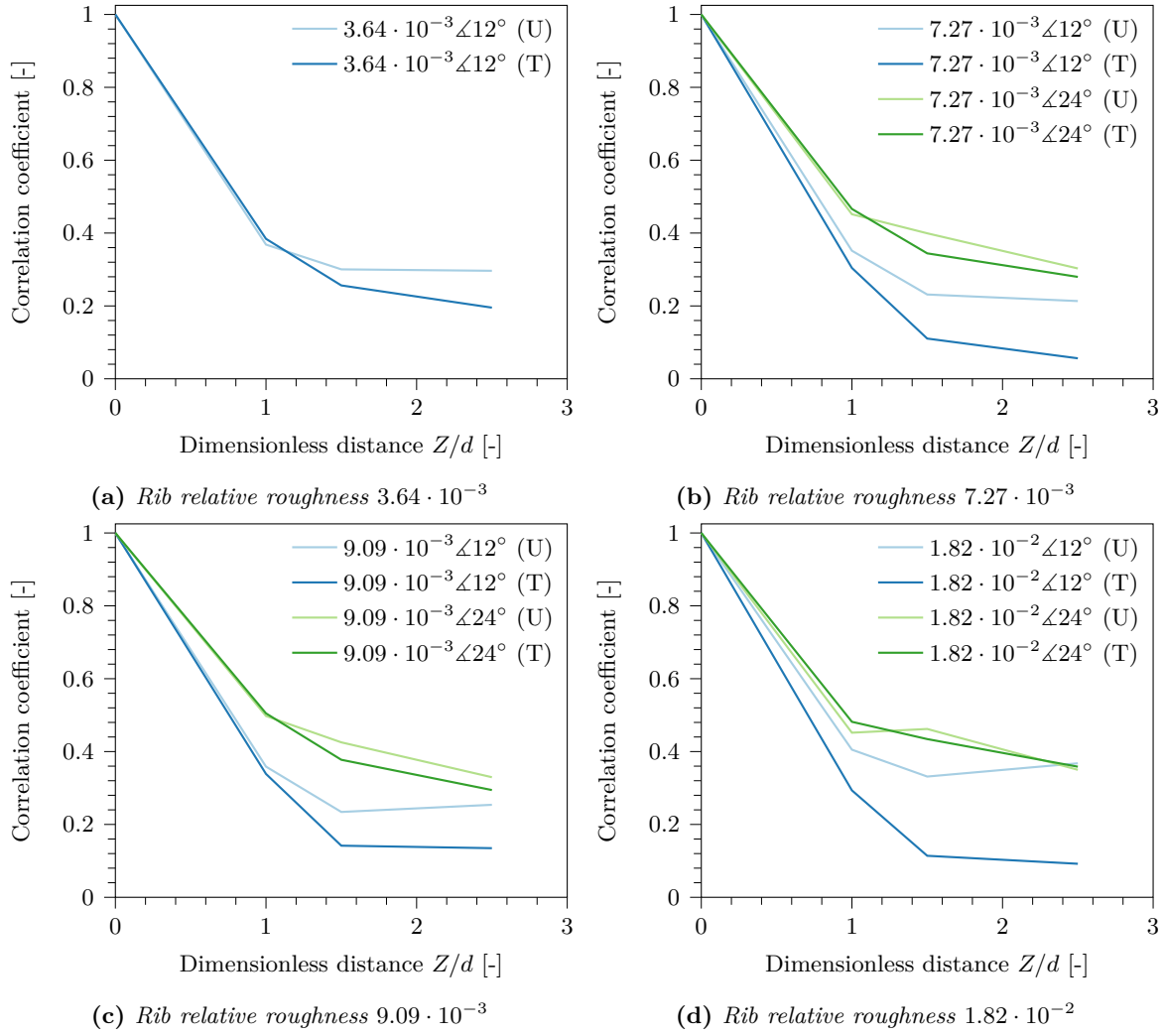

(a) *Rib relative roughness* $3.64 \cdot 10^{-3}$

(b) *Rib relative roughness* $7.27 \cdot 10^{-3}$

(c) *Rib relative roughness* $9.09 \cdot 10^{-3}$

(d) *Rib relative roughness* $1.82 \cdot 10^{-2}$

Figure B.15: *Correlation for all rib configurations at super-critical Reynolds numbers per table B.2.*

Table B.4: *Bayesian inference results comparing Strouhal numbers obtained from pressure tap and vortex lift's chronos.*

H_1 (conservative test model)	$P(H_2\|data)$	$BF_{H_2:H_1}$	$BF_{H_1:H_2}$	Interpretation
No difference in mean Strouhal number between pressure tap data and vortex lift's chronos	0.439	0.784	1.28	No evidence worth mentioning for H_1
No difference in mean Strouhal number bandwidth between pressure tap data and vortex lift's chronos	0.273	0.375	2.70	No evidence worth mentioning for H_1

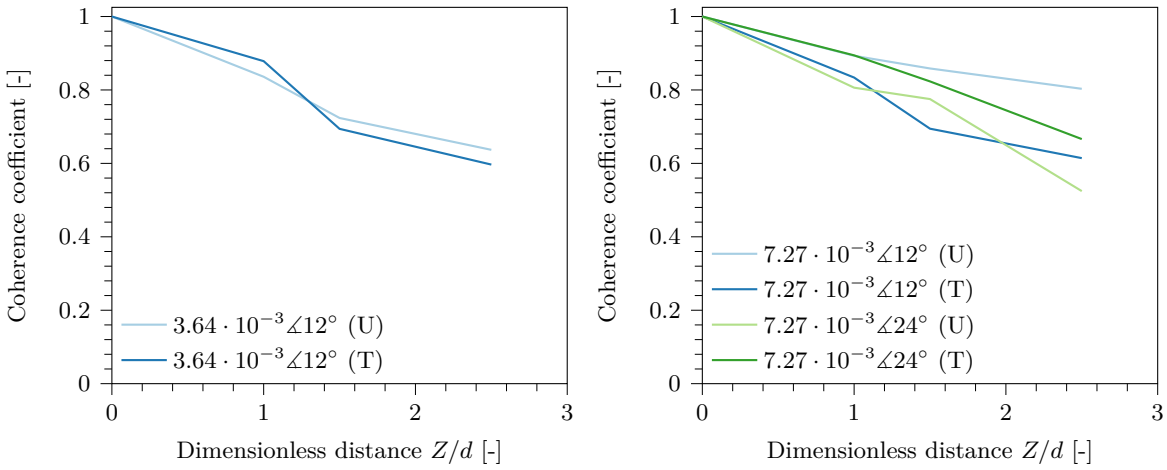

(a) *Rib relative roughness* $3.64 \cdot 10^{-3}$

(b) *Rib relative roughness* $7.27 \cdot 10^{-3}$

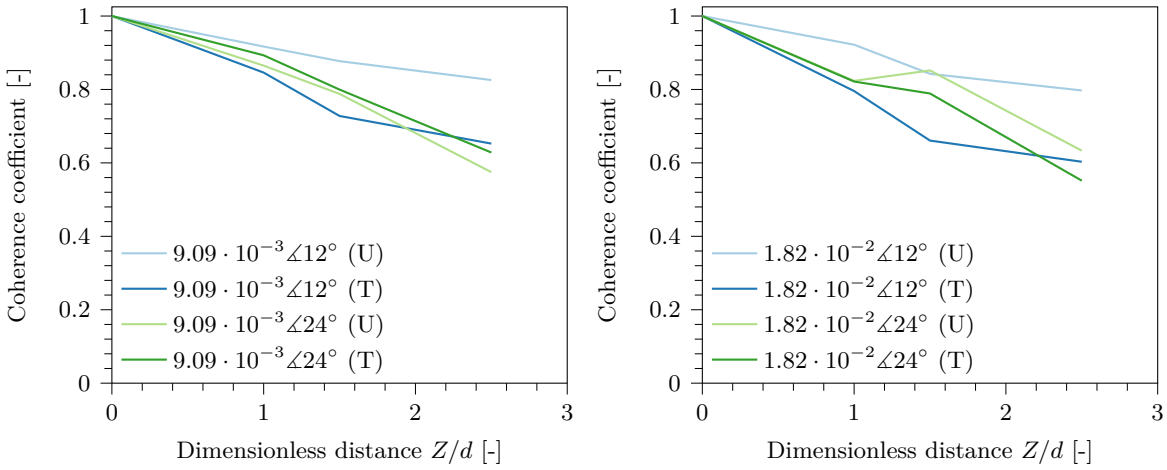

(c) *Rib relative roughness* $9.09 \cdot 10^{-3}$

(d) *Rib relative roughness* $1.82 \cdot 10^{-2}$

Figure B.16: *Coherence for all rib configurations at super-critical Reynolds numbers per table B.2.*

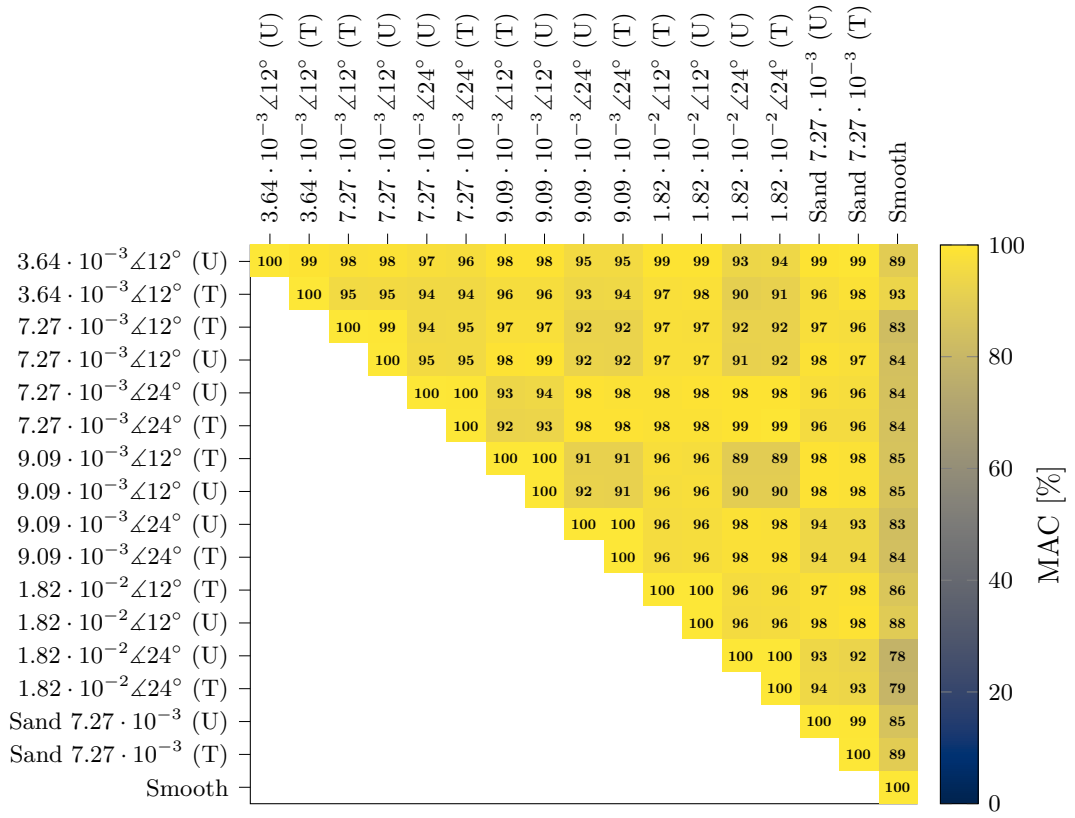

Figure B.17: *MAC matrix for mean topos at super-critical Reynolds numbers using the configurations in table B.2.*

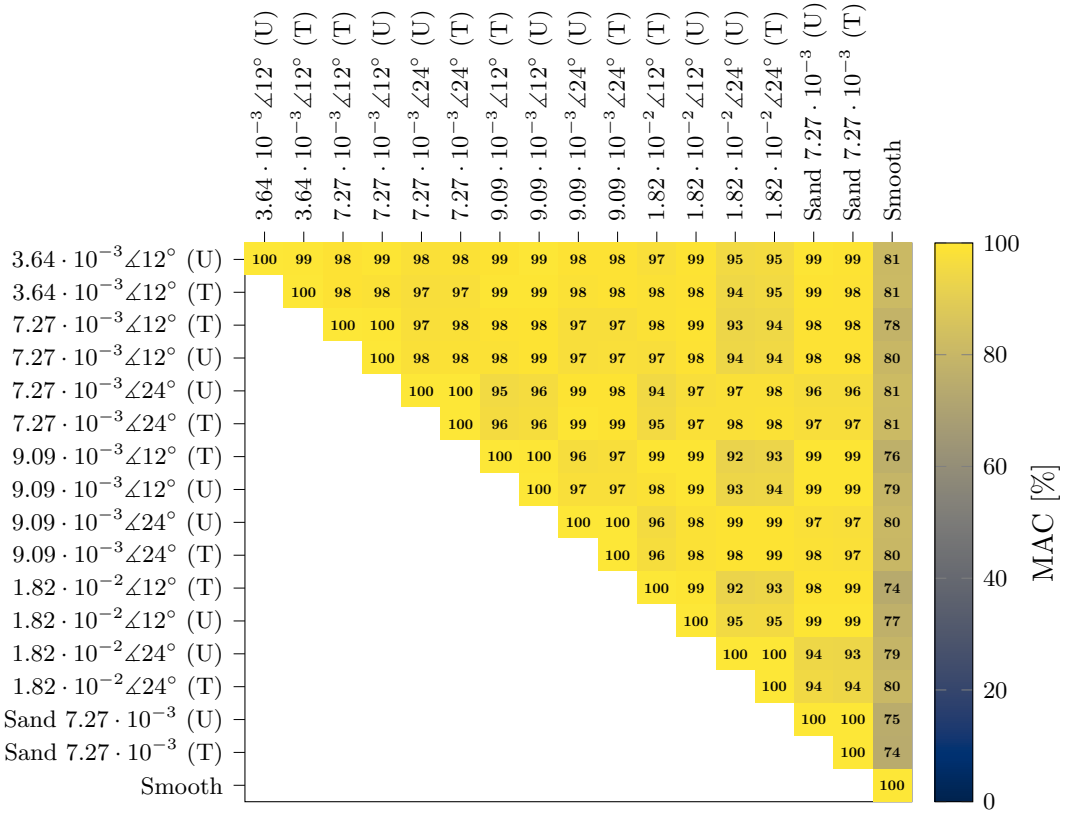

Figure B.18: *MAC matrix for vortex-lift topos at super-critical Reynolds numbers using the configurations in table B.2.*

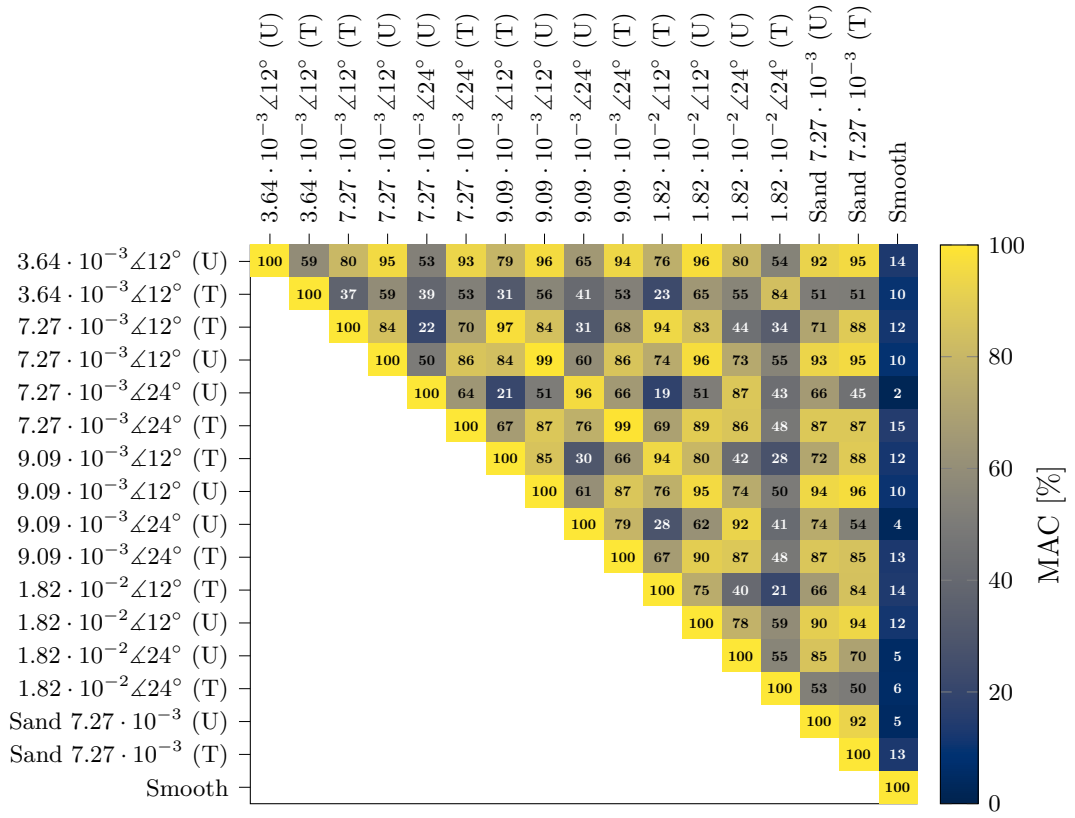

Figure B.19: *MAC matrix for vortex-drag topos at super-critical Reynolds numbers using the configurations in table B.2.*

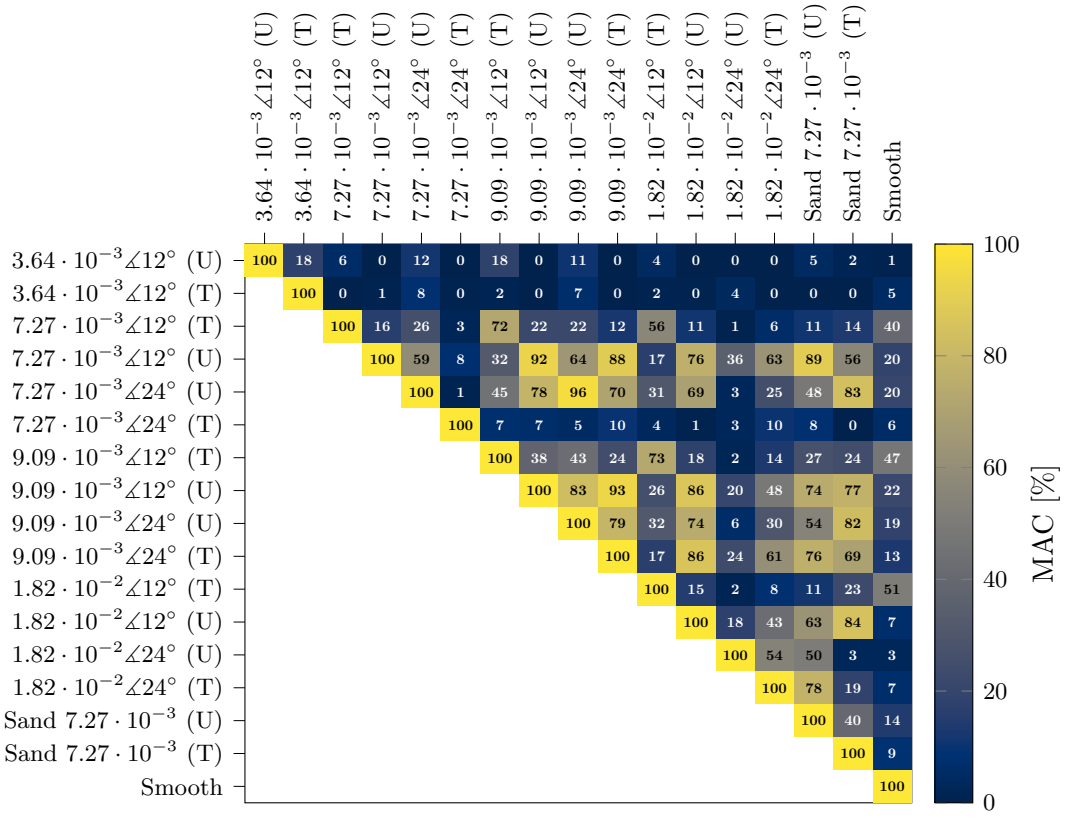

Figure B.20: *MAC matrix for secondary vortex-lift topos at super-critical Reynolds numbers using the configurations in table B.2.*

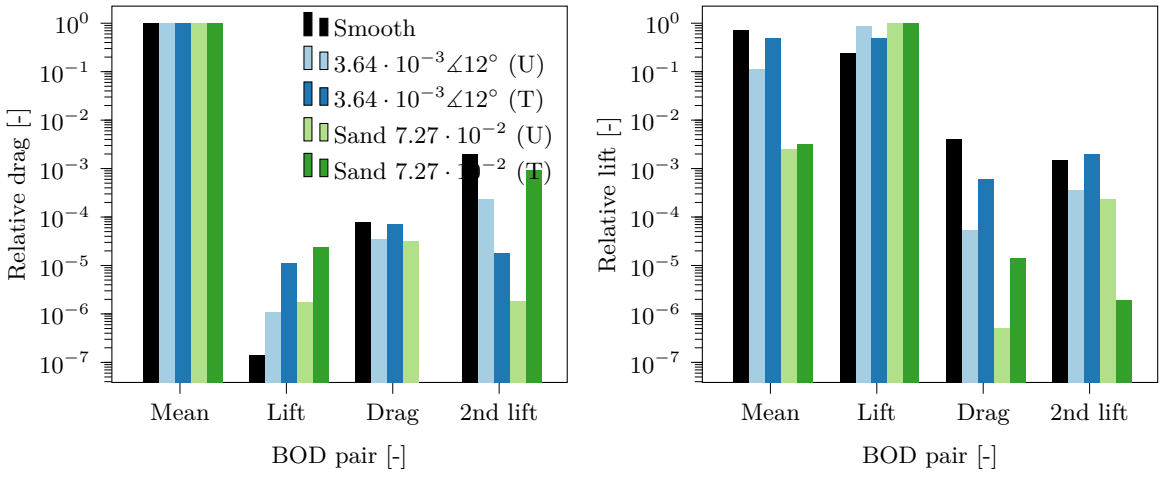

(a) *Relative drag.* **(b)** *Relative lift.*

Figure B.21: *Comparison of relative forces at super-critical Reynolds numbers using the* $3.64 \cdot 10^{-3}$ *and sand roughness configurations in table B.2.*

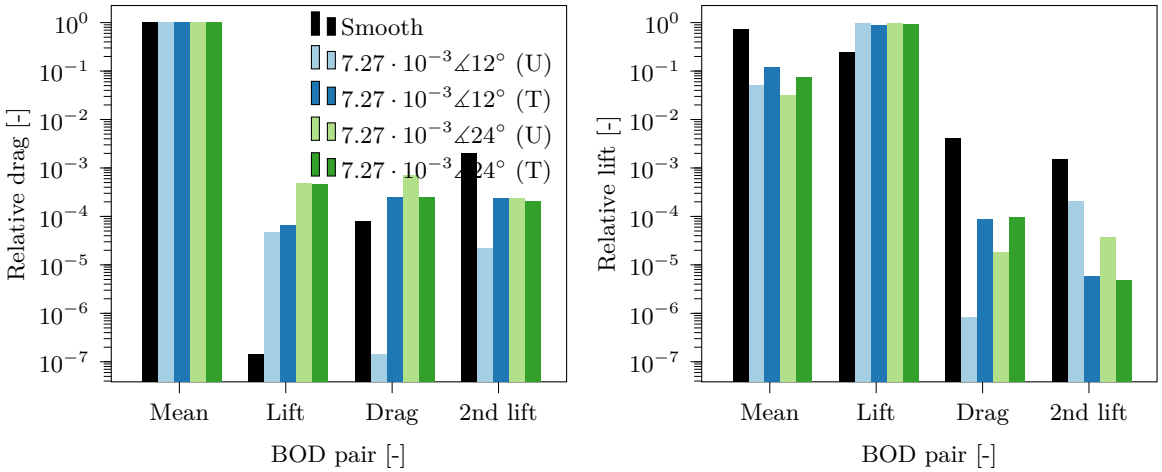

(a) *Relative drag.* **(b)** *Relative lift.*

Figure B.22: *Comparison of relative forces at super-critical Reynolds numbers using the* $7.27 \cdot 10^{-3}$ *configurations in table B.2.*

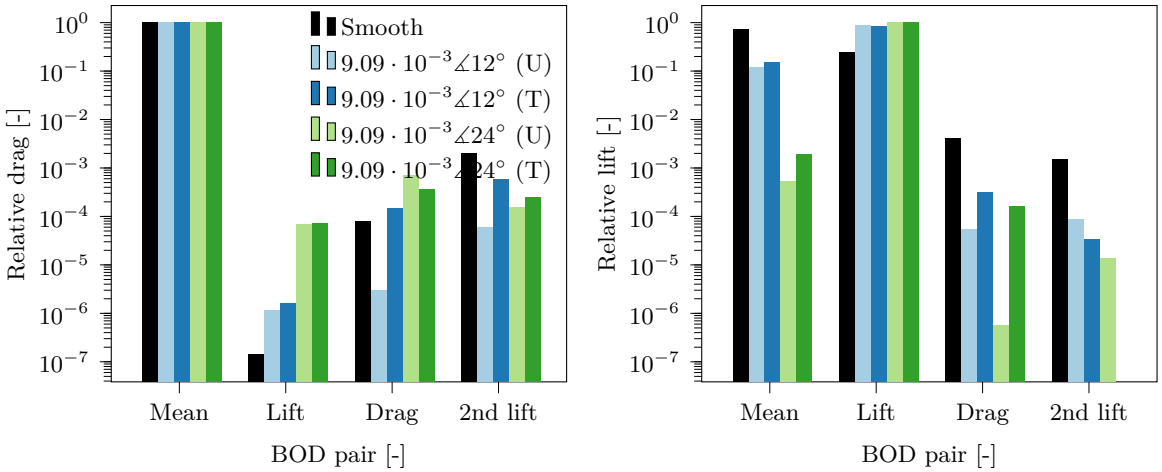

(a) *Relative drag.* **(b)** *Relative lift.*

Figure B.23: *Comparison of relative forces at super-critical Reynolds numbers using the* $9.09 \cdot 10^{-3}$ *configurations in table B.2.*

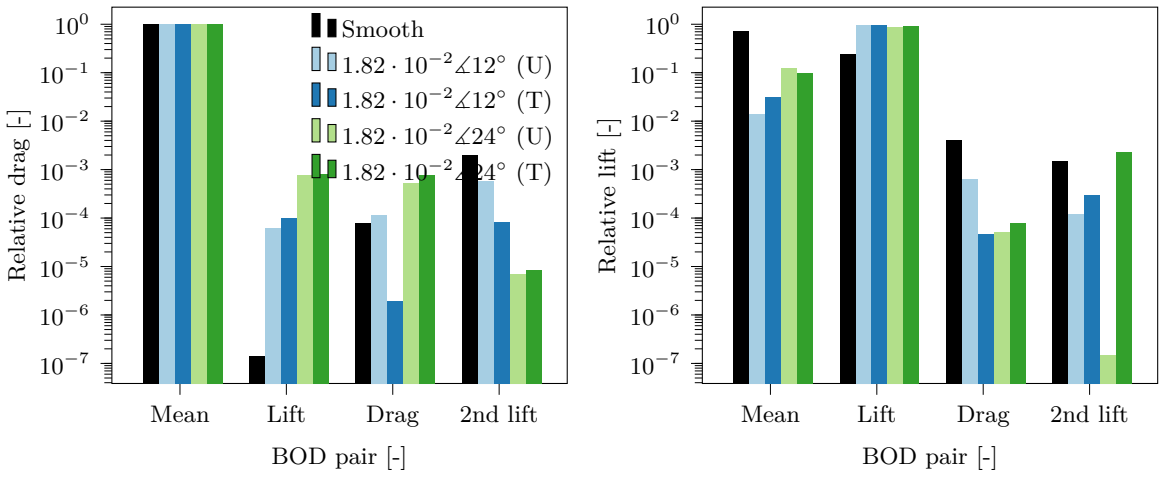

(a) *Relative drag.*

(b) *Relative lift.*

Figure B.24: *Comparison of relative forces at super-critical Reynolds numbers using the* $1.82 \cdot 10^{-2}$ *configurations in table B.2.*

Table B.5: *Bayesian inference results testing the effect of roughness and turbulence intensity on Strouhal number obtained from vortex lift's chronos.*

H_1 (conservative test model)	$P(H_2\|data)$	$BF_{H_2:H_1}$	$BF_{H_1:H_2}$	Interpretation
No difference in mean Strouhal number when changing turbulence	0.983	60.7	0.0165	Strong evidence against H_1
No difference in mean Strouhal number bandwidth when changing turbulence	0.0916	0.101	9.92	Positive evidence for H_1
No difference in mean Strouhal number when changing turbulence at super-critical Reynolds numbers	1.00	$\sim 10^6$	~ 0	Very strong evidence against H_1
No difference in mean Strouhal number bandwidth when changing turbulence at super-critical Reynolds numbers	0.104	0.116	8.61	Positive evidence for H_1
No difference in mean Strouhal number when changing rib spacing	1.00	$\sim 10^4$	~ 0	Very strong evidence against H_1
No difference in mean Strouhal number bandwidth when changing rib spacing	0.131	0.151	6.63	Positive evidence for H_1
No difference in mean Strouhal number when changing rib size at super-critical Reynolds numbers	1.00	$\sim 10^{13}$	~ 0	Very strong evidence against H_1
No difference in mean Strouhal number bandwidth when changing rib size at super-critical Reynolds numbers	0.960	23.8	0.0421	Strong evidence against H_1

Table B.6: *Bayesian inference results testing the effect of roughness and turbulence intensity on Strouhal numbers from wake measurements.*

H_1 (conservative test model)	P(H_2|data)	$BF_{H_2:H_1}$	$BF_{H_1:H_2}$	Interpretation
No difference in mean Strouhal number when changing turbulence	0.873	6.85	0.146	Positive evidence against H_1
No difference in mean Strouhal bandwidth when changing turbulence	0.0877	0.0962	10.4	Positive evidence for H_1
No difference in mean Strouhal number when changing turbulence at super-critical Reynolds numbers	1.00	$\sim 10^4$	~ 0	Very strong evidence against H_1
No difference in mean Strouhal bandwidth when changing turbulence at super-critical Reynolds numbers	0.104	0.116	8.62	Positive evidence for H_1
No difference in mean Strouhal number when changing rib spacing	1.00	$\sim 10^5$	~ 0	Very strong evidence against H_1
No difference in mean Strouhal bandwidth when changing rib spacing	0.709	2.44	0.409	No worthwhile evidence against H_1
No difference in mean Strouhal number when changing rib size at super-critical Reynolds numbers	1.00	$\sim 10^{19}$	~ 0	Very strong evidence against H_1
No difference in mean Strouhal bandwidth when changing rib size at super-critical Reynolds numbers	0.951	19.6	0.0510	Positive evidence against H_1

Table B.7: *Bayesian inference results testing the effect of roughness and turbulence intensity on global unsteady drag coefficients.*

H_1 (conservative test model)	P(H_2|data)	$BF_{H_2:H_1}$	$BF_{H_1:H_2}$	Interpretation
No difference in mean drag coefficient when changing turbulence	1.00	$\sim 10^{19}$	~ 0	Very strong evidence against H_1
No difference in mean SD drag when changing turbulence	1.00	$\sim 10^{30}$	~ 0	Very strong evidence against H_1
No difference in mean drag coefficient when changing turbulence at super-critical Reynolds numbers	1.00	$\sim 10^{17}$	~ 0	Very strong evidence against H_1
No difference in mean SD drag when changing turbulence at super-critical Reynolds numbers	1.00	$\sim 10^{43}$	~ 0	Very strong evidence against H_1
No difference in mean drag coefficient when changing rib spacing	0.881	7.39	0.135	Positive evidence against H_1
No difference in mean SD drag when changing rib spacing	1.00	$\sim 10^{12}$	~ 0	Very strong evidence against H_1
No difference in mean drag coefficient when changing rib size at super-critical Reynolds numbers	0.999	1570	0.135	Very strong evidence against H_1
No difference in mean SD drag when changing rib size at super-critical Reynolds numbers	0.0927	0.102	9.78	Positive evidence for H_1

Table B.8: *Bayesian inference results testing the effect of roughness and turbulence intensity on global unsteady lift coefficients.*

H_1 (conservative test model)	$P(H_2\|data)$	$BF_{H_2:H_1}$	$BF_{H_1:H_2}$	Interpretation
No difference in mean lift coefficient when changing turbulence	0.181	0.222	4.510	Positive evidence for H_1
No difference in mean SD lift when changing turbulence	0.960	24.1	0.0414	Strong evidence against H_1
No difference in mean lift coefficient when changing turbulence at super-critical Reynolds numbers	0.129	0.148	6.77	Positive evidence for H_1
No difference in mean SD lift when changing turbulence at super-critical Reynolds numbers	1.00	$\sim 10^8$	~ 0	Very strong evidence against H_1
No difference in mean lift coefficient when changing rib spacing	1.00	$\sim 10^4$	~ 0	Very strong evidence against H_1
No difference in mean SD lift when changing rib spacing	1.00	$\sim 10^{10}$	~ 0	Very strong evidence against H_1
No difference in mean lift coefficient when changing rib size at super-critical Reynolds numbers	1.00	$\sim 10^6$	~ 0	Very strong evidence against H_1
No difference in mean SD lift when changing rib size at super-critical Reynolds numbers	0.0755	0.0817	12.2	Positive evidence for H_1

Appendix

C Additional data for the 3D wind tunnel experiment

C.0.1 The first mode shape

To further refine the approximated mode shape, the adjusted R^2 (defined in equation (C.1)) was used to evaluate the best fit. This statistic is a goodness-of-fit indicator that prevents overfitting and takes into account the number of explanatory variables and the residual error [155]. Here, var_{res} is the unbiased variance of the residuals (var_{res} =measured value-predicted value) and var_{tot} the unbiased variance of the measured values. To be unbiased, the degrees of freedom used in the denominator uses the number of measurements with the number of independent variables subtracted from it ($p+1$ where the $+1$ is from the mean).

$$\text{Adjusted } R^2 = 1 - \frac{var_{\text{res}}}{var_{\text{tot}}} = 1 - (1 - R^2)\frac{n-1}{n-p-1} \tag{C.1}$$

From table C.1, it can be seen that the mode shape $\psi(z) = 0.221z^2 + 0.786z$ has a slightly better goodness-of-fit than $\psi(z) = 1.01z - 0.0344$ but that the mode shape integrals used for the equivalent mass $\int_0^1 \psi(z)^2 dz$ are similar. $\psi(z) = z$ is a worse fit with a larger mode shape integral. Overall, $\psi(z) = 1.01z - 0.0344$ was chosen as the best fit to the experimental mode shape.

Table C.1: *Goodness-of-fit and mode shape integral for three functions fitted to the experimental mode shape in figure 5.4.*

$\psi(z)$	Adjusted R^2	$\int_0^1 \psi(z)^2 dz$
z	0.879	0.333
$1.01z - 0.0344$	0.996	0.309
$0.221z^2 + 0.786z$	1.00	0.303

Appendix

D Chimneys compared

Table D.1 shows the structural details of the chimneys used to compare the predicted maximum response in chapter 8. The sources used by Lupi et al. are: Basu and Vickery [32], Basu [79], Clobes et al. [165], Daly [166], Dyrbye and Hansen [108], Frandsen [167], Hansen [158], Hirsch et al. [168], Langer et al. [169], Nakagawa [170], Pritchard [171], Ruscheweyh and Verwiebe [172], Ruscheweyh [173], Tranvik and Alpsten [174] and van Koten [118].

Table D.1: *Chimneys used in model comparison of section 8.5 from the work of Lupi et al. [115].*

No [−]	h $[m]$	d $[m]$	λ [−]	m_e $[kg/m]$	Sc [−]	f_n $[Hz]$	Re_{crit} [−]	$r_{y,meas}$ [−]
1	90	5.1	17.6	2090	4.04	0.75	6500000	0.062
2	91.5	5.13	17.8	2010	3.42	0.68	5970000	0.057
3	83	4.1	20.2	1360	4.88	1.15	6440000	0.063
4	60	1.58	38.0	233	2.24	0.5	420000	0.25
5	60	1	60.0	148	3.08	1.375	460000	0.4
6	55	2.14	25.7	323	1.69	1.12	1710000	0.18
7	45	1.26	35.7	341	16.5	0.642	340000	0.013
8	50	2.2	22.7	945	4.37	0.919	1480000	0.016
9	45	1.1	40.9	258	11.6	0.629	250000	0.025
10	54	2.2	24.5	834	16.27	0.61	980000	0.012
11	64	2.8	22.9	1085	3.1	0.578	1510000	0.357
12	56	2.2	25.5	593	5.88	0.62	1000000	0.227
13	75	2.4	31.3	490	4.08	0.37	710000	0.417
14	56	1.8	31.1	386	4.77	0.49	530000	0.278
15	80	3.96	20.2	5090	8.31	0.53	2770000	0.174
16	60	2	30.0	340	1.63	0.802	1070000	0.28
17	60	2	30.0	344	17.2	0.77	1030000	0.025
18	28	0.914	30.6	89	2.56	1.72	480000	0.153
19	38	1.016	37.4	230	10.71	0.68	230000	0.073
20	52	2	26.0	340	1.63	0.75	1000000	0.25
21	120	4.9	24.5	2418	2.9	0.49	3920000	0.122
22	99	4.25	23.3	3057	3.25	0.425	2560000	0.089
23	29	1.016	28.5	328	8.65	1.3	450000	0.07
24	140	6	23.3	1440	1.92	0.51	6120000	0.2
25	76.2	2.62	29.1	535	1.87	0.55	1260000	0.29
26	100	6	16.7	1639	3.06	0.61	7320000	0.133
27	35	0.728	48.1	155	14	0.52	90000	0.124

Appendix

E Publications

1. Ellingsen, Ø.M., Amandolese, X., Flamand, O., Hémon, P., *Velocity response of VIV models for vertical structures*, in Proceedings of the 15th International Conference on Wind Engineering, Beijing, China, 2019.

2. Ellingsen, Ø.M., Amandolese, X., Hémon, P., *Assessing maximum amplitude and corresponding frequency for vortex-induced vibrations*, in Proceedings of the Second International Symposium on Flutter and its Application, Paris, France, 2020.

3. Ellingsen, Ø.M., Flamand, O., Amandolese, X., Coiffet, F., Hémon, P., *Field tests on a full-scale steel chimney subjected to vortex-induced vibrations*, Structural Engineering International, 2021. DOI:10.1080/10168664.2021.1936352

4. Ellingsen, Ø.M., Flamand, O., Amandolese, X., Hémon, P., *Twin Strouhal numbers in flow around circular cylinder at high Reynolds numbers*, To be submitted to JFM Rapids.

Velocity response of VIV models for vertical structures

Øyvind Mortveit Ellingsen [a,b], Xavier Amandolese [a,c], Olivier Flamand [b], Pascal Hémon [a]

[a]*LadHyX, École polytechnique-CNRS, Palaiseau, France*
[b]*CSTB, Nantes, France*
[c]*Conservatoire National des Arts et Métiers, Paris, France*

ABSTRACT: Slender vertical structures such as chimneys, towers or stacks can be prone to vibrations under wind effect. Cross-wind vibrations due to the vortex signature, known as vortex-induced vibrations (VIV), is of importance. It is the consequence of a nonlinear coupling between the fluid force due to the Kármán vortex wake and the structure's motion. Significant oscillations of self-limited amplitude can then be observed in a limited range of velocities. Various VIV models can be found in the literature and some codified methods are also proposed in civil-engineering standards. This work aims to evaluate different models and methods for estimating the amplitude as a function of wind velocity for structures with circular cross-section.

KEYWORDS: Vortex-induced vibrations, aeroelasticity, design models, wind-effects, chimney

1 INTRODUCTION

Bluff bodies in cross-flow can be submitted to unsteady transverse forcing due to the periodic build-up and shedding of vortices in their wake. The wake organisation and associated aerodynamic loading are affected by the incoming flow characteristics and motion of the structure[1]. For a tall vertical structure in the atmospheric boundary layer, both the wind speed and turbulence vary along the height. The Reynolds number can be high and close to the critical condition for circular cross-section. Structural elasticity further complicates the phenomena, as its motion and deformation change the vortex organisation and fluid forcing in a complex nonlinear coupling mechanism.

Two design approaches are familiar to the authors for estimating the response of civil engineering structures due to VIV: the spectral method first developed by Vickery and Basu[2] and the effective correlation length method proposed by Ruscheweyh[3]. The latter is adapted from the single mode response of a structure due to a harmonic forcing term partially correlated along the structure. The former is derived from linear random vibration theory using a forcing term dependent on turbulence intensity. Both methods are codified in the Eurocode[4] and the spectral method is also codified in the CICIND standard[5].

In addition to those design methods, fluid-structure interaction models using different forcing models can be used. These models can be separated into three groups[6]: those based on harmonic forcing independent of motion, those based on motion dependent forcing (aeroelastic) and the ones based on coupling the structural motion with a wake oscillator model.

The aim of this paper is to evaluate and discuss different models and codified approaches for estimating the VIV response as a function of wind velocity for a slender structure with circular cross section. Experimental results provided in Vickery and Basu[7] for a tall chimney is used as a reference.

2 VORTEX-INDUCED VIBRATION MODELS

2.1 *Simplified spectral method*

The spectral method is derived from linear random vibration theory where a nonlinear damping term is added. Assuming that the forcing term due to the vortex shedding and wind turbulence is acting on the top third of the structure and averaging the wind speed in that area, the simplified spectral method as described by Vickery and Basu[7] is expressed as:

$$\frac{\sigma_Y}{d}=\frac{\frac{C_{L,rms}}{8\pi^2 St^2}\frac{\rho d^2}{m_e}\left(\frac{\sqrt{\pi}l}{2(\lambda+2)}\right)^{0.5}B^{-1/2}k^{3/2}\exp\left(-0.5\left(\frac{1-k^{-1}}{B}\right)^2\right)}{\left(\frac{1}{h}\int_0^h \psi^2(z)\,dz\right)^{0.5}(\zeta-K_a)^{0.5}} \tag{1}$$

Where the following notations are used: σ_Y is the standard deviation at the top of the structure, d and h are the diameter and height, l is the characteristic length (in diameters), z is the vertical position, ψ is the mode shape, λ is the aspect ratio, ζ is the structural damping ratio, f_n is the natural frequency, K_a is an aerodynamic damping parameter, St is the Strouhal number defined as $f_s d/V$, where f_s is the shedding frequency and V is the wind speed, B is a coefficient related to the forcing spectrum and turbulence, k is the ratio of wind speed to critical wind speed where $V_{cr}=f_n d/St$, $C_{L,\,rms}$ is the standard deviation of the lift coefficient, a_L is a limiting factor, m_e is the equivalent mass and ρ is the fluid density.

Equation 1 will hereby be referred to as "Simplified V&B I". The aerodynamic damping K_a is calculated using σ_Y and defined as: $K_a=K_{a,0}(1-(\sigma_Y/d/a_L)^2)$ where $K_{a,0}$ is Reynolds number dependent. The equation is rewritten in the form $a\sigma_Y^4+b\sigma_Y^2+c=0$ and solved. A different approach for solving equation 1, is to determine the aerodynamic damping directly from surface roughness data. This version is referred to as "Simplified V&B II".

A further simplification of equation 1 is used in the CICIND design code and Eurocode where maximum amplitude is calculated at k=1.1. l is also assumed constant for all structures and St is set to either 0.2 (CICIND) or 0.18 (Eurocode).

2.2 *Effective correlation length method*

The effective correlation length method is derived from the modal response of the structure to a harmonic lateral forcing for which the correlation length along the structure depends on the response amplitude. In the present study, the procedure recommended in the Eurocode[4] is used. The correlation length is solved in an iterative process until the oscillation amplitude converges or is out of bounds. The forcing coefficient used in the model is based on an envelope of a series of experimental measurements and gives a secure "worst case" forcing scenario. A statistical maximum speed must be used in the Eurocode but here a variable incoming speed is used.

2.3 *Fluid-structure interaction models*

Two other types of fluid-structure interaction models can be used for predicting the VIV response with variable wind velocity. The first are aeroelastic models using a single degree of freedom system with either modified harmonic forcing, $F(A_y, f_s, t)$, where A_y is the lateral response amplitude, or a nonlinear motion-induced expression of the lateral force $F(\ddot{y}, \dot{y}, y, t)$. The second type, wake oscillator models, use two coupled equations, one for the structure and one for the vortex-induced loading. Equation 2 is an example of such a coupled system model where the first equa-

tion is related to the structural motion and the second one is for a fluid variable that can be interpreted as a dimensionless reduced lift coefficient[6]. The coupling terms are *s* and *f* where *s* is typically *q* but *f* can be the acceleration, velocity or displacement of the structure, or a combination of them. In the present study, the coupled-system model will be used with *f* equal the acceleration of the structure and parameters used by Facchinetti *et al*.[8]. In this model, δ is the ratio of stationary shedding frequency to natural frequency, γ is the added damping coefficient, μ is the mass ratio (structure to fluid) and ε is the van der Pol damping coefficient.

$$\ddot{y}+\left(2\zeta\delta+\frac{\gamma}{\mu}\right)\dot{y}+\delta^2 y=s,\quad \ddot{q}+\epsilon\left(q^2-1\right)\dot{q}+q=f \tag{2}$$

3 COMPARISON WITH EXPERIMENT

Experimental results provided in Vickery and Basu[7] for a tall chimney are compared with the predictions of vortex-induced vibration models and standard methods. The chimney's structural and aerodynamic parameters are listed in table 1 and 2 respectively. Mode shape is $\psi=(z/h)^2$.

Table 1. Structural parameters

Parameter	Value	Unit
h	201	m
d	12.8	m
λ	15.7	[-]
m_e	23000	kg/m
f_n	0.37	[-]
a_L	0.4	[-]
ζ	0.01	[-]

Table 2. Aerodynamic parameters

Parameter	Value	Unit
$C_{L,\,rms}$	0.146	[-]
St	0.207	[-]
B	0.25	[-]
l	1	[-]
ρ	1.225	kg/m^3
$K_{a,0}$	1	[-]

Figure 1 compares the evolution of the amplitude response with the wind velocity as predicted by the simplified spectral methods (using the aerodynamic parameters in table 2), the effective correlation length method (using the parameters provided in the Eurocode), the CICIND standard (using the parameters provided in the CICIND model code) and the coupled model. The amplitude response is here plotted as the maximum dimensionless amplitude defined as: $A_y=\sigma_Y k_p/d$, where σ_Y is the standard deviation of the displacement at the top of the structure and k_p is a peak factor set here equal to 3.5.

As expected, the CICIND model quickly converges towards a unique value associated to the maximum amplitude prediction at high speed. One can also notice that this maximum value is slightly overestimated. Following the procedure recommended in the Eurocode[4], the effective correlation length method highlight an interesting shape response but overestimates the maximum amplitude and predict this maximum at a lower velocity ratio. The coupled system model also predicts a maximum amplitude close to V/V_{cr}=1.1 and strongly reduces the lock-in region. Simplified V&B I and II best match the response shape, but the location of the maximum ampli-

tude is also predicted at a lower velocity. One can also notice that simplified V&B II gives lower amplitudes than the simplified V&B I.

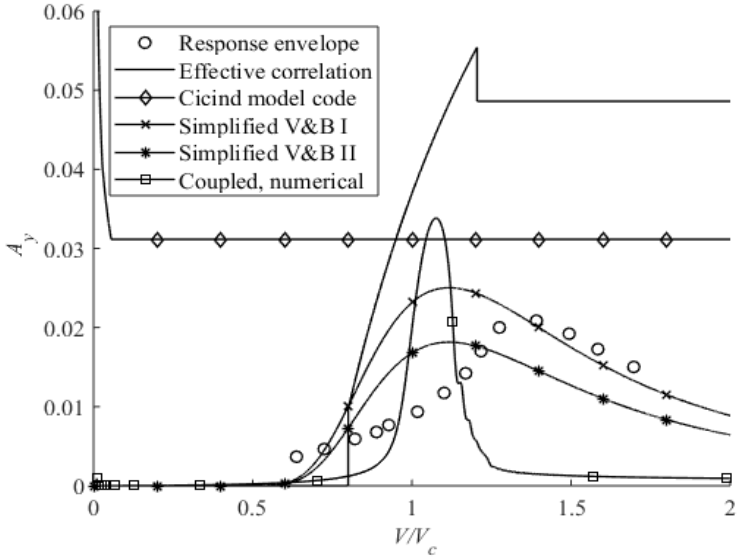

Figure 1 Evolution of the dimensionless amplitude response with the wind velocity, comparison of model predictions with experiment from Vickery and Basu[7].

4 CONCLUSION

Among the two codified approaches that have been tested, the effective correlation length method, as proposed in the Eurocode standard, is the only one exhibiting a velocity dependant response. The maximum amplitude is however strongly overestimated in comparison with the CICIND prediction. As expected, the simplified Vickery and Basu methods better fit the data extrapolated from their paper. Using a coupled system model the shape response is too sharp but a wider response could be obtained by tweaking the model parameters and coupling terms. Further work need to be done to better catch the shape of the response and the location of the maximum amplitude. Comparison with further experimental data is going on.

5 REFERENCES

1 E. Simiu and R.H. Scanlan, Wind effects on structures: an introduction to wind engineering. New York, Wiley, 1978

2 B.J. Vickery and R.I. Basu, Across-wind vibrations of structures of circular cross-section. Part I. Development of a mathematical model for two-dimensional conditions, JWEIA, 12 (1983), pp 49-73

3 H. Ruscheweyh, Vortex Excited Vibrations, In: Sockel H. (Ed.) Wind-Excited Vibrations of Structures. International Centre for Mechanical Sciences (Courses and Lectures) 1994, vol 335. Springer, Vienna, pp 51-84

4 Eurocode 1: Actions on Structures, Part 1–4: General Actions – Wind Actions, 2010.

5 CICIND Model Code for Steel Chimneys, 2010. The CICIND Chimney Standard.

6 M.P. Paidoussis, S.J. Price and E. de Langre, Fluid-structure interactions cross-flow-induced instabilities, Cambridge University Press, New York, 2011, pp 105-153

7 B.J. Vickery and R.I. Basu, The response of reinforced concrete chimneys to vortex shedding, Engineering Structures, 6 (1984), pp 324-333

8 M.L. Facchinetti, E. de Langre and F. Biolley, Coupling of structure and wake oscillators in vortex-induced vibrations, Journal of Fluids and Structures, 2 (2004), pp 123-140

Assessing maximum amplitude and corresponding frequency for vortex-induced vibrations

Øyvind Mortveit Ellingsen [1,2], Xavier Amandolese [2,3], Pascal Hémon [2]

[1] *CAPE , CSTB, Nantes , France, oyvind@ladhyx.polytechnique.fr*
[2] *LadHyX, CNRS-École Polytechnique, Palaiseau, France*
[3] *LMSSC, CNAM, Paris , France*

Abstract
Vortex-induced vibrations can damage structures exposed to cross-flows. The current design estimates of structural amplitude are based on structural nonlinearity but we will here derive a different estimate based on a coupled system with nonlinear fluid forcing. Two estimates of maximum structural amplitude is investigated based on approximations the coupled system and fluid speed at maximum amplitude. Our result shows that both estimates are close to the maximum amplitude found using numerical integration but that the predicted fluid speed differs. With further refinement, the result presented may prove useful in designing structures to withstand vortex-induced vibrations.

Keyword: Vortex-induced vibrations, nonlinear approximation, design estimates, prediction error

1 Introduction

Structures in cross-flow will experience unsteady periodic, loading due to shedding of vortexes (Blevins, 2001) that can lead to severe vortex-induced vibrations (VIV). For a designer, there are two useful pieces of information: when vibrations occurs and how severe vibration amplitudes are. These information pieces enables us to find the lifetime of a structure and to design a good tuned-mass damper.

When designing structures to withstand these aerodynamic loads, simple estimates of loading and response reduces the time spent iterating designs. In the Eurocode (2010) and CICIND (2010) building codes, structural excitation due to VIV is modeled using random vibration theory and a simplified structural nonlinearity (Vickery and Basu, 1983). This simplified model is made for the design offices of the early 1980s and often only the maximum response is found.

Another approach in modeling VIV is to couple a structural equation with a nonlinear equation describing or mimicking the vortex forcing. This approach was used Facchinetti et al. (2004) and several other researchers before them (Païdoussis et. al, 2010). A benefit of Facchinetti's model is that it has a simple but powerful coupling between wake and structure. The problem is that it's a set of nonlinear differential equations. This is numerically solvable but work is needed to make it as simple and useful as the current design model.

Why should a designer consider using something other than the existing design model? According to Lupi et al. (2018), it is overly conservative and can be unrealistic for many

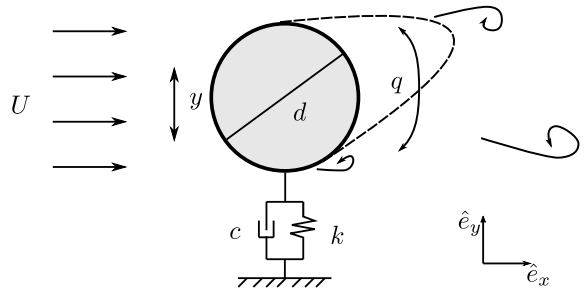

Figure 1 – Sketch of the vortex-induced vibration system

designs. This is partly due to the formulation of the method and the parameters used; their effect is especially prevalent at low Scruton numbers.

We will take steps to address the above concerns by creating a new predictive model that perform better at low Scruton number (Sc<10). Based on an approximation of structural and forcing amplitudes, we will define two approximations of the fluid speed at maximum response. The speed estimates is then plugged back into the amplitude approximates. Amplitude and speed results from both estimates will then be compared with numerical simulations.

2 Vortex-induced vibrations model and approximation

2.1 Model definition

Fig 1 shows a simple system experiencing vortex-induced vibrations. The structure is left free to vibrate in the $\hat{e}_y$ direction and the wake oscillates on it. This has been modeled using a combination of a linear structural oscillator and a nonlinear wake oscillator shown respectively in Eqs. 1 and 2 below

$$\ddot{y}+D\dot{y}+y=\omega_q^2 Mq, \tag{1}$$

$$\ddot{q}+\epsilon\left(q^2-1\right)\dot{q}+\omega_q^2 q=A\ddot{y}. \tag{2}$$

where the variables y and q are dimensionless. Here, A and ϵ are experimentally determined constants and M is the unsteady lift force, F, scaled by the mass-ratio μ ($M=F/\mu$). The parameters D, F and μ as defined as

$$\mu=\frac{m+0.25\pi\rho d^2 C_m}{\rho d^2}, \tag{3}$$

$$D=2\zeta+\frac{C_D}{4\pi\mu St}, \tag{4}$$

$$F=\frac{C_{Lo}}{16\pi^2 St^2}, \tag{5}$$

m is structural mass per unit length, ρ fluid density, d diameter, ζ critical damping ratio and St Strouhal number. C_m, C_D and C_{Lo} are the added mass, mean drag and unsteady lift amplitude coefficients respectively.

One variable is undefined and it's one of the most important: the fluid speed variable ω_q. It's defined as the product of the reduced velocity based on the structure's natural frequency and the Strouhal number ($\omega_q = U_R St$). It is therefore a reduced fluid frequency equivalent to the ratio of shedding frequency to the natural structural frequency.

If we assume that the equations are weakly nonlinear, then they can be approximated. This system can be shown to have the approximate steady-state solutions below when using the method of averaging:

$$r_y(\omega_q, \theta) = 2\frac{\omega_q^2 M}{D}\left[1 + \frac{\omega_q AM \sin(\theta)}{\epsilon D}\left(\sin(\theta) - D\cos(\theta)\right)\right]^{0.5} \sin(\theta), \tag{6}$$

$$0 = \omega_q^2(1 - AM) - 1 + \omega_q^2 AM \sin^2(\theta) + \left(\frac{D}{\sin(\theta)} + \frac{\omega_q^2 AM}{D}\sin(\theta)\right)\cos(\theta). \tag{7}$$

where r_y is the structural amplitude and θ is the phase difference between q and y, i.e. phase difference between force and motion. Notice that there is no equation for the wake amplitude. As the structural equation and coupling is linear, the equations for wake amplitude can be expressed as a function of phase difference only. This then enables us to write the structural amplitude as a function of phase difference only.

2.2 Amplitude scaling

If we ignore the square root term and the last $\sin\theta$ term in Eq. Eq. 6, we get an equation that depend linearly on the ratio of M to D. If we expand this ratio, we get the scaling relationship

$$r_y \propto \frac{2\pi F}{Sc + 2\pi^2\zeta + \frac{C_D}{2St}}. \tag{8}$$

where Sc is the Scruton number defined as

$$Sc = \frac{4\pi\zeta m}{\rho d^2}. \tag{9}$$

In words, predicted amplitude is dependent on four parameters: geometry, mass, structural damping and aerodynamics. This differs from some previous notions on maximum amplitude scaling. However, it corroborates the opinion that combining mass and damping into a parameter is arbitrary (Sarpkaya 2004).

2.3 Model validation

To find the amplitude at a given speed, the first step is to find the phase difference using Eq. 7. This may look daunting, but it can be rewritten to a cubic equation. One of the closed form solutions corresponds to the high amplitude VIV response, another to low amplitude and the last to an unstable solution. Only the phase differences between 0 and 180° are used.

A "postcritical Reynolds" experiment with dampers by Belloli et al. (2015) is used for validation and for comparison with the maximum amplitude of the CICIND model (2010). See Tab. 1 for parameters. Fig. 2 shows the comparison and the design code over predict by more than a factor of 2. Our model does well at $\omega_q < 1$ and less well above. The maximum amplitude between experiment and model is similar as is the range of high amplitude vibrations.

Second International Symposium on Flutter and its Application, 2020

Table 1 – Parameters used to compare the approximations and the numerical results.

Case	ϵ	A	γ	F	ζ	d	ρ
Exp.	0.3 [-]	12 [-]	0.479 [-]	0.0401 [-]	0.01200 [-]	0.72 [m]	1.225 [kg/m^3]
Low dam	0.3 [-]	12 [-]	0.442 [-]	0.0401 [-]	0.00191 [-]	2.00 [m]	1.225 [kg/m^3]
High damp	0.3 [-]	12 [-]	0.442 [-]	0.0401 [-]	0.00955 [-]	2.00 [m]	1.225 [kg/m^3]

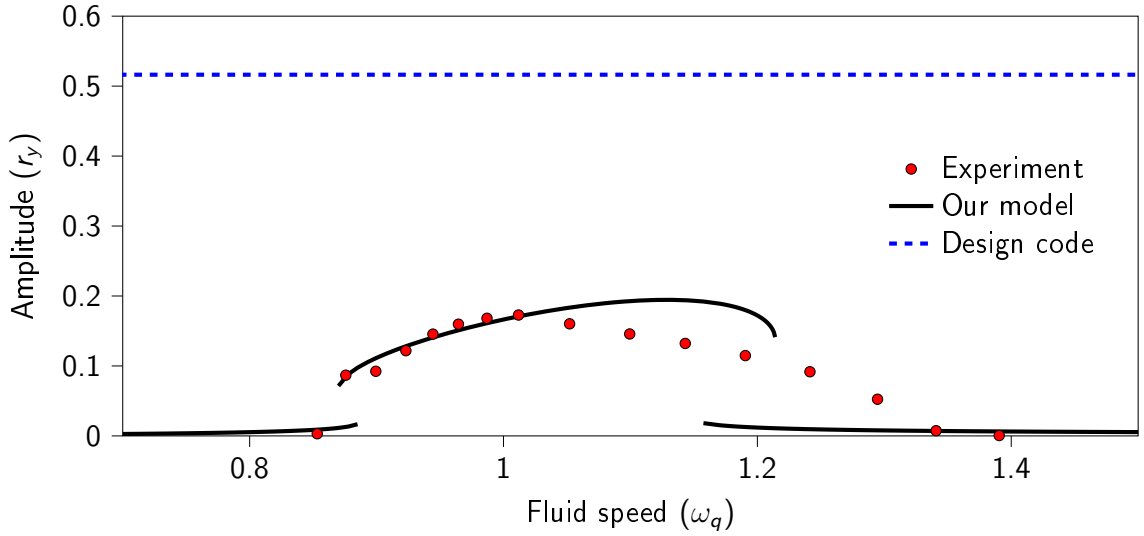

Figure 2 – Comparison of models and experiment of Belloli et al. (2015)

3 Estimates of maximum

3.1 The approximations

Two different approximates of the frequency at maximum amplitude are tested:

$$\omega_{q1} = \frac{1}{1-\sqrt{AM}}, \tag{10}$$

$$\omega_{q2} = \sqrt{\frac{D\left(\sin\left(\theta\right) - D\cos\left(\theta\right)\right)}{AMD\sin\left(\theta\right)^3 + AM\cos\left(\theta\right)\sin\left(\theta\right)^2 + D\left(1-AM\right)\sin\left(\theta\right)}}. \tag{11}$$

The first approximate (Eq. 10), dubbed "method 1", is based on the work of de Langre (2006). Our guess is that maximum amplitude corresponds to the upper limit of the linear synchronization definition. In terms of Fig. 2, this corresponds to the start of our rightmost low amplitude solutions. Method 1 is independent of the structural damping parameter D and depends only on the coupling terms associated with forcing.

The second approximate, "method 2", is based on assuming that maximum response coincide with a specific phase difference. The form of method 2 is shown in Eq. 11 and includes structural damping and the forcing terms. An added benefit of this approach, is that it reduces the calculation process to one longer equation; we are assuming we know θ, so there is no need to calculate the value. By inspection, the phase difference at maximum response is $\approx 0.65\pi$.

The estimates of maximum amplitude and dimensionless fluid speed are compared to results from numerical simulations at several Sc using two damping cases. One corresponds to a low damping case and the other to a high damping. The values of μ are inferred from Sc using the constants given in Tab. 1 and Eqs. 3 and 9. For comparison, both absolute values and the relative difference in percentage are used in the next two subsections.

3.2 Approximation of fluid speed at maximum response

The evolution of dimensionless fluid speed as a function of Sc when structural damping is low is shown in Fig. 3. When comparing the results using method 1 and numerical, it is easy to spot differences. Predicted speed changes differently with Scruton number and the values are inconsistent for method 1 and numerical. The approximate speed using method 2 is consistently higher than the numerical result but does drop similarly with increasing Sc.

To further evaluate the approximations, a second damping case is studied. The evolution of fluid speed at maximum response when damping is five times greater is shown in Fig. 4. With the higher damping, predicted speed drops similarly for method 1 and numerical although the predicted speed is consistently much higher. Increasing damping barely changed the differences between numerical results and method 2. The main difference would be a slightly increased difference in predicted value.

3.3 Maximum response

Maximum response is predicted to decrease similarly to how the fluid speed at maximum response drops, i.e. like Sc^{-1}. This gives a rapid drop in predicted vibration amplitude as seen in Figs. 5 and 6 showing the progression for the lightly and higher damped cases respectively.

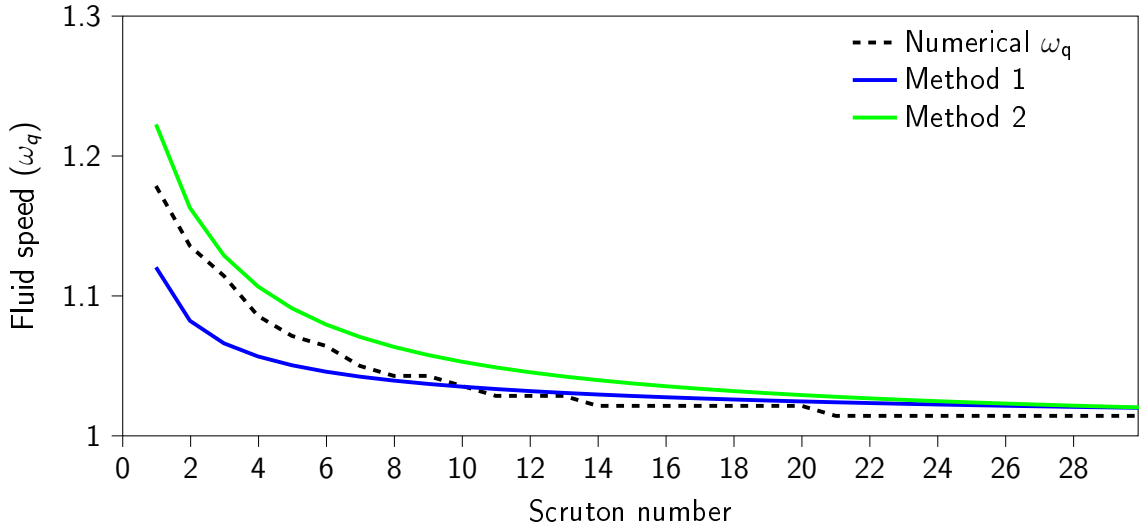

Figure 3 – ω_q corresponding to maximum r_y for low damping case

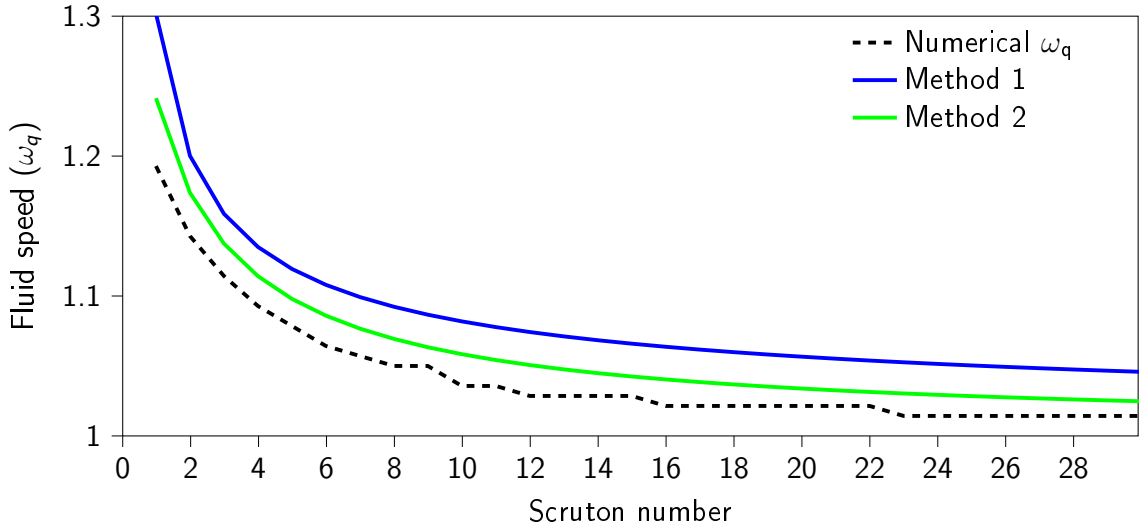

Figure 4 – ω_q corresponding to maximum r_y for high damping case

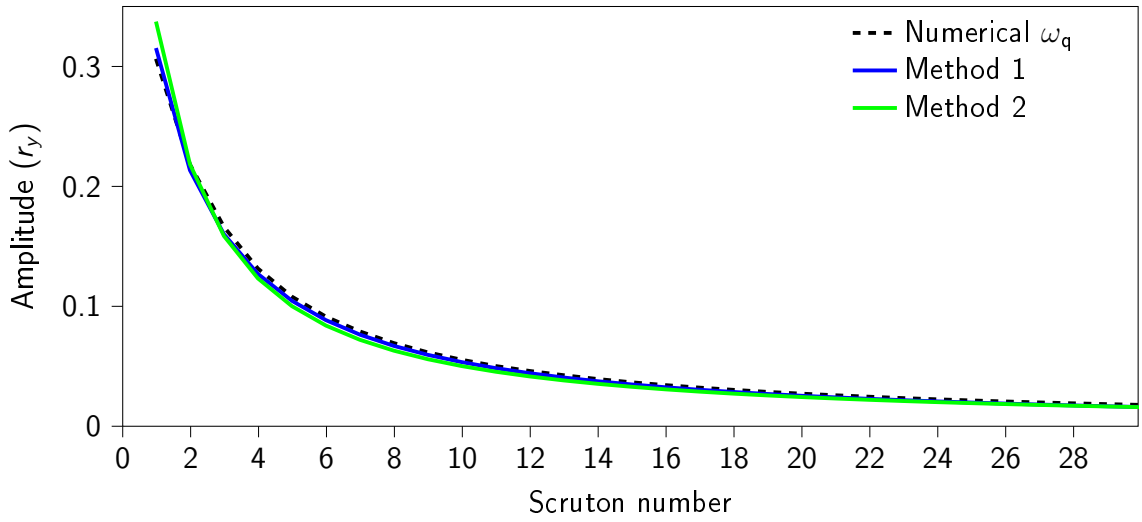

Figure 5 – Comparison of maximum response amplitude using approximates and numerical integration at low structural damping

Even with the difference in predicted speed, method 1 predict similar amplitudes as the numerical results for most tested Scruton numbers in the lightly damped case. This could be an indication of low sensitivity in fluid speed when it comes to estimating maximum amplitude. For the higher damped case, this is not true. At Scruton numbers below 2, the amplitude becomes noticeably over predicted and then under predicts for all Scruton numbers. The more egregious error, is that the predicted speed corresponds to the low amplitude solution for Scruton numbers higher than nine.

Method 2 performs similarly to method 1 for the lightly damped case but with a difference, the predicted amplitude is noticeably higher at $Sc = 1$. The real point of improvement is in the higher damped case. While it has the same over predicting behavior at Scruton numbers below 2, the predicted amplitude is close to the numerical results for all other tested Scruton numbers. In other words, the maximum speed predicted is within the VIV region and close to the amplitude peak.

At the shown damping levels, method 1 performed passably for Scruton numbers less than 10. If we increase the damping, method 1 eventually under predicts for all Scruton numbers. The best estimate of maximum amplitude and fluid speed at maximum is method 2 which is based on assuming we know the phase difference that give maximum amplitude. The results are promising and in the next section we will further explore the usefulness of our estimate.

4 Applicability of our estimate of maximum amplitude

We have so far compared the absolute differences between our approximates and the numerical results for two different damping levels. This section is focused on the applicability of our predictions and a comparison with other predictive models, more specifically the model of Vickery and Basu used in building codes (CICIND, 2010; Eurocode, 2010).

As seen in section 2.3 and Fig. 2, there is room for improvement in the models used in the

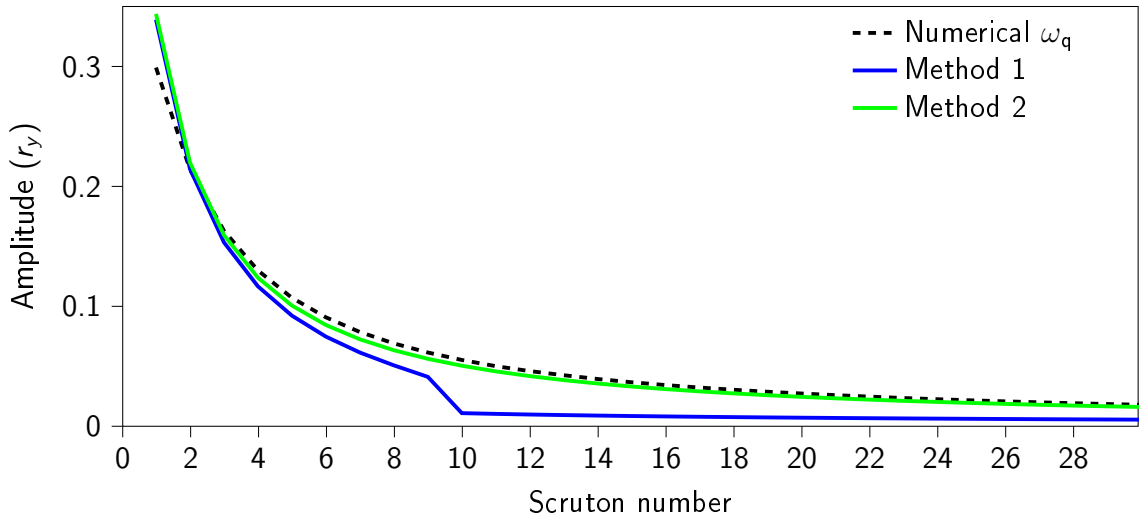

Figure 6 – Comparison of maximum response amplitude using approximates and numerical integration at high structural damping

mentioned building code. We will focus on two connected, negative properties. The first of them, is that they tend to be overly conservative in estimating amplitudes. Lupi et al. (2017) studied the difference between predicted and actual VIV amplitude and found that the predicted amplitude tended to be much larger than the actual vibration amplitude.

The second property has to do with predictive amplitude as a function of Scruton number (Lupi et al., 2017). The formulation used in the building codes can have abrupt jumps in predicted amplitude when slightly changing structural damping or aerodynamics. This is associated with a critical Scruton number that marks the transition from positive linear structural damping to negative. High amplitude prediction can also be connected with the imposed negative aerodynamic damping effect.

Our estimates of maximum amplitude follows a different trend and there is a smooth increase in predicted amplitude as Scruton number decreases without abrupt jumps. Our predicted maximum amplitude can have large changes with Scruton number at $Sc < 2$, but this is not as pronounced as the behavior of the design models..

How applicable is our two dimensional model in predicting the dynamic response of a three dimensional structure? Due to three dimensional effects, lengthwise force correlation and structural mode shapes, it is not unthinkable that our predictions will be wrong. But it may be possible to simplify and include the mentioned effects into our model. If we follow the same reasoning as Vickery and Basu (1983), we can modify our lift force by assuming a constant average speed over the top part of the cylinder. The lift force is then weighted and integrated over the cylinder length with a weighting factor proportional to the structural mode shape.

Another aerodynamic effect not accounted for in our model, but is in the design models, is the effect of turbulence and noise on the prediction. We can theoretically get the response amplitude using unsteady aerodynamic coefficients measured in turbulent conditions, but predicting the correct wind speed is harder; amplitude might be correct but the speed not. Getting the correct coefficients at super-critical (or "postcritical") Reynolds numbers is another story

and requires extensive work.

5 Conclusions

Two estimates of maximum structural amplitude due to vortex-induced vibrations has been tested and shown to accurately estimate maximum response. The best of the two is to assume that maximum amplitude occurs at a predefined phase difference between forcing and motion. Using a phase difference of $\theta = 0.65\pi$ gives an approximate fluid speed at maximum response slight higher than numerical results but similar evolution with Scruton number. The difference in fluid speed has a small effect on the difference in predicted maximum amplitude and the numerical result and estimate are similar.

References

Belloli, M., Giappino, S., Morganti, S., Muggiasca, S., Zasso, A., 2015. Vortex induced vibrations at high Reynolds numbers on circular cylinders. Ocean Eng, 94, 140–154.
Blevins, R. D., 2001. Flow-Induced Vibration (2nd ed.). Krieger Pub Co., Malabar, FL.
CICIND, 2010. CICIND Model Code for Steel Chimneys: September 2010 Revision 2. CICIND.
de Langre, E., 2006. Frequency lock-in is caused by coupled-mode flutter. J Fluids Struct, 22(6–7), 783–791.
Eurocode., 2010. 1: Actions on structures, Part 1–4: General Actions (EN–1991). Eurocode.
Facchinetti, M.L., de Langre, E., Biolley, F., 2004. Coupling of structure and wake oscillators in vortex-induced vibrations. J Fluids Struct, 19(2), 123–140.
Païdoussis, M. P., Price, S. J., de Langre, E., 2010. Fluid-Structure Interactions Cross-Flow-Induced Instabilities. Cambridge University Press., Cambridge, NY.
Sarpkaya, T., 2004. A critical review of the intrinsic nature of vortex-induced vibrations. J Fluids Struct, 19(4), 389–447.
Vickery, B.J., Basu, R., 1983. Simplified approaches to the evaluation of the across-wind response of chimneys.J Wind Eng Ind Aerod, 14(1), 153–166.

Field tests on a full-scale steel chimney subjected to vortex-induced vibrations

Øyvind Mortveit Ellingsen[1,2], Olivier Flamand[1], Xavier Amandolese[2,3], Francois Coiffet[4], Pascal Hémon[2]

[1]CSTB, Nantes, France; [2]LadHyx, CNRS-Ecole polytechnique, IP-Paris, France; [3]LMSSC, CNAM, Paris, France; [4]CERIC, Poujoulat Group, Granzay-Gript, France

1 Abstract

Industrial chimneys, launch vehicles and stacks are examples of large diameter circular cross section structures which can be prone to cross-wind vortex-induced vibrations. VIV has been extensively studied for both fundamental and applied issues, but few documented studies concern high Reynolds number regime (> $5{\cdot}10^5$) in atmospheric turbulent wind. This paper introduces a field test on a slender light and low damped chimney designed to experience "supercritical" VIV at moderate wind velocity. The chimney was recently erected in a wind monitored field, near the Atlantic coast of France. The purpose of this paper is to present the first vibration results obtained during a sequential 13-days period in September 2020. A statistical analysis has been performed on the amplitude and dominant frequency responses and results are reported in term of probability distribution as a function of wind speed and direction. VIV events of low (< 15 % of diameter) to moderate amplitude (> 30 % of diameter) have been highlighted in a range of wind velocity 25 % lower than expected, along with significant influence of the wind direction. Low turbulent easterly wind giving vortex-induced vibrations with the highest amplitude.

Keywords: Vortex-induced vibration; super-critical Reynolds number; full-scale experiment; chimney

2 Introduction

Slender structures with circular cross section can be prone to vibrations under wind effects and must be designed and/or treated accordingly. For an isolated tower, stack or chimney, one generally considers two kinds of vibrations: in-line vibrations due to atmospheric turbulence and cross-wind vibrations due to the vortex signature. The former concerns extreme wind speed and is the consequence of random aerodynamic load due to turbulence. Since this load can be considered as independent from the structure's dynamic response, the problem can be addressed using well-accepted random vibration methods or simplified equivalent static formulation (see for example [9, 26]). The latter is more complex. It is the consequence of a nonlinear coupling between the fluid force due to the Karman vortex wake and the chimney's motion. This phenomenon, known as vortex-induced vibration (VIV), has been extensively studied for both fundamental and applied issues (see for example [5, 20, 26] for a review).

VIV is characterized by significant oscillations of self-limited amplitude in a limited velocity range where the wake frequency is controlled by the motion, a phenomenon referred as lock-in. Both the oscillation amplitude and range of lock-in strongly depend on the structure to fluid mass ratio and on the damping ratio of the structure. This is encapsulated in the Scruton number (Sc, a dimensionless mass-damping ratio parameter) with low values leading to higher vibration amplitudes and a wider lock-in range. The Reynolds number and turbulence characteristic of the incoming flow can also have significant impact on the VIV of slender structure in atmospheric boundary layer [23, 28]. It is well established that the VIV response is strong for low turbulence flow in the sub-critical Reynolds number regime (< $3{\cdot}10^5$), comparatively negligible in the critical-transitional Reynolds number regime and that a recovering VIV response can be observed in the super-critical Reynolds number regime (> 10^6) [23].

Tall industrial chimneys, launch vehicles and stacks are examples of large diameter circular cross section structures which can be prone to vortex-induced vibrations at supercritical Reynolds number in atmospheric turbulent wind. It

is then necessary to validate appropriate methodology for their design and/or the design of additional damping devices (cf. [4] for simulations on the effect of additional damping devices). VIV models are numerous and codified methods can be found in many standards but their ability to capture the VIV amplitude response at super-critical Reynolds numbers and with real atmospheric boundary layers needs validation. Wind tunnels are also important in response prediction though the scaled models can cause cross-wind loads to be highly overestimated [29]. A method for overcoming the scaling effect is to artificially increase the Reynolds number by adding surface roughness to the cylinder's surface [20, 21]. While this can satisfactorily change the vortex wake signature (e.g. mean drag and rms lift) for a fixed cylinder, the impact on an 3D slender cylinder during lock-in is less clear and wind tunnel studies shows various conclusions so that it needs to be further investigated [2, 6, 11, 27].

Continuous measurements from monitored industrial chimneys can be found in the literature [7, 13, 14, 18, 19, 25, 30] but the monitoring is often limited to acceleration data and a reference velocity. These chimneys have been designed to or treated to limit VIV meaning that the observed vibrations were small. Additionally, the access and opportunity to install extra sensors were limited as they are in use. More response data on industrial chimneys are available but often only the maximum amplitudes are mentioned and are used to validate VIV models in design standards [15, 16].

For other more well-studied circular structures using field-experiments, there is a problem of dimensions [12, 23, 32]. Due to their smaller size, the high amplitude VIV response was at sub-critical or critical Reynolds numbers rather than super-critical. The same problem was observed in wind tunnels when using larger scale wind tunnel experiments [3] as the speed needed to reach super-critical wind speed is large.

In that context, a custom-made 35,5 m steel chimney have been recently erected and instrumented on a monitored wind field, in Bouin (near the Atlantic coast of France). This chimney was designed to have a low Scruton number ($Sc < 2$) and to experience "super-critical" VIV at moderate wind speeds (< 10 m/s). The paper is organized as follows: field test information and methodology including the structural characteristics of the chimney are presented in Section 3. Characterization of the incoming wind is reported in Section 4. Vibration results obtained during a sequential 13-days period in September 2020 are presented in section 5, before the conclusion and outlooks of this new test platform.

3 Field-test platform details and methodology

3.1 Structural characteristics of the chimney

The chimney was designed, manufactured and erected by Beirens (Poujoulat group) during the summer of 2020. Figure 1 shows a view of the chimney in the field. This custom-made steel chimney of height h = 35,5 m has a diameter d_{lower} = 1 m for its 12 m long bottom part and a diameter d_{top} = 2 m for its 20,5 m long upper part, with a 3 m long tapered connecting element (see figure 2). This unusual shape (for a chimney) was chosen to ensure vortex-induced vibrations in the super-critical Reynolds number range (> 10^6) at moderate wind speed (< 10 m/s) for the purpose of this experiment.

Structural characteristics of the chimney are given table 1, along with the expected Reynolds number at the critical wind speed, referred to as Re_{VIV}.

Table 1 Structural characteristic of the chimney (as identified at the start of the experiment).

d_{top} [m]	d_{lower} [m]	h [m]	$h_{d=2m}$ [m]	m_e [kg/m]	f_1 [Hz]	ζ_1 [%]	Sc [-]	Re_{VIV} [-]
2	1	35,5	20,5	322,6	0,78	0,22	1,82	$1{,}16 \cdot 10^6$

The equivalent mass, m_e, has been calculated using equation (1) where $\psi(z)$ is the shape of the first bending mode and $m(z)$ is the mass per unit height (both being identified during the design phase of the chimney using CAD). Experimental tests performed at the beginning of the test campaign identified first natural frequency, f_1, as 0,78 Hz and allowed the identification of the associated damping ratio ζ_1. The Scruton number, calculated using formula (2),

was rather low *Sc*=1,82 and high amplitude response was expected. Using the Eurocode's recommendations [10], the critical wind speed (f_s=f_n with a Strouhal number St=0,18) was close to 8,7 m/s ($Re_{VIV} \approx 1{,}16 \cdot 10^6$) and the maximum dimensionless amplitude (in top diameter) would be either 0,31 (method 1 of Ruscheweyh [23]) or 0,53 (method 2 of Vickery and Basu [28]).

Figure 1 Experimental chimney in the monitored field (the mast with wind anemometers is slightly visible, see figure 2 for details).

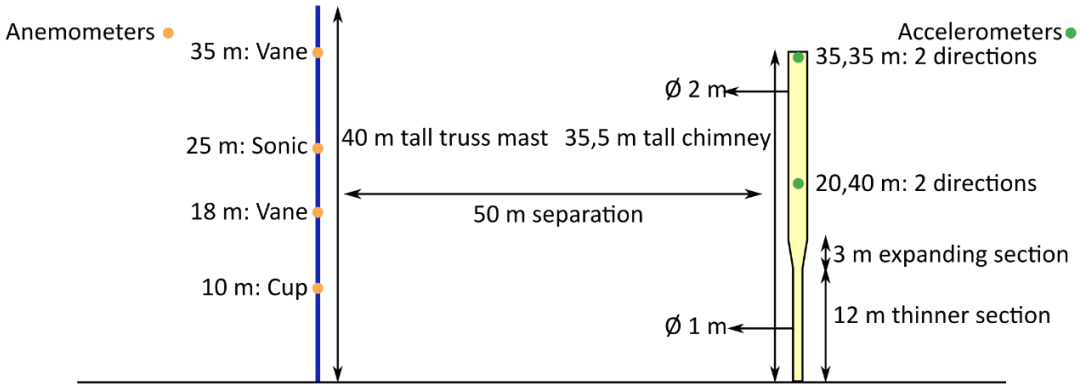

Figure 2 Sketch of the chimney and anemometer's mast, dimensions and locations of anemometers and accelerometers sensors.

$$m_e = \frac{\int_0^h \psi(z)^2 m(z) dz}{\int_0^h \psi(z)^2 dz} \tag{1}$$

$$Sc = \frac{4\pi\zeta m_e}{\rho d^2} \tag{2}$$

It is important to note that due to a damaged bolt, the natural frequency decreased to around 0,71 Hz at the end of the experimental campaign. In that context, an increase of the associated damping ratio, not measured, is also suspected. This will be discussed further in section 5.

3.2 Field-test location and instrumentation

The chimney was mounted in a monitored wind field, in Bouin (GPS coordinates 46,975, -1,998), near the Atlantic coast of France. According to the Eurocode [10], this area is in a wind zone category with a 50-years reference wind equal to 26 m/s. The site is surrounded by farmland with sparse gathering of trees and the terrain category is classified as type II [10]. Due to the remote location of the field, and lack of nearby structures, the model chimney has been designed without fearing for loss of human life, animal life or damage to nearby structures.

The chimney was instrumented with two bi-directional accelerometers, one at 20,4 m and one at 35,35 m (near the top) as shown in figure 2. Their measuring range was ±2 g and the acquisition frequency was set to 10 Hz. Wind velocity was measured at several heights using wind anemometers mounted to a 40 m tall truss mast, located 50 m North-West of the chimney (see figure 2). Vane anemometers, measuring speed and direction, were placed at heights of 18 and 35 m and a cup anemometer was located at 10 m. Both Vane and cup anemometers record the wind statistics (mean, standard deviation, maximum of speed and direction for the vane anemometers) over a 10-minute period. An additional sonic anemometer was located at 25 m height. It could measure the unsteady velocity (3 components) at a rate of 5 Hz. While the recording frequency of the sonic anemometer was different from the accelerometers, the recordings were time synchronized. Locations of sensors are sketched in figure 2.

3.3 Data analysis process

Vibration and wind results shown in the present study are based on 1872 ten-minutes records gathered at 35 m over a sequential 13-days period in September 2020. Additional wind data, gathered with all the anemometers distributed along the truss mast, were used to plot the mean and turbulent velocity profiles of the incoming wind.

Each sample of ten-minutes top wind was analyzed by first getting the mean velocity and dominant wind direction. As the accelerometer directions are constant, the displacements are transformed to cross and inline vibrations using the direction of incoming wind. This was used to calculate, using the top bi-directional accelerometer, an associated 10-minute cross-wind acceleration signal. The displacement, *y(t)*, was calculated from the acceleration signal using the inverse Fourier transform of the spectrum $Y(\omega)$ obtained from the Fourier transform of the acceleration $A(\omega)$ and relation (4). A fifth order high-pass Butterworth filter with cutoff frequency of 0,3 Hz has been applied to the acceleration data to eliminate low frequency noise amplified by the Fourier identity [17].

$$A(\omega) = -\omega^2 Y(\omega) \tag{4}$$

The Hilbert transform [8] was used to calculate the response envelopes of the displacement in order to get the mean, maximum and standard deviation of the displacement amplitude over a 10-minute recording. The associated dominant vibration frequency was identified by peak detection on the spectrum *Y(ω)*.

For each ten-minutes sample two cross-wind vibration values were gathered: the maximum amplitude of vibration and the associated dominant frequency along with two wind values: the mean velocity and the dominant direction. Statistical analysis was performed using the 1872 samples in order to plot the probability distribution of the vibration amplitudes and associated dominant frequency as a function of wind velocity or direction. These probability distributions were calculated using a statistical kernel function [31]. The kernel used here is the standard Gaussian kernel used in R and the ggplot2 library (version 4.0.2 and 3.3.2 respectively).

4 Wind characterization

4.1 Wind speed and directional distribution

The top vane anemometer was used to create the "wind rose" plotted in Figure 3 which shows the distribution of wind speeds and directions. The two most frequent wind directions were north-westerly and north-easterly. Additionally, the most frequently observed speed range was 4 to 6 m/s with speeds above 6 m/s having a long tail and short tail for speeds below 4 m/s. When ignoring the direction, the distribution of all wind speeds resembles a discrete log-normal probability distribution or a negative binomial distribution. The probability of a specific wind direction was found using the relative frequencies and are: S -4,4 %, SW -1,5 %; W -1,9 %; NW -29,5%; N -16,8%; NE-31,4%; E -11,4% and SE -3,1%.

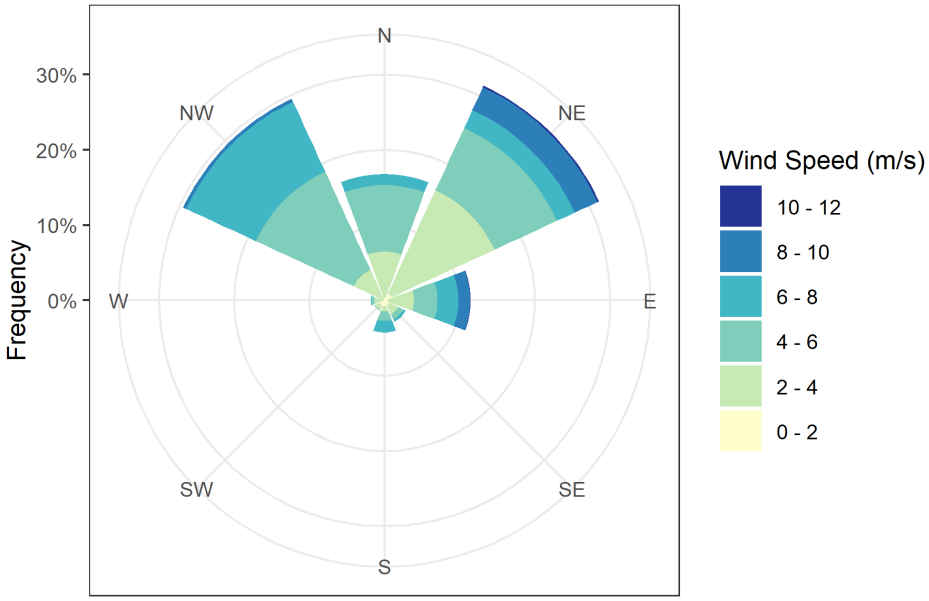

Figure 3 Frequency of incoming wind velocity (with 8 directional bins) using the 10-mintue mean directions and speeds at 35 m.

Using the measured wind speeds and U_{crit} = 8,7 m/s, the probability of seeing a speed above 0,8·U_{crit} (Eurocode's recommendations for the onset of VIV), is 21,3 %. As vortex-induced vibrations is only observed in a specific speed range, an upper limit to the investigated wind speed range can be added and is defined as 1,2·U_{crit} which is when one of the Eurocode design methods gives the highest amplitude [10]. With this, 21,3 % of the observed incoming wind speeds can be found in the vortex-induced wind speed range of 7 to 10,5 m/s. The two given percentages are the same as 10,44 m/s was the maximum observed mean wind speed.

4.2 Wind speed and turbulence profiles

The mean wind velocity and turbulence intensity evolution with height, for all eight cardinal and ordinal directions are plotted in figure 4, gathering wind data over the anemometer masts, for wind speeds greater than 5 m/s at 35 m height. The turbulence intensity I(z), is defined as the standard deviation of speed at a given height divided by the corresponding mean speed. Eurocode mean wind velocity and turbulence profiles, for terrain category II is also plotted in figure 4.

One can first notice that those mean velocity and turbulence profiles, for which ten-minute wind speed at 35 m remain lower that 12 m/s, strongly depend on the wind direction. While the Eurocode type II mean velocity profile

was close to a median profile in comparison with the experiments, the Eurocode type II turbulent profile overestimate the turbulent intensity for all the direction. A direct comparison with Eurocode profiles, which concern reference wind (ten-minutes at 10 meters) of higher mean value (50-years wind), should then be considered with some cautions. Nevertheless, for this low to moderate wind speed campaign one can highlight some relevant information regarding the incoming wind that will be useful for the vibration analysis.

The north-westerly wind which has the highest probability of occurrence has a mean velocity profile close to Eurocode type II model but a turbulence intensity value twice lower with a value slightly less than 10 % at 35 m. The easterly wind which concerns 11,4 % of the observed direction but highlight significant sequences of vortex-induced vibrations of the chimney, was characterized by an important speed gradient with height and a low turbulent intensity less than 2 % at 35 m. This means that wind coming from inland and headed towards the ocean has the strongest shear but the lowest mean turbulence intensity at the heights measured.

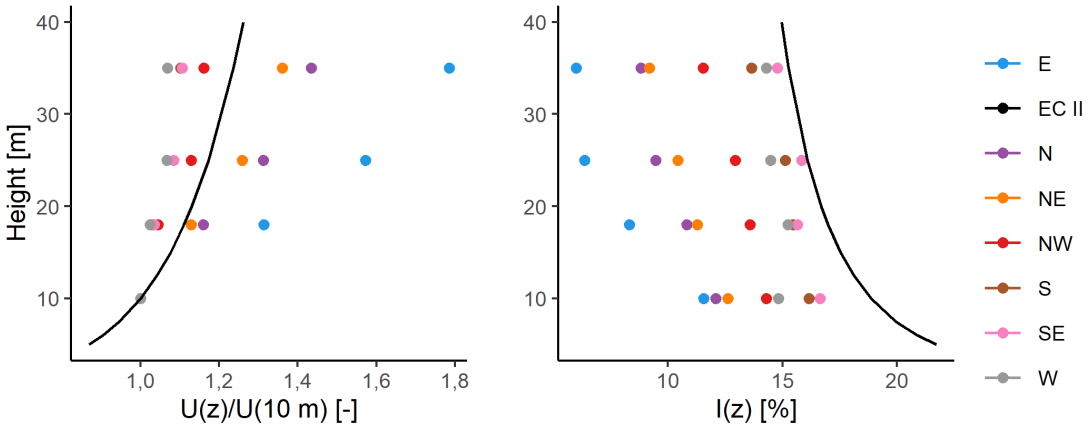

Figure 4 Mean incoming speed and turbulence profiles (filled dots) compared with the Eurocode profile for terrain category II (solid lines).

5 Cross-wind vibrations of the chimney

Following the data analysis process recalled in section 3.3, a statistical analysis of the chimney's cross-wind vibration was performed. An example of build-up to vortex-induced vibrations and the steadiness of it during lock-in is shown in figure 5. This figure shows the displacement and amplitude envelope for a segment with easterly wind which starts at 4,5 m/s but steadily increased to above 5 m/s according to the sonic data. Statistical distributions of the maximum dimensionless amplitude of vibration (normalized with the top diameter) and associated dominant frequency (normalized with the chimney's natural frequency), are plotted in figures 6 and 7 as a function of wind velocity.

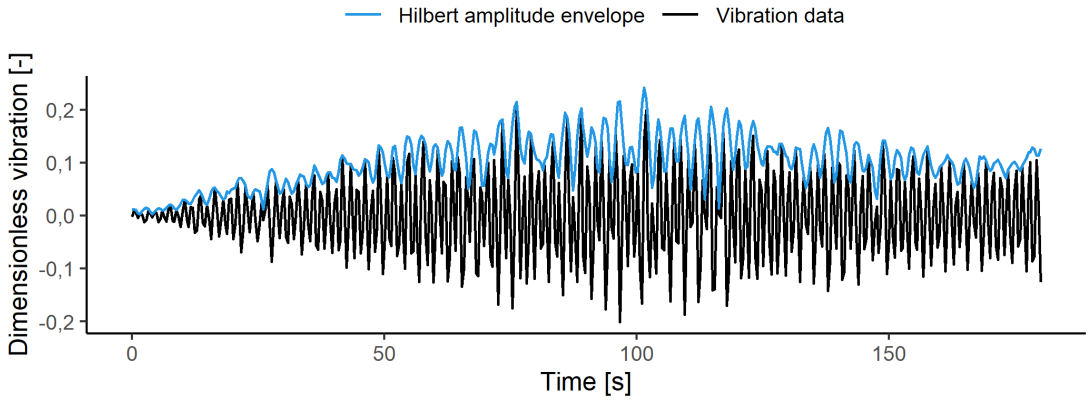

Figure 5 Example of cross-wind displacement signal with build-up to vortex-induced vibrations and the vibration during lock-in at 5 m/s.

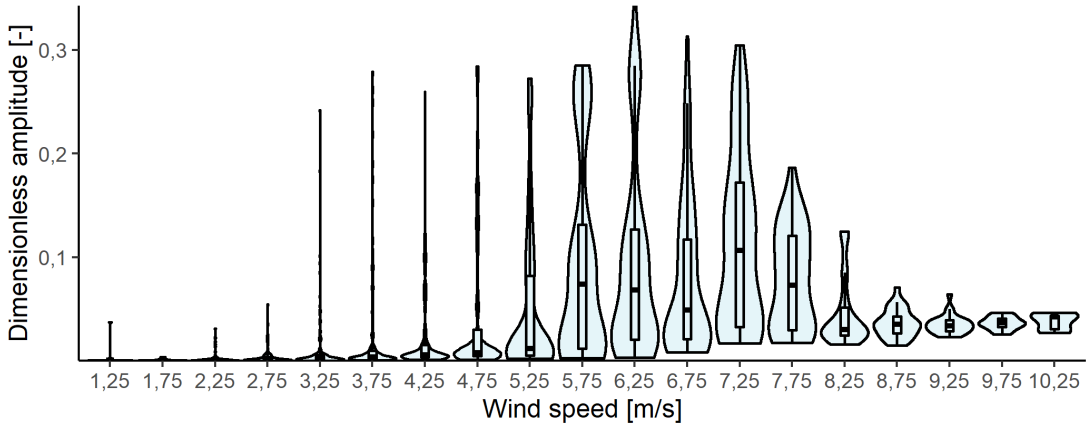

Figure 6 Probability distributions of maximum dimensionless amplitude (normalized with tip diameter) at given speed range. The interior rectangle and lines are boxplots showing summary statistics.

Results are reported using violin plots, mirroring the probability distribution of the data along the y-axis, as a function of discrete wind speed groups (nominal speed value ±0,25 m/s). The exceptions are for 1,25 and 10,25 m/s which groups all speeds below 1,5 and above 10 m/s respectively. In addition to the violin plot, boxplots highlighting the summary statistics (median and quartiles) are shown. A benefit of violin plots over boxplots, is that it shows the distribution of the data. It is particularly relevant for multimodal processes [31] for which the most likely value, associated to the widest point of the violin shape, can differ from the median value. It should also be noted that for the sake of visibility, the mirrored probability distributions shown in figures 6-8 were scaled so that their width were fixed for all speeds. Moreover, the tails of the probability distributions, which contain artifacts of the kernels used, were removed from these plots.

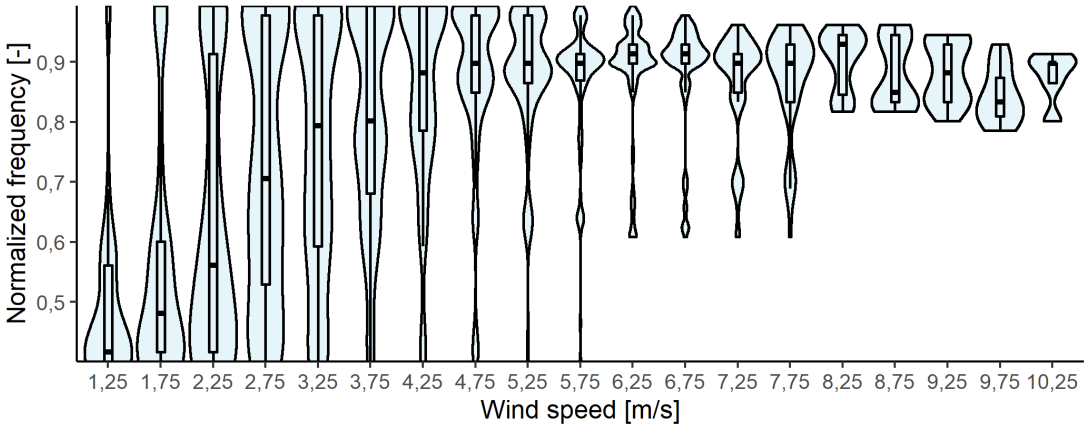

Figure 7 Probability distributions of the dominant frequency of motion (normalized with chimney's first natural frequency) at given speed range. The interior rectangle and lines are boxplots showing summary statistics.

As pointed out in section 4.2, the direction of the incoming wind strongly affects the mean wind velocity and turbulent intensity profiles. One then expects a significant impact of the wind direction on the chimney's cross-vibration. Statistical distributions of the maximum dimensionless amplitude of vibration are then plotted in figure 8 as a function of wind direction. Direction groups used in figure 8 were the cardinal and ordinal directions ±22,5°, with 0°±22,5° defined as northerly wind and 90±22,5° as easterly. Both of the groups were based on the mean values from the vane anemometer at 35 m.

Figure 6 clearly shows that cross-wind vibrations of significant amplitude can be observed for wind speeds between 5 and 8,5 m/s. With a maximum amplitude up to 35% of the diameter (0,7 m) observed at speeds between 6 and 6,5 m/s. This maximum amplitude was close to the one calculated using the Eurocode's method 1 (based on Ruscheweyh's approach [23]) and 35 % lower than the one calculated using the Eurocode's method 2 (based on Vickery and Basu's approach [28]). However, this maximum amplitude was observed at a wind speed 2 m/s lower than the one recommended by Eurocode, suggesting a higher Strouhal number value (closer to 0,25) at high Reynolds number ($Re \approx 8{,}3 \cdot 10^5$ for U = 6,25 m/s).

At speeds below 5 m/s, there were cases of amplitudes greater than 20 % of the diameter. In most of these cases, the mean speed was slowly reducing from the VIV lock-in speed region over several 10-minute recordings. The vibration amplitude continued to be high and it was possible for high amplitude VIV to continue until mean wind speeds as low as 3,3 m/s. In a few other cases, high amplitudes response could be due to the speed increasing towards the end of the 10-minute recording.

Lower amplitude levels (less than 15 % of diameter) were also observed in the wind speed range 5 to 8,5 m/s. Based on the shape of the violin plot, the lower amplitude vibrations have higher conditional probability than the high amplitude vibrations. The statistical distributions of the maximum amplitude as a function of the wind direction, reported in figure 8, suggest that the lower VIV data are likely to be attributed to north-westerly wind which was the most frequently observed direction and that the sequences of vortex-induced vibrations with the highest amplitude were due to the low turbulent easterly wind.

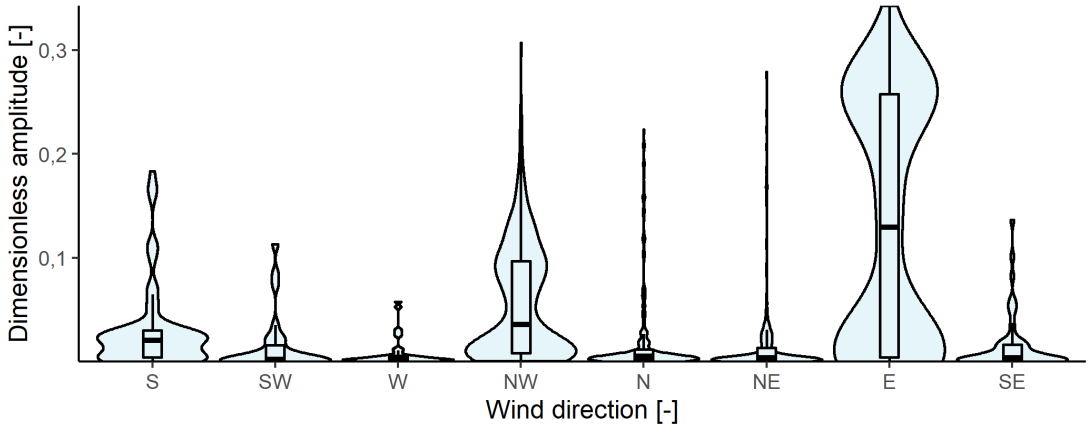

Figure 8 Probability distributions of maximum dimensionless amplitude (normalized with tip diameter) for different directions ±22,5°. The interior rectangle and lines are boxplots showing summary statistics.

No vibration amplitudes greater than 7,5 % of the diameter were observed for wind speeds higher than 8,5 m/s. From 8,5 m/s up the 10,25 m/s (which groups all speeds above 10 m/s), one can observe that the probability distributions of the maximum amplitude are more centered with a median value gradually increasing with the velocity. The vibrations can then be due to turbulence-induced vibrations. In this range of wind velocities, the probability distributions of dominant frequency are more surprising. For turbulence-induced vibrations one would expect a dominant frequency close to the first natural frequency of the chimney (and thus a dominant normalized frequency close to 1). Nevertheless, the shape of the violin plot reveals two areas of high probability for the dominant frequency (see for example figure 7, for U = 8,75 m/s), one with normalized frequencies between 0,9 and 1 and the other with normalized frequency between 0,8 and 0,9. As reported in section 3.1, a damaged bolt was observed at the end of the test campaign. A check showed a decrease of 10 % for the chimney's first natural frequency that could explain this peculiar distribution of the dominant frequency in this turbulence-induced vibration regime.

Even if the probability of occurrence of cross-vibrations with significant amplitude was rather low below 5 m/s, it is interesting to focus on the evolution of the probability distribution of the dominant frequency with wind speed before the lock-in (see figure 7). Up to 4,75±0,25 m/s, two distinct frequency groups can be highlighted. One group contains the median frequency which increases almost linearly with the wind speed while the other group concern normalized frequencies between 0,9 and 1 with increasing conditional probability with speed. The first group is clearly related to the vortex shedding signature while the second is due to turbulence-induced vibrations.

Relevant information on response can be found in figure 8 which shows the statistical distributions of maximum amplitude as a function of the wind direction. Easterly (low turbulent) winds were the most favorable to generate high amplitude (>30 % of top diameter) vortex-induced vibrations. Easterly winds also have the highest conditional probability of maximum amplitudes greater than 15 % of the diameter (near 50 % of the maximum amplitudes were above 15 % of the diameter). Vortex-induced vibrations were also observed with the more turbulent north-westerly winds, but with lower amplitude of vibrations. Vibrations up to 18% of the diameter was observed for southerly winds but with a low probability of occurrence. The shape of the violin plot for southerly direction shows a high conditional probability for vibrations lower than 5 % of the top diameter and this could be due to turbulence induced vibration (according to figure 4, the turbulent intensity was high, close to 15 % at 35 m height, for southerly winds).

The conditional probability of wind speeds in the range 5 to 8 m/s was higher for easterly, north-westerly and southerly winds (it was 59,6 % for north-westerly wind, 47,6 % for southwardly and 42,7 % for easterly wind, see figure 3). For northerly and north-easterly wind, on the other hand, it's much more likely to see speeds below 5 m/s

and the most likely amplitudes are low. This might be a reason for why the first three mentioned directions have higher conditional probability for VIV of significant amplitude. Easterly wind (towards the ocean) also has the strongest speed gradient with height and the lowest turbulent intensity (less than 2 % at a height of 35 m in comparison to 12 % for the north-westerly wind). While the full impact of shear flow on vortex wake signature and VIV is not well understood, it is well known that VIV is stronger for low turbulent flow in 2D experiments [1, 11, 22, 26, 29]. This is also shown in the present study in the presence of atmospheric boundary layers with different turbulence intensity profiles.

6 Conclusion

A custom-made chimney with large top diameter (2 m) and low Scruton number (Sc = 1,82) was erected in a monitored wind field, near the Atlantic coast of France. Details on the field-test platform and methodology, including the structural characteristics of the chimney and the wind "potential", have been presented. Preliminary vibration results, obtained during a sequential 13-days period in September 2020, was presented and discussed. Amplitude and frequency responses were reported in term of probability distributions plotted as a function of both wind speed and direction. As expected two types of cross-wind vibrations were observed, turbulence-induced vibrations and vortex-induced vibrations.

Vortex-induced vibrations of significant amplitude were mostly observed for wind speeds between 5 and 8,5 m/s with maximum amplitude near 6,25 m/s. This "critical" velocity value was lower than expected, suggesting a higher Strouhal number (closer to 0,25) for high Reynolds numbers ($Re \approx 8{,}3 \cdot 10^5$ for U = 6,25 m/s). Several VIV events of low (< 15 % of diameter) to moderate amplitude (> 30 % of diameter) were observed with lower amplitudes being more likely. The results also show that easterly (low turbulent) winds were mainly responsible for the highest amplitudes of vibration (> 30 % of top diameter) while the low amplitude VIV response were mainly due to north-westerly and south winds with higher turbulence intensity.

The goal of this test platform is to gather VIV data at supercritical Reynolds number in real atmospheric wind. These preliminary results will help to forecast specific VIV events on this chimney in order to strengthen the present results and perform additional unsteady pressure measurement, to better understand the 3D vortex signature, loading and VIV response at "super-critical" Reynolds numbers and for different turbulence conditions.

7 Acknowledgement

This work is part of a partnership co-funded by Beirens (of the Poujoulat Group), Centre Scientifique et Technique du Bâtiment (CSTB), Centre National d'Etudes Spatiales (CNES) and LadHyX, CNRS-Ecole polytechnique. Special acknowledgement is extended to Aurélien Jeanneton (of Beirens) for designing and constructing the chimney used in the field experiment.

8 References

1. Basu RI, Vickery BJ. Across-wind vibrations of structure of circular cross-section. Part II. Development of a mathematical model for full-scale application. J Wind Eng Ind Aerod. 1983;12(1):75–97.

2. Batham JP. Wind tunnel tests on scale models of a large power station chimney. J Wind Eng Ind Aerod. 1985;18(1):75–90.

3. Belloli M, Giappino S, Morganti S, Muggiasca S, Zasso A. Vortex induced vibrations at high Reynolds numbers on circular cylinders. Ocean Eng. 2015;94:140–54.

4. Blanchard A, Bergman LA, Vakakis AF. Vortex-induced vibration of a linearly sprung cylinder with an internal rotational nonlinear energy sink in turbulent flow. Nonlinear Dyn. 2020 Jan 1;99(1):593–609.

5. Blevins RD. Flow-Induced Vibration. 2nd ed. Krieger Pub Co: Krieger Pub Co; 2001.

6. Cheng C, Kareem A. Acrosswind response of reinforced concrete chimneys. J Wind Eng Ind Aerod. 1992 Jan;43(1–3):2141–52.

7. Christensen O, Askegaard V. Wind forces on and excitation of a 130-m concrete chimney. J Wind Eng Ind Aerod. 1978;3(1):61–77.

8. Cohen L. Time-frequency analysis. Englewood Cliffs, N.J: Prentice Hall PTR; 1995. 299 p. (Prentice Hall signal processing series).

9. Davenport AG. The spectrum of horizontal gustiness near the ground in high winds. Q J R Meteorol Soc. 1961 Apr;87(372):194–211.

10. Eurocode. 1: Actions on structures, Part 1 – 4: General Actions (EN–1991). Eurocode; 2010.

11. Fox TA, West GS. Fluid-Induced Loading of Cantilevered Circular Cylinders in a Low-Turbulence Uniform Flow. Part 2: Fluctuating Loads on a Cantilever of Aspect Ratio 30. J Fluids Struct. 1993 Jan 1;7(1):15–28.

12. Galemann T, Ruscheweyh H. Measurements of wind induced vibrations of a full-scale steel chimney. J Wind Eng Ind Aerod. 1992 Oct;41(1–3):241–52.

13. Hansen SO. Cross-wind vibrations of a 130-m tapered concrete chimney. J Wind Eng Ind Aerod. 1981 Jul;8(1–2):145–55.

14. Hirsch G, Ruscheweyh H. Full-scale measurements on steel chimney stacks. J Wind Eng Ind Aerod. 1975 Jan;1:341–7.

15. Lipecki T, Bec J, Jamińska P. A comparative study of along-wind and crosswind responses of steel chimneys according to Polish and Eurocode standards. Czasopismo Techniczne. 2016;

16. Lupi F, Niemann H-J, Höffer R. A novel spectral method for cross-wind vibrations: Application to 27 full-scale chimneys. J Wind Eng Ind Aerod. 2017;171:353–65.

17. Meirovitch L. Fundamentals of vibrations. Long Grove, Illinois: Waveland Press; 2010.

18. Melbourne WH, Cheung JCK, Goddard CR. Response to wind action of 265-m Mount Isa stack. J Struct Eng. 1983;109(11):2561–77.

19. Müller FP, Nieser H. Measurements of wind-induced vibrations on a concrete chimney. J Wind Eng Ind Aerod. 1975;1:239–48.

20. Paidoussis MP, Price SJ, de Langre E. Fluid-Structure Interactions Cross-Flow-Induced Instabilities. Cambridge, New York: Cambridge University Press; 2010.

21. Ribeiro JLD. Effects of surface roughness on the two-dimensional flow past circular cylinders I: mean forces and pressures. J Wind Eng Ind Aerod. 1991 Apr;37(3):299–309.

22. Ribeiro JLD. Effects of surface roughness on the two-dimensional flow past circular cylinders II: fluctuating forces and pressures. J Wind Eng Ind Aerod. 1991 Apr;37(3):311–26.

23. Ruscheweyh H. Vortex Excited Vibrations. In: Sockel H, editor. Wind-Excited Vibrations of Structures. Springer Vienna; 1994. p. 51–84.

24. Ruscheweyh H, Galemann T. Full-scale measurements of wind-induced oscillations of chimneys. J Wind Eng Ind Aerod. 1996 Dec;65(1–3):55–62.

25. Sanada S, Suzuki M, Matsumoto H. Full scale measurements of wind force acting on a 200m concrete chimney, and the chimney's response. J Wind Eng Ind Aerod. 1992 Jan;43(1–3):2165–76.

26. Simiu E, Scanlan RH. Wind effects on structures: fundamentals and applications to design. Wiley New York; 1996.

27. Stansby PK. The locking-on of vortex shedding due to the cross-stream vibration of circular cylinders in uniform and shear flows. J Fluid Mech. 1976 Apr;74(4):641–65.

28. Vickery BJ, Basu RI. Across-wind vibrations of structures of circular cross-section. Part I. Development of a mathematical model for two-dimensional conditions. J Wind Eng Ind Aerod. 1983;12(1):49–73.

29. Vickery BJ, Daly A. Wind tunnel modelling as a means of predicting the response of chimneys to vortex shedding. Eng Struct. 1984 Oct 1;6(4):363–8.

30. Waldeck JL. The measured and predicted response of a 300 m concrete chimney. J Wind Eng Ind Aerod. 1992 Oct;41(1–3):229–40.

31. Wickham H. ggplot2: Elegant Graphics for Data Analysis. 2nd ed. 2016. Cham: Springer International Publishing : Imprint: Springer; 2016. 1 p. (Use R!).

32. Zuo D. Full-scale measurement of wind pressure on the surface of an oscillating circular cylinders. J Wind Eng Ind Aerod. 2014 Oct;133:65–79.

Twin Strouhal numbers in flow around circular cylinder at high Reynolds numbers

Pascal Hémon[1] †, Ø. M. Ellingsen[1 2], X. Amandolese[3], and O. Flamand[2]

[1]LadHyX, CNRS-Ecole polytechnique, IP Paris, France

[2]CSTB, Nantes, France

[3]LMSSC, CNAM, Paris, France

(Received xx; revised xx; accepted xx)

Large diameter structures of circular cross section encountered in wind engineering are often prone to supercritical Reynolds number issues. This paper aims at invetigating the technique of artificially increasing the Reynolds number by means of surface roughness in order to simulate the supercritical vortex shedding regime at small scale. Two wind tunnel studies are performed, one for a large scale smooth cylinder up to the supercritical regime which is intented to serve as the reference, and the other for a 1/100 scale model with added roughness. Twin Strouhal numbers are measured for the large scale cylinder up to supercritical regime: by using a spatio-temporal analysis of the wall pressures, we show that each Strouhal number is associated to a specific wall pressure distribution. Comparison with the small scale experiment shows that the technique of artificially increasing the Reynolds number by means of surface roughness is not achieved, while it approaches some global coefficients.

Key words: Authors should not enter keywords on the manuscript

1. Introduction

The circular cylinder is one of the most studied bodies in aerodynamics, for both fundamental issues and engineering applications. Industrial chimneys and launch vehicles are examples of civil engineering structures with circular cross section, for which the fundamental properties of the mean and unsteady flow signature are of great interest. The flow regime around those structures strongly depends on the Reynolds number, $Re = \bar{U}D/\nu$, which combines the effect of the cylinder's diameter D, mean wind velocity $\bar{U}$ and air kinematic viscosity ν. As a first approach, the drag force coefficient of a 2D smooth circular cylinder is given in Figure 1 versus the Reynolds number (Roshko 1961; Lienhard 1966; Blevins 2001). For practical applications, i.e. Re greater than 1000, three kinds of regime can be observed, namely subcritical, critical and supercritical (Hoerner 1965).

In the subcritical regime the boundary layer around the cylinder is laminar and the

† Email address for correspondence: pascal.hemon@ladhyx.polytechnique.fr

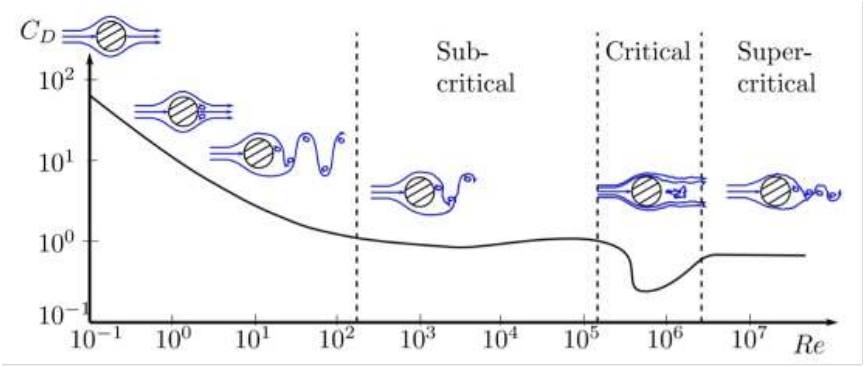

Figure 1: Reynolds number regions and drag coefficient, inspired by (Roshko 1961; Lienhard 1966; Blevins 2001).

drag coefficient $C_D \approx 1.2$. The alternate vortex shedding is well established and its non dimensional frequency is given by the Strouhal number $St = fD/\bar{U}$ in which f is the dimensional frequency. In the subcritical regime one observes that $St = 0.19 - 0.20$. As the Reynolds number increases, the boundary layer becomes progressively turbulent at the separation point and the cylinder is subject to the "drag crisis" which characterizes the critical regime. In this regime the drag coefficient decreases down to 0.4 before increasing again and the alternate vortex shedding is not well organized. When the Reynolds number is further increased, reaching the supercritical regime, the boundary layer is fully turbulent with a drag coefficient $C_D = 0.55 - 0.60$. One can observe a re-organization of the wake with an alternate vortex shedding having a Strouhal number subject to scattering, in the range $0.19 - 0.27$ (Schewe 1983; Roshko 1961). From these data, it is obvious that wind tunnel tests have to be made at the right Reynolds number, which can be up to the supercritical regime for wind engineering of circular cross section (Lupi et al. 2017; Ellingsen et al. 2021).

In practice, wind tunnel tests for such structures are performed with scaled models typically of the order of 1/100 that do not allow to ensure the Reynolds number similarity. To compensate for this, a number of authors have considered the technique of added roughness on the cylinder model (Achenbach 1971; Szechenyi 1975; Achenbach and Heinecke 1981; Nakamura and Tomonari 1982; Shih et al. 1993; Adachi 1997; van Hinsberg 2015). Rough cylinders are indeed known for shifting the drag crisis at smaller Reynolds numbers, depending on the roughness height. However those studies were based on global parameters, the drag force coefficient C_D, the unsteady lift coefficient (RMS value) C_l' and the Strouhal number St, leaving aside the wall pressure distribution around the cylinder. The simulation of the supercritical regime in wind tunnel by means of added roughness on low scale models still requires investigations.

In this paper two wind tunnel experimental studies are presented. The most important one is for a large scale cylinder up to the supercritical regime and the other one for a 1/100 scale model with added roughness. The reproduction of the supercritical vortex shedding regime is the main goal that justifies the study. The large scale experiments are presented in section 2 and the small scale results are reported in section 3. Further analysis, based on bi-orthogonal decomposition of the unsteady pressure distribution are presented in section 4 prior to a conclusion section.

2. Large Reynolds number wind tunnel tests

This experiment is devoted to the measurement of reference data for wind tunnel tests at supercritical Reynolds number up to 2.2×10^6 without any added roughness.

Figure 2: Views of the large 0.5 m diameter cylinder in the CSTB wind tunnel test section.

2.1. *Experimental apparatus*

Tests were performed in CSTB's climatic wind tunnel in Nantes, having a closed rectangular test-section of $6 \times 5\ m^2$, a maximum wind speed of 70 m/s and a turbulence intensity between 1 and 1.5 %. A smooth rigid circular cylinder with diameter 0.5 m and height-to-diameter ratio of 10 was mounted vertically in the wind tunnel to extend the entire height, as shown in Figure 2. With a blockage ratio of 8.3 %, the effect on the wake flow and Strouhal number is expected to be negligible (West and Apelt 1982). The setup also makes the first natural frequency close to 64 Hz with a high damping ratio, 36.4 %. Any residual vibrations should then be of minor impact. Sixty uniformly spaced pressure taps were drilled at mid-height. The first pressure tap is placed at the stagnation point ($\theta = 0°$) and the others are spaced out uniformly with a separation of 6°. The pressure taps were pneumatically connected to two 32 channels unsteady pressure scanners fitted inside the model (32HD ESP pressure scanners from Pressure Systems Inc.) with multiplex frequency of 70 kHz. Both pressure scanners, rated up to 7000 Pa, have static errors within ± 0.03 %. As the 1 meter length tubing can introduce resonance and damping effects, signal corrections were performed using a theoretical transfer function based on the work of Bergh and Tijdeman (1965). Four-hole Cobra probes were used to measure the wake characteristics. They were mounted at different heights and placed 2 diameters behind the cylinder and 0.25 diameters aside. A reference Pitot tube, mounted upstream of the model was also used to quantify the reference wind speed. For each wind speed, the unsteady pressures are measured during 180 s, that is roughly 5000 periods of the vortex shedding, at the sampling frequency of 400 Hz.

2.2. *Global results*

Integration of the wall pressure signals provides the global force coefficients on the cylinder. The mean drag coefficient C_D and the root-mean square value of the lift coefficient C_l' are shown in Figure 3a versus the Reynolds number in the range [150 000 – 2 170 000]. The end of the critical region and the beginning of the super-critical regime are then covered. In Figure 3b the mean drag coefficient is compared to the results of Achenbach and Heinecke (1981). The global trend is quite similar but our results are slightly lower. This is probably due to the higher blockage ratio (16.7 %) in the experiment of Achenbach and Heinecke, which was uncorrected. However our results match very well the values obtained with the Eurocode formula (European Committee for Standardization 2005) in the critical region. As expected, the unsteady lift coefficient exhibits a bump during the drag crisis, i.e. the critical regime, and slightly increases in the supercritical region. At $Re = 10^6$, C_l' is close to 0.1, that

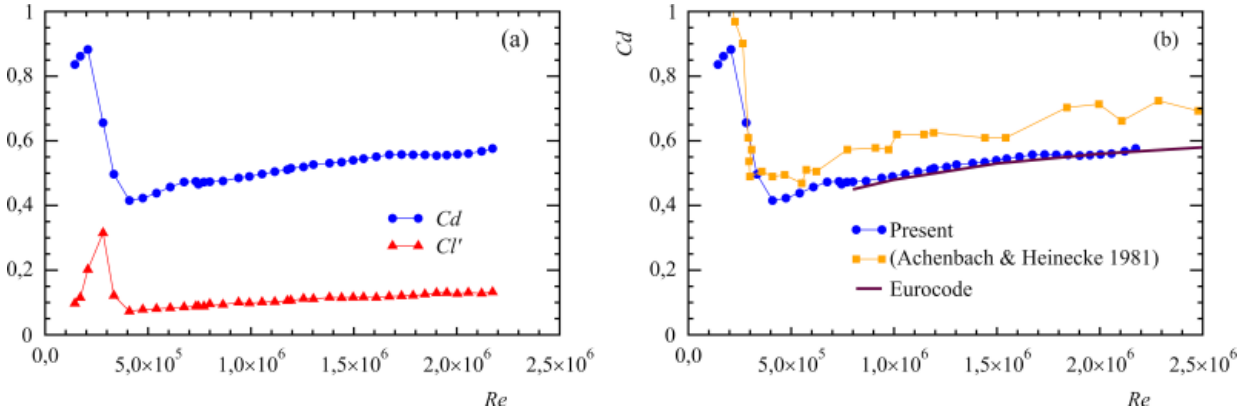

Figure 3: (a) Mean drag coefficient and standard deviation of the lift coefficient versus Re and (b) comparison of the drag coefficient with (Achenbach and Heinecke 1981) and Eurocode formula (European Committee for Standardization 2005).

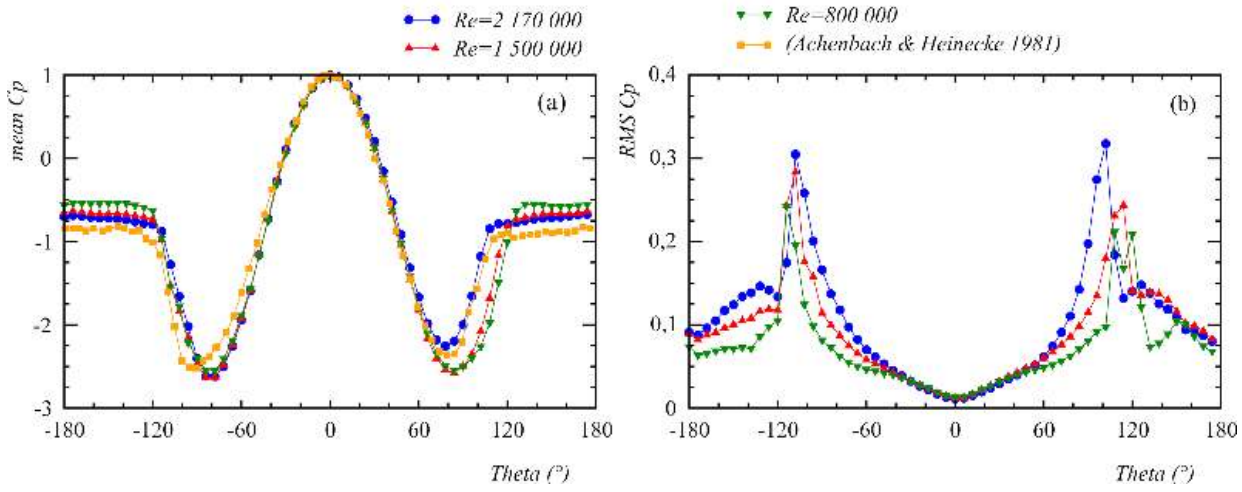

Figure 4: Cp distribution at different Re (a) mean values compared with (Achenbach & Heinecke 1981) at Re = 3600000, (b) standard deviation values

is slightly lower than the value of 0.12 reported by Fung (1960) and higher than the range [0.04- 0.095] reported in Schmidt (1966).

The distribution of the time-averaged wall pressure coefficients is shown in Figure 4a for three Reynolds number values that span the supercritical regime achieved in the study. It exhibits a classical supercritical shape, with a minimum $Cp_{min} \approx -2.5$ located at $\theta = 80°$ and a small Reynolds number effect can be observed in the separated area $|\theta| > 120°$. For the highest Reynolds number (2 170 000), the comparison with the results of (Achenbach and Heinecke 1981) at Re = 3600000 is relatively good. One can however observe a slight asymmetry of the curves which, in the present study, is attributed to circular section static deformation at high speed velocity (up to 67 m/s). The associated distribution of the standard deviation of the pressure is given in Figure 4b. Two remarkable peaks are observed around $\theta = 110°$ which are the main contributors to the unsteady lift coefficient. A deeper analysis of these unsteady signals will be done further in Section 4.

Power Spectral Densities (PSD) of the lateral unsteady velocity measured in the cylinder wake were used to identify the vortex shedding periodicity. As reported in Figure 5b two frequencies emerge on the PSD. The two associated Strouhal number are reported in Figure 5a. The upper one, which is the strongest and will be referred as "second" Strouhal number, agrees well with the high Strouhal number values reported in (Adachi 1997) in the critical regime. It also fits well the wake measurement reported in the supercritical regime. The

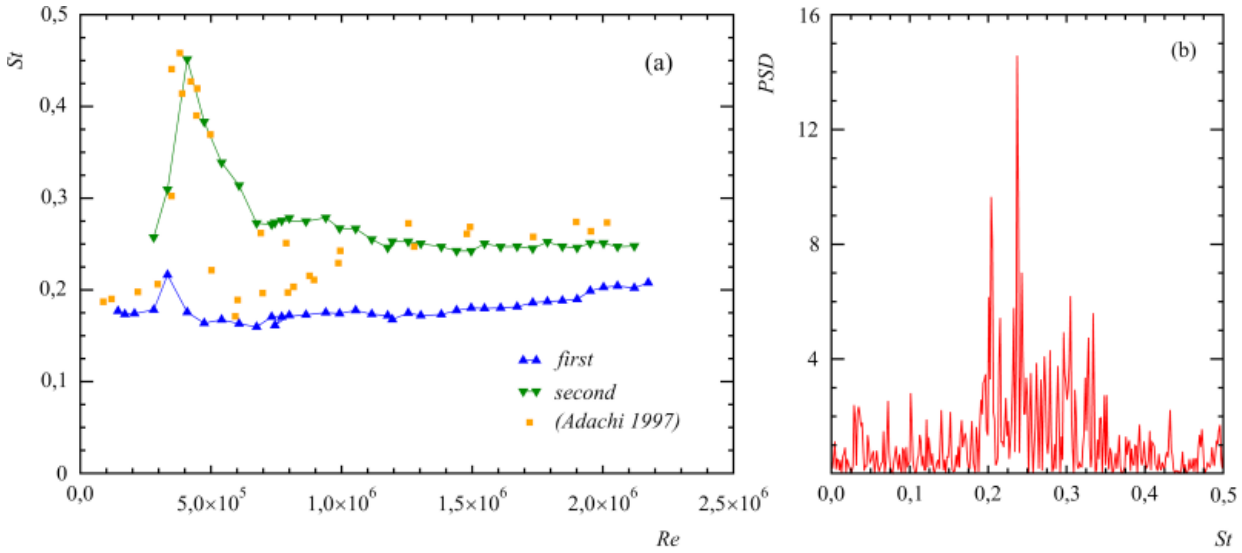

Figure 5: (a) St versus Re (b) PSD of lateral velocity from a Cobra probe at $Re = 2170000$.

lower one, referred as "first" Strouhal number, has an almost constant value which is close to the one found in subcritical regime. It agrees well with the results of Shih et al. (1993), obtained from surface pressure measurement, and it is also coherent with the lower Strouhal number values reported in Adachi (1997) in the critical and early supercritical regimes. Further discussion on these results will be done in Section 4.

3. Small scale wind tunnel tests

Experiments on a 1/100 scale model are performed. In order to reach the supercritical regime, the technique of adding roughnesses on the cylinder surface is used.

3.1. *Experimental apparatus*

Experiments were carried out in the $2 \times 4\ m^2$ test section of the NSA CSTB's wind tunnel in Nantes, that has a maximum wind speed of 30 m/s. The turbulence is 1 % in the main flow direction and 0.8 % in the transverse directions. The test model consists of a circular cylinder made of carbon fiber reinforced polymer of diameter 0.055 m, vertically mounted in the wind tunnel and extending the entire 2 m height (see Figure 6a). The cylinder has a first damped natural frequency of 25 Hz and a critical damping ratio of 21.4 % which make the vibration level negligible. The central section is equipped with 30 uniformly spaced pressure taps, as shown Figure 6b. Measurement systems and acquisition parameters are identical to the large wind tunnel experiment, except that the pressure sensor has a 2500 Pa full scale range.

To add roughness to the circular cylinder, ribs with rectangular cross-section of constant width 0.8 mm were glued and spaced out uniformly with a separation of 12° (see Figure 6b). Ribs were made with acrylic sheets of different thicknesses $h = 0.2$, 0.5 and 1 mm. Three different roughness configurations characterized with non-dimensional roughness $k = h/D = 0.0036, 0.0091$ and 0.0182 were tested.

3.2. *Global results*

The drag and unsteady lift coefficients versus Reynolds number are shown in Figure 7a for the three ribs configurations. One can observe that each roughness configuration promotes an earlier critical regime, down to Reynolds number values at least ten times lower than for the reference values reported in Figure 3a. The supercritical regime is not reached for the thinner

Figure 6: (a) Photo of the small scale cylinder in the test section and (b) detail of the measurement section equipped with pressure taps and ribs.

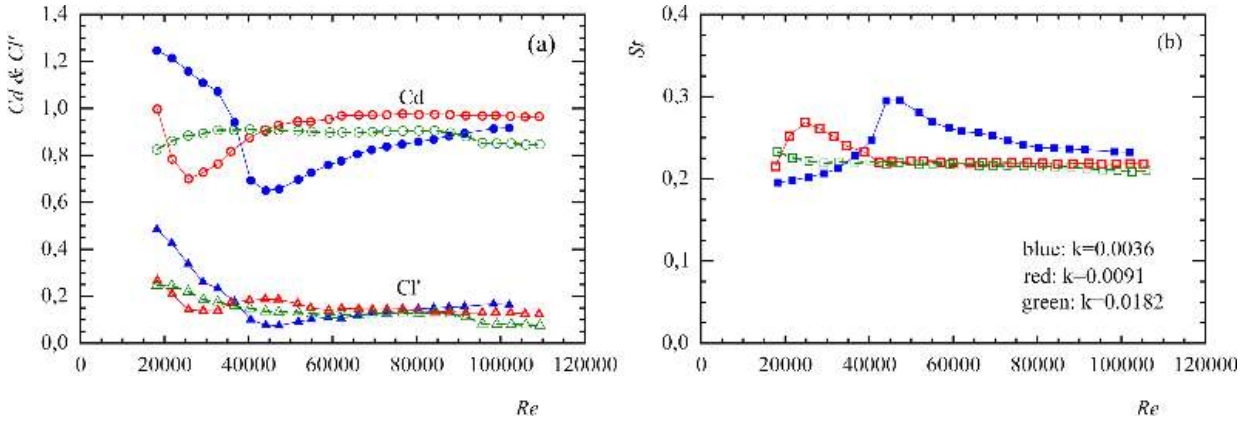

Figure 7: (a) C_D and C_l' and (b) St versus Re for different ribs heights.

ribs configuration $k = 0.0036$ but it is for the two others. Nevertheless, the associated mean drag and unsteady lift coefficients are both higher than in the reference smooth supercritical configuration. For the medium roughness $k = 0.0091$ the supercritical regime seems to be reached for $Re > 30000$ and even earlier than the minimum wind tunnel speed for the highest roughness $k = 0.0182$ that has been tested.

Unlike the reference supercritical configuration, only one clear frequency is observed on the PSD of the lateral wake velocity component at small scale, whatever the roughness size tested. The associated Strouhal number is given in Figure 7b. By comparison with the large scale experiment those results exhibit maximum Strouhal number values (at the drag crisis) significantly lower than for the second Strouhal number observed at large scale and an asymptotic value between those reported for the first and second Strouhal numbers.

Concerning the pressure distribution, results obtained at small scale supercritical regimes are found quite different from the reference supercritical data. If the Cp_{min} occurs for the same azimuth angle, its absolute value is twice lower, around -1.25. On another hand, Cp_{base} are similar, around 0.7 in both cases. Differences are also important in the distribution of the standard deviation, with two main peaks around $\theta = 80°$ at small scale, while they were sharper, twice higher and located around 110° for the reference case. While some similarities can be pointed out, there is no complete simulation of the supercritical regime in the small scale (1/100) model.

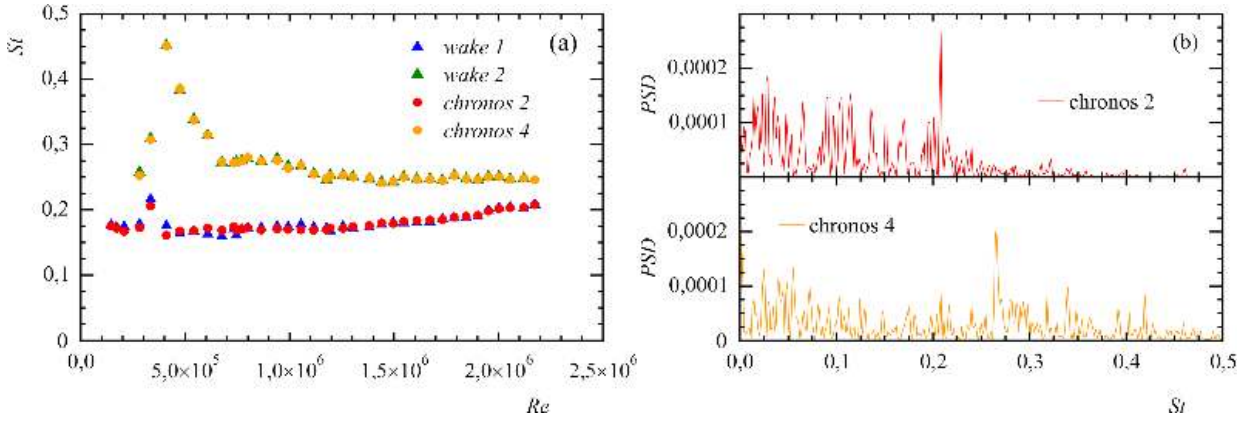

Figure 8: (a) Comparison of the Strouhal numbers (St_1 and St_2) measured in the wake with those issued from PSD of chronos 2 & 4 and (b) PSD of chronos 2 & 4 at $Re = 2170000$.

4. Analysis of the unsteady wall pressure

A bi-orthogonal decomposition (BOD) of the wall pressure signals is performed now to analyse the vortex shedding impact on the unsteady loading for both experiments.

4.1. *The bi-orthogonal decomposition*

The BOD was first introduced by Aubry et al. (1991) to decompose spatio-temporal signals in a series of spatial functions named further as "topos" and associated temporal functions named as "chronos". For a spatio-temporal distribution of pressure coefficient, the BOD can be written as $Cp(\theta,t) = \sum_{i=1}^{N} \alpha_i \phi_i(\theta)\psi_i(t)$ where α_i are the eigenvalues of the spatial or temporal covariance matrix of the distribution and N is the number of terms retained for the decomposition. Chronos $\psi_i(t)$ and topos $\phi_i(\theta)$ are orthogonal between them and normed. Mathematical details can be found in Aubry et al. (1991) and practical applications are presented in Hémon and Santi (2003). It was shown that the eigenvalues α_i are common to chronos and topos and that the series converge rapidly so that N is smaller than the original size T of the problem (number of pressure taps or number of time records). This means that α_i value decreases rapidly with their sum, $A = \sum_{i=1}^{T} \alpha_i$ representing the total energy in the original signal. Then each couple of chronos and topos have their contribution to the signal which decreases as long as their rank i increases. Note that BOD is very similar to proper orthogonal decomposition, except that the mean value of the original signal is kept in the analysis, refer to Hémon and Santi (2003) for a discussion on that point.

4.2. *BOD of wall pressure signals*

BOD is performed on the reference large Reynolds numbers data. Analyzing the chronos in terms of their frequency content, we observe that chronos 2 and 4 present a significant peak in their PSD which is related to vortex shedding. Results plotted in Figure 8a are in full agreement with the ones issued from the wake analysis. Moreover, it is interesting to notice that both St_1 and St_2 are physically separated through the BOD and associated to chronos 2 and 4 respectively.

The first four topos issued from the BOD of the wall pressure at high Reynolds numbers are shown in Figure 9. The first one represents the mean value of the wall pressure and contributes to the mean drag. The topos 2 has an anti-symmetrical shape and is the main contributor to the unsteady lift at the first Strouhal number value. It is characterized by a sharp peak at $\theta \approx 105°$ with a width of about 15°. The third topos mainly contributes to the unsteady drag at a dominant frequency twice the value of the one observed in chronos 2. The topos 4 also contributes to the unsteady lift but at a dominant frequency corresponding to

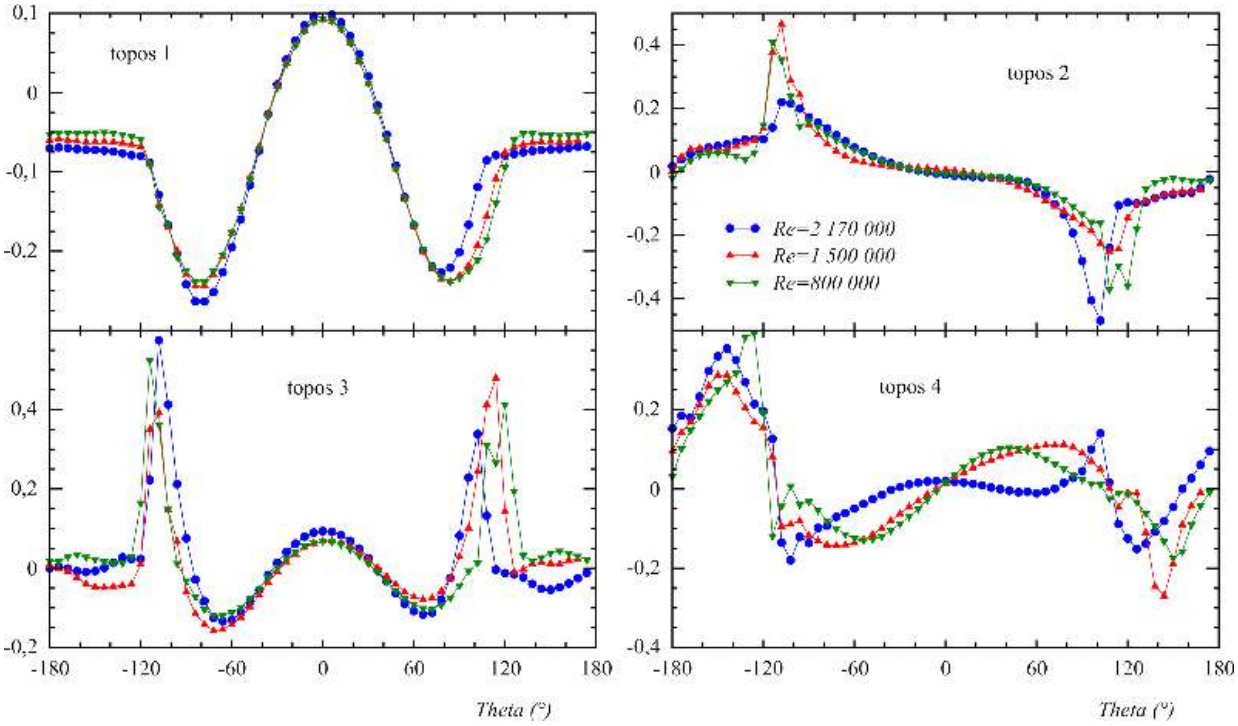

Figure 9: First four topos of the wall pressure at different supercritical Reynolds numbers.

the second Strouhal number value. As topos 2 it exhibits an anti-symmetrical shape but with a wider region in the rear part and a bump starting at $\theta \approx 120°$ up to 160°.

The relative energy contribution of the unsteady BOD "modes" can be assessed by checking their relative contribution $\tilde{\alpha}_i$ to the unsteady energy, which reads: $\tilde{\alpha}_i = 100\frac{\alpha_i}{1-\alpha_1/A}$. It appears that the Reynolds number does not influence this energy distribution in the supercritical regime tested here. The second "mode" contributes to about 34 % of the unsteady energy and the fourth one to about 7.4 %. One should note that, contrary to what was found in the wake analysis, the most energetic structure is at the lower Strouhal number value, referred as St_1 while the less energetic fourth mode is associated to St_2.

BOD analysis is also performed for the small scale cylinder equipped with the medium roughness $k = 0.0091$. The Strouhal number found with the PSD of the chronos 2 is in full agreement with the one which was found in the wake. The unsteady energy contribution shows that the contribution of this second term increase up to 79 %. The topos 2 is shown in Figure 10. In the range of Reynolds number explored, its shape is not influenced by the Reynolds number. It is characterized by two anti-symmetrical bumps with their maximum located at $\theta \approx 80°$, which creates a strong unsteady lift. It is then quite different from the case of the reference supercritical flow. Remaining terms are not participating in the vortex shedding mechanism, as there is no emerging frequency in the corresponding chronos.

5. Conclusion

A large scale experiment was performed on a smooth cylinder at supercritical Reynolds number in order to obtain a reference case. It is compared to another study at lower scale for which artificially increased Reynolds numbers are tentatively performed by means of roughness fixed at the surface of the cylinder. The main findings are summarized in Table 1. In the supercritical regime, one of the most important results is the detection of twin Strouhal numbers which might explain the scattering results usually found in previous studies. These two frequencies mechanisms are well separated by means of a BOD of the wall pressure

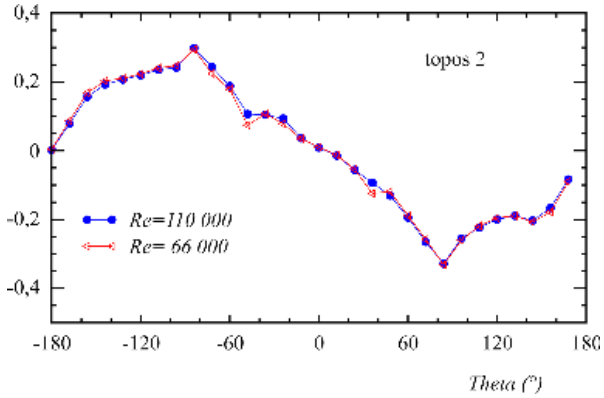

Figure 10: Topos 2 for rough cylinder with $k = 0.0091$ at various Re.

Smooth cylinder	$Re = 2000000$	Rough cylinder	$Re = 66000$
C_D	0.55	C_D	0.97
C_l'	0.127	C_l'	0.146
St_1	0.20	St	0.22
St_2	0.25		
Cp_{min}	-2.5 at 80°	Cp_{min}	-1.25 at 80°
Cp'_{max}	0.3 at 105°	Cp'_{max}	0.13 at 80°
$\phi_2(\theta)$ on St_1	ϕ_{2max} at 110°	$\phi_2(\theta)$ on St	ϕ_{2max} at 80°
$\phi_4(\theta)$ on St_2	ϕ_{4max} at 140°		

Table 1: Comparison of the main characteristics between the large and small cylinder.

distribution around the cylinder and recovered on the second and the fourth term of the decomposition.

Small scale experiments with a cylinder equipped with roughness show that the flow at supercritical regime can be roughly approached, as on the unsteady lift coefficient, but not completely reproduced. A single Strouhal number is observed with value between the two ones of the reference supercritical case. The corresponding unsteady lift is recovered by one single BOD mode. Moreover the shape of the associated topos 2 is quite different from the one identified in the large Reynolds number reference configuration. The lift production at supercritical Reynolds number is concentrated in a narrow region of the azimuth angle, while it is produced in a wider range for the artificially simulated supercritical flow case.

6. Funding

This work is part of a partnership co-funded by Beirens (Poujoulat Group), Centre Scientifique et Technique du Bâtiment (CSTB), Centre National d'Etudes Spatiales (CNES) and LadHyX, CNRS-Ecole polytechnique.

7. Declaration of Interests

The authors report no conflict of interest.

Achenbach, E. 1971 Influence of surface roughness on the cross-flow around a circular cylinder *J. Fluid Mech.*, **46.2**, pp. 321–335.

Achenbach, E. and Heinecke, E. 1981 On vortex shedding from smooth and rough cylinders in the range of Reynolds numbers $6x10^3$ to $5x10^6$ *J. Fluid Mech.*, **109**, pp. 239–251.

Adachi, T. 1997 Effects of surface roughness on the universal Strouhal number over the wide Reynolds number range *J. Wind Eng. & Indus. Aerod.*, **69-71**, pp. 399–412.

Aubry, N., Guyonnet, R. and Lima, R. 1991 Spatiotemporal analysis of complex signals: Theory and applications *J. Stat. Phys.*, **64.3**, pp. 683–739.

Bergh, H. and Tijdeman, H. 1965 Theoretical and experimental results for the dynamic response of pressure measuring systems. *Tech. Rep.* NLR-TR F.238 Nationaal Luchten Ruimtevaartlaboratorium.

Blevins, R.D. 2001 *Flow-Induced Vibration. 2nd edition*, Krieger. ISBN: 978-1-57524-183-8

Ellingsen, Ø.M., Flamand, O., Amandolese, X., Coiffet, F. and Hémon, P. 2021 Field tests on a full-scale steel chimney subjected to vortex-induced vibrations *Struct. Eng. Int.*, http://dx.doi.org/10.1080/10168664.2021.1936352.

European Committee for Standardization 2005 Eurocode 1: Actions on structures - Part 1-4: General actions - Wind actions. *Tech. Rep.* EN 1991-1-4:2005 F

Fung, Y.C. 1960 Fluctuating Lift and Drag Acting on a Cylinder in a Flow at Supercritical Reynolds Numbers *J. Aerosp. Sci.*, **27.11**, pp. 801–814.

Hémon, P. and Santi, F. 2003 Applications of biorthogonal decompositions in fluid-structure interactions *J. Fluids & Struct.*, **17.8**, pp. 1123–1143.

Hoerner, S.F. 1965 *Résistance à l'avancement dans les fluides*, ed. Gauthiers-Villars, Paris.

Lienhard, J.H. 1966 Synopsis of lift, drag, and vortex frequency data for rigid circular cylinders **300**, Technical Extension Service, Washington State University.

Lupi, F., Niemann, H.-J. and Höffer, R. 2017 A novel spectral method for cross-wind vibrations: Application to 27 full-scale chimneys *J. Wind Eng. & Indus. Aerod.*, **171**, pp. 353–365.

Nakamura, Y. and Tomonari, Y. 1982 The effects of surface roughness on the flow past circular cylinders at high Reynolds numbers *J. Fluid Mech.*, **123**, pp. 363-378.

Roshko, A. 1961 Experiments on the flow past a circular cylinder at very high Reynolds number *J. Fluid Mech.*, **10**, pp. 345-346.

Schewe, G. 1983 On the force fluctuations acting on a circular cylinder in crossflow from subcritical up to transcritical Reynolds numbers *J. Fluid Mech.*, **133**, pp. 265-285.

Schmidt, L.V. 1966 Fluctuating force measurements upon a circular cylinder at Reynolds numbers up to 5.10^6. *Meeting on Ground Wind Load Problems in Relation to Launch Vehicles*, NASA Langley Research Center, pp. 19.1-19.7.

Shih, W.C.L., Wang, C., Coles, D. and Roshko, A. 1993 Experiments on flow past rough circular cylinders at large Reynolds numbers *J. Wind Eng. & Indus. Aerod.*, **49.1**, pp. 351–368.

Szechenyi, E. 1975 Supercritical Reynolds number simulation for two-dimensional flow over circular cylinders *J. Fluid Mech.*, **70.3**, pp. 529-542.

van Hinsberg, N. P. 2015 The Reynolds number dependency of the steady and unsteady loading on a slightly rough circular cylinder: From subcritical up to high transcritical flow state *J. Fluids & Struct.*, **55**, pp. 526-539.

West, G. S. and Apelt, C. J. 1982 The effects of tunnel blockage and aspect ratio on the mean flow past a circular cylinder with Reynolds numbers between 10^4 and 10^5 *J. Fluid Mech.*, **114**, pp. 361–377.

Appendix

F Changes suggested by the jury

Following the defense, the jury suggested minor improvements to this work. Many of these were of grammatical nature, to improve text flow and readability or to improve legends, labels and figure texts. In addition to these improvements, the jury raised a few questions that could help improve this work and future works based on it; some of these would require major studies that could be spun-off into new research projects. These were:

- Further investigate the twin Strouhal numbers for the smooth, large-scale cylinder. While its been discovered that the two different shedding frequencies found from the BOD pairs can be found when investigating two different pressure taps, a better temporal investigation needs to be conducted. This will indicate how intermittent and bi-stable the vortex-shedding is.

- Investigate the effect of turbulent length-scale. The turbulent length-scale was sadly not included in this work though the author shares the belief of Claudio Mannini: Changing the turbulent length-scale will change the effect of turbulence. This parameter could explain some of the differences between the tests with ribs with small and large-scale cylinders, but the actual Reynolds number should still be an important factor for the differences. In addition, this investigation could be combined with an investigation on the effect of wind shear and turbulence profile as suggested by Carlo Cossu.

- Verify that having ribs not extending the entire height didn't affect the flow around it as pointed out by Claudio Mannini. On the lower and upper parts of the cylinder, there will be sub-critical/normal flow and circulation of this flow can change the simulated super-critical flow. To verify the results here, it would be useful to test with cylinders that have roughness strips attached along the entire height. This improvement would require a new experimental campaign.

- Better explain why the chosen ribs for simulating 2D super-critical flow were the best. The jury found the justification unclear and the reasoning was clarified and improved in the relevant chapters.

- Isolate vortex-induced vibrations from the experiments (especially the field-test) so that it can be investigated independently of turbulent-induced vibrations or buffeting. This will give a much clearer pictures of the effect of direction and incoming atmospheric boundary layer on vortex-induced vibrations. The author agrees that this could improve the results and that this would be a valuable addition in future projects dealing with similar vortex-induced vibration results.

- Investigate how to improve the predictive models more thoroughly. Many jury members shared this sentiment, but mostly focused on how the coefficients in the wake oscillator model could be improved. Vincent Denoël (specifically) wanted a deeper investigation of how the coefficients could be analytically defined using 2D forcing coefficients, the correlation or coherence, the mode shape, geometrical factors and combined using an aerodynamic projection along the height; this sentiment was shared by the author but

would require an additional, deep investigation. Another suggestion, or rather question, was to determine how to better improve the models used in design codes. The author believes that the correlation length model can be improved with better coefficients but that the spectral model requires more modifications: It's the author's belief that this model needs fundamental changes. Instead of included the effect of aerodynamic damping due to motion in the structural damping, this should be included in the rms forcing used in the numerator and that the structural damping should instead be the sum of structural damping and added drag-induced damping.

- The Scruton number may not be the best dimensionless variable for characterizing a chimney. Instead, something like the Skop-Griffin number, that includes the effect of added fluid-mass, should be used. This number can be further improved by including the effect of drag-induced damping in the which might make it possible to compare cylinders with different shapes. This new number would also help reduce the differences between vortex-induced vibrations in water and in air.

This marks the end of this thesis and three years of hard labor. I would like to extend a final thank you to my advisers (Pascal, Xavier and Olivier) and the rest of the project group (Aurélien, François and Julien). Finally, I would like to thank the jury (Vincent, Carlo, Claudio, Emmanuel and François) for making this thesis even better.

Appendix

G Résumé en français

G.1 L'état de l'art

G.1.1 Écoulement 2D et 3D

L'écoulement autour d'un cylindre circulaire est complexe et varie en fonction du nombre de Reynolds, de la rugosité de la surface et de l'intensité de la turbulence. Lorsque le nombre de Reynolds augmente jusqu'à environ 80, l'écoulement autour des cylindres circulaires commence à se déplacer selon un modèle alternatif. C'est ce qu'on appelle le tourbillon de von Karman. A ces faibles nombres de Reynolds, l'écoulement dans le sillage et au-dessus du cylindre est laminaire mais l'écoulement dans le sillage devient turbulent lorsque le nombre de Reynolds augmente au-delà de 10^3. A partir d'un nombre de Reynolds de 1000 jusqu'à environ $3 \cdot 10^5$ (région du nombre de Reynolds sous-critique), les paramètres de l'écoulement (coefficient de traînée moyen, coefficient de portance SD et fréquence de délestage tourbillonnaire sans dimension ou nombre de Strouhal) restent assez constants.

Une fois que le nombre de Reynolds passe $3 \cdot 10^5$, il y a un changement abrupt dans la dynamique des fluides autour des cylindres circulaires lisses. Ce point est lié à la crise de la traînée (fortement réduite, tout comme la portance SD) et la région du nombre de Reynolds est qualifiée de critique. À ces nombres de Reynolds, l'écoulement autour des cylindres circulaires commence par être laminaire avant de se séparer puis de se rattacher au cylindre avec une couche limite turbulente. Ce comportement de délestage rend le délestage tourbillonnaire et le sillage très irréguliers et le nombre de Strouhal est classiquement soit inexistant (pas de délestage tourbillonnaire cohérent), soit à une valeur plus élevée qu'aux nombres de Reynolds sous-critiques.

Lorsque le nombre de Reynolds augmente pour dépasser $Re > 10^6$, l'écoulement autour du cylindre et dans le sillage commence à devenir plus régulier. À ces nombres de Reynolds, l'écoulement autour du cylindre est entièrement turbulent et il ne devrait pas y avoir de rattachement après la séparation. En raison de l'écoulement plus régulier, les coefficients de traînée et de portance SD augmentent à des valeurs inférieures à celles des nombres de Reynolds sous-critiques et deviennent à nouveau presque constants avec la vitesse. Il en va de même pour le nombre de Strouhal, mais il diminue jusqu'à une valeur supérieure à celle du nombre sous-critique.

Ce changement avec le nombre de Reynolds crée un problème lorsqu'on essaie de recréer l'écoulement de grandes cheminées dans des souffleries qui ne peuvent atteindre que de faibles nombres de Reynolds. Pour contrer ce problème, on a essayé de simuler des nombres de Reynolds plus élevés en utilisant une rugosité de surface uniforme et des turbulences. Le meilleur traitement et la possibilité de reproduire précisément l'écoulement sont discutables, mais la rugosité et la turbulence ajoutées modifient les caractéristiques de l'écoulement autour et derrière les cylindres circulaires.

Le premier changement notable dans les caractéristiques de l'écoulement autour des cylindres avec une rugosité de surface ou une turbulence ajoutée, est que la transition vers et depuis les nombres de Reynolds critiques se produit à des nombres de Reynolds plus bas. C'est ce phénomène qui a conduit les chercheurs à utiliser la rugosité de surface comme un outil pour obtenir des nombres de Reynolds supercritiques similaires. Des tentatives ont été faites pour

calculer la transition exacte vers l'écoulement critique et supercritique sur la base de la hauteur de rugosité, mais elles ne tiennent pas compte de tous les paramètres (par exemple, le type, l'espacement et la turbulence).

En plus de la transition antérieure, l'ajout de la rugosité et de la turbulence affecte les constantes aérodynamiques. Une rugosité de surface accrue augmente la traînée moyenne aux nombres de Reynolds critiques et supercritiques, tandis qu'une turbulence accrue la diminue aux nombres de Reynolds sous-critiques et l'augmente au nombre critique ; l'effet est similaire au lissage de la courbe.

La rugosité et la turbulence ajoutées affectent également les caractéristiques instationnaires. L'effet de la rugosité est de diminuer le nombre de Strouhal aux nombres de Reynolds critiques et supercritiques alors que la turbulence ajoutée l'augmente dans les deux régions. L'effet de la rugosité sur la portance et la traînée instationnaires est moins étudié que l'effet de la turbulence et il affecte les forces instationnaires d'une manière similaire à la traînée moyenne.

En plus de ces changements d'écoulement en 2D, l'écoulement autour des cheminées et autres cylindres circulaires est plus complexe en raison de leur hauteur finie. Ces effets 3D font que la traînée moyenne augmente jusqu'à un maximum à un diamètre de la pointe (lorsqu'elle est mesurée à partir de la pointe) avant de diminuer jusqu'à une valeur stable (inférieure à la 2D) à 3-4 diamètres de la pointe. Ceci a pour effet global d'abaisser le coefficient de traînée moyen 2D.

Les coefficients de force instationnaire changent différemment avec la distance de la pointe. En s'éloignant de la pointe, les coefficients de traînée et de portance SD diminuent jusqu'à une valeur minimale à quelques diamètres de la pointe avant d'augmenter jusqu'à une valeur plus élevée et stable à quelques diamètres du minimum. Le nombre de Strouhal augmente jusqu'au nombre 2D avec la distance mais avec un comportement bizarre. En raison de la formation de cellules tourbillonnaires, la fréquence de déversement des tourbillons est constante sur de petites régions.

Le dernier effet 3D est la corrélation et la cohérence des forces et du processus d'éjection des tourbillons avec la hauteur. La différence entre ces statistiques est que la corrélation est mesurée dans le domaine temporel, alors que la cohérence est mesurée dans le domaine fréquentiel et évaluée à la fréquence de l'éjection des tourbillons. Bien que les données sur la cohérence manquent dans la littérature, on suppose que de nombreuses études antérieures ont calculé la cohérence plutôt que la corrélation (par exemple, en raison du filtrage ou de la confusion des statistiques par inadvertance).

La littérature montre que la corrélation dépend à la fois de l'intensité de la turbulence et du degré de mouvement. L'effet de la turbulence est la diminution de la corrélation, ce qui est attendu ; un flux moins uniforme devrait donner moins de corrélation. L'effet du mouvement est d'augmenter la corrélation. Cela pourrait être lié au verrouillage et au renforcement du délestage des tourbillons avec le mouvement lorsque la fréquence d'oscillation est proche de la fréquence de délestage des tourbillons. Des effets similaires sont observés dans l'écoulement autour de cylindres circulaires 3D, mais avec une corrélation réduite à toutes les distances.

G.1.2 Réponse aéroélectrique

Les vibrations induites par les tourbillons des structures circulaires sont compliquées car le forçage et le mouvement s'influencent mutuellement. Bien qu'elles soient souvent modélisées de manière similaire aux systèmes à réponse forcée, avec une oscillation sinusoïdale ou à cycle limite forçant et un oscillateur structurel linéaire, les vibrations induites par les tourbillons présentent des aspects de synchronisation qui les font davantage penser à des flotteurs. Cette synchronisation est appelée "lock-in" et fait passer la fréquence de délestage de la fréquence de Strouhal, qui augmente linéairement, à la fréquence naturelle ou à la fréquence de l'oscillation forcée. Au fur et à mesure que l'amplitude de la vibration augmente, la plage de vitesse donnant

lieu au "lock-in" augmente.

La réponse aéroélectrique est plus complexe sur le terrain qu'en 2D. Sur le terrain, le vent entrant est affecté par la couche limite atmosphérique turbulente, ce qui signifie que l'intensité de la turbulence peut être élevée et que la vitesse moyenne et l'intensité de la turbulence le long de la cheminée changent avec la hauteur. Néanmoins, de nombreux paramètres sans dimension utilisés sont similaires et la principale différence consiste à inclure l'effet de la principale forme de mode d'intérêt ; pour de nombreux cas de vibrations induites par les tourbillons (en particulier pour les cylindres et les cheminées), une seule forme de mode structurel est importante pour obtenir la réponse.

Outre l'estimation de la réponse des cylindres circulaires 3D sur le terrain en utilisant des souffleries à couche limite (avec une correction appropriée du nombre de Reynolds), l'amplitude structurelle due aux vibrations induites par les tourbillons peut être estimée à l'aide de modèles mathématiques. Cela va de l'ajustement simpliste des courbes de données à des modèles de vibration unidimensionnels simplifiés, en passant par des modèles couplés plus complexes de force et de structure (modèles d'oscillateur de sillage).

Les codes de conception actuels, comme l'Eurocode et le code modèle CICIND, ont tendance à se baser sur les modèles de vibration simplifiés, car ils permettent d'estimer facilement la réponse. Les deux modèles les plus populaires sont connus sous le nom de "modèle spectral" et de "modèle de longueur de corrélation" et ont tous deux été utilisés dans l'Eurocode. Le premier modèle est basé sur l'estimation du forçage en utilisant une forme supposée du spectre de puissance et un amortissement aérodynamique non linéaire qui est exprimé comme un amortissement structurel ; cet amortissement change avec le nombre de Reynolds et la turbulence. Le deuxième modèle est un modèle simple qui n'est valable que pendant le verrouillage et à la vitesse de l'amplitude maximale. Ceci est dû aux hypothèses concernant la fréquence, la force et la forme du forçage pendant la conception. De ces deux modèles, seul le "modèle spectral" sera utilisé dans les futurs codes modèles Eurocode et CICIND.

Un type de modèle qui pourrait être utile pour prédire la réponse mais qui n'est pas utilisé dans les codes de conception, est un groupe de modèles d'oscillateur de sillage. Ces modèles modélisent la réponse de la structure et le forçage tourbillonnaire comme deux équations différentielles couplées où l'équation de forçage est un oscillateur de van der Pol. Le couplage entre ces modèles varie selon les études mais celui qui est étudié ici est basé sur l'accélération et la force dans le sillage et l'équation de structure respectivement. Comme ces modèles sont non linéaires, leur solution a été basée sur l'intégration numérique, ce qui peut être amélioré par une meilleure approximation non linéaire.

G.1.3 Objectifs de la thèse

Beaucoup des phénomènes mentionnés dans ce résumé de l'état de l'art sont étudiés mais pas suffisamment. Cette thèse rectifiera cela et fournira de nouvelles connaissances sur le processus de déversement des tourbillons et la modélisation des vibrations induites par les tourbillons. Ceci sera fait en réalisant des expériences 2D supercritiques, en simulant à plus petite échelle, en réalisant des tests aéroélectriques 3D en soufflerie et sur le terrain et enfin en créant une meilleure méthodologie pour prédire les vibrations induites par les vortex en utilisant des modèles mathématiques.

G.2 Expériences en soufflerie 2D sur des cylindres stationnaires

Ce travail a présenté et relié plusieurs études visant à améliorer la réponse prédite des cheminées industrielles due aux vibrations induites par les tourbillons à des nombres de Reynolds élevés ($Re > 10^6$, c'est-à-dire à des nombres de Reynolds supercritiques). La première étape a consisté à déterminer les forces instationnaires sur un cylindre circulaire stationnaire à des nombres

de Reynolds supercritiques réels dans une grande soufflerie. Avec cette base de référence, la meilleure configuration de rugosité pour simuler l'écoulement à nombre de Reynolds supercritique a été déterminée à des échelles plus petites. Les exigences pour une bonne reproduction de l'écoulement supercritique étaient les suivantes : 1) simuler les nombres de Reynolds supercritiques à des vitesses de vent raisonnables ; 2) avoir des caractéristiques de force instationnaire similaires (valeurs moyennes et SD) ; et 3) avoir une fréquence de délestage tourbillonnaire caractéristique similaire (nombre de Strouhal).

Deux nombres de Strouhal bi-stables ont été trouvés pour le cylindre lisse à de grands nombres de Reynolds. En décomposant la distribution de pression instable à l'aide de la décomposition bi-orthogonale (BOD), les deux nombres de Strouhal différents proviennent de différentes distributions spatiales de pression instable (topos). Le nombre de Strouhal le plus faible ($St \approx 0.2$) a été associé à la paire BOD vortex-lift, avec une énergie spatiale concentrée près du "sommet" qui a produit la plus grande partie du lift fluctuant ($\theta \in \pm[90°, 110°]$), tandis que le nombre de Strouhal le plus élevé ($St \approx 0.25$) a été associé à la distribution "vortex-lift secondaire". Au lieu d'être près du sommet, l'énergie spatiale du second soulèvement tourbillonnaire était concentrée à l'arrière ($\theta \in \pm[120°, 180°]$) ce qui produisait une certaine fluctuation de la portance et de la traînée.

La découverte de ces nombres de Strouhal a permis de consolider une littérature contradictoire sur le décollement des tourbillons à des nombres de Reynolds supercritiques : Selon le type de mesure, les expériences précédentes ont donné un nombre de Strouhal soit dans la plage $St \in [0,25, 0,27]$, soit proche de $St = 0.2$ [8, 13, 17, 21, 23–25, 36, 54, 56]. Ce travail a montré que les deux existent dans les mesures de pression de sillage et instationnaire et ne sont pas une dispersion de valeurs possibles. La force relative de ces deux fréquences de délestage (mesurée dans le domaine fréquentiel) dépendait de l'endroit où elle était mesurée. Dans le sillage, le pic spectral le plus fort correspondait au nombre de Strouhal le plus élevé, tandis que le nombre de Strouhal le plus faible était relativement faible. Dans la pression instable décomposée, le nombre de Strouhal inférieur avait un pic spectral et une énergie totale beaucoup plus forts que le nombre de Strouhal supérieur.

L'ajout d'une rugosité de surface sous la forme de nervures a éliminé l'instabilité qui conduisait à la fréquence supérieure de délestage des tourbillons. Le nombre de Strouhal restant a été trouvé dans le sillage et dans les paires de BOD tourbillon-lift et second tourbillon-lift. Cette fréquence de délestage dépendait de la configuration et de l'échelle de la rugosité. Aux petites échelles et aux nombres de Reynolds, l'augmentation de la rugosité diminuait le nombre de Strouhal, tandis que l'augmentation de la rugosité aux grands nombres de Reynolds l'augmentait légèrement.

La rugosité et l'échelle ajoutées ont également modifié la corrélation et la cohérence le long de la hauteur. Cela a été clairement constaté en comparant la corrélation à petite échelle avec les résultats à grande échelle : La corrélation et la cohérence étaient beaucoup plus importantes lors des essais avec les côtes plus grandes à petite échelle. L'augmentation de la corrélation et de la cohérence pourrait expliquer en partie pourquoi l'écart-type (SD) du coefficient de portance était plus important à petite échelle, mais ne l'explique pas entièrement. Aux petites échelles et aux nombres de Reynolds, l'augmentation de l'espacement des nervures diminue la corrélation mais augmente considérablement les coefficients de portance et de traînée SD, tandis que l'augmentation de la taille des nervures modifie à peine la force mais augmente la corrélation. Cela indique qu'il y a une différence de nombre de Reynolds ou de champ de vent.

La distribution spatiale de la pression instationnaire a été étudiée et comparée entre les essais à grande échelle lisses et les essais à petite échelle avec rugosité. Cette comparaison a utilisé les quatre premières paires de DBO qui représentent (par ordre d'énergie relative décroissante) les distributions de pression moyenne, de soulèvement par vortex, de traînée par vortex et de second soulèvement par vortex. Les deux paires les plus importantes à faire correspondre étaient les distributions de pression moyenne et de pression de soulèvement tourbillonnaire, car elles

représentent la majeure partie de la force et de l'énergie de soulèvement fluctuante des signaux temporels.

Même si le cylindre lisse aux nombres de Reynolds supercritiques réels avait une distribution de pression moyenne asymétrique, il correspondait bien aux cylindres rugueux à petite échelle aux nombres simulés. Cette asymétrie a également provoqué un biais dans la distribution du soulèvement tourbillonnaire qui a affecté la différence de soulèvement relatif pour les configurations rugueuses et lisses. Cette différence était moins importante si l'on ne considérait que les composantes de la force instationnaire, mais elle restait perceptible. La plupart des différences spatiales entre les configurations à petite échelle et à grande échelle étaient dues au point de séparation plus précoce pour les cylindres rugueux et à l'énergie spatiale accrue à l'arrière. Malgré ces différences, la concordance du soulèvement tourbillonnaire était bonne pour les configurations rugueuses et lisses, comme l'indiquent les valeurs élevées de MAC.

Les différences entre les cylindres lisses et rugueux étaient plus importantes pour le vortex-drag et le second vortex-lift, le vortex-drag étant plus ou moins incomparable. L'asymétrie de la moyenne et du vortex-lift aurait également dû affecter le second vortex-lift et une partie des différences entre les cylindres lisses et rugueux était due à cette asymétrie. Néanmoins, il y avait d'autres différences plus importantes : De nombreuses différences dans le soulèvement du second tourbillon étaient dues au fait que l'énergie spatiale des cylindres rugueux était concentrée plus loin à l'arrière que celle du cylindre lisse et que les distributions d'énergie spatiale correspondent à peine comme l'indiquent les faibles valeurs MAC.

G.3 Expériences aéroélectriques

La réponse d'un cylindre flexible à des nombres de Reynolds supercritiques simulés a été déterminée en utilisant l'étude précédente et comparée à un cylindre sous-critique. En plus de tester l'effet de la rugosité sur le nombre de Reynolds simulé, des tests ont été effectués avec et sans couche limite Eurocode de type II pour tester l'effet d'une couche limite atmosphérique turbulente. Ces tests nous ont permis de vérifier deux hypothèses : 1) La mauvaise région de nombre de Reynolds donne une réponse très différente et 2) Les couches limites atmosphériques turbulentes peuvent être suffisantes pour simuler des nombres de Reynolds supercritiques.

Trois résultats donnent à penser que la couche limite atmosphérique turbulente ajoutée était suffisante pour simuler la réponse d'une hypothétique cheminée supercritique et que l'effet de la rugosité n'est perceptible qu'en l'absence de couche limite. Premièrement, les nombres de Strouhal étaient assez similaires pour les cylindres supercritiques et sous-critiques lors des essais avec la couche limite ; cela suggère une aérodynamique similaire. Deuxièmement, bien que les essais aux nombres de Reynolds supercritiques simulés en utilisant la rugosité aient eu une réponse d'amplitude différente de celle du cylindre sous-critique lors des essais avec la couche limite atmosphérique, les différences étaient principalement dues à un nombre de Scruton différent (un paramètre d'amortissement de la masse). Ce résultat est également observé en comparant l'amplitude maximale pour plusieurs nombres de Scruton et les résultats des cylindres lisses et rugueux semblent faire partie de la même courbe exponentielle ou loi de puissance.

Enfin, l'élimination de la couche limite atmosphérique supprime ces similitudes entre les cylindres et le cylindre rugueux aux nombres de Reynolds supercritiques a des fréquences de délestage tourbillonnaire et une réponse différentes de celles du cylindre lisse sous-critique. L'effet de la couche limite sur le délestage était également plus important pour le cylindre lisse que pour le cylindre rugueux, ce qui suggère que la couche limite atmosphérique turbulente ajoutée pourrait être suffisante pour simuler les nombres de Reynolds supercritiques d'expériences similaires.

Les essais aéroélectriques à petite échelle ont été accompagnés d'une expérience sur le terrain sur une cheminée sur mesure de 35,5 m de haut qui avait un diamètre de 2 m au sommet mais seulement 1 m à la base. Le seul paramètre aérodynamique mesuré sur le terrain était la vitesse

du vent à quatre hauteurs, mais la cheminée a été construite de manière à ce que la pression instationnaire puisse être mesurée à plusieurs hauteurs. Cette cheminée a été conçue pour avoir un faible nombre de Scruton et pour subir des vibrations de grande amplitude induites par les tourbillons à des vitesses modérément faibles.

La réponse de cette cheminée et du vent entrant a été enregistrée sur une période de 13 jours et les données ont été divisées en segments de 10 minutes pour une analyse statistique. La réponse a suivi des modèles de réponse typiques de la vie réelle, basés sur la vitesse du vent et la fréquence du mouvement. À faible vitesse, la fréquence dominante se situait soit à la fréquence de délestage de Strouhal qui augmente linéairement (vibrations induites par les tourbillons), soit à la fréquence naturelle (vibrations induites par les turbulences). À des vitesses élevées, la réponse était principalement due aux vibrations induites par la turbulence.

La réponse était plus intéressante à des vitesses intermédiaires (5-8 m/s) où la réponse était soit importante et due aux vibrations induites par les tourbillons, soit faible et due aux turbulences. L'amplitude des vibrations induites par les tourbillons dépendait des profils de la couche limite atmosphérique et ce paramètre changeait avec la direction. La direction du vent donnant les plus grandes amplitudes de mouvement avait un gradient de vitesse abrupt mais une faible turbulence à toutes les hauteurs alors que les directions ayant une faible réponse avaient une forte turbulence avec la hauteur. Ces couches limites atmosphériques étaient différentes de la couche limite de type II de l'Eurocode et les intensités de turbulence étaient significativement plus faibles dans le champ pour toutes les directions.

G.4 Prédiction de la réponse due aux vibrations induites par les vortex

Des solutions approximatives d'un modèle d'oscillateur de sillage non linéaire ont été dérivées pour améliorer les prédictions des vibrations induites par les tourbillons à l'aide de modèles mathématiques. Cette nouvelle approximation correspond bien à l'intégration numérique du même modèle mais nécessite un amortissement structurel constant (à la fréquence naturelle) au lieu d'un amortissement dépendant de la vitesse. Avec cette approximation, deux nouvelles études sur la taille des régions de verrouillage et l'amplitude maximale ont été réalisées.

En étudiant la stabilité et la différence de phase entre le forçage et le mouvement, une équation biquadratique pour les limites des trois régions de verrouillage en termes de vitesse sans dimension a été trouvée. À faible vitesse, il existe une région de verrouillage conditionnel (nécessitant de fortes amplitudes existantes) qui n'existe qu'avec une faible force à l'échelle de la masse M et un faible rapport d'amortissement structurel. La région de verrouillage suivante est une région de verrouillage absolu et cette région augmente en taille avec le forçage à échelle de masse. En augmentant le rapport d'amortissement, la région absolue n'a pas commencé à se rétrécir avant la disparition de la région conditionnelle à faible vitesse. À ce stade, un amortissement supplémentaire a diminué la taille des régions de verrouillage absolu à des vitesses sans dimension élevées et faibles.

La dernière région de verrouillage était une région de verrouillage conditionnelle à vitesse plus élevée. Alors que la région inférieure a disparu avec l'augmentation de la force, la région supérieure a persisté : À mesure que la force augmentait, la région conditionnelle augmentait, puis diminuait jusqu'à ce que la force atteigne une certaine valeur où la région conditionnelle supérieure recommençait à croître. L'effet du facteur d'amortissement sur la région conditionnelle supérieure était similaire à celui de la région inférieure et diminuait avec l'amortissement. La principale différence entre eux était que la région supérieure était plus grande à faible amortissement, ce qui a conduit à la persistance de la région supérieure à des taux d'amortissement beaucoup plus élevés.

Les concepteurs n'utilisent souvent que la réponse maximale lors de la conception d'une

cheminée et une expression pour la réponse maximale a donc été dérivée. Il a été constaté que l'amplitude maximale avait tendance à se produire à la même différence de phase et une expression pour la vitesse à la réponse maximale a été dérivée de cela. Ceci est différent des modèles de conception qui supposent que le maximum se produit à une vitesse spécifique. Cette nouvelle expression a été comparée à des simulations numériques pour plusieurs nombres de Scruton et la vitesse maximale et l'amplitude maximale correspondaient bien.

Pour s'assurer que ce nouveau modèle constitue une amélioration par rapport aux modèles existants du code de conception, la réponse prédite à l'aide de ce modèle approximatif de l'oscillateur de sillage, du modèle spectral et du modèle de la longueur de corrélation a été comparée aux données expérimentales. On a constaté que le meilleur modèle pour prédire la réponse en amplitude dépendait du nombre de Scruton. Lorsque le nombre de Scruton est faible, le meilleur modèle pour reproduire la réponse en amplitude est la nouvelle approximation, tandis que le modèle spectral est meilleur lorsque le nombre de Scruton est élevé. Ceci est logique car la réponse est plus harmonique à faible nombre de Scruton, ce qui favorise les modèles harmoniques comme l'oscillateur de sillage, et plus aléatoire à nombre de Scruton élevé, ce qui favorise les modèles de vibration aléatoire comme le modèle spectral utilisé dans le code du modèle CICIND et l'Eurocode.

En comparant la réponse maximale prédite avec celle trouvée dans la littérature, la nouvelle approximation s'est avérée être significativement meilleure que le modèle spectral en moyenne. L'exception était pour six cheminées où le modèle approximatif de sillage-oscillateur a sévèrement sous-estimé la réponse. L'amplitude pour la plupart de ces cheminées a été mesurée pendant la nuit et a connu un événement rare où la densité était beaucoup plus élevée et où l'intensité de la turbulence est devenue négligeable. Il est possible que la sous-estimation ne soit pas aussi sévère que ce qui est montré et qu'un facteur de sécurité sous la forme d'un modificateur d'événement extrême puisse atténuer les problèmes. Cela étant, le modèle approximatif de l'oscillateur de sillage doit toujours être considéré comme le meilleur modèle pour prédire la réponse à de faibles nombres de Scruton.

Bibliography

[1] *SkyscraperPage.com | https://SkyscraperPage.com* *Cited on page 3.*

[2] *BEIRENS | http://www.beirens.com/* *Cited on page 4.*

[3] *VL Staal A/S | https://vlstaal.com/en/references* *Cited on page 4.*

[4] B. J. Vickery and A. Daly. "Wind tunnel modelling as a means of predicting the response of chimneys to vortex shedding". en. In: *Eng. Struct.* 6.4 (Oct. 1984), pp. 363–368. ISSN: 0141-0296. DOI: 10.1016/0141-0296(84)90036-1 *Cited on pages 4, 11, 15, 75, 84.*

[5] Eurocode. *1: Actions on structures, Part 1 4: General Actions (EN1991)*. Brussels, Belgium: Eurocode, 2010 *Cited on pages 4, 11, 22, 25, 28, 30, 40, 76, 77, 79, 84, 89, 91, 93, 101, 108, 111, 112, 115, 118.*

[6] R. D. Blevins. *Flow-Induced Vibration*. 2nd. Malabar, FL: Krieger Pub Co, 2001. ISBN: 978-1-57524-183-8 *Cited on pages 4–7, 9–11, 18–22, 24, 25.*

[7] M. P. Paidoussis, S. Price, and E. de Langre. *Fluid-Structure Interactions Cross-Flow-Induced Instabilities*. eng. Cambridge, New York: Cambridge University Press, 2010. ISBN: 1-282-94842-3 *Cited on pages 4, 19–21, 27, 30, 31.*

[8] A. Roshko. "Experiments on the flow past a circular cylinder at very high Reynolds number". In: *J. Fluid. Mech.* 10.03 (May 1961), p. 345. DOI: 10.1017/s0022112061000950 *Cited on pages 5–7, 9–11, 14, 15, 26, 35, 48, 123, 202.*

[9] J. H. Lienhard. *Synopsis of lift, drag, and vortex frequency data for rigid circular cylinders*. Vol. 300. Technical Extension Service, Washington State University, 1966 *Cited on pages 5, 6, 11.*

[10] E. Szechenyi. "Supercritical Reynolds number simulation for two-dimensional flow over circular cylinders". In: *J. Fluid. Mech.* 70.03 (Aug. 1975), pp. 529–542. DOI: 10.1017/s0022112075002170 *Cited on pages 5–7, 11, 12, 14, 39, 40, 53.*

[11] F. M. White. *Fluid mechanics*. English. OCLC: 960210431. 2017. ISBN: 978-93-85965-49-4 *Cited on pages 5, 7, 8, 11.*

[12] S. T. Fleischmann and D. W. Sallet. "Vortex shedding from cylinders and the resulting unsteady forces and flow phenomenon, part 1". In: *SVICD* 13 (Nov. 1981) *Cited on pages 6, 7, 10, 11.*

[13] R. I. Basu. "Aerodynamic forces on structures of circular cross-section. Part 1. Model-scale data obtained under two-dimensional conditions in low-turbulence streams". In: *J. Wind. Eng. Ind. Aerod.* 21.3 (Dec. 1985), pp. 273–294. DOI: 10.1016/0167-6105(85)90040-6 *Cited on pages 6–12, 14, 35, 39–41, 53, 123, 202.*

[14] M. L. Facchinetti, E. de Langre, and F. Biolley. "Coupling of structure and wake oscillators in vortex-induced vibrations". In: *J. Fluids. Struct.* 19.2 (2004), pp. 123–140. ISSN: 0889-9746. DOI: 10.1016/j.jfluidstructs.2003.12.004 *Cited on pages 6, 9, 11, 20, 21, 23, 31, 101, 102, 108.*

[15] M. M. Zdravkovich. *Flow around circular cylinders: a comprehensive guide through flow phenomena, experiments, applications, mathematical models, and computer simulations*. Oxford science publications. Oxford ; New York: Oxford University Press, 1997. ISBN: 978-0-19-856396-9 *Cited on pages 7, 45.*

[16] G. Schewe. "On the force fluctuations acting on a circular cylinder in crossflow from subcritical up to transcritical Reynolds numbers". en. In: *J. Fluid. Mech.* 133 (Aug. 1983). Publisher: Cambridge University Press, pp. 265–285. ISSN: 1469-7645, 0022-1120. DOI: 10.1017/S0022112083001913 *Cited on pages 7, 9–11, 35.*

[17] W. C. L. Shih et al. "Experiments on flow past rough circular cylinders at large Reynolds numbers". In: *J. Wind. Eng. Ind. Aerod.* 49.1 (Dec. 1993), pp. 351–368. ISSN: 0167-6105. DOI: 10.1016/0167-6105(93)90030-R *Cited on pages 7, 11, 12, 35, 40, 48, 123, 202.*

[18] L. P. Erm and M. V. Ol. *An assessment of the usefulness of water tunnels for aerodynamic investigations*. Tech. rep. DEFENCE SCIENCE and TECHNOLOGY ORGANISATION VICTORIA (AUSTRALIA) AIR , 2012 *Cited on page 7.*

[19] E. Achenbach. "Distribution of local pressure and skin friction around a circular cylinder in cross-flow up to Re = $5x10^6$". In: *J. Fluid. Mech.* 34.4 (1968), pp. 625–639. DOI: 10.1017/S0022112068002120 *Cited on pages 7, 8, 12, 26, 35, 40, 45, 62.*

[20] E. Achenbach. "Influence of surface roughness on the cross-flow around a circular cylinder". In: *J. Fluid. Mech.* 46.2 (1971), pp. 321–335. DOI: 10.1017/S0022112071000569 *Cited on pages 7, 8, 12, 35, 40.*

[21] E. Achenbach and E. Heinecke. "On vortex shedding from smooth and rough cylinders in the range of Reynolds numbers $6x10^3$ to $5x10^6$". In: *J. Fluid. Mech.* 109 (1981), pp. 239–251. DOI: 10.1017/S002211208100102X *Cited on pages 7, 10–13, 35, 40, 48, 53, 58, 64, 123, 202.*

[22] N. P. van Hinsberg. "The Reynolds number dependency of the steady and unsteady loading on a slightly rough circular cylinder:From subcritical up to high transcritical flow state". In: *J. Fluids. Struct.* 55 (2015), pp. 526–539. ISSN: 0889-9746. DOI: 10.1016/j.jfluidstructs.2015.04.002 *Cited on pages 7–10, 12, 35, 40, 41.*

[23] T. Adachi et al. "On the force and vortex shedding on a circular cyliner from subcritical up to transcritical Reynolds numbers". In: *Bull. JSME* (1985) *Cited on pages 7, 10–12, 35, 40, 123, 202.*

[24] G. W. Jones Jr, J. J. Cincotta, and R. W. Walker. *Aerodynamic forces on a stationary and oscillating circular cylinder at high Reynolds numbers*. Tech. rep. NASA Langley Research Center, 1969 *Cited on pages 7, 8, 10, 11, 20, 35, 123, 202.*

[25] T. Adachi. "Effects of surface roughness on the universal Strouhal number over the wide Reynolds number range". In: *J. Wind. Eng. Ind. Aerod.* 69-71 (1997), pp. 399–412. ISSN: 0167-6105. DOI: 10.1016/S0167-6105(97)00172-4 *Cited on pages 7, 10–12, 14, 15, 35, 48, 49, 58, 64, 123, 202.*

[26] C. Barré and G. Barnaud. "High Reynolds number simulation techniques and their application to shaped structures model test". In: *J. Wind. Eng. Ind. Aerod.* 57.2-3 (July 1995), pp. 145–157. DOI: 10.1016/0167-6105(94)00111-p *Cited on pages 7, 8, 12, 15, 40.*

[27] M. Belloli et al. "Vortex induced vibrations at high Reynolds numbers on circular cylinders". In: *Ocean Eng.* 94 (2015), pp. 140–154. ISSN: 0029-8018. DOI: 0.1016/j.oceaneng.2014.11.017 *Cited on pages 7, 12, 40, 75, 89.*

[28] J. L. D. Ribeiro. "Effects of surface roughness on the two-dimensional flow past circular cylinders I: mean forces and pressures". In: *J. Wind. Eng. Ind. Aerod.* 37.3 (Apr. 1991), pp. 299–309. DOI: 10.1016/0167-6105(91)90014-n *Cited on pages 7, 11, 12, 39, 53, 59.*

[29] Y. C. Fung. "Fluctuating Lift and Drag Acting on a Cylinder in a Flow at Supercritical Reynolds Numbers". In: *J. Aerosp. Sci.* 27.11 (1960), pp. 801–814. DOI: 10.2514/8.8769 *Cited on pages 7, 10, 35, 41.*

[30] J. Cheung and W. Melbourne. "Turbulence effects on some aerodynamic parameters of a circular cylinder at supercritical numbers". en. In: *J. Wind. Eng. Ind. Aerod.* 14.1-3 (Dec. 1983), pp. 399–410. ISSN: 01676105. DOI: 10.1016/0167-6105(83)90041-7 *Cited on pages 7, 9, 10, 12–14, 60, 61, 87.*

[31] C. Demartino and F. Ricciardelli. "Aerodynamics of nominally circular cylinders: A review of experimental results for Civil Engineering applications". In: *Eng. Struct.* 137 (Apr. 2017), pp. 76–114. ISSN: 0141-0296. DOI: 10.1016/j.engstruct.2017.01.023 *Cited on pages 7, 9–13, 40.*

[32] R. I. Basu and B. J. Vickery. "Across-wind vibrations of structure of circular cross-section. Part II. Development of a mathematical model for full-scale application". In: *J. Wind. Eng. Ind. Aerod.* 12.1 (1983), pp. 75–97. ISSN: 0167-6105. DOI: 10.1016/0167-6105(83)90081-8 *Cited on pages 7, 19, 25, 27, 28, 82, 86, 89, 91, 95, 97, 101, 111, 112, 114, 159.*

[33] R. E. D. Bishop and A. Y. Hassan. "The lift and drag forces on a circular cylinder oscillating in a flowing fluid". In: *P. Roy. Soc. A-Math Phy.* 277.1368 (Jan. 1964), pp. 51–75. DOI: 10.1098/rspa.1964.0005 *Cited on pages 7, 10, 20, 21, 30, 31, 102, 106.*

[34] T. A. Fox, C. J. Apelt, and G. S. West. "The aerodynamic disturbance caused by the free-ends of a circular cylinder immersed in a uniform flow". In: *J. Wind. Eng. Ind. Aerod.* 49.1 (Dec. 1993), pp. 389–399. ISSN: 0167-6105. DOI: 10.1016/0167-6105(93)90033-K *Cited on pages 7, 15–17.*

[35] A. Kareem, C. .-. Cheng, and P. C. Lu. "Pressure and force fluctuations on isolated circular cylinders of finite height in boundary layer flows". In: *J. Fluids. Struct.* 3.5 (Sept. 1989), pp. 481–508. ISSN: 0889-9746. DOI: 10.1016/S0889-9746(89)80027-1 *Cited on pages 7, 15, 86.*

[36] C. Norberg. "Fluctuating lift on a circular cylinder: review and new measurements". en. In: *J. Fluids. Struct.* 17.1 (Jan. 2003), pp. 57–96. ISSN: 0889-9746. DOI: 10.1016/S0889-9746(02)00099-3 *Cited on pages 7, 9, 11, 35, 123, 202.*

[37] J. L. D. Ribeiro. "Effects of surface roughness on the two-dimensional flow past circular cylinders II: fluctuating forces and pressures". In: *J. Wind. Eng. Ind. Aerod.* 37.3 (Apr. 1991), pp. 311–326. DOI: 10.1016/0167-6105(91)90015-o *Cited on pages 7, 11, 12, 39, 53, 58, 59, 61, 97.*

[38] L. V. Schmidt. "Measurements of fluctuating air loads on a circular cylinder". In: *J. Aircraft.* 2.1 (1965), pp. 49–55. DOI: 10.2514/3.43618 *Cited on pages 7, 10, 35, 41.*

[39] L. V. Schmidt. "Fluctuating force measurements upon a circular cylinder at Reynolds numbers up to 5$\times$ 106". In: *Meeting on Ground Wind Load Problems in Relation to Launch Vehicles, NASA Langley Research Center*. 1966, pp. 19–1 *Cited on pages 7, 10, 35, 41.*

[40] Y. Uematsu and M. Yamada. "Aerodynamic forces on circular cylinders of finite height". In: *J. Wind. Eng. Ind. Aerod.* 51.2 (Feb. 1994), pp. 249–265. DOI: 10.1016/0167-6105(94)90007-8 *Cited on pages 7, 11–14, 40.*

[41] G. S. West and C. J. Apelt. "Measurements of Fluctuating Pressures and Forces on a Circular Cylinder in the Reynolds Number Range 10^4 to 2.5x10^5". In: *J. Fluids. Struct.* 7.3 (Apr. 1993), pp. 227–244. DOI: 10.1006/jfls.1993.1014 *Cited on pages 7–9, 45.*

[42] J. D. Anderson and J. D. Anderson. *Fundamentals of aerodynamics*. 5th ed. Anderson series. OCLC: ocn463634144. New York: McGraw-Hill, 2011. ISBN: 978-0-07-339810-5 *Cited on pages 8, 15.*

[43] M. Novak and H. Tanaka. "Pressure Correlations on a Vibrating Cylinder". In: *4th Int. Conf. Wind effects on buildings and Structures*. Cambridge Univ. Press, 1975 *Cited on pages 8, 13, 17, 18, 27, 41, 42, 61, 62.*

[44] T. A. Fox and C. J. Apelt. "Fluid-Induced Loading of Cantilevered Circular Cylinders in a Low-Turbulence Uniform Flow. Part 3: Fluctuating Loads with Aspect Ratios 4 to 25". In: *J. Fluids. Struct.* 7.4 (May 1993), pp. 375–386. ISSN: 0889-9746. DOI: 10.1006/jfls.1993.1022 *Cited on pages 8, 10, 15–17.*

[45] P. Hémon and F. Santi. "On the aeroelastic behaviors of rectangular cylinders in cross-flow". en. In: *J. Fluids. Struct.* 16.7 (Oct. 2002), pp. 855–889. ISSN: 0889-9746. DOI: 10.1006/jfls.2002.0452 *Cited on page 9.*

[46] P. Hémon and F. Santi. "Applications of biorthogonal decompositions in fluidstructure interactions". en. In: *J. Fluids. Struct.* 17.8 (July 2003), pp. 1123–1143. ISSN: 0889-9746. DOI: 10.1016/S0889-9746(03)00057-4 *Cited on pages 9, 43, 44.*

[47] H. M. Blackburn and W. H. Melbourne. "Lift on an oscillating cylinder in smooth and turbulent flow". In: *J. Wind. Eng. Ind. Aerod.* 41.1-3 (Oct. 1992), pp. 79–90. DOI: 10.1016/0167-6105(92)90395-q *Cited on pages 9, 10, 13, 14.*

[48] J. L. D. Ribeiro. "Fluctuating lift and its spanwise correlation on a circular cylinder in a smooth and in a turbulent flow: a critical review". In: *J. Wind. Eng. Ind. Aerod.* 40.2 (June 1992), pp. 179–198. DOI: 10.1016/0167-6105(92)90364-g *Cited on pages 9–13, 39, 53, 59.*

[49] H. Ruscheweyh. "Vortex Excited Vibrations". In: *Wind-Excited Vibrations of Structures*. Ed. by H. Sockel. Vienna, Austria: Springer Vienna, 1994, pp. 51–84. DOI: 10.1007/978-3-7091-2708-7_2 *Cited on pages 9, 11, 18, 19, 25, 28, 30, 86, 89, 91, 95, 97, 101, 107, 111, 112.*

[50] M. Hallam, N. Heaf, and L. R. Wootton. *Dynamics of marine structures: methods of calculating the dynamic response of fixed structures subject to wave and current action*. Tech. rep. 1977 *Cited on page 9.*

[51] C. Wieselberg. "New data on the laws of fluid resistance". In: *National Advisory Committee For Aeronautics* (1922) *Cited on page 9.*

[52] C. H. Williamson. *Oblique and Parallel Modes of Vortex Shedding in the Wake of a Circular Cylinder at Low Reynolds Numbers*. en. Tech. rep. Section: Technical Reports. CALIFORNIA INST OF TECH PASADENA GRADUATE AERONAUTICAL LABS, Dec. 1989 *Cited on page 9.*

[53] H. M. Blackburn and W. H. Melbourne. "The effect of free-stream turbulence on sectional lift forces on a circular cylinder". In: *J. Fluid. Mech.* 306 (Jan. 1996), pp. 267–292. DOI: 10.1017/s0022112096001309 *Cited on pages 10, 12–14, 39, 58, 60.*

[54] S. J. Zan. "Experiments on circular cylinders in crossflow at Reynolds numbers up to 7 million". In: *J. Wind. Eng. Ind. Aerod.* 96.6-7 (June 2008), pp. 880–886. DOI: 10.1016/j.jweia.2007.06.015 *Cited on pages 10–13, 35, 48, 49, 58, 123, 202.*

[55] CICIND. *CICIND Model Code for Steel Chimneys: September2010 Revision 2*. CICIND, 2010. ISBN: 1-902998-16-2 *Cited on pages 11, 22, 25, 28, 30, 50, 77, 79, 84, 91, 101, 111, 112, 115, 118.*

[56] W. Lenharth and R. W. Corell. "Thoughts on the relationship between Reynolds and Strouhal numbers". In: *J. Sound. Vib.* 36.1 (Aug. 1974), pp. 147–149. DOI: 10.1016/s0022-460x(74)80349-4 *Cited on pages 11, 35, 123, 202.*

[57] T. V. Lawson. "The use of roughness to produce high reynolds number flows around circular cylinders at lower reynolds numbers". In: *J. Wind. Eng. Ind. Aerod.* 10.3 (Dec. 1982), pp. 381–387. DOI: 10.1016/0167-6105(82)90009-5 *Cited on pages 11, 14.*

[58] Y. Nakamura and Y. Tomonari. "The effects of surface roughness on the flow past circular cylinders at high Reynolds numbers". en. In: *J. Fluid. Mech.* 123 (Oct. 1982), pp. 363–378. ISSN: 1469-7645, 0022-1120. DOI: 10.1017/S0022112082003103 *Cited on pages 11, 12, 14, 39, 40.*

[59] F. Lupi, H.-J. Niemann, and R. Hüffer. "Aerodynamic damping model in vortex-induced vibrations for wind engineering applications". In: *J. Wind. Eng. Ind. Aerod.* 174 (2018), pp. 281–295. ISSN: 0167-6105. DOI: 10.1016/j.jweia.2018.01.006 *Cited on pages 11, 28, 120.*

[60] J. P. Batham. "Wind tunnel tests on scale models of a large power station chimney". In: *J. Wind. Eng. Ind. Aerod.* 18.1 (1985), pp. 75–90. ISSN: 0167-6105. DOI: 10.1016/0167-6105(85)90075-3 *Cited on pages 11, 14, 15, 75, 85.*

[61] Y. Gao et al. "Experimental study of the effects of surface roughness on the vortex-induced vibration response of a flexible cylinder". In: *Ocean Eng.* 103 (July 2015), pp. 40–54. DOI: 10.1016/j.oceaneng.2015.04.052 *Cited on pages 12, 20.*

[62] G. Buresti. "The effect of surface roughness on the flow regime around circular cylinders". In: *J. Wind. Eng. Ind. Aerod.* 8.1-2 (July 1981), pp. 105–114. DOI: 10.1016/0167-6105(81)90011-8 *Cited on pages 12, 14, 39, 40, 53.*

[63] O. Güven, C. Farell, and V. C. Patel. "Surface-roughness effects on the mean flow past circular cylinders". en. In: *J. Fluid. Mech.* 98.4 (June 1980). Publisher: Cambridge University Press, pp. 673–701. ISSN: 1469-7645, 0022-1120. DOI: 10.1017/S0022112080000341 *Cited on pages 12, 40.*

[64] W. Ma et al. "The effect of surface roughness on aerodynamic forces and vibrations for a circular cylinder in the critical Reynolds number range". In: *J. Wind. Eng. Ind. Aerod.* 187 (2019), pp. 61–72 *Cited on page 12.*

[65] H. H. Nigim and S. M. Batill. "Flow about cylinders with surface perturbations". en. In: *J. Fluids. Struct.* 11.8 (Nov. 1997), pp. 893–907. ISSN: 08899746. DOI: 10.1006/jfls.1997.0116 *Cited on pages 13, 59, 60.*

[66] A. E. Perry, W. H. Schofield, and P. N. Joubert. "Rough wall turbulent boundary layers". en. In: *J. Fluid. Mech.* 37.2 (June 1969), pp. 383–413. ISSN: 0022-1120, 1469-7645. DOI: 10.1017/S0022112069000619 *Cited on pages 13, 59, 60.*

[67] D. Surry. "Some effects of intense turbulence on the aerodynamics of a circular cylinder at subcritical Reynolds number". en. In: *J. Fluid. Mech.* 52.3 (Apr. 1972), pp. 543–563. ISSN: 1469-7645, 0022-1120. DOI: 10.1017/S0022112072001582 *Cited on pages 13, 61.*

[68] R. H. Barnard and Z. Q. Yun. "Vortex shedding from bodies of finite length in smooth and turbulent flows". In: *Proc. 2nd Asia Pacific symposium on wind engineering.* 1989 *Cited on pages 13, 61.*

[69] R. I. Basu. "Aerodynamic forces on structures of circular cross-section. Part 2. The influence of turbulence and three-dimensional effects". In: *J. Wind. Eng. Ind. Aerod.* 24.1 (Aug. 1986), pp. 33–59. DOI: 10.1016/0167-6105(86)90071-1 *Cited on pages 13, 15, 16, 58, 61.*

[70] O. M. Griffin. “A universal Strouhal number for the ’locking-on’ of vortex shedding to the vibrations of bluff cylinders”. In: *J. Fluid. Mech.* 85.3 (1978), pp. 591–606. DOI: 10.1017/S0022112078000804 *Cited on pages 14, 15, 20.*

[71] T. Okamoto and M. Yagita. “The Experimental Investigation on the Flow Past a Circular Cylinder of Finite Length Placed Normal to the Plane Surface in a Uniform Stream”. In: *Bul.l JSME* 16.95 (1973), pp. 805–814. DOI: 10.1299/jsme1958.16.805 *Cited on pages 15, 16.*

[72] G. L. Larose et al. “Sectional model investigation at high Reynolds number for a super tall building”. In: *J. Wind. Eng. Ind. Aerod.* 13th International Conference on Wind Engineering 104-106 (May 2012), pp. 49–55. ISSN: 0167-6105. DOI: 10.1016/j.jweia.2012.03.028 *Cited on page 15.*

[73] T. L. Brower. “Titan Launch Vehicle: Ground Test History”. In: *J. Spacecraft Rockets* 43.1 (Jan. 2006), pp. 147–160. DOI: 10.2514/1.12863 *Cited on page 15.*

[74] G. Grillaud and J. Gandemer. “Dynamic wind effects on the waiting Ariane carrier rocket on launch pad”. In: *Structural dynamics. Proceedings of the european conference on structural dynamics EURODYN 90*. 1990, pp. 1177–1182 *Cited on page 15.*

[75] T. G. Ivanco and D. F. Keller. “Investigation of Ground-Wind Loads for Ares Launch Vehicles”. In: *J. Spacecraft Rockets* 49.4 (July 2012), pp. 574–585. DOI: 10.2514/1.a32177 *Cited on page 15.*

[76] W. H. Reed III. “Ground-wind-load considerations for space shuttle vehicles”. In: 1970 *Cited on page 15.*

[77] R. Gould, P. Ponsford, and W. Raymer. “Wind tunnel tests on chimneys of circular section at high Reynolds numbers”. In: *Processings of Symposium on Wind Effects on Buildings and Structures*. Loughborough University of Technology, Loughborough, UK: NPL, 1968 *Cited on pages 15, 16.*

[78] T. A. Fox and G. S. West. “Fluid-Induced Loading of Cantilevered Circular Cylinders in a Low-Turbulence Uniform Flow. Part 2: Fluctuating Loads on a Cantilever of Aspect Ratio 30”. In: *J. Fluids. Struct.* 7.1 (Jan. 1993), pp. 15–28. ISSN: 0889-9746. DOI: 10.1006/jfls.1993.1002 *Cited on pages 15–17, 97.*

[79] R. I. Basu. “Across-wind response of slender structures of circular cross-section to atmospheric turbulence”. PhD thesis. London, Ontario: University of Western Ontario, 1983 *Cited on pages 15, 119, 159.*

[80] P. Stoica and R. L. Moses. *Spectral analysis of signals*. Upper Saddle River, N.J: Pearson/Prentice Hall, 2005. ISBN: 978-0-13-113956-5 *Cited on page 16.*

[81] S. Balasubramanian and R. A. Skop. “A nonlinear oscillator model for vortex shedding from cylinders and cones in uniform and shear flows”. In: *J. Fluids. Struct.* 10.3 (Apr. 1996), pp. 197–214. DOI: 10.1006/jfls.1996.0013 *Cited on page 17.*

[82] T. G. Ivanco. “Aeroelastic Ground Wind Loads Analysis Tool for Launch Vehicles”. In: *15th Dynamics Specialists Conference*. American Institute of Aeronautics and Astronautics, Jan. 2016. DOI: 10.2514/6.2016-2047 *Cited on page 17.*

[83] B. R. Noack, F. Ohle, and H. Eckelmann. “On cell formation in vortex streets”. In: *J. Fluid. Mech.* 227.-1 (June 1991), p. 293. DOI: 10.1017/s0022112091000125 *Cited on page 17.*

[84] P. K. Stansby. "The locking-on of vortex shedding due to the cross-stream vibration of circular cylinders in uniform and shear flows". en. In: *J. Fluid. Mech.* 74.4 (Apr. 1976), pp. 641–665. ISSN: 1469-7645, 0022-1120. DOI: 10.1017/S0022112076001985 *Cited on pages 17, 20.*

[85] J. F. Howell and M. Novak. "Vortex shedding from circular cylinders in turbulent flow". In: *Wind Engineering*. Ed. by J. E. Cermak. Vol. 1. Pergamon, Jan. 1980, pp. 619–629. ISBN: 978-1-4832-8367-8. DOI: 10.1016/B978-1-4832-8367-8.50061-9 *Cited on pages 17, 18, 20, 21, 24, 85, 86.*

[86] E. H. Dowell. *A Modern Course in Aeroelasticity: Fifth Revised and Enlarged Edition*. eng. 5th ed. 2015. Vol. 217. Solid Mechanics and Its Applications. Cham: Springer International Publishing, 2015. ISBN: 978-3-319-09452-6 *Cited on pages 18–20, 22, 25, 27, 131.*

[87] L. Meirovitch. *Fundamentals of vibrations*. English. OCLC: 981315419. Long Grove, Illinois: Waveland Press, 2010. ISBN: 978-1-57766-691-2 *Cited on pages 19, 22, 23, 27, 31, 131.*

[88] B. J. Vickery and R. I. Basu. "Across-wind vibrations of structures of circular cross-section. Part I. Development of a mathematical model for two-dimensional conditions". In: *J. Wind. Eng. Ind. Aerod.* 12.1 (1983), pp. 49–73. ISSN: 0167-6105. DOI: 10.1016/0167-6105(83)90080-6 *Cited on pages 19, 27, 28, 82, 86, 91, 95, 97, 101, 111, 112, 114.*

[89] R. L. Bisplinghoff, H. Ashley, and R. L. Halfman. *Aeroelasticity*. Dover ed. Dover science books. New York: Dover Publications, 1996. ISBN: 978-0-486-69189-3 *Cited on pages 19, 25.*

[90] E. Simiu and R. H. Scanlan. *Wind effects on structures: fundamentals and applications to design*. Wiley New York, 1996 *Cited on pages 19, 20, 22, 25, 27, 30, 97.*

[91] E. de Langre. "Frequency lock-in is caused by coupled-mode flutter". In: *J. Fluids. Struct.* 22.6-7 (Aug. 2006), pp. 783–791. DOI: 10.1016/j.jfluidstructs.2006.04.008 *Cited on pages 19, 104.*

[92] W. Zhang et al. "Mechanism of frequency lock-in in vortex-induced vibrations at low Reynolds numbers". In: *J. Fluid. Mech.* 783 (Oct. 2015), pp. 72–102. DOI: 10.1017/jfm.2015.548 *Cited on pages 19, 20, 104.*

[93] R. D. Gabbai and H. Benaroya. "A first-principles derivation procedure for wake-body models in vortex-induced vibration: Proof-of-concept". en. In: *J. Sound. Vib.* 312.1 (Apr. 2008), pp. 19–38. ISSN: 0022-460X. DOI: 10.1016/j.jsv.2007.07.086 *Cited on pages 19, 27.*

[94] P. Meliga and J.-M. Chomaz. "An asymptotic expansion for the vortex-induced vibrations of a circular cylinder". In: *J. Fluid. Mech.* 671 (Feb. 2011), pp. 137–167. DOI: 10.1017/s0022112010005550 *Cited on pages 19, 27, 31.*

[95] A. Balanov et al. *Synchronization: From Simple to Complex*. eng. Springer Series in Synergetics. Berlin: Springer, 2009. ISBN: 978-3-540-72127-7 *Cited on pages 20, 21, 103, 133.*

[96] P. W. Bearman. "Circular cylinder wakes and vortex-induced vibrations". In: *J. Fluids. Struct.* 27.5-6 (July 2011), pp. 648–658. DOI: 10.1016/j.jfluidstructs.2011.03.021 *Cited on page 20.*

[97] F. M. Besem et al. "Vortex-Induced Vibration and Frequency Lock-In of an Airfoil at High Angles of Attack". In: *J. Fluid. Eng.* 138.1 (Aug. 2015), p. 011204. DOI: 10.1115/1.4031134 *Cited on pages 20, 106.*

[98] R. D. Blevins and C. S. Coughran. “Experimental Investigation of Vortex-Induced Vibration in One and Two Dimensions With Variable Mass, Damping, and Reynolds Number”. en. In: *J. Fluids. Eng.* 131.10 (Oct. 2009). ISSN: 0098-2202. DOI: 10.1115/1.3222904 *Cited on pages 20, 21, 24.*

[99] R. D. Gabbai and H. Benaroya. “An overview of modeling and experiments of vortex-induced vibration of circular cylinders”. In: *J. Sound. Vib.* 282.3 (2005), pp. 575–616. ISSN: 0022-460X. DOI: 10.1016/j.jsv.2004.04.017 *Cited on page 20.*

[100] R. Govardhan and C. H. K. Williamson. “Modes of vortex formation and frequency response of a freely vibrating cylinder”. In: *J. Fluid. Mech.* 420 (2000), pp. 85–130. DOI: 10.1017/S0022112000001233 *Cited on page 20.*

[101] A. Khalak and C. Williamson. “MOTIONS, FORCES AND MODE TRANSITIONS IN VORTEX-INDUCED VIBRATIONS AT LOW MASS-DAMPING”. en. In: *J. Fluid. Mech.* 13.7-8 (Oct. 1999), pp. 813–851. ISSN: 08899746. DOI: 10.1006/jfls.1999.0236 *Cited on pages 20, 23, 24, 81.*

[102] T. L. Morse and C. H. K. Williamson. “Prediction of vortex-induced vibration response by employing controlled motion”. In: *J. Fluid. Mech.* 634 (Aug. 2009), p. 5. DOI: 10.1017/s0022112009990516 *Cited on page 20.*

[103] K. Raghavan and M. M. Bernitsas. “Experimental investigation of Reynolds number effect on vortex induced vibration of rigid circular cylinder on elastic supports”. In: *Ocean Eng.* 38.5-6 (Apr. 2011), pp. 719–731. DOI: 10.1016/j.oceaneng.2010.09.003 *Cited on pages 20, 75.*

[104] R. A. Skop and O. M. Griffin. “A model for the vortex-excited resonant response of bluff cylinders”. In: *J. Sound. Vib.* 27.2 (1973), pp. 225–233. ISSN: 0022-460X. DOI: 10.1016/0022-460X(73)90063-1 *Cited on pages 20, 21, 30.*

[105] R. A. Skop and S. Balasubramanian. “A NEW TWIST ON AN OLD MODEL FOR VORTEX-EXCITED VIBRATIONS”. en. In: *J. Fluids. Struct.* 11.4 (May 1997), pp. 395–412. ISSN: 0889-9746. DOI: 10.1006/jfls.1997.0085 *Cited on pages 20, 21, 24, 30.*

[106] T. Sarpkaya. “A critical review of the intrinsic nature of vortex-induced vibrations”. In: *J. Fluids. Struct.* 19.4 (May 2004), pp. 389–447. DOI: 10.1016/j.jfluidstructs.2004.02.005 *Cited on pages 20, 23, 24, 81, 102, 108.*

[107] N. Srinil and H. Zanganeh. “Modelling of coupled cross-flow/in-line vortex-induced vibrations using double Duffing and van der Pol oscillators”. In: *Ocean Eng.* 53 (Oct. 2012), pp. 83–97. ISSN: 0029-8018. DOI: 10.1016/j.oceaneng.2012.06.025 *Cited on pages 21, 31.*

[108] C. Dyrbye and S. O. Hansen. *Wind loads on structures.* Chichester ; New York: J. Wiley, 1997. ISBN: 978-0-471-95651-8 *Cited on pages 22, 159.*

[109] C. H. K. Williamson and R. Govardhan. “Vortex-Induced Vibrations”. In: *Annu. Rev. Fluid. Mech.* 36.1 (Jan. 2004), pp. 413–455. DOI: 10.1146/annurev.fluid.36.050802.122128 *Cited on pages 23, 24, 81.*

[110] D. Akin. “Akins laws of spacecraft design”. In: *UMD Space Systems Laboratory* (2003) *Cited on page 25.*

[111] L. C. Pagnini, G. Piccardo, and G. Solari. “VIV regimes and simplified solutions by the spectral model description”. en. In: *J. Wind. Eng. Ind. Aerod.* 198 (Mar. 2020), p. 104100. ISSN: 0167-6105. DOI: 10.1016/j.jweia.2020.104100 *Cited on page 25.*

[112] Y. Tamura and G. Matsui. “Wake-oscillator model of vortex-induced oscillation of circular cylinder”. In: *Preceedings of the 5th International Conference on Wind Engineering, Vol. 2.* 1979, pp. 1085–1094 *Cited on pages 25, 30.*

[113] B. J. Vickery and R. Basu. "Simplified approaches to the evaluation of the across-wind response of chimneys". en. In: *J. Wind. Eng. Ind. Aerod.* 14.1 (Dec. 1983), pp. 153–166. ISSN: 0167-6105. DOI: 10.1016/0167-6105(83)90019-3 *Cited on pages 25, 27, 28, 97, 101, 107, 112, 120.*

[114] T. Lipecki, J. Bec, and P. Jamiska. "A comparative study of along-wind and crosswind responses of steel chimneys according to Polish and Eurocode standards". In: *Czasopismo Techniczne* (2016). DOI: 10.4467/2353737XCT.15.128.4165 *Cited on page 25.*

[115] F. Lupi, H.-J. Niemann, and R. Höffer. "A novel spectral method for cross-wind vibrations: Application to 27 full-scale chimneys". In: *J. Wind. Eng. Ind. Aerod.* 171 (2017), pp. 353–365. ISSN: 0167-6105. DOI: 10.1016/j.jweia.2017.10.014 *Cited on pages 25, 28, 111, 112, 117, 118, 120, 159.*

[116] H. van Koten and B. N. Pritchard. "Predicting crosswind movements of chimneys". In: *J. Wind. Eng. Ind. Aerod.* 23 (Jan. 1986), pp. 477–485. DOI: 10.1016/0167-6105(86)90064-4 *Cited on page 25.*

[117] R. Ciesielski, M. Gaczek, and J. Kawecki. "Observation results of cross-wind response of towers and steel chimneys". In: *J. Wind. Eng. Ind. Aerod.* 43.1-3 (Jan. 1992), pp. 2205–2211. DOI: 10.1016/0167-6105(92)90659-x *Cited on page 25.*

[118] H. van Koten. "Experiences with cross-wind vibrations of columns and chimneys". In: *Symposium on Practical Experiences with Flow-induced Vibrations*. Karlsruhe, Germany, 1979, pp. 720–723 *Cited on pages 25, 119, 159.*

[119] G. K. Verboom and H. van Koten. "Vortex excitation: Three design rules tested on 13 industrial chimneys". In: *J. Wind. Eng. Ind. Aerod.* 98.3 (Mar. 2010), pp. 145–154. DOI: 10.1016/j.jweia.2009.10.008 *Cited on page 25.*

[120] B. J. Vickery and R. I. Basu. "The response of reinforced concrete chimneys to vortex shedding". In: *Eng. Struct.* 6.4 (1984), pp. 324–333. ISSN: 0141-0296. DOI: 10.1016/0141-0296(84)90030-0 *Cited on pages 25, 97.*

[121] G. Hirsch and H. Ruscheweyh. "Full-scale measurements on steel chimney stacks". In: *J. Wind. Eng. Ind. Aerod.* 1 (Jan. 1975), pp. 341–347. DOI: 10.1016/0167-6105(75)90028-8 *Cited on pages 25, 89.*

[122] W. H. Melbourne, J. C. K. Cheung, and C. R. Goddard. "Response to wind action of 265-m Mount Isa stack". In: *J. Struct. Eng.* 109.11 (1983), pp. 2561–2577 *Cited on pages 25, 89.*

[123] F. P. Müller and H. Nieser. "Measurements of wind-induced vibrations on a concrete chimney". In: *J. Wind. Eng. Ind. Aerod.* 1 (1975), pp. 239–248. ISSN: 0167-6105. DOI: 10.1016/0167-6105(75)90019-7 *Cited on pages 25, 89.*

[124] R. Scherer. "Stochastic characteristics of vortex shedding at a 230 m high concrete chimney". In: *Proc. ICOSSAR'93*. Vol. 93. 1993 *Cited on pages 25, 26, 32.*

[125] S. Sanada, M. Suzuki, and H. Matsumoto. "Full scale measurements of wind force acting on a 200m concrete chimney, and the chimney's response". In: *J. Wind. Eng. Ind. Aerod.* 43.1-3 (Jan. 1992), pp. 2165–2176. DOI: 10.1016/0167-6105(92)90651-p *Cited on pages 25, 26, 32, 89.*

[126] J. L. Waldeck. "The measured and predicted response of a 300 m concrete chimney". In: *J. Wind. Eng. Ind. Aerod.* 41.1-3 (Oct. 1992), pp. 229–240. DOI: 10.1016/0167-6105(92)90415-7 *Cited on pages 25, 26, 89.*

[127] T. Galemann and H. Ruscheweyh. “Measurements of wind induced vibrations of a full-scale steel chimney”. In: *J. Wind. Eng. Ind. Aerod.* 41.1-3 (Oct. 1992), pp. 241–252. DOI: 10.1016/0167-6105(92)90416-8 *Cited on pages 25, 26, 89.*

[128] O. Christensen and V. Askegaard. “Wind forces on and excitation of a 130-m concrete chimney”. In: *J. Wind. Eng. Ind. Aerod.* 3.1 (1978), pp. 61–77. ISSN: 0167-6105. DOI: 10.1016/0167-6105(78)90028-4 *Cited on pages 25, 26, 89.*

[129] S. O. Hansen. “Cross-wind vibrations of a 130-m tapered concrete chimney”. In: *J. Wind. Eng. Ind. Aerod.* 8.1-2 (July 1981), pp. 145–155. DOI: 10.1016/0167-6105(81)90015-5 *Cited on pages 26, 89.*

[130] J. L. Waldeck. “Measurement of wind effects on a 300-M concrete chimney reference paramters”. en. In: *J. Wind. Eng. Ind. Aerod.* 32.1 (Sept. 1989), pp. 199–209. ISSN: 0167-6105. DOI: 10.1016/0167-6105(89)90030-5 *Cited on page 26.*

[131] H. Ruscheweyh. “Wind loadings on the television tower, Hamburg, Germany”. In: *J. Wind. Eng. Ind. Aerod.* 1 (Jan. 1975), pp. 315–333. DOI: 10.1016/0167-6105(75)90026-4 *Cited on page 26.*

[132] J. Van Nunen. “Steady and unsteady pressure and force measurements on a circular cylinder in a cross flow at high Reynolds numbers”. In: *NLR MP 72013 U* (1972). Publisher: Nationaal Lucht-en Ruimtevaartlaboratorium *Cited on page 26.*

[133] D. Zuo. “Full-scale measurement of wind pressure on the surface of an oscillating circular cylinders”. In: *J. Wind. Eng. Ind. Aerod.* 133 (Oct. 2014), pp. 65–79. DOI: 10.1016/j.jweia.2014.08.001 *Cited on pages 26, 89.*

[134] B. J. Vickery and A. W. Clark. “Lift or across-wind response to tapered stacks”. In: *J. Struct. Div.* 98.1 (1972), pp. 1–20 *Cited on page 27.*

[135] A. Kareem and K. Gurley. “Damping in structures: its evaluation and treatment of uncertainty”. en. In: *J. Wind. Eng. Ind. Aerod.* Meeting on Structural Damping International Wind Engineering Forum and Additional Papers 59.2 (Mar. 1996), pp. 131–157. ISSN: 0167-6105. DOI: 10.1016/0167-6105(96)00004-9 *Cited on page 27.*

[136] H. Ruscheweyh. *The vortex excited amplitude*. Tech. rep. RWTH Aachen, 1985 *Cited on pages 29, 30.*

[137] E. Berger. “On a mechanism of vortex excited oscillations of a cylinder”. In: *J. Wind. Eng. Ind. Aerod.* 28.1-3 (Aug. 1988), pp. 301–310. DOI: 10.1016/0167-6105(88)90126-2 *Cited on page 30.*

[138] G. Birkhoff and E. H. Zarantonello. *Jets, Wakes, and Cavities*. en. Elsevier, Dec. 2012. ISBN: 978-0-323-16271-5 *Cited on page 30.*

[139] A. H. Nayfeh and D. T. Mook. *Nonlinear Oscillations*. John Wiley & Sons, 1995 *Cited on pages 30, 133.*

[140] Y. Tamura and A. Amano. “Mathematical model for vortex-induced oscillations of continuous systems with circular cross section”. In: *Wind Engineering 1983*. Elsevier, 1984, pp. 431–442. DOI: 10.1016/b978-0-444-42341-2.50053-2 *Cited on page 30.*

[141] R. H. M. Ogink and A. V. Metrikine. “A wake oscillator with frequency dependent coupling for the modeling of vortex-induced vibration”. en. In: *J. Sound. Vib.* 329.26 (Dec. 2010), pp. 5452–5473. ISSN: 0022-460X. DOI: 10.1016/j.jsv.2010.07.008 *Cited on pages 31, 112.*

[142] M. S. Aswathy and S. Sarkar. “Effect of stochastic parametric noise on vortex induced vibrations”. In: *Int. J. Mech. Sci.* 153-154 (Apr. 2019), pp. 103–118. DOI: 10.1016/j.ijmecsci.2019.01.039 *Cited on pages 31, 83, 127.*

[143] E. Boujo and N. Noiray. "Robust identification of harmonic oscillator parameters using the adjoint FokkerPlanck equation". In: *P. Roy. Soc. A-Math Phy.* 473.2200 (Apr. 2017), p. 20160894. DOI: 10.1098/rspa.2016.0894 *Cited on page 31.*

[144] V. Denoël. "Derivation of a slow phase model of vortex-induced vibrations for smooth and turbulent oncoming flows". en. In: *J. Fluids. Struct.* 99 (Nov. 2020), p. 103145. ISSN: 08899746. DOI: 10.1016/j.jfluidstructs.2020.103145 *Cited on pages 31, 104, 127.*

[145] F. Rüdinger and S. Krenk. "Stochastic Analysis of Self-Induced Vibrations". en. In: *Meccanica* 37.1 (Jan. 2002), pp. 3–14. ISSN: 1572-9648. DOI: 10.1023/A:1019696627696 *Cited on page 31.*

[146] J. B. Roberts. "Stationary response of oscillators with non-linear damping to random excitation". en. In: *J. Sound. Vib.* 50.1 (Jan. 1977), pp. 145–156. ISSN: 0022-460X. DOI: 10.1016/0022-460X(77)90557-0 *Cited on page 31.*

[147] G. S. West and C. J. Apelt. "The effects of tunnel blockage and aspect ratio on the mean flow past a circular cylinder with Reynolds numbers between 104 and 105". en. In: *Journal of Fluid Mechanics* 114 (Jan. 1982). Publisher: Cambridge University Press, pp. 361–377. ISSN: 1469-7645, 0022-1120. DOI: 10.1017/S0022112082000202 *Cited on page 36.*

[148] H. Bergh and H. Tijdeman. *Theoretical and experimental results for the dynamic response of pressure measuring systems*. en. Tech. rep. NLR-TR F.238. Publisher: Nationaal Lucht- en Ruimtevaartlaboratorium. Amsterdam, Netherlands: National aero- and astronautical research institute, 1965 *Cited on page 39.*

[149] N. Aubry, R. Guyonnet, and R. Lima. "Spatiotemporal analysis of complex signals: Theory and applications". en. In: *J. Stat. Phys.* 64.3 (Aug. 1991), pp. 683–739. ISSN: 1572-9613. DOI: 10.1007/BF01048312 *Cited on page 43.*

[150] M. Pastor, M. Binda, and T. Harik. "Modal Assurance Criterion". en. In: *Procedia Eng.* 48 (2012), pp. 543–548. ISSN: 18777058. DOI: 10.1016/j.proeng.2012.09.551 *Cited on pages 65, 132.*

[151] Z. J. Ding et al. "Lift and Damping Characteristics of Bare and Straked Cylinders at Riser Scale Reynolds Numbers". en. In: *Offshore Technology Conference*. OnePetro, May 2004, pp. 1–9. DOI: 10.4043/16341-MS *Cited on page 75.*

[152] S. B. Swithenbank et al. "Reynolds Number Dependence of Flexible Cylinder VIV Response Data". en. In: *Proceedings of the ASME 27th International Conference on Offshore Mechanics and Arctic Engineering*. American Society of Mechanical Engineers Digital Collection, July 2009, pp. 503–511. DOI: 10.1115/OMAE2008-57045 *Cited on page 75.*

[153] L. Cohen. *Time-frequency analysis*. Prentice Hall signal processing series. Englewood Cliffs, N.J: Prentice Hall PTR, 1995. ISBN: 978-0-13-594532-2 *Cited on pages 79, 92, 131.*

[154] H. Ruscheweyh and T. Galemann. "Full-scale measurements of wind-induced oscillations of chimneys". In: *J. Wind. Eng. Ind. Aerod.* 65.1-3 (Dec. 1996), pp. 55–62. DOI: 10.1016/s0167-6105(97)00022-6 *Cited on page 89.*

[155] J. Wakefield. *Bayesian and frequentist regression methods*. eng. Softcover re-print of the hardcover 1st edition 2013. Springer series in statistics 555. New York: Springer, 2013. ISBN: 978-1-4419-0925-1 *Cited on pages 92, 157.*

[156] J. L. Hintze and R. D. Nelson. "Violin Plots: A Box Plot-Density Trace Synergism". en. In: *Am. Stat.* 52.2 (May 1998), pp. 181–184. ISSN: 0003-1305, 1537-2731. DOI: 10.1080/00031305.1998.10480559 *Cited on page 94.*

[157] Ø. M. Ellingsen, X. Amandolese, and P. Hémon. "Assessing maximum amplitude and corresponding frequency for vortex-induced vibrations". In: *Proceedings of the Second Internation Symposium on Flutter and its Applications*. Paris, May 2020, pp. 333–341 *Cited on pages 102, 107.*

[158] S. O. Hansen. *Vortex induced vibrations of line-like structures*. Tech. rep. Vol. 15, No. 1. CICIND, 1999, pp. 15–23 *Cited on pages 118, 119, 159.*

[159] A. V. Oppenheim, A. S. Willsky, and S. H. Nawab. *Signals & systems*. 2nd ed. Prentice-Hall signal processing series. Upper Saddle River, N.J: Prentice Hall, 1997. ISBN: 978-0-13-814757-0 *Cited on page 131.*

[160] M. Feldman. "Hilbert transform in vibration analysis". en. In: *Mech. Syst. Signal Pr.* 25.3 (Apr. 2011), pp. 735–802. ISSN: 08883270. DOI: 10.1016/j.ymssp.2010.07.018 *Cited on page 131.*

[161] R. J. Allemang. "The Modal Assurance Criterion - Twenty Years of Use andAbuse". In: *J. Sound. Vib.* (Aug. 2003) *Cited on page 132.*

[162] H. Jeffreys. *Theory of probability*. 3rd ed. Oxford classic texts in the physical sciences. Oxford [Oxfordshire] : New York: Clarendon Press ; Oxford University Press, 1998. ISBN: 978-0-19-850368-2 *Cited on page 132.*

[163] C. Rundel et al. *statsr: Companion Software for the Coursera Statistics with R Specialization*. 2020 *Cited on page 132.*

[164] R. E. Kass and A. E. Raftery. "Bayes Factors". en. In: *J. Am. Stat. Assoc.* 90.430 (June 1995), pp. 773–795. ISSN: 0162-1459, 1537-274X. DOI: 10.1080/01621459.1995.10476572 *Cited on page 133.*

[165] M. Clobes, A. Willecke, and U. Peil. "Vortex excitation of steel chimneys: Two ultimate limit states". In: *Proceedings of the 13th International Conference on Wind Engineering, Amsterdam*. 2011 *Cited on page 159.*

[166] A. F. Daly. "Evaluation of methods of predicting the across-wind response of chimneys". In: *CICIND report* 2.1 (1986), pp. 9–46 *Cited on page 159.*

[167] S. Frandsen. *RISØ kontrakt rapport: Tværsvingninger af stålskorstene*. Feltmålinger, 1979 *Cited on page 159.*

[168] G. Hirsch, H. Ruscheweyh, and H. Zutt. "Schadensfall an einem 140 m hohen Stahlkamin infolge winderregter Schwingungen quer zur Windrichtung". In: *Der Stahlbau* 44.2 (1975), pp. 33–41 *Cited on page 159.*

[169] W. Langer, H. Ruscheweyh, and C. Verwiebe. *Untersuchung des Querschwingungsverhaltens von Original-Stahlschornsteinen: Forschungsbericht P 230*. Studienges. Stahlanwendung, 1996 *Cited on page 159.*

[170] K. Nakagawa. "An experimental study of aerodynamic devices for reducing wind-induced oscillatory tendencies of stacks". In: *Bull. Univ/ Osaka Prefect, Ser A* 13(2) (1965), pp. 1–18. DOI: 10.24729/00008907 *Cited on page 159.*

[171] B. N. Pritchard. "Oscillation of steel stacks-a new design parameter". In: *Proc. 5th Intern. Congress*. CICIND Essen, W. Germany, 1984, pp. 147–153 *Cited on page 159.*

[172] H. Ruscheweyh and C. Verwiebe. "Experiences with vortex excited oscillations of steel chimneys". In: *CICIND Report* 11.2 (1995), pp. 30–39 *Cited on page 159.*

[173] H. Ruscheweyh. *Ein verfeinertes, praxisnahes Berechnungsverfahren wirbelerregter Schwingungen von schlanken Baukonstruktionen im Wind*. Beiträge zur Anwendung der Aeroelastik im Bauwesen. Universität Innsbruck, 1986 *Cited on page 159.*

[174] P. Tranvik and G. Alpsten. "Long-term measurements of structural response of a tall steel chimney equipped with different damping devices". In: *4th European and African Conference on Wind Engineering*. Prague, Czech Republic, 2005, pp. 322–323 *Cited on page 159.*

ECOLE DOCTORALE

Titre : Effet de l'excitation des structures cylindriques par les tourbillons alternés : modélisation de l'amplitude pour les codes de construction

Mots clés : Aeroelasticité, Ingénierie du vent, Vibrations, Vibrations induites par vortex, Cheminée

Résumé : Les vibrations causées par le détachement de tourbillons alternés (vibrations induites par vortex) constituent une préoccupation majeure lors de la conception de cheminées industrielles. Cette excitation est due à un couplage non linéaire entre le lâcher tourbillonnaire et le mouvement d'oscillation. Elle peut engendrer des amplitudes de vibration élevées à faible vitesse de vent. Il existe de nombreuses méthodes pour les prédire et la plupart d'entre elles doivent être améliorées.
Pour améliorer les prédictions en soufflerie, il est nécessaire de connaître l'écoulement autour des cylindres circulaires à des nombres de Reynolds élevés. Une expérience dans une grande soufflerie a révélé une nouvelle information concernant la fréquence de lâcher des tourbillons à grands nombres de Reynolds : au lieu d'une seule fréquence, nous avons trouvé deux nombres de Strouhal bien distincts, 0.2 et 0.25 environ. Or de nombreuses études antérieures avaient trouvé des nombres de Strouhal dispersés dans l'intervalle 0.2-0.25 sans plus de précision.
De plus, les distributions de pression instationnaire et les mesures de force à grande échelle sont utilisées pour valider une méthode expérimentale pour simuler un écoulement à haut nombre de Reynolds dans une soufflerie à petite échelle. Des éléments de rugosité collés sur la surface peuvent déclencher un écoulement à nombre de Reynolds élevé et reproduire en grande partie les distributions de pression instationnaire. Néanmoins, les fréquences de lâcher de tourbillons et les efforts restent différents à petite échelle.
Dans des essais aéroélastiques 3D, on trouve que la couche limite atmosphérique turbulente affecte davantage l'écoulement que les rugosités artificielles. Sans couche limite atmosphérique, la réponse augmente et diffère entre le cylindre rugueux et le cylindre lisse. Ces résultats ont été corroborés par une expérience vraie grandeur sur site avec des profils de couche limite variant naturellement.
Une autre méthode pour prédire les vibrations induites par les tourbillons consiste à utiliser des modèles analytiques. Pour trouver le meilleur modèle, deux modèles classiques sont comparés à un nouveau modèle approximatif. Les résultats dépendent du produit masse-amortissement. Lorsque ce produit est faible, le nouveau modèle fonctionne mieux, tandis que l'un des modèles classiques reste meilleur lorsque ce produit masse-amortissement est élevé.

Title : Vortex-induced vibrations on industrial chimneys

Keywords : Aeroelasticity, Wind engineering, Vibrations, Vortex-induced vibrations, Chimney

Abstract : Vibrations due to the alternating shedding of vortexes (vortex-induced vibrations) are a great concern when designing industrial chimneys. These vibrations are complex and can give large amplitudes of motion at low speeds. There are many methods for predicting these vibrations (e.g. wind tunnels or predictive models) but they need improvements.
An experiment in a large wind tunnel revealed important, new knowledge on the vortex-shedding frequency which will help predict vortex-induced vibrations using wind tunnels. Instead of a finding a single vortex-shedding frequency, either in the range 0.25-0.27 or near 0.2 as in previous studies, two distinct Strouhal numbers were found at around 0.2 and 0.25. In addition, the spatial unsteady pressure distributions and forcing results at large-scale helped validate an experimental method for simulating the high Reynolds number flow in smaller wind tunnels. These tests showed that surface roughness can trigger high Reynolds number flow and mostly reproduce the spatial pressure distributions. While promising, the vortex-shedding frequencies and forces were different at small-scale than at large-scale.
Turbulent atmospheric boundary layers were found to affect the response more than the surface roughness in 3D aeroelastic tests. When testing a rough and a smooth cylinder with a turbulent boundary layer, the responses were similar but the vibration amplitudes and differences increased when testing without the boundary layer. The importance of the turbulent boundary layer on the response was corroborated in a field experiment on a chimney exposed to naturally varying turbulence profiles.
Lastly, ways to improve analytic modeling of predicting vortex-induced vibrations were found by finding the best model for a given situation. This was done using two classical design models and a newly approximated model and the best predictive model was found to depend on the product of mass and damping. When this product was low, the newly approximated model worked best while one of the design models was better when the mass-damping product was high.

Institut Polytechnique de Paris
91120 Palaiseau, France